Physik-Department

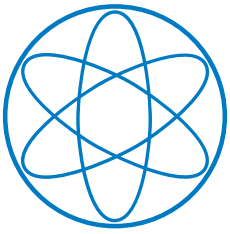

Superconducting flux quantum circuits: characterization, quantum coherence, and controlled symmetry breaking

Dissertation
von

Frank Deppe

Technische Universität
München

TECHNISCHE UNIVERSITÄT MÜNCHEN

Lehrstuhl E23 für Technische Physik

Walther-Meißner-Institut für Tieftemperaturforschung
der Bayerischen Akademie der Wissenschaften

Superconducting flux quantum circuits: characterization, quantum coherence, and controlled symmetry breaking

Frank Deppe

Vollständiger Abdruck der von der Fakultät für Physik der Technischen Universität München zur Erlangung des akademischen Grades eines

Doktors der Naturwissenschaften

genehmigten Dissertation.

Vorsitzender:		Univ.-Prof. Dr. P. Vogl
Prüfer der Dissertation:	1.	Univ.-Prof. Dr. R. Gross
	2.	Hon.-Prof. Dr. G. Rempe

Die Dissertation wurde am 29.12.2008 bei der Technischen Universität München eingereicht und durch die Fakultät für Physik am 25.03.2009 angenommen.

Half a bee, philosophically,
Must, ipso facto, half not be.
But half the bee has got to be
Vis a vis, its entity. D'you see?

But can a bee be said to be
Or not to be an entire bee
When half the bee is not a bee
Due to some ancient injury?

from: Monty Python, "Eric The Half A Bee"

Contents

Contents v

1 Introduction 1

2 Superconducting flux quantum circuits 5
2.1 The Josephson junction . . . 5
2.2 The DC SQUID . . . 6
2.3 Quantization of charge and flux . . . 9
2.4 Superconducting qubits . . . 10
2.5 The three-Josephson-junction flux qubit . . . 11
2.6 Bloch vector and Bloch sphere . . . 15
2.7 The LC-resonator . . . 15
2.8 Circuit QED . . . 16
2.9 Spurious fluctuators . . . 18

3 Experimental techniques 19
3.1 Capacitance of nanoscale Josephson junctions . . . 19
3.1.1 Capacitance from DC SQUID resonances . . . 20
3.1.2 Ambegaokar-Baratoff relation . . . 23
3.1.3 Capacitance from continuous-wave qubit spectroscopy . . . 24
3.2 Conventional readout of a flux qubit . . . 25
3.2.1 Slow-sweep readout . . . 26
3.2.2 Continuous-wave qubit microwave spectroscopy . . . 27
3.2.3 Resistive-bias pulsed readout . . . 28
3.2.4 Adiabatic-shift pulse method . . . 30
3.3 Capacitive-bias readout of a flux qubit . . . 32
3.4 Qubit operation . . . 35
3.4.1 Qubit rotations on the Bloch sphere . . . 35
3.4.2 The microwave antenna . . . 36
3.4.3 Pulse sequences . . . 36
3.4.4 The Phase-cycling method . . . 36
3.5 Pulse generation and detection . . . 38

4 Decoherence of a superconducting flux qubit 41
4.1 Quantum coherence and decoherence . . . 42
4.2 Spectroscopy results . . . 43
4.3 Coherence properties of the flux qubit . . . 46
4.3.1 Energy relaxation . . . 46
4.3.2 Dephasing . . . 49

4.4 Ramsey and spin echo beatings . . . 53
4.5 Noise sources . . . 57
4.6 Conclusions . . . 60

5 Controlled symmetry breaking in circuit QED 63
5.1 Qubit-resonator system . . . 64
5.2 Anticrossing under two-photon driving . . . 65
5.3 Upconversion dynamics . . . 69
5.4 Selection rules and symmetry breaking . . . 70
5.5 Conclusions . . . 72

6 Summary 73

7 Outlook: Two-resonator circuit QED 75

A Sample fabrication 79
A.1 Josephson junctions . . . 79
A.2 DC SQUIDs . . . 80
A.3 Flux qubits . . . 80

B Cryogenic setup 83
B.1 The dilution refrigerator . . . 83
B.2 Slow-sweep qubit spectroscopy . . . 83
B.3 Pulsed qubit measurements . . . 86

C Multiphoton excitations 89
C.1 Dyson-series approach . . . 89
C.1.1 The commutator theorem . . . 89
C.1.2 Two-photon driving via commutator theorem . . . 90
C.2 Schrieffer-Wolff transformation . . . 91
C.3 Bessel expansion in a nonuniformly rotating frame . . . 95
C.3.1 Weak-driving regime . . . 95
C.3.2 Beyond the weak-driving regime . . . 97

D Spectroscopy simulations 103
D.1 Time-trace-averaging method . . . 103
D.2 Lindblad approach . . . 104

Bibliography 105

List of Publications 118

Acknowledgments 120

Chapter 1

Introduction

In recent years, the investigation of superconducting quantum circuits has evolved into a prospering branch of solid-state physics. Although these systems are macroscopic in size – some of them can reach dimensions of up to several millimeters and are visible to the naked eye – they still exhibit a behavior unique to the world of quantum mechanics when cooled to millikelvin temperatures. This is a quite remarkable phenomenon, considering that due to the small but finite value of the Planck constant, the experimental observability of quantum effects is, at a first glance, expected only for objects whose size is not significantly larger than that of natural atoms or small molecules. Consequently, with respect to their electrical properties, conventional solid-state circuits should behave mostly as classical objects because they consist of a large number of atoms and the current flowing through them is carried by a large number of electrons. This argument, however, does not apply to superconducting circuits. Since in the superconducting state all Cooper pairs can be described by a single macroscopic wave function [1–3], they show quantum mechanical behavior in a macroscopic degree of freedom (charge or flux/phase), a feature referred to as macroscopic quantum coherence [4, 5]. In this way, superconducting quantum circuits can act as artificial atoms on a chip, allowing for the controlled design of experiments addressing fundamental quantum phenomena. When the two lowest energy levels of such an artificial atom are well isolated from the higher ones, one obtains a quantum two-level system [6] or qubit. Qubits are the central elements in the field of quantum information processing [7], promising significant speedup for certain computational tasks [8–13], an efficient simulation of large quantum systems [14], and secure quantum communication and cryptography. In contrast to their natural counterparts, artificial atoms made from superconducting quantum circuits are tunable to a high degree, both by design and in-situ during the experiments. Furthermore, superconducting quantum circuits are, from the fabrication point of view, easily scalable to larger units. The reason is that the fabrication process mainly involves state-of-the-art lithographic patterning and thin-film deposition.

Of critical importance for the construction of solid-state qubits are nonlinear elements. Their existence gives rise to the required anharmonicity in the qubit potential. In superconducting circuits, superconductor-insulator-superconductor Josephson tunnel junctions [2, 15] constitute by far the most prominent source of nonlinearity. Artificial two-level systems based on such tunnel junctions are referred to as Josephson qubits [16–19]. They can be divided into three major groups, depending

on the quantum variable governing their dynamics. In charge qubits [20], the quantum information is encoded in the presence or absence of an excess Cooper pair on a small superconducting island, which is separated from a reservoir by two Josephson junctions. Further optimization this original design has lead to the development of the quantronium [21] and the transmon [22–24]. The conjugate variable of the charge is the magnetic flux. In flux qubits, persistent currents of opposite sign in a superconducting loop interrupted by one [25, 26] or more [27, 28] Josephson junctions carry the qubit information. In phase qubits [29], the quantum information is stored in oscillatory states of a suitably anharmonic potential of a current-biased Josephson junction. Experimentally, the required current bias is often applied via the flux degree of freedom [30] exploiting the fluxoid quantization in a superconducting loop [2, 3].

The quantum nature of all types of Josephson qubits mentioned above has been confirmed experimentally by measuring coherent oscillations [29, 31–35]. However, despite the fact that superconducting qubits are protected by the superconducting gap [2, 3] from the solid-state environment, decoherence due to uncontrolled entanglement with environmental degrees of freedom still represents a major problem. In particular, low-frequency noise causes the loss of phase coherence, whereas high-frequency noise induces qubit decay [35, 36]. Deteriorating noise can arise from external sources such as the qubit control and readout circuitry [35, 37], but also the impact of internal sources such as charge noise [38] or fluctuators in the tunnel barriers [35, 39–43] is considered to be significant. Experiments suggest that ensembles of fluctuators can cause low-frequency $1/f$-noise [35, 44, 45] as well as high-frequency noise [30]. To date, the best decoherence times of Josephson qubits are of the order of a few microseconds [23, 24, 44, 46]. Nevertheless, basic two-qubit gate operations have been demonstrated, both in fixed coupling schemes [47–50] and in setups allowing for controllable coupling [51–54]. In addition, the nonlinearity and tunability of the qubit circuits stimulated several studies about the rich variety of phenomena related to multiphoton transitions induced by a classical microwave driving [31, 55–59].

By means of a mutual capacitance or inductance, superconducting qubits can be coupled to linear quantum circuits acting as resonators. In this way, it becomes possible to perform experiments on a chip, which are analogous to those probing the interaction of light and matter in quantum-optical cavity quantum electrodynamics (QED) [60–63]. This exciting field is referred to as circuit QED [64–66]. There, the qubit plays the role of the natural atom (matter), whereas the resonator is identified with the cavity (light). The main advantages of circuit QED over cavity QED reside in the tunability of the qubits and resonators [67] and the possibility to reach the strong coupling limit [68–70], where the coupling is larger than all relevant decoherence rates. Recently, a variety of phenomena has been addressed in circuit QED experiments. Vacuum Rabi oscillations between a flux qubit and a resonator were observed [71]. The photon number splitting of a transmon qubit coupled to a coplanar waveguide resonator could be shown [69, 72, 73] and single microwave photons created and detected [74]. The principle of a cavity behaving as a quantum bus [52, 53] or a quantum memory [53] was successfully demonstrated. Furthermore, a DC-pumped maser working only with a single artificial atom [75] and microwave cooling schemes for Josephson qubits [76, 77] were realized. Very recently, two-qubit entanglement mediated by a resonator via sideband transitions was generated [78,

79] and three transmon qubits were coupled to a single resonator [80].

This thesis concentrates on the investigation of superconducting flux quantum circuits, which are, intrinsically, insensitive to charge noise. In particular, the three-Josephson-junction flux qubit [27, 28] is the center of our studies. After introducing the basic ingredients for building superconducting flux quantum circuits in chapter 2, we first investigate the capacitance of the used $Al/AlO_x/Al$ Josephson junctions in Sec. 3.1. A good control over this capacitance (and other junction properties, of course) is indispensable for the proper design and reliable fabrication of more complex circuits such as DC SQUIDS and qubits. The rest of chapter 3 is devoted to the discussion of basic experimental techniques required for the control and readout of our flux qubit. In particular, we explain the conventional DC SQUID-based readout scheme and, in Sec. 3.3, a novel variant based on a capacitive bias for the DC SQUID. The qubit decay and phase coherence times measured with this scheme are discussed in detail in chapter 4. We probe the $1/f$- and white noise contributions to the total flux noise spectral density in the vicinity of the so-called optimal point, where the qubit phase coherence is expected to be best, and away from it. Comparing to measurements with the conventional method on the same qubit, we can examine the effect of different electromagnetic environments – bandpass filter type and low-pass filter type – on the qubit coherence properties. In addition, we address the important question of the relevant noise sources for our system. Next, in chapter 5, we investigate fundamental symmetry properties of a flux-based circuit QED system. The latter consists of our flux qubit coupled to a superconducting lumped-element resonator, which is part of the qubit readout circuitry. In particular, we discuss the appearance of electric-dipole type selection rules for multiphoton excitations at the qubit optimal point. We further focus on the upconversion dynamics emerging when the symmetry of the system is broken, either by deliberately changing the qubit control parameter or by the presence of spurious fluctuators. After a brief summary in chapter 6, we shine a spotlight on the promising new research field of two-resonator circuit QED, where two resonators are simultaneously coupled to a single qubit. Finally, in the appendices, we describe in detail our substantial effort in fabrication, cryogenics, analytical theory and simulations, which was necessary to obtain the results presented in this work.

Chapter 2

Superconducting flux quantum circuits

In this chapter, an overview of superconducting flux quantum circuits and their functional elements is given. First, we describe the fundamental source of nonlinearity, the Josephson junction. It can be used to design quantum circuits behaving as artificial two-level atoms. Next, we describe one particular flux quantum circuit, the flux qubit. It is the key element in the experiments presented in chapters 3-5. We then introduce the field of circuit quantum electrodynamics (QED). There, in analogy to quantum-optical cavity QED [60–63], qubits are coupled to linear quantum circuits, harmonic oscillators. In this way, the interaction of solid-state artificial atoms with single microwave photons can be studied. Finally, we discuss the effect of spurious fluctuators in the tunneling barriers.

2.1 The Josephson junction

Josephson junctions, which are discussed in detail in Ref. [15] and Ref. [2], are generally defined as a weak link between two superconductors. In this work, we are concerned with superconductor-insulator-superconductor-type Josephson junction, where an insulating material is sandwiched between two superconducting electrodes. In particular, the electrodes and barrier are made of aluminum and aluminum oxide, respectively. Following the laws of quantum mechanics, Cooper pairs can tunnel through this insulating barrier when it is sufficiently thin. Semiclassically, this process is described by the two Josephson equations

$$I = I_{\mathrm{c}} \sin \gamma \tag{2.1}$$

$$\frac{d\gamma}{dt} = \frac{2\pi V}{\Phi_0} \tag{2.2}$$

Here, I is the superconducting zero-voltage current, I_{c} the junction critical current, γ the difference in the phase of the macroscopic wave function across the junction, V a voltage difference maintained across the junction, $\Phi_0 \equiv h/(2e)$ the superconducting flux quantum, and e the elementary charge. A real Josephson junction can be described with the equivalent circuit sketched in Fig. 2.1(a). In this resistively-and-capacitively-shunted Josephson junction (RCSJ) model, a capacitance C and a tunnel resistance R shunt the ideal Josephson supercurrent branch. When applying

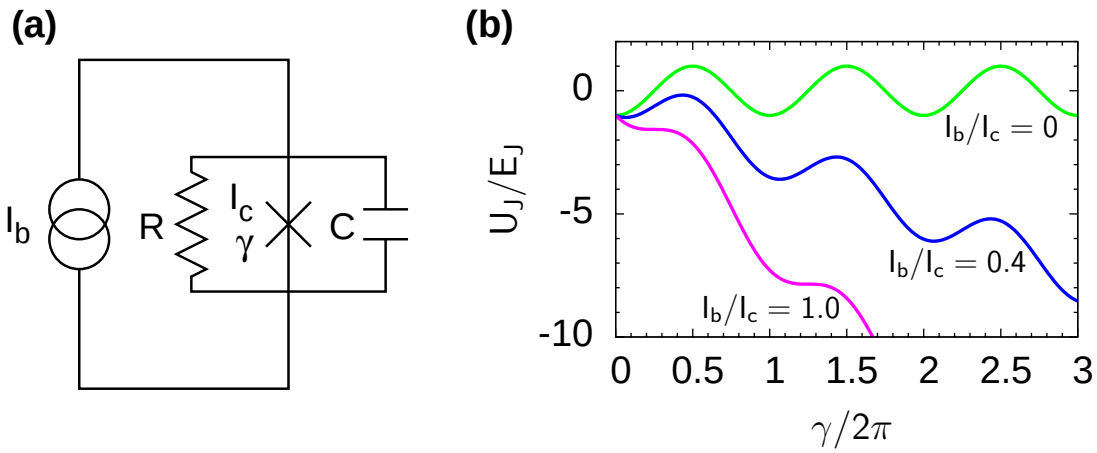

Figure 2.1: The resistively-and-capacitively-shunted Josephson junction (RCSJ) model. **(a)** Equivalent circuit. The supercurrent branch (cross symbol) can also be interpreted as a nonlinear inductor, the Josephson inductance. **(b)** Sketch of the tilted washboard potential of Eq. (2.3) for various bias currents.

a bias current I_b to the junction, the equations of motion are equivalent to those of a particle of mass $C(\Phi_0/2\pi)^2$ moving in the one-dimensional potential

$$U_\mathrm{J}(\gamma) = -E_\mathrm{J}\left(\cos\gamma + \frac{I_\mathrm{b}}{I_\mathrm{c}}\gamma\right) . \tag{2.3}$$

Here, $E_\mathrm{J} \equiv I_\mathrm{c}\Phi_0/2\pi$ is the Josephson energy. The potential U_J is visualized in Fig. 2.1(b). For $I_\mathrm{b} \neq 0$, it has the shape of a tilted washboard. When $I_\mathrm{b} \geq I_\mathrm{c}$, the metastable minima disappear. The motion of the phase particle inside the washboard potential is damped by the resistor, the damping factor is $1/R$. For $I_\mathrm{b} \gg I_\mathrm{c}$, the junction essentially behaves like a normal resistance R.

We note that the supercurrent branch in Fig. 2.1(a) can also be interpreted in terms of a nonlinear inductor. This Josephson inductance $L_\mathrm{J} = (d^2U_\mathrm{J}/d\Phi^2)^{-1}$ is phase- and, hence, bias-current dependent. Using the Josephson equations, Eq. (2.1) and Eq. (2.2), and the relation $\gamma = 2\pi\Phi/\Phi_0$, one obtains $L_\mathrm{J} = \Phi_0/(2\pi I_\mathrm{c}\cos\gamma) = \pm\Phi_0/(2\pi\sqrt{I_\mathrm{c}^2 - I_\mathrm{b}^2})$. In contrast to an ordinary nonlinear inductance, L_J can assume negative values. In addition to the Josephson energy E_J, the junction behavior is governed by another characteristic energy scale, the charging energy $E_\mathrm{c} \equiv e^2/2C$. E_J and E_c are the energies required to store one flux quantum in the Josephson inductance L_J and one elementary charge in the capacitance C of the junction, respectively.

Josephson junctions are a key ingredient for the design of nonlinear superconducting flux quantum circuits. In Sec. 2.2 and Sec. 2.5, we introduce the Josephson-junction-based circuits which are relevant for this work.

2.2 The DC SQUID

A superconducting loop containing two Josephson junctions is called DC superconducting quantum interference device (SQUID). Such a device can be used as a highly sensitive detector for magnetic flux. For this reason, a DC SQUID is suitable to read out the state of the superconducting flux qubit described in Sec. 2.5. This readout

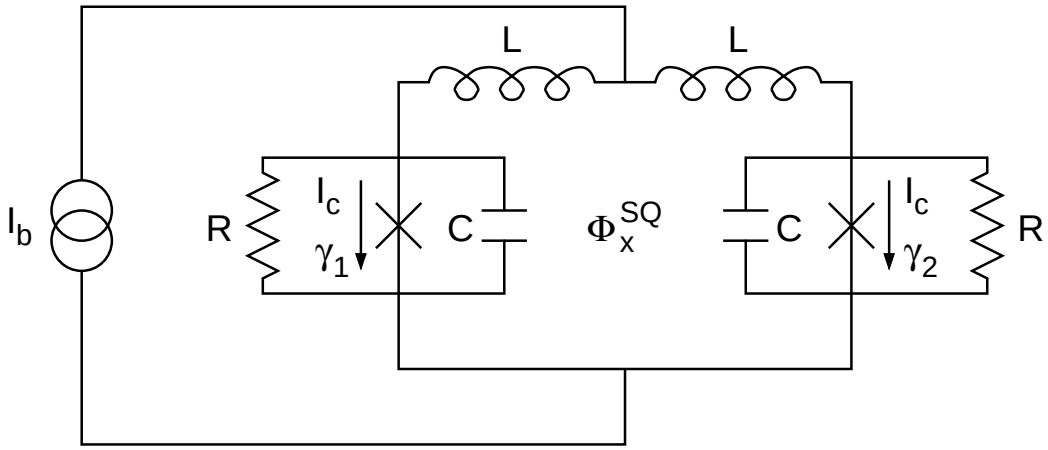

Figure 2.2: Current-biased DC SQUID in the RCSJ model. A current source supplies the bias current I_b to a superconducting loop, which is interrupted by two Josephson junctions. Each of the two supercurrent branches (symbolized by a cross) has a resistance R and a capacitance C connected in parallel. The critical current I_c is the maximum supercurrent which can be carried by the junction. The arrows denote the phase differences γ_1 and γ_2 across the junctions. The loop has a total inductance $2L$ and is penetrated by an external flux $\Phi_\mathrm{x}^\mathrm{SQ}$ in perpendicular direction. The sketched DC SQUID is symmetric, i.e., R, C, I_c, and L are equal for the left and the right branch.

process is explained in detail in Sec. 3.2 and Sec. 3.3. Furthermore, DC SQUIDs play a crucial role in the capacitance estimation method of Sec. 3.1.

The equivalent circuit of a symmetric DC SQUID is sketched in Fig. 2.2. We note that for the purpose of this work, a semiclassical description is sufficient. Then, similar to the single Josephson junction introduced in Sec. 2.1, the phase dynamics of the DC SQUID is equivalent to the motion of a particle in a potential U_SQ. However, for a DC SQUID the effective mass of this particle is $2C(\Phi_0/2\pi)^2$ and U_SQ becomes two-dimensional[1] [82],

$$\frac{U_\mathrm{SQ}(\gamma_+,\gamma_-)}{E_\mathrm{J}} = -\left[\cos(\gamma_+ + \gamma_-) + \cos(\gamma_+ - \gamma_-) + \frac{I_\mathrm{b}}{I_\mathrm{c}}\gamma_+ + \frac{4\pi\Phi_\mathrm{x}^\mathrm{SQ}}{\Phi_0\beta}\gamma_- - \frac{2}{\beta}\gamma_-^2\right]. \tag{2.4}$$

Here, $\beta \equiv 4\pi L I_\mathrm{c}/\Phi_0$ is the screening parameter, $2L$ the geometric self-inductance of the DC SQUID loop. I_b and $\Phi_\mathrm{x}^\mathrm{SQ}$ are the bias current and the external magnetic flux applied to the DC SQUID, respectively. The phase differences γ_1 and γ_2 across the two SQUID junctions are rewritten in terms of the outer phase $\gamma_+ \equiv (\gamma_1+\gamma_2)/2$ and the inner phase $\gamma_- \equiv (\gamma_1-\gamma_2)/2$. Conceptually, this situation is similar to the motion of two coupled pendulums. When $\beta \ll 1$, the two junctions are rigidly coupled. Then, the inner phase is constant and fluxoid quantization [2] in the DC SQUID loop directly yields $\gamma_- = \pi\Phi_\mathrm{x}^\mathrm{SQ}/\Phi_0$. Consequently, the potential $U_\mathrm{SQ}(\gamma_+,\gamma_-) = U_\mathrm{SQ}(\gamma_+)$ of the DC SQUID has the same form as that of a tunable single Josephson junction, where the maximum transport current of the zero-voltage state

$$I_\mathrm{max} \equiv I_\mathrm{max}(\Phi_\mathrm{x}^\mathrm{SQ}) = 2I_\mathrm{c}\left|\cos\left(\pi\frac{\Phi_\mathrm{x}^\mathrm{SQ}}{\Phi_0}\right)\right| \tag{2.5}$$

[1]Please note that Eq. (2) in Ref. [81] is missing a factor $2\pi/\Phi_0$ in one term. The key results remain unaffected. Nevertheless, the correct potential is given here.

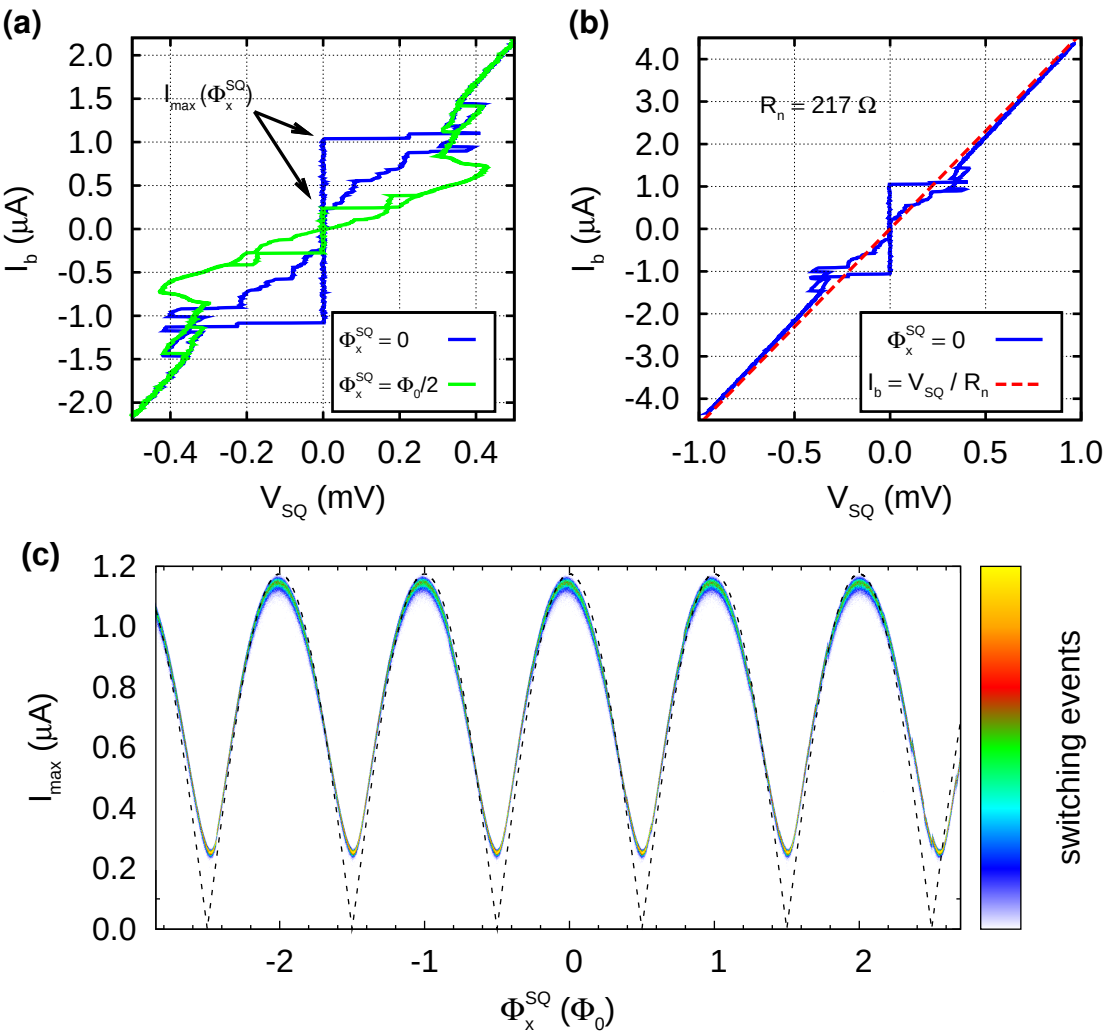

Figure 2.3: Measurements on a typical DC SQUID consisting of two Al/ALO$_x$/Al junctions. **(a)** Current-voltage characteristics for two different values of Φ_x^{SQ}. The black arrows indicate the switching currents I_{sw}. For this sample, $I_{sw} \approx I_{max}$. **(b)** The trace for $\Phi_x^{SQ} = 0$ of (a) plotted in a larger range. The red dashed line in (b) is a fit to the linear part of the data, allowing one to extract R_n. **(c)** Switching current plotted as a function of the external flux for the same device. The switching histograms are color-coded (white corresponds to zero events). The black dashed line is a fit to the center values of the histograms using Eq. (2.5).

can be controlled via Φ_x^{SQ}. Experimentally, I_{max} can be determined from the current-voltage characteristic of the DC SQUID. In absence of noise, I_{max} is equal to the switching current $I_{sw} = I_{sw}(\Phi_x^{SQ})$, where the DC SQUID switches to the finite-voltage state. We note that this switching is a statistical process because it corresponds to a tunneling event. When recording many switching events at the same Φ_x^{SQ}, one obtains an approximately Gaussian switching current distribution, the switching current histogram. We take I_{sw} to be the center value of this histogram. The presence of noise broadens the histogram and causes I_{sw} to be suppressed below I_{max}. In Fig. 2.3(a) and Fig. 2.3(b), current-voltage characteristics for a DC SQUID consisting of two Al/AlO$_x$/Al-junctions with dimensions similar to the devices used throughout this thesis are displayed. The flux-dependence of I_{max} for this sample is shown in Fig. 2.3(c). It clearly exhibits the cosine shape predicted by Eq. (2.5).

The suppression of the switching current due to noise is negligible in this sample. Differently from Fig 2.3, we always denote experimental switching currents with I_{sw} from hereon.

The Ambegaokar-Baratoff relation, originally stated for a single tunnel junction [2, 15, 83], relates the maximum switching current $I_{\mathrm{sw}} \approx 2I_{\mathrm{c}}$, the normal resistance $R_{\mathrm{n}} \approx R/2$, and the superconducting energy gap $\Delta_{\mathrm{g}} \equiv eV_{\mathrm{g}}$ of the DC SQUID via

$$I_{\mathrm{sw}}R_{\mathrm{n}} \approx I_{\mathrm{c}}R = \frac{\pi}{2}\frac{\Delta_{\mathrm{g}}}{e} = \frac{\pi}{2}V_{\mathrm{g}}\,. \tag{2.6}$$

For a superconductor obeying the BCS theory [2], the energy gap $2\Delta_{\mathrm{g}}^{\mathrm{BCS}} = 1.764k_{\mathrm{B}}T_{\mathrm{c}}$ can be expressed in terms of the critical temperature T_{c}. The normal resistance R_{n} of the DC SQUID can be obtained from its current-voltage characteristic as shown in Fig. 2.3(b). We use Eq. (2.6) in Sec. 3.1 to verify the accuracy of our R_{n}-estimation.

Periodic fluctuations of the inner phase γ_- around its mean value $\pi\Phi_{\mathrm{x}}^{\mathrm{SQ}}/\Phi_0$ play an important role in exciting self-induced resonances in the DC SQUID loop. These resonances are analyzed in detail in Sec. 3.1. Their angular frequency ω_{SQ} is determined by the sample geometry: Along the loop, the junctions are connected in series, giving rise to a total geometric inductance $2L$ and a total capacitance $C/2$. Consequently, $\omega_{\mathrm{SQ}} = 1/\sqrt{LC}$. In contrast, the outer phase simply determines the voltage across the DC SQUID. As above, we consider the DC SQUID to be symmetric, i.e., left and right branch are assumed to have equal L, I_{c}, R, and C. If for an integer n the resonance voltage

$$V_{\mathrm{SQ}} = n\frac{\Phi_0}{2\pi\sqrt{LC}} \tag{2.7}$$

is smaller than $2V_{\mathrm{g}}$ and I_{max} is suppressed sufficiently, steps can be observed in the current-voltage characteristic of the DC SQUID [84]. For known V_{SQ} and L, the junction capacitance C can be calculated from Eq. (2.7). An intuitive understanding of the resonances is provided by the following consideration. When applying a DC bias current to the DC SQUID, we obtain a transport current $I_{\mathrm{trans}} = 2I_{\mathrm{c}}\cos\gamma_-\sin\gamma_+$ and a circulating current $I_{\mathrm{circ}} = I_{\mathrm{c}}\sin\gamma_-\cos\gamma_+$ [85] in the loop. Due to the ac-Josephson effect [2], the circulating current has an ac-component which excites the resonances.

2.3 Quantization of charge and flux

In the descriptions of the Josephson junction in Sec. 2.1 and the DC SQUID in Sec. 2.2, apart from the macroscopic quantum model [1] and Cooper-pair tunneling, a classical formalism has been applied. For the DC SQUID devices used in the experiments presented in this work, this semiclassical approach is sufficient. However, in order to understand the physics of superconducting quantum circuits properly, a fully quantized description is indispensable. This is obtained by promoting the classical variables charge Q and flux/phase Φ to operators, $Q \to \hat{Q}$ and $\Phi \to \hat{\Phi}$. As it turns out, $\hat{Q}$ and $\hat{\Phi}$ are conjugated variables in the sense that they obey a commutation relation equivalent to the one between position and momentum in mechanics [86, 87],

$$\left[\hat{Q}, \hat{\Phi}\right] = -i\hbar\,. \tag{2.8}$$

Equivalently, one can write down the operators in their conjugate representations,

$$\hat{Q} = -i\hbar\frac{\partial}{\partial\Phi} \quad \text{and} \quad \hat{\Phi} = i\hbar\frac{\partial}{\partial Q}\,, \tag{2.9}$$

or the uncertainty relation

$$\Delta Q \Delta\Phi \leq \frac{\hbar}{2}\,. \tag{2.10}$$

A concrete example for this procedure is the quantization of the superconducting flux qubit circuit, which is explained in detail in Sec. 2.5.

2.4 Superconducting qubits

Generally, nonlinear systems exploiting properties specific to quantum mechanics such as, e.g., quantum superpositions or entanglement, are of great significance for research and technology. In particular, quantum two-level systems [6] (also referred to as qubits) give rise to new and fascinating possibilities in fundamental research as well as in communication and information processing. Consequently, the development of hardware concepts, which have to satisfy stringent requirements known as the DiVincenzo criteria [88], is the subject of intensive research efforts. The implementation of qubits has first been proposed and successfully demonstrated for NMR systems [89], trapped ions [90, 91], and cavity-QED setups [61, 63, 92–94]. These *microscopic* systems exhibit sufficiently long coherence times, but they have drawbacks regarding another crucial requirement for practical quantum information processing: scalability to large architectures. However, potential scalability together with a high degree of tunability are specific advantages of solid-state quantum qubits. The reason is that these devices are *macroscopic* quantum objects [4, 5], whose fabrication is based on well-established techniques from micro- and nanoelectronics such as lithography and thin-film technology. Furthermore, it is noteworthy to mention that solid-state quantum systems possess a great potential in modern electronics because the ongoing miniaturization of integrated circuits makes the deliberate use of quantum-mechanical effects opportune in the near future.

In solid-state qubit realizations, the unwanted decoherence due to the interaction with the numerous environmental degrees of freedom presents one of the major issues. For this reason, superconducting devices are particularly promising. Due to the fact that the superconducting state possesses a macroscopic quantum nature and is separated by an energy gap Δ_g from the continuum of normal conducting states, it gives rise to intrinsic quantum coherence. Furthermore, design-dependent internal symmetries can reduce the influence of noise arising from the control and readout circuitry. In general, superconducting qubits [16–19] consist of one or more Josephson junctions (cf. Sec. 2.1) connected by superconducting lines. The junctions act as fundamental source of nonlinearity. Quantum information can be stored in the number of superconducting Cooper pairs (e.g., the charge qubit [20, 31, 47], the quantronium [21, 36] and the transmon [22–24]), in the direction of a circulating persistent current (e.g., the three-junction flux qubit [27, 28, 34, 85] and the RF-SQUID-based flux qubit [25]) or in oscillatory states (e.g., the phase qubit [29, 33, 95]).

Depending on the chosen qubit implementation, either charge or flux/phase can be the good quantum variable. There exist two major regimes depending on the

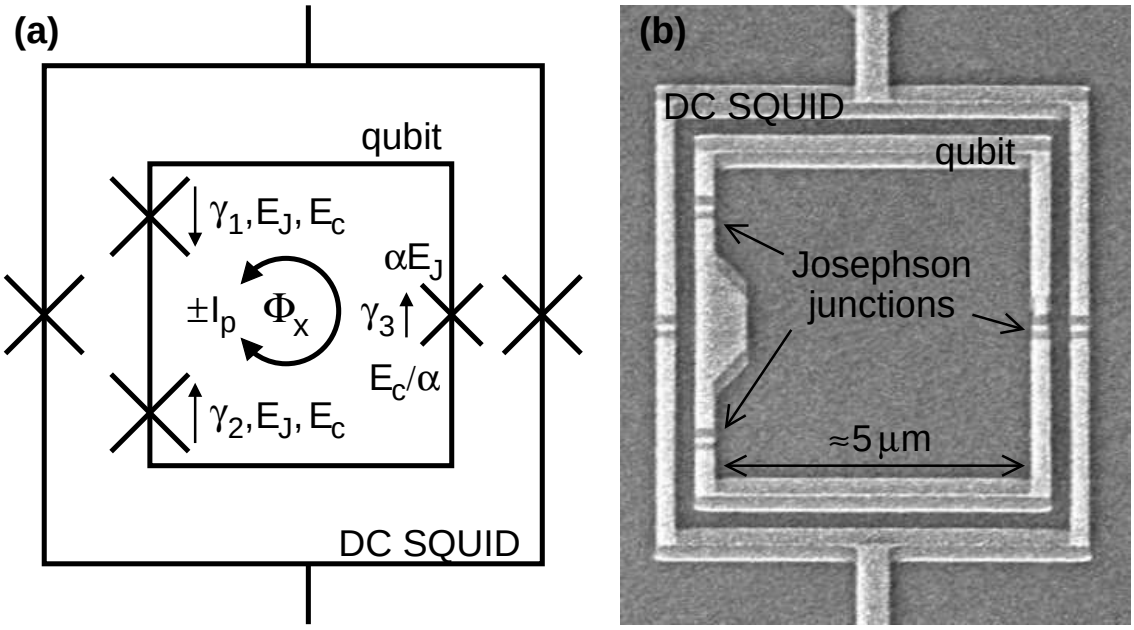

Figure 2.4: The three-Josephson-junction flux qubit. **(a)** Sketch of the flux qubit (inner loop). The physical Josephson junctions are denoted with crosses. The circular double arrow symbolizes the persistent currents $\pm I_\mathrm{p}$ in the loop. The outer loop represents the DC SQUID used for detection of these states. **(b)** Scanning electron microscopy micrograph of a flux qubit and readout DC SQUID with the same layout as the one used in this work.

ratio between the Josephson energy E_J and the charging energy E_c. In the case $E_\mathrm{J} \gg E_\mathrm{c}$, changing the flux/phase Φ requires a large energy. In such a circuit, Φ is well defined whereas Q fluctuates strongly. The phase qubit exploits this regime. Charge qubits operate in the opposite regime, $E_\mathrm{J} < E_\mathrm{c}$. Here, the charge Q is the good quantum number and the phase/flux degree of freedom is smeared out. The three-Josephson-junction flux qubit as well as the transmon work in an intermediate regime, $E_\mathrm{J}/E_\mathrm{c} \simeq 50$. Interestingly, both flux/phase (flux qubit) and charge (transmon) can serve as quantum variable for a qubit in this regime. The specific choice depends on the experimental requirements. The transmon offers coherence times of more than a microsecond over a broad range of parameters [23, 24], but has a small level anharmonicity. In contrast, the flux qubit is a well-isolated two-level system. However, comparable coherence times are only demonstrated in a small flux interval around an optimal point [44, 46].

2.5 The three-Josephson-junction flux qubit

In this thesis, we report on experiments on one specific type of superconducting qubits, namely the three-Josephson-junction flux qubit [27, 28]. As shown in Fig. 2.4, such a device consists of a square-shaped superconducting aluminum loop interrupted by three nanoscale Al/AlO_x/Al Josephson junctions. The area of two of these junctions is chosen to be the same ($0.03\,\mu\mathrm{m}^2$), whereas the third one is designed to be smaller by a factor $\alpha_\mathrm{design} = 0.7$. The details of the fabrication process are described in appendix A.3.

We now derive the qubit potential following the sketch of Fig. 2.4(a). We first

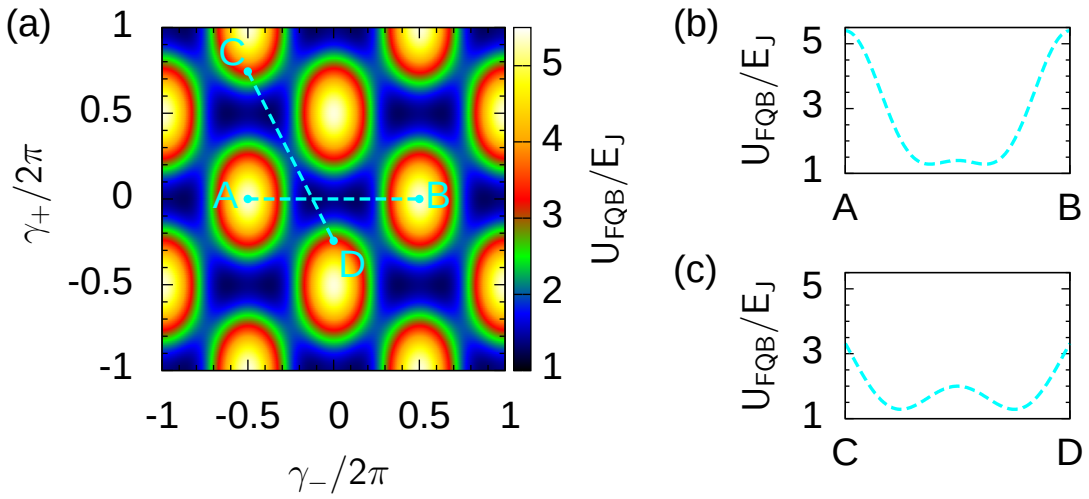

Figure 2.5: Potential landscape of the three-Josephson-junction flux qubit for $\alpha = 0.7$ and $\Phi_x/\Phi_0 = 0.5$. **(a)** Two-dimensional potential landscape. The figure-8-shaped structures are double wells. The dashed lines mark the cuts shown in (b) and (c). **(b)** Cut along the line A–B of (a), revealing a double well with a low intracell tunnel barrier. **(c)** Cut along the line C–D of (a), revealing a high intercell tunnel barrier.

notice that we assume the resistive channels of the junctions and the loop inductance to be negligible. Then, the qubit potential can be written as the sum of three single-junction potentials of Eq. (2.3). Due to the absence of an explicit bias current, we obtain

$$U_{\mathrm{FQB}}(\gamma_1, \gamma_2, \gamma_3) = E_{\mathrm{J}}\big[(1 - \cos\gamma_1) + (1 - \cos\gamma_2) + \alpha(1 - \cos\gamma_3)\big]\,. \tag{2.11}$$

In contrast to Eq. (2.3) and Eq. (2.4), the energy offset in the above expression is chosen such that U_{FQB} represents the total energy stored in the junctions[2]. Since we consider the geometric inductance of the qubit loop, $L_{\mathrm{loop}} \ll L_{\mathrm{J}}$, to be negligible, the phase γ_3 of the small junction can be eliminated utilizing the fluxoid quantization,

$$\gamma_1 - \gamma_2 + \gamma_3 = -2\pi\frac{\Phi_{\mathrm{x}}}{\Phi_0}\,. \tag{2.12}$$

In the next step, we move to the modified phase coordinates $\gamma_+ \equiv (\gamma_1 + \gamma_2)/2$ and $\gamma_- \equiv (\gamma_1 - \gamma_2)/2$. Hence, we can write the qubit potential in the form

$$U_{\mathrm{FQB}}(\gamma_+, \gamma_-) = E_{\mathrm{J}}\left[2 + \alpha - 2\cos\gamma_+\cos\gamma_- - \alpha\cos\left(2\pi\frac{\Phi_{\mathrm{x}}}{\Phi_0} + 2\gamma_-\right)\right]\,, \tag{2.13}$$

For $\alpha > 0.5$, the above potential exhibits a periodic double-well structure. At the so-called degeneracy or optimal points, the condition $\Phi_{\mathrm{x}} = \Phi_{(n)}$, where $\Phi_{(n)} \equiv \left(n + \frac{1}{2}\right)\Phi_0$ and n is an integer, is satisfied. There, the potential is symmetric with two degenerate minima located at $\gamma_+^\star = 0$ and $\gamma_-^\star = \pm\arccos(1/2\alpha)$. This situation is shown for $\alpha = \alpha_{\mathrm{design}}$ in Fig. 2.5. The two classical minima correspond to two

[2]Generally, the dynamics of a system remains unaffected by arbitrarily large constant energy offsets in its Hamiltonian.

degenerate stable states, which are characterized by the clockwise and counterclockwise DC persistent circulating currents $\pm I_{\rm p}$ flowing in the qubit loop, where

$$I_{\rm p} \equiv \sqrt{1-\left(\frac{1}{2\alpha}\right)^2}\,. \tag{2.14}$$

These two states are predominantly coupled by intracell quantum tunneling as shown in Fig. 2.5(b) and Fig. 2.5(c). Following the procedure introduced in Sec. 2.3, we can write the full quantum-mechanical Hamiltonian of the three-junction flux qubit as

$$\begin{aligned}\hat{H}_{\rm FQB} = \frac{1}{2}\left(\frac{\hat{Q}_+^2}{2C}+\frac{\hat{Q}_-^2}{2C(1+2\alpha)}\right)\\ + E_{\rm J}\left[2+\alpha-2\cos\hat{\gamma}_+\cos\hat{\gamma}_- - \alpha\cos\left(2\pi\frac{\Phi_{\rm x}}{\Phi_0}+2\hat{\gamma}_-\right)\right]\,.\end{aligned} \tag{2.15}$$

Here, the charge operators $\hat{Q}_+ \equiv -i\hbar(2\pi/\Phi_0)\partial/\partial\gamma_+$ and $\hat{Q}_- \equiv -i\hbar(2\pi/\Phi_0)\partial/\partial\gamma_-$ are conjugate to the phase operators $\hat{\gamma}_+$ and $\hat{\gamma}_-$, respectively.

Near an optimal point $\Phi_{\rm x} \approx \Phi_{(n)}$, the flux qubit Hamiltonian of Eq. (2.15) can be reduced to that of an effective two-level system [6, 16, 27, 28],

$$\hat{H}_{\rm q} = \frac{\epsilon(\Phi_{\rm x})}{2}\hat{\sigma}_z + \frac{\Delta}{2}\hat{\sigma}_x\,. \tag{2.16}$$

Here, $\hat{\sigma}_z$ and $\hat{\sigma}_x$ are Pauli operators and

$$\epsilon(\Phi_{\rm x}) \equiv 2\left(\left.\frac{\partial U_{\rm FQB}}{\partial\Phi_{\rm x}}\right|_{\gamma_-=\gamma_-^\star}\right)\delta\Phi_{\rm x} = 2I_{\rm p}\delta\Phi_{\rm x} \tag{2.17}$$

can be considered linear in the external flux, $\delta\Phi_{\rm x} \equiv \Phi_{\rm x} - \Phi_{(n)}$. The two classical persistent-current states $|-\rangle$ and $|+\rangle$, which are the eigenstates of $[\epsilon(\Phi_{\rm x})/2]\hat{\sigma}_z$, are coupled by a tunneling matrix element Δ. For an opportune choice of the parameters $E_{\rm J}$, $E_{\rm c}$, and α, the condition $k_{\rm B}T \ll \Delta$ required for the observation of quantum effects can be satisfied at millikelvin temperatures. In particular, this is the case for the device discussed in chapter 4 and chapter 5, where we experimentally find a critical current density $J_{\rm c} \simeq 1300\,{\rm A/cm^2}$, $E_{\rm J}/E_{\rm c} \simeq 50$, and $\Delta/h \simeq 4\,{\rm GHz}$. These numbers imply that $k_{\rm B}T \ll \Delta$ is satisfied for the typical operation temperature of a standard dilution refrigerator, $T \simeq 50\,{\rm mK}$. Furthermore, we note that this sample is designed to be operated near the degeneracy point $\Phi_{(1)}$.

In the case that the tunnel coupling can be neglected, $\Delta \ll \epsilon(\Phi_{\rm x})$, the energy ground state $|{\rm g}\rangle$ and the excited state $|{\rm e}\rangle$ of the qubit Hamiltonian of Eq. (2.16) are identical to the classical states $|-\rangle$ and $|+\rangle$. They are separated by the flux-dependent energy $\epsilon(\Phi_{\rm x}) = 2I_{\rm p}\delta\Phi_{\rm x}$. For nonnegligible coupling, $\Delta \gtrsim \epsilon(\Phi_{\rm x})$, $|{\rm g}\rangle$ and $|{\rm e}\rangle$ are linear superpositions of $|-\rangle$ and $|+\rangle$. In this situation, the energy difference between the qubit levels [6],

$$E_{\rm ge} \equiv E_{\rm e} - E_{\rm g} = \sqrt{\epsilon(\Phi_{\rm x})^2+\Delta^2} = \sqrt{(2I_{\rm p}\delta\Phi_{\rm x})^2+\Delta^2}\,, \tag{2.18}$$

has a hyperbolic flux dependence with a characteristic level anticrossing (cf. Fig 2.6). At the degeneracy point, where $\delta\Phi_{\rm x} = 0$, $\epsilon(\Phi_{\rm x}) = 0$, and $\partial E_{\rm ge}/\partial\Phi_{\rm x} = 0$, the qubit is

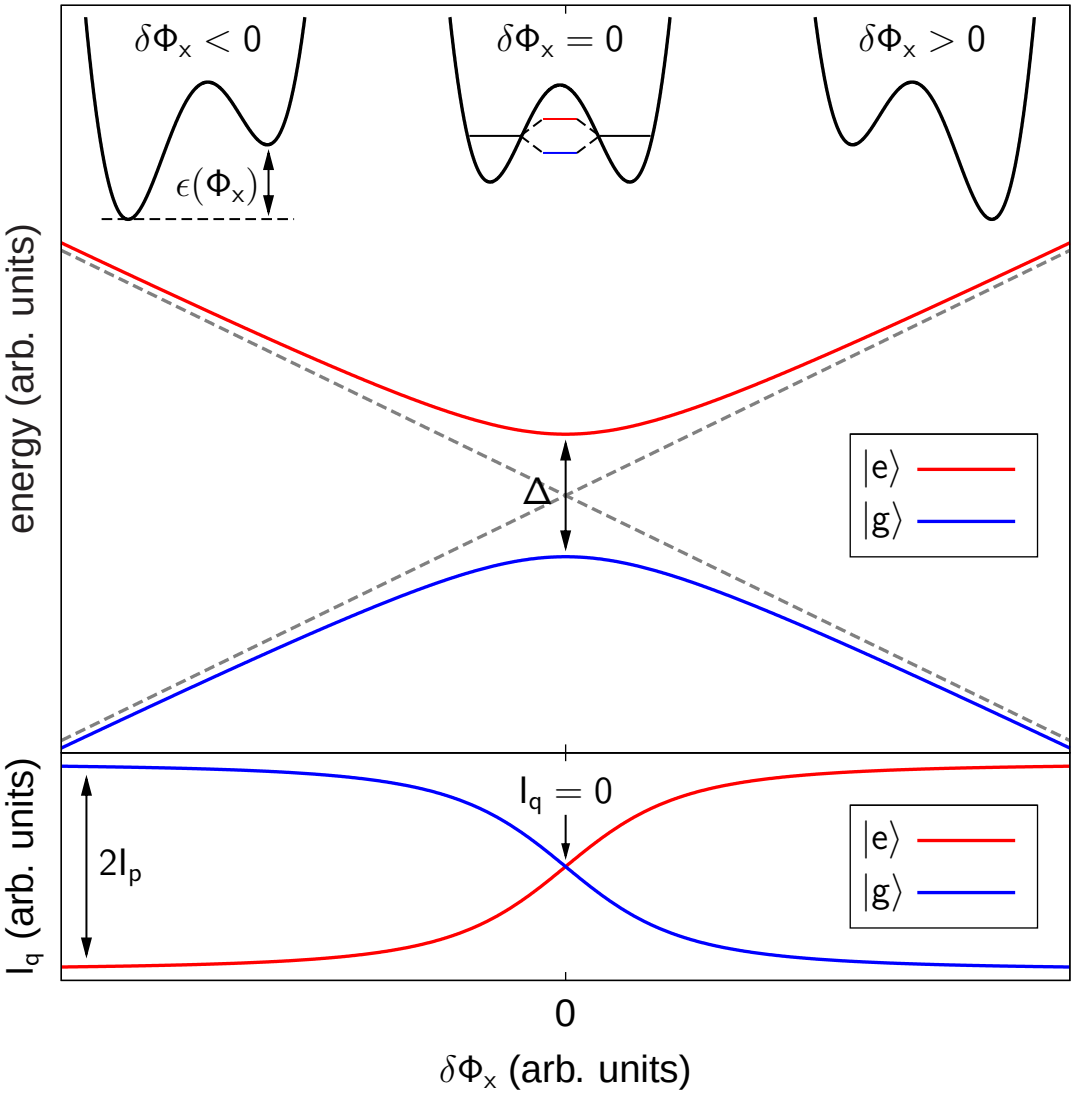

Figure 2.6: Sketch of the energy diagram and circulating current of a flux qubit in the two-level approximation of Eq. (2.16). The gray dotted lines correspond to the classical states $|+\rangle$ and $|-\rangle$. Three typical shapes of the qubit potential are displayed at the top of the panel.

protected from dephasing because E_{ge} is stationary with respect to small variations of the control parameter $\delta\Phi_x$. Therefore, this point represents the optimal point for the coherent manipulation of the qubit. The qubit eigenstate at the optimal point is an equal superposition of $|-\rangle$ and $|+\rangle$ and the expectation value of the current circulating in the qubit loop, $I_q \equiv \partial E_{ge}/\partial\Phi_x = I_p\langle\hat{\sigma}_z\rangle = 0$, vanishes. Far away from the degeneracy point[3] ($\epsilon(\Phi_x) \gg \Delta$), the effect of quantum tunneling becomes negligible and the qubit behaves as a classical two-level system. This example clearly shows the flexibility offered by superconducting qubits due to their high degree of tunability.

[3]Here and in the following, the expression "far away from the optimal point" implies that Φ_x is chosen far enough from the optimal point that the relation $\epsilon(\Phi_x) \gg \Delta$ holds, but not so far away that the two-level approximation would be violated.

2.6 Bloch vector and Bloch sphere

When describing the influence of fluctuations $\delta\boldsymbol{\omega}$ on the qubit in chapter 4, the two-level Hamiltonian of Eq. (2.16) is conveniently expressed in a two-dimensional Bloch vector representation,

$$\hat{H}_{\mathrm{q}} = \hbar\boldsymbol{\omega}\hat{\boldsymbol{\sigma}}/2. \tag{2.19}$$

Here, $\hat{\boldsymbol{\sigma}} \equiv \hat{\boldsymbol{\sigma}}^{(\mathbf{2})} \equiv (\hat{\sigma}_{\perp}, \hat{\sigma}_{\parallel}) = (\hat{\sigma}_x, \hat{\sigma}_z)$ and $\boldsymbol{\omega} \equiv (\omega_{\perp}, \omega_{\parallel}) = \hbar^{-1}\big(\Delta, \epsilon(\Phi_{\mathrm{x}})\big)$ is the two-dimensional Bloch vector. The representation of $\boldsymbol{\omega}$ in the qubit energy eigenbasis is obtained by multiplying $\boldsymbol{\omega}$ with the rotation matrix

$$D \equiv \begin{pmatrix} \cos\theta & -\sin\theta \\ \sin\theta & \cos\theta \end{pmatrix} \tag{2.20}$$

from the left. The Bloch angle θ is defined [6] via the relation $\tan\theta \equiv \Delta/\epsilon(\Phi_{\mathrm{x}})$, $\sin\theta = \Delta/E_{\mathrm{ge}}$, and $\cos\theta = \epsilon(\Phi_{\mathrm{x}})/E_{\mathrm{ge}}$. At the qubit optimal point, one finds $\cos\theta = 0$ and $\sin\theta = 1$.

More generally, the qubit state $|\psi\rangle$ at any point of time during its evolution is described with its density matrix $\rho \equiv |\psi\rangle\langle\psi| \equiv \boldsymbol{r}\hat{\boldsymbol{\sigma}}^{(\mathbf{3})}$. Here, $\hat{\boldsymbol{\sigma}}^{(\mathbf{3})} \equiv (\hat{\sigma}_x, \hat{\sigma}_y, \hat{\sigma}_z)$ is the three-dimensional vector and $\boldsymbol{r} \equiv (r_x, r_y, r_z) \equiv (r, \vartheta, \phi)$ is a coefficient vector with a modulus $r \equiv |\boldsymbol{r}|$ smaller than or equal to unity. We note that $|\psi\rangle$ is a pure state ($r = 1$), but in presence of dissipation $\boldsymbol{r}\hat{\boldsymbol{\sigma}}^{(\mathbf{3})}$ can also describe a mixed state ($r < 1$). In other words, the time evolution of the qubit can be mapped onto the time evolution of the vector $\boldsymbol{r}$. Since $r \leq 1$, this evolution happens within a spherical portion of the $r_x r_y r_z$-space, the so-called Bloch-sphere.

2.7 The LC-resonator

A nonresistive loop containing an inductor L and a capacitor C forms a lumped-element LC-resonator. The corresponding circuit diagram is displayed in Fig. 2.7. The classical Hamiltonian of such a circuit can be written as the sum of the energies stored in the capacitor and the inductor,

$$H_{LC} = \frac{\Phi^2}{2L} + \frac{Q^2}{2C}\,. \tag{2.21}$$

This Hamiltonian can be quantized straightforwardly following the procedure given in Sec. 2.3, yielding

$$\hat{H}_{LC} = \frac{\hat{\Phi}^2}{2L} + \frac{\hat{Q}^2}{2C}\,. \tag{2.22}$$

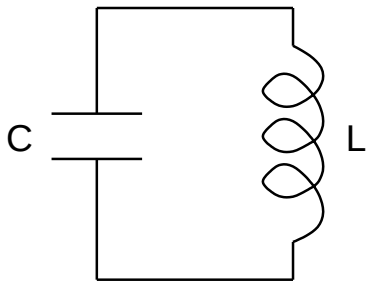

Figure 2.7: Circuit diagram of a lumped-element LC-resonator.

We can now readily compare the LC-resonator of Eq. (2.21) and Eq. (2.22) to a standard harmonic oscillator, $H_{\mathrm{HO}} = p^2/(2m) + (m\omega^2/2)x^2$. We identify the quantities momentum $p \to \Phi$, position $x \to Q$, mass $m \to L$, and resonance frequency $\omega \to (\omega_{\mathrm{r}} \equiv 1/\sqrt{LC})$. Then, the Hamiltonian of Eq. (2.22) can be expressed in terms of the bosonic creation and annihilation operators [96],

$$\hat{a}^\dagger \equiv \frac{\omega_{\mathrm{r}} L\hat{Q} - i\hat{\Phi}}{\sqrt{2\omega_{\mathrm{r}} L\hbar}} \quad \text{and} \quad \hat{a} \equiv \frac{\omega_{\mathrm{r}} L\hat{Q} + i\hat{\Phi}}{\sqrt{2\omega_{\mathrm{r}} L\hbar}}\,, \tag{2.23}$$

respectively. They obey the well-known commutation relation $[\hat{a}, \hat{a}^\dagger] = 1$. One finally obtains the Hamiltonian of a quantum harmonic oscillator,

$$\hat{H}_{\mathrm{r}} = \hbar\omega_{\mathrm{r}} \left(\hat{a}^\dagger \hat{a} + \frac{1}{2} \right) . \tag{2.24}$$

Experimentally, the condition $k_{\mathrm{B}}T \ll \hbar\omega_{\mathrm{r}}$ must be fulfilled in order to be able to probe quantum mechanical behavior of the harmonic oscillator. This is the case for the resonator discussed in chapter 5, where $\omega_{\mathrm{r}}/2\pi \simeq 6\,\mathrm{GHz}$ and $T \simeq 50\,\mathrm{mK}$. There, the LC-resonator is formed by a superconducting loop with the geometric inductance L and a thin-film parallel-plate capacitance C.

Formally, Eq. (2.24) is equivalent to the description of a cavity in quantum optics. The average number of photons $\langle \hat{N} \rangle$ inside the resonator is described by the photon number operator $\hat{N} \equiv \hat{a}^\dagger \hat{a}$. Its eigenstates are the Fock states $|\mathrm{N}\rangle$, where N is a nonnegative integer. They form an orthonormal set and $|0\rangle$ is referred to as the vacuum state. In the actual experiments, the resonance frequency $\nu_{\mathrm{r}} \equiv \omega_{\mathrm{r}}/2\pi$ is measured instead of ω_{r}. Furthermore, photons can only enter into or decay from the resonator at the finite rate κ. Usually, κ is expressed in terms of the quality factor $Q \equiv \omega_{\mathrm{r}}/\kappa$.

2.8 Circuit QED

Recently, the interaction of superconducting qubits with microwave resonators has attracted increasing attention. It turned out that the qubit-resonator interaction is the circuit equivalent of the atom-photon interaction in cavity quantum electrodynamics (QED) [61, 63, 92–94]. In this scenario, the qubit behaves as a tunable artificial two-level atom and the quantized resonator plays the role of the cavity. Hence, the formalism developed for cavity QED can be readily transferred to the realm of superconducting quantum circuits. This has given rise to a new field commonly referred to as circuit QED [64, 97]. There, the large tunability of solid-state quantum circuits, both by design and in-situ in the experiment, opens the possibility to go beyond the limits of cavity QED (a typical example is Ref. [75]).

In cavity QED, a natural atom interacts with the quantized modes of an optical or microwave cavity. The information on the coupled system is encoded both in the atom and in the cavity states. The latter can be accessed spectroscopically by measuring the transmission properties of the cavity [60], whereas the former can be read out by suitable detectors [62, 63]. In circuit QED, the solid-state counterpart of cavity QED, the first category of experiments was implemented by measuring the microwave radiation emitted by an on-chip resonator strongly coupled to a charge qubit [65]. In a dual experiment, the state of a flux qubit was detected with a

DC SQUID and vacuum Rabi oscillations were observed [71]. More recently, both approaches have been exploited to create a toolbox for quantum optics on a chip. Of particular relevance in this context are the experimental works regarding methods for the manipulation and dispersive readout of qubits [65, 66, 71, 98, 99], single photon generation [74], single-artificial-atom lasing [75] and cooling [76, 77], and quantum bus systems [52, 53]. Additionally, there exist several promising proposals to further extend this toolbox in the future [64, 97, 100–103].

The Hamiltonian of a qubit-resonator system is the sum of the qubit Hamiltonian of Eq. (2.16), the quantum resonator Hamiltonian of Eq. (2.24), and a linear interaction term:

$$\hat{H}_{\mathrm{q,r}} = \frac{\epsilon}{2}\hat{\sigma}_z + \frac{\Delta}{2}\hat{\sigma}_x + \hbar\omega_{\mathrm{r}}\left(\hat{a}^\dagger\hat{a} + \frac{1}{2}\right) + \hbar g_{\mathrm{q,r}}\big(\hat{a}^\dagger + \hat{a}\big)\hat{\sigma}_z\,. \tag{2.25}$$

Here, $g_{\mathrm{q,r}}$ is the vacuum coupling constant between qubit and resonator. For a flux qubit coupled to a lumped-element LC-resonator, the interaction between the qubit circulating current $I_{\mathrm{q}} = I_{\mathrm{p}}\hat{\sigma}_z$ and the resonator vacuum current $I_{\mathrm{r}} \equiv \Phi/L = (\sqrt{(2L)(\hbar\omega_{\mathrm{r}}/4)})/L = \sqrt{\hbar\omega_{\mathrm{r}}/(2L)}$ is mediated by the mutual inductance $M_{\mathrm{q,r}}$. Consequently, one finds

$$\hbar g_{\mathrm{q,r}} = M_{\mathrm{q,r}} I_{\mathrm{p}} \sqrt{\frac{\hbar\omega_{\mathrm{r}}}{2L}}\,. \tag{2.26}$$

When $g_{\mathrm{q,r}}$ is much larger than the relaxation and dephasing rates of qubit and resonator, the system is in the strong coupling regime. It is one of the central features of circuit QED that for geometric reasons this regime can be reached easily.

In order to further simplify the Hamiltonian of Eq. (2.25), we transform it to an interaction picture with respect to qubit and resonator, in which $\hat{\sigma}_\pm \to \hat{\sigma}_\pm \mathrm{e}^{\pm i\omega_{\mathrm{ge}}t}$, $\hat{a} \to \hat{a}\mathrm{e}^{-i\omega_{\mathrm{r}}t}$, and $\hat{a}^\dagger \to \hat{a}^\dagger \mathrm{e}^{+i\omega_{\mathrm{r}}t}$. Here, $\hat{\sigma}_+ \equiv |\mathrm{e}\rangle\langle\mathrm{g}|$ and $\hat{\sigma}_- \equiv |\mathrm{g}\rangle\langle\mathrm{e}|$ are the qubit raising and lowering operators, respectively. In the case of $\omega_{\mathrm{ge}} + \omega_{\mathrm{r}} \gg \tilde{\Delta}, g_{\mathrm{q,r}}$, where $\tilde{\Delta} \equiv \omega_{\mathrm{ge}} - \omega_{\mathrm{r}}$ is the frequency detuning, a rotating-wave approximation can be made and we are left with the interaction Hamiltonian in the well-known Jaynes-Cummings form [104],

$$\hat{H}^{\mathrm{JC}}_{\mathrm{q,r}} = \hbar g_{\mathrm{q,r}}\left(\hat{a}^\dagger\hat{\sigma}_-\mathrm{e}^{-i\tilde{\Delta}t} + \hat{a}\hat{\sigma}_+\mathrm{e}^{+i\tilde{\Delta}t}\right)\,. \tag{2.27}$$

When qubit and resonator are largely detuned, $\tilde{\Delta} \gg g_{\mathrm{q,r}}$, the physics contained in Eq. (2.27) is better described by the second-order effective Hamiltonian [64]

$$\hat{H}^{\mathrm{eff}}_{\mathrm{q,r}} = \hbar g^{\mathrm{eff}}_{\mathrm{q,r}}\,\hat{\sigma}_z\left(\hat{a}^\dagger\hat{a} + \frac{1}{2}\right)\,. \tag{2.28}$$

This Hamiltonian is also referred to as dispersive Hamiltonian or Hamiltonian in the dispersive regime. In analogy to atomic physics, the terms $\hbar g^{\mathrm{eff}}_{\mathrm{q,r}}\,\hat{\sigma}_z\,\hat{a}^\dagger\hat{a}$ and $\hbar g^{\mathrm{eff}}_{\mathrm{q,r}}\,\hat{\sigma}_z/2$ are often called ac Stark/Zeeman shift and Lamb shift, respectively. When the dispersive coupling constant, $g^{\mathrm{eff}}_{\mathrm{q,r}} \equiv g^2_{\mathrm{q,r}}/\tilde{\Delta}$, becomes much larger than the relaxation and dephasing rates of qubit and resonator, strong dispersive coupling is reached. Recently, in a circuit QED experiment this regime has been realized for the first time [69].

2.9 Spurious fluctuators

The impact of spurious fluctuators in the tunnel barrier of the Josephson junctions on a qubit was first studied for superconducting phase qubits [16–18, 29]. In these systems, which consist of a single Josephson junction shunted with an extra capacitor, numerous small anticrossings in the spectroscopy data accompanied by beatings and unexpected loss of coherence in Rabi-oscillation measurements were observed [30]. These beatings were attributed to two-level defects in the tunnel barrier causing either critical current or charge fluctuations [30, 105]. Any single one of these fluctuators can be modeled with the (flux-independent) Hamiltonian

$$\hat{H}_{\mathrm{f}} = \frac{\epsilon^\star}{2}\hat{\sigma}_z^\star + \frac{\Delta^\star}{2}\hat{\sigma}_x^\star \,. \tag{2.29}$$

It is known that an ensemble of such fluctuators produces $1/f$-noise when the distributions of $\epsilon^\star$ and $\Delta^\star$ are constant and proportional to $1/\Delta^\star$, respectively [30, 42, 106–108]. As discussed in chapter 4, $1/f$-noise is the main source of qubit dephasing. At frequencies comparable to the qubit transition frequency, the ensemble of spurious fluctuators causes a dielectric loss. This is suspected to cause qubit relaxation at a rate [39]

$$\Gamma_1^{\mathrm{f}} = \frac{K}{\hbar} A \tag{2.30}$$

proportional to the junction area A. Experimentally, one finds $K/\hbar \equiv \delta_i E_{\mathrm{ge}}/(\hbar A) \simeq 10\,\mathrm{MHz}/\mu\mathrm{m}^2$ for both AlO_x tunnel barriers and sputtered SiO_2 films [39]. The quantity $\delta_i \simeq 1.6 \times 10^{-3}$ can be interpreted as the loss tangent of the dielectric forming the tunnel barrier and is significantly higher than that of crystalline aluminum oxide.

The fluctuators are expected to exist is any Josephson qubit. For the qubit studied in this work, a three-Josephson-junction flux qubit, we discuss that the interaction with microscopic fluctuators can give rise to Ramsey and spin-echo beatings (cf. Sec. 4.4), are one possible source of relaxation (cf. Sec. 4.5), and influence the symmetry properties of the system (cf. Sec. 5.4).

Chapter 3

Experimental techniques

Performing measurements on superconducting quantum circuits requires substantial experimental effort. In this chapter, we introduce the relevant measurement concepts. For more technical details regarding the sample fabrication and the cryogenic setup, we refer the reader to appendix A and appendix B, respectively. In Sec. 3.1, we discuss measurements of the capacitance of Josephson junctions used for three-Josephson-junction flux qubits. A reliable estimate of the junction capacitance greatly facilitates the qubit design. Next, we explain the role of the DC SQUID as readout device for a three-Josephson-junction flux qubit. The conventional resistive-bias method is presented in Sec. 3.2 and the novel capacitive-bias readout in Sec. 3.3. Finally, the qubit operation with microwave control pulses is described in Sec. 3.4.

3.1 Capacitance of nanoscale Josephson junctions

In order to build complex quantum circuits containing multiple Josephson junctions, a well-controlled fabrication process with sufficiently low parameter spread is essential. The sample quality can be verified by determining the junction parameters experimentally. In this section, we concentrate on one of these parameters: the capacitance of the $Al/AlO_x/Al$ tunnel junctions used in flux qubits. These junctions typically have a 5-10 Å thick oxide layer and lateral dimensions of several hundreds of nanometers. This means that the junction area is in an intermediate regime between the small-area limit, where the charging energy dominates, and the large-area limit, where the Josephson coupling energy dominates. In this case, standard capacitance measurement methods cannot be applied. For example, neither the single electron transistor [109] (small-area limit) nor the Fiske-step analysis [110] (large-area limit) can be used. In principle, the capacitance can also be obtained from qubit microwave spectroscopy. However, these measurements are susceptible to influences from the electromagnetic environment of the qubit, i.e., their results presently contain substantial error bars (cf. section 3.1.3).

In sections 3.1.1 and 3.1.2, we present measurements of the specific capacitance (capacitance per unit junction area) of the nm-scale Josephson junctions described above. These measurements require considerably less experimental effort but provide a better accuracy than qubit microwave spectroscopy. The junction capacitance is obtained analyzing resonant voltage steps in the current-voltage characteristics of DC SQUIDs [84, 111]. The junction area is derived from scanning electron micro-

scope (SEM) images. Knowing the specific capacitance, in principle the capacitance of any other Josephson junction of the same type produced under sufficiently similar conditions can be determined with good accuracy and reasonable experimental effort. In a second step, in section 3.1.3, we compare our results to junction capacitance measurements using microwave spectroscopy of a three-Josephson-junction flux qubit. The qubit junctions are of the same type and are produced under the same conditions as the DC SQUID junctions used in the voltage step measurements. We find that, compared to microwave spectroscopy, the DC SQUID resonance method clearly allows a more accurate determination of the junction capacitance. The results presented in this section are published in Ref. [81].

3.1.1 Capacitance from DC SQUID resonances

The junction capacitance is determined from experiments on a set of specially designed DC SQUIDs. To this end, the DC SQUID current-voltage characteristics are recorded using the slow sweep protocol, which is explained in Sec. 3.2.1. Fig. 3.1 shows a typical current-voltage characteristic from our measurements. For low bias current I_b the DC SQUID is in the zero-voltage state. When increasing I_b above the switching current I_sw, the voltage jumps abruptly to a finite value. From Eq. (2.5) one finds that I_sw assumes a maximum when the frustration $f \equiv \Phi_\mathrm{x}/\Phi_0$ has integer values and a minimum when f has half-integer values. In the case of maximum I_sw the voltage jumps to approximately $2V_\mathrm{g}$. Note that our DC SQUIDs are not shunted

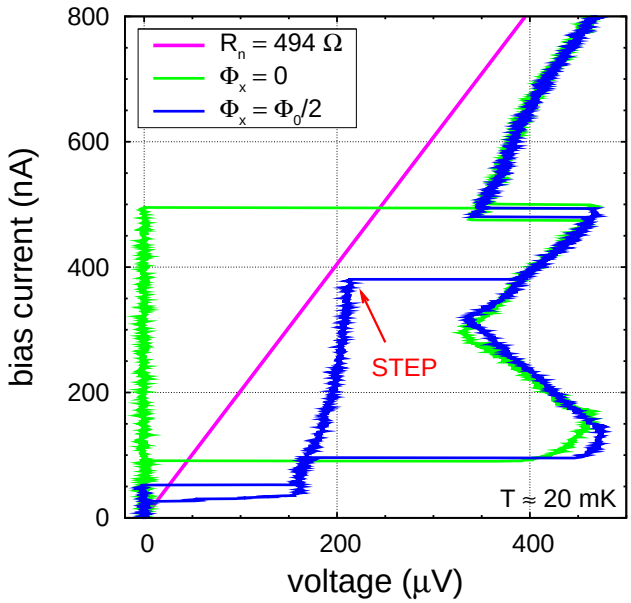

Figure 3.1: Typical hysteretic current-voltage characteristic of a DC SQUID showing a self-induced resonance. For this device, the geometrical loop inductance is $2L_\mathrm{geo} = 555\,\mathrm{pH}$, the nominal junction area $0.03\,\mu\mathrm{m}^2$, and the measured average junction area $0.044\,\mu\mathrm{m}^2$. The green curve is recorded in absence of external magnetic flux ($\Phi_\mathrm{x} = 0$). The normal-resistance branch asymptotically approaches an ohmic law (magenta line). The blue curve is recorded with an external magnetic flux $\Phi_\mathrm{x} = \Phi_0/2$ in the DC SQUID loop. In this situation, the switching current is suppressed to its minimum value and the self-induced voltage step is clearly visible. The step voltage is indicated by the red arrow.

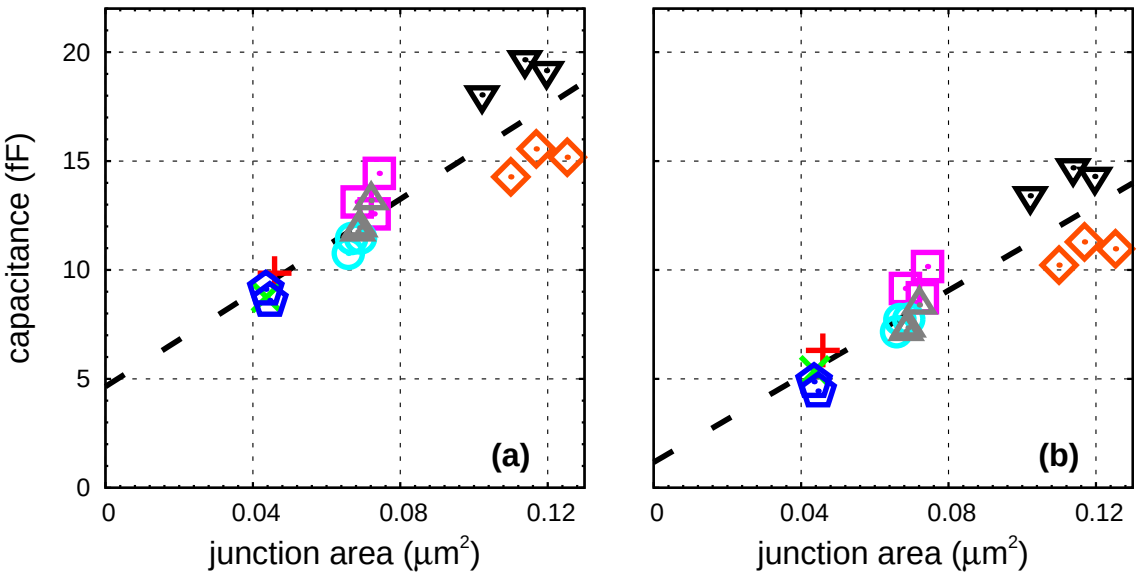

Figure 3.2: Junction capacitance C determined from DC SQUID voltage steps plotted versus the junction area S obtained from SEM images. Different symbols denote different DC SQUID geometries. The thick black dashed lines are linear fits to the data. **(a)** Without applying any corrections, we find a specific capacitance $C_s^\star = 108 \pm 13\,\mathrm{fF}/\mu\mathrm{m}^2$ and an offset $C_0^\star = 4.6 \pm 1.1\,\mathrm{fF}$. **(b)** As in (a), however, kinetic inductance and stray capacitance of the loop are taken into account. For a superconducting penetration depth $\lambda = 0.2 \pm 0.1\,\mu\mathrm{m}$, we find a specific capacitance $C_s = 100 \pm 25\,\mathrm{fF}/\mu\mathrm{m}^2$. The offset $C_0 = 1.6 \pm 1.3\,\mathrm{fF}$ has become small.

by an external capacitance or resistance. Hence, the normal resistance derived from the current-voltage characteristic for $I_b \gg I_{sw}$ is $R_n = R/2$. For intermediate bias current we observe the quasi-particle branch, which is strongly nonlinear due to self-heating effects. The current-voltage characteristics exhibits a hysteresis. When lowering the bias current starting with the DC SQUID in the voltage state, the retrapping to the zero-voltage state happens at a current smaller than I_{sw}.

When I_{sw} is suppressed sufficiently, voltage steps become visible within the superconducting gap as shown in Fig. 3.1. We observe such steps in eight out of the nine (cf. appendix A.2) measured DC SQUID geometries.[1] From the step voltages, the junction capacitances are calculated using the resonance condition given in Eq. (2.7). In Fig. 3.2, these capacitances are plotted as a function of the junction area measured with the SEM. When modeling the Josephson junctions as simple parallel plate capacitors, we expect their capacitance to be proportional to the junction area. Fig. 3.2(a) confirms this model, i.e., we observe a linear dependence with a specific capacitance $C_s^\star = 108 \pm 13\,\mathrm{fF}/\mu\mathrm{m}^2$. However, there is a considerable capacitance offset $C_0^\star = 4.6 \pm 1.1\,\mathrm{fF}$. Additionally, points belonging to the same DC SQUID geometry tend to form clusters. Such a systematic error cannot be caused by random fluctuations in the measurement environment or in the fabrication process. Furthermore, the observed clustering cannot be explained by extrinsic effects (e.g., noise from the measurement lines) because the conditions outside of the sample chip are different even for DC SQUIDs with the same geometry.

[1] For the geometry not exhibiting a step, the minimum switching current is probably higher than the step amplitude.

We now investigate the influence of a random fabrication spread on the observed junction capacitance for the prototypical example of a possible asymmetry effect. In such a situation, the two DC SQUID junctions have the areas $S_1 = (1+\chi)S$ and $S_2 = (1-\chi)S$. The corresponding capacitances are $C_1 = (1+\chi)C$ and $C_2 = (1-\chi)C$, respectively. Consequently, the effective loop capacitance becomes $(1-\chi^2)C/2$. Inspecting Fig. 3.2(a), we estimate an upper limit for the asymmetry parameter, $\chi \lesssim 10\%$, from the area spread among different samples of the same DC SQUID geometry. When simply assuming two junctions with equal areas S instead of an asymmetric configuration, the deviation of the measured capacitance from the mean junction capacitance C is at most 1%. Additionally, we note that the shape of the magnetic field dependence of I_{sw} (data not shown) does not indicate a significant DC SQUID asymmetry for our samples.

Next, we investigate two possible sources of the observed systematic error: stray capacitances due to the details of the DC SQUID layout and the kinetic inductance in the superconducting material. The former is estimated with the help of numerical simulations using a field solver [112, 113]. As it turns out, the two half-loops of the DC SQUID only have a mutual capacitance of approximately 0.5 fF $\ll C_0^\star$. However, they exhibit a significant capacitance to ground (stray capacitance), which is on the order of $C_0^\star$. When investigating the impact of the kinetic inductance L_{kin} our results, we have to take into account that it critically depends on the superconducting penetration depth λ. To this end, we numerically simulate [114, 115] the total loop inductance $L = L_{\mathrm{geo}} + L_{\mathrm{kin}}$ of our DC SQUIDS. Varying the parameter λ in these simulations, we find that the scatter of the data points in Fig. 3.2(a) is minimized for $0.1\,\mu\mathrm{m} \leq \lambda \leq 0.3\,\mu\mathrm{m}$. Assuming the penetration depth of a thin film superconductor in the dirty limit instead of the one derived from the London theory, the kinetic inductance can also be estimated analytically from the normal resistance R_{loop} of the DC SQUID loop without the Josephson junctions [1, 116]:

$$L_{\mathrm{kin}} = \frac{\Phi_0}{\pi^2}\frac{4R_{\mathrm{loop}}}{V_{\mathrm{g}}} \tag{3.1}$$

When comparing L_{kin} calculated from Eq. (3.1) to the numerical results, we find $\lambda \lesssim 0.25\,\mu\mathrm{m}$ in good agreement with the value inferred from the capacitance-junction area data. R_{loop} is estimated by subtracting contact resistances as well as the normal resistance R_{n} due to the Josephson junctions from the total normal transport resistance of the DC SQUID circuit.[2] R_{n} is obtained from the slope of the ohmic part of the current-voltage characteristic as described above. Using the Ambegaokar-Baratoff relation (cf. Sec. 3.1.2), we find that the error in determining R_{n} is small.

Finally, the corrected results taking into account the combined effects of stray capacitance and kinetic inductance are displayed in Fig. 3.2(b). We find $C_{\mathrm{s}} = 100 \pm 25\,\mathrm{fF}/\mu\mathrm{m}^2$ and $C_0 \simeq 1\,\mathrm{fF}$. The remaining clustering of data points belonging to the same DC SQUID geometry is attributed to the influence of the on-chip part of the measurement lines. Although the step analysis could be improved by designing samples with improved control of the electrical environment, we think that it is more desirable to keep the sample design and the experimental setup as simple as

[2]Note that Eq. (3.1) differs from Eq. (9) of Ref. [81] by a factor of 4. There, this factor is absorbed in the definition of R_{loop} as the transport resistance through the loop.

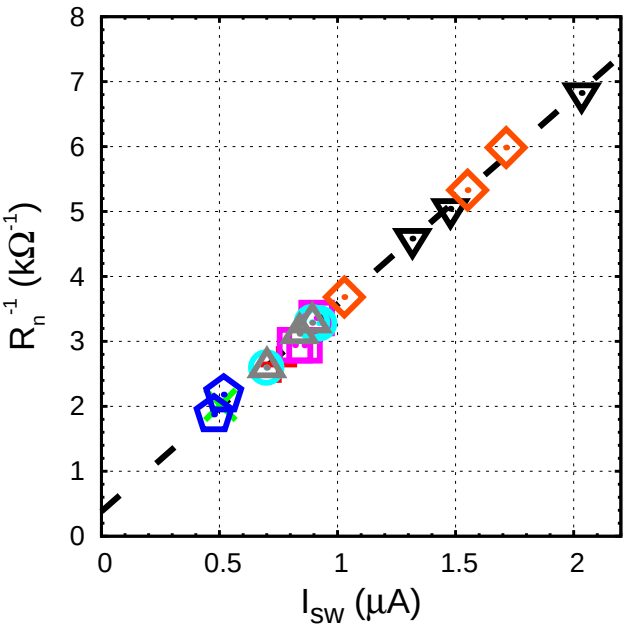

Figure 3.3: Inverse normal resistance R_n^{-1} plotted versus the maximum switching current $I_{sw}(\Phi_x^{SQ} = 0)$. As in Fig. 3.2, different DC SQUID geometries are encoded by different symbols. The dashed black line is a linear fit to the data.

possible. We note that for our purposes, i.e., to design a flux qubit, the achieved accuracy of the junction capacitance measurement presented here is well sufficient.

3.1.2 Ambegaokar-Baratoff relation

In this section, we estimate the accuracy of the determination of the normal resistance from the slope of the ohmic part of the DC SQUID current-voltage characteristics by means of confirming the Ambegaokar-Baratoff relation, Eq. (2.6) in Sec. 2.2, for our samples. Fig. 3.3 clearly shows the expected linear relation between the inverse normal resistance and the switching current of the DC SQUIDs. The scatter of the data points is less than 1.5%. From a numerical fit of Eq. (2.6) to the data, we find $2V_g = 399 \pm 6\mu V$, which is very close to the onset of the normal current branch in Fig. 3.1.

The theoretical value of the gap voltage for bulk aluminum calculated with the BCS theory [2] is $2V_g^{BCS} = 1.764 k_B T_c/e = 365\,\mu V$, where k_B is the Boltzmann constant and $T_c = 1.2\,K$ is the critical temperature of aluminum. The fact that this is slightly smaller than the experimental value contradicts the expectation that the superconducting gap is suppressed by external noise. One explanation for the enhanced gap voltage is that in thin films (thickness $0.09\,\mu m$), T_c can be higher than for the bulk material (cf. Ref. [117] and references therein). Furthermore, as discussed in section 3.1.1, the junction capacitance results suggest that our superconducting films are not satisfactorily described by the simple macroscopic quantum model [1]. Instead, a microscopic extension assuming the dirty limit, where the scattering length is smaller than the correlation length, seems more appropriate. This assumption is also supported by the sample structure, since the aluminum surface is strongly structured and there is the oxide layer within the film.

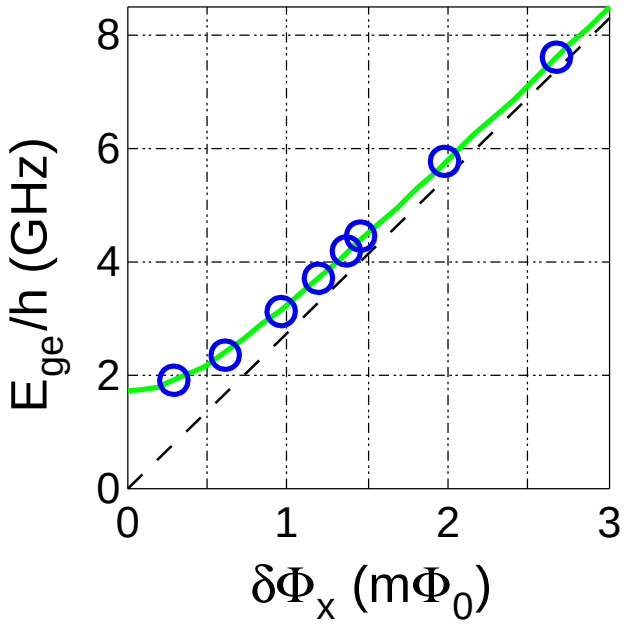

Figure 3.4: Dependence of the energy level splitting E_{ge} on the external flux $\delta\Phi_{\mathrm{x}}$ for a three-Josephson-junction flux qubit measured with continuous-wave qubit microwave spectroscopy. The solid green curve is a numerical fit to the data points (open circles). The dashed black line denotes the asymptotic limit, $\Delta \ll \epsilon$.

3.1.3 Capacitance from continuous-wave qubit spectroscopy

An alternative, but experimentally more demanding way to determine the junction capacitance is the analysis of the flux dependence of the qubit energy level separation $E_{\mathrm{ge}}(\delta\Phi_{\mathrm{x}})$. In Fig. 3.4, we present the results of continuous-wave qubit microwave spectroscopy of a three-Josephson-junction flux qubit fabricated on the same chip and under the same conditions as the DC SQUID samples. The details regarding the setup and the measurement protocol of this experiment are described in sections 3.2.1 and 3.4 and in appendix B.2. The junction capacitance $C_{\mathrm{qb}}^{\mathrm{mw}}$ can be estimated from a numerical fit of the full qubit Hamiltonian of Eq. (2.15) to the spectroscopy data.

The qubit layout is shown in Fig. 2.4. The nominal area S_{qb} of the larger Josephson junctions is $0.03\,\mu\mathrm{m}^2$ and $\alpha = 0.7$. Assuming an uncertainty $\delta\alpha = 0.05$, we find $C_{\mathrm{qb}}^{\mathrm{mw}} = 6.5 \pm 2.7\,\mathrm{fF}$. The relative uncertainty due to α is approximately 40%, which is almost twice as large as the one of the specific capacitance C_{s} determined from the DC SQUID resonance step analysis presented in section 3.1.1. Using the specific capacitance derived from Fig. 3.2(b), one can see that the resulting capacitance $C_{\mathrm{qb}}^{\mathrm{SQ}}$ of junctions with a nominal area of $0.03\,\mu\mathrm{m}^2$ is $4.5 \pm 1.1\,\mathrm{fF}$. Here, the relative error is the one of C_{s} and, consequently, already contains the uncertainty due to the scatter of the junction areas. Thus, for this specific qubit, the results from microwave spectroscopy are consistent with those from the DC SQUID resonance step analysis in the sense that the error bars exhibit a significant overlap. We note, however, that we do not find $C_{\mathrm{qb}}^{\mathrm{mw}} \propto S_{\mathrm{qb}}$ for other qubits on the same sample chip (data not shown). This suggests the presence of other sources of noise in the qubit environment. Their presence could, for example, lead to a suppression of the measured tunnel matrix element Δ, giving rise to a not well controlled contribution $\delta C_{\mathrm{qb}}^{\mathrm{mw}}$ to the capacitance estimate.

3.2 Conventional readout of a flux qubit

One of the fundamental tasks in experiments with qubits is the state detection process [88]. For a prospective use in quantum information processing, a qubit readout should satisfy the following requirements. First, the readout procedure must happen on a timescale much faster than the qubit relaxation time, i.e., the characteristic time in which the qubit suffers uncontrolled state transitions induced by its environment (including the detector itself). Next, a single-shot readout, where the two qubit states can be perfectly distinguished from each other without averaging over an ensemble of readout events, is desirable. This situation is equivalent to a visibility of 100 %. Finally, in a quantum nondemolition measurement, the interaction between qubit and detector preserves the eigenstates of one specific operator of interest [118, 119], usually $\hat{\sigma}_z$. Hence, the destructive effect of the detector backaction on the qubit is eliminated. However, when the qubit-detector system is used in fundamental research, some of the above requirements can be substantially relaxed, depending on the experiment. In such a situation, readout techniques, which can be implemented easily, can be favorable.

For flux qubits, several readout methods have been proposed and successfully implemented. They range from the simple switching-DC-SQUID method [28, 120, 121] to more sophisticated techniques such as the inductive readout [122–126] or the bifurcation amplifier [127–130]. The two latter have the potential to achieve quantum non-demolition measurements [131] and very large signal visibility, which are important features for future applications. In this study, we have chosen a switching-DC-SQUID readout, which is attractive because of its simple technical implementation. In particular, no cold amplifiers or similarly sophisticated high-frequency components are needed. Furthermore, in the experiments presented in chapter 4, the switching-DC-SQUID readout enables us to study the effect of two fundamentally different electromagnetic environments (capacitive and resistive) on the decoherence of one and the same flux qubit easily.

As shown in Fig. 2.4, the qubit is surrounded by a DC SQUID. The latter is coupled to the qubit via a purely geometric mutual inductance $M_{\mathrm{SQ,qb}} = 6.7\,\mathrm{pH}$. In contrast to other flux qubit designs [44, 46], there is no galvanic connection between DC SQUID and qubit in our samples. This is expected to reduce the effect of asymmetry-related issues as well as the detector back-action on the qubit. In fact, we do not find any measurable bias current dependence of the qubit decay time, which has recently been reported for shared-edge designs [44, 46].

In order to detect the qubit state, we utilize the fact that the switching current of the DC SQUID depends on the total flux threading its loop. This flux is the sum of the externally applied bias Φ_{x} and the small contribution due to the qubit persistent current $\pm I_{\mathrm{p}}$. Away from the degeneracy point, the latter reflects the qubit energy eigenstate, which coincides with one of the persistent current states there. Depending on the measurement setup, the switching current can be recorded in two ways. When the bandwidth of the measurement lines is low, I_{sw} can be detected by slowly sweeping the DC SQUID bias current as explained in section 3.2.1. In section 3.2.3, we discuss the case of high-bandwidth lines, where pulsed readout schemes are possible. These allow for more sophisticated experimental protocols such as the adiabatic shift pulse method introduced in section 3.2.4.

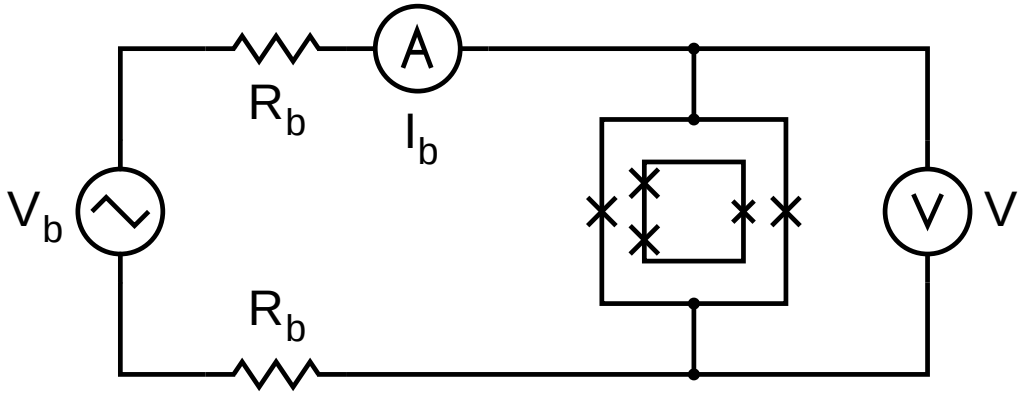

Figure 3.5: Circuit diagram representation of the slow sweep setup. The bias current is generated with a triangular source voltage V_b and two bias resistors $R_\mathrm{b} = 100\,\mathrm{k}\Omega$.

3.2.1 Slow-sweep readout

One of the most straightforward ways to detect the qubit state is the so-called slow-sweep readout, which is also explained in detail in chapter 3 of Ref. [120]. Together with continuous-wave qubit microwave spectroscopy it can be used to reconstruct the energy level splitting of a flux qubit as explained in section 3.2.2. Fig. 3.5 shows a sketch of the slow-sweep readout setup. The voltage drop V across the DC SQUID is continuously monitored while applying a triangular transport bias current I_b to it. Due to the limited bandwidth of the measurement lines, amplifiers, and AD converter, the frequency of I_b is typically restricted to a few tens or hundreds of Hertz.[3] As shown in Fig. 2.3(a) and Fig. 3.1, the switching current I_sw corresponds to the value of I_b at which V changes abruptly from zero to a finite value.

Ignoring the effect of the qubit, $I_\mathrm{sw} = I_\mathrm{sw}^\mathrm{SQ}$ has the cosine dependence on the external magnetic flux given by Eq. (2.5), $I_\mathrm{sw}^\mathrm{SQ} \propto \left|\cos[(A_\mathrm{SQ}/A_\mathrm{q})(\Phi_\mathrm{x}/\Phi_0)]\right|$. Here, A_SQ and A_q are the areas enclosed by the DC SQUID and qubit loop, respectively. Considering the inductive coupling of the flux qubit to the DC SQUID, the supercurrent circulating in the qubit loop, $I_\mathrm{q} \propto \langle\hat{\sigma}_z\rangle$ (cf. Sec. 2.5), superposes a small flux signal onto the DC SQUID switching current. The latter is changed by the amount $\delta I_\mathrm{sw} = (I_\mathrm{sw} - I_\mathrm{sw}^\mathrm{SQ}) \propto I_\mathrm{q} \propto \langle\hat{\sigma}_z\rangle$. Then, as shown in Fig. 2.6 for the case of zero temperature, a step structure is expected to appear in the switching current when sweeping Φ_x during a slow-sweep experiment near one of the qubit optimal points, $\Phi_\mathrm{x} \approx (n + 0.5)\Phi_0$ (n is an integer). For finite temperatures T, the step broadens [132], yielding $\delta I_\mathrm{sw} \propto (\epsilon/\omega_\mathrm{ge}) \tanh[\omega_\mathrm{ge}/(2k_\mathrm{B}T)]$.

In an experiment, the tunneling associated with the switching of the DC SQUID is a statistical process (cf. Sec. 2.2). Hence, typically, averaging over 50-1000 switching events is necessary to resolve the qubit step. In order to obtain the step signal shown in Fig. 3.6, 400 single readout events are used for each value of the applied flux. For optimal detection sensitivity, the switching histogram of the DC SQUID should be narrow. Consequently, the experiment is performed at millikelvin temperatures in a dilution refrigerator. Also, the ratio $A_\mathrm{SQ}/A_\mathrm{q}$ should be such that

[3] When recording current-voltage characteristics or when a quantitative measurement of I_sw is necessary, the sweep rates are between $0.1 - 1\,\mathrm{Hz}$. When measuring the qubit signal δI_sw, the only restriction for the background signal $I_\mathrm{sw}^\mathrm{SQ}$ is that it should be approximately linear. In this situation, sweep rates up to $300\,\mathrm{Hz}$ are used.

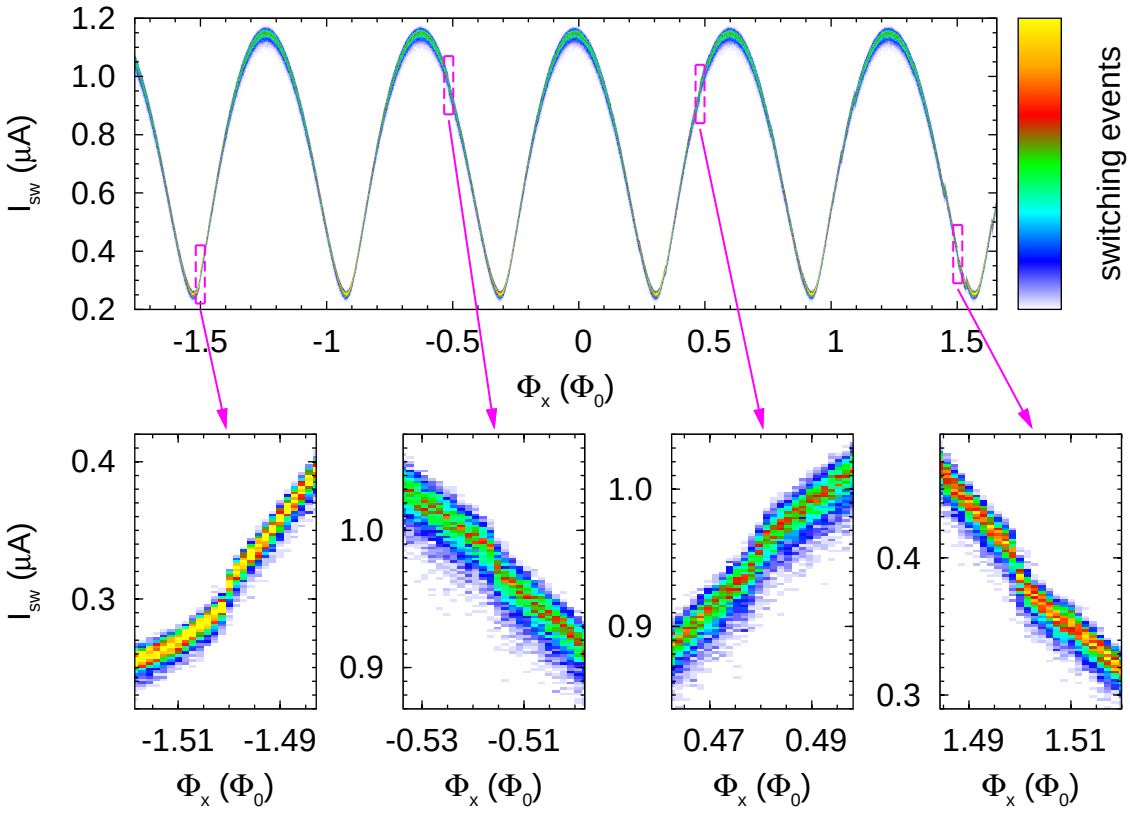

Figure 3.6: I_{sw}-over-Φ_{x} curve of a DC SQUID surrounding a flux qubit. The device is the same as the one used to record the data of Fig. 2.3. The switching histograms are color coded (white corresponds to zero events). When the flux Φ_{x} through the qubit loop equals $(n + 0.5)\Phi_0$, n being an integer, a small step structure is superimposed on the cosine-shaped Φ_{x}-dependence of the DC SQUID.

the qubit optimal point is not close to a maximum of $I_{\mathrm{sw}}^{\mathrm{SQ}}$, where the switching histogram is particularly broad and the flux-sensitivity of the DC SQUID is low. Instead, our qubits are designed to be operated near $\Phi_{\mathrm{x}} \simeq .5\Phi_0$, which is close to but not right at the minimum $\Phi_{\mathrm{x}}^{\mathrm{SQ}} = 2.5\Phi_0$. Finally, we note that the slow-sweep readout is not suitable for detecting the qubit energy eigenstate in close vicinity of the optimal point because there the persistent current $I_{\mathrm{p}}\langle\hat{\sigma}_z\rangle$ vanishes. As explained in Sec. 3.2.4, this restriction can be evaded using pulsed readout schemes.

3.2.2 Continuous-wave qubit microwave spectroscopy

The first step in the characterization of a flux qubit is the reconstruction of its energy level splitting E_{ge} as a function of the external flux Φ_{x}, following Eq. (2.18). Experimentally, E_{ge} can be determined with continuous-wave microwave spectroscopy, which is also explained in detail in chapter 3 of Ref. [120]. The measurement protocol is intriguingly simple: during the slow-sweep readout process, the qubit is irradiated continuously with a microwave signal of angular frequency ω. When the qubit is detuned from the microwave driving, mainly the ground state is populated at low temperatures. Under resonant conditions, $\omega \approx E_{\mathrm{ge}}/\hbar$, the excited state becomes populated and the qubit contribution δI_{sw} to the DC SQUID switching current changes. Consequently, sweeping Φ_{x} in the qubit step region near the op-

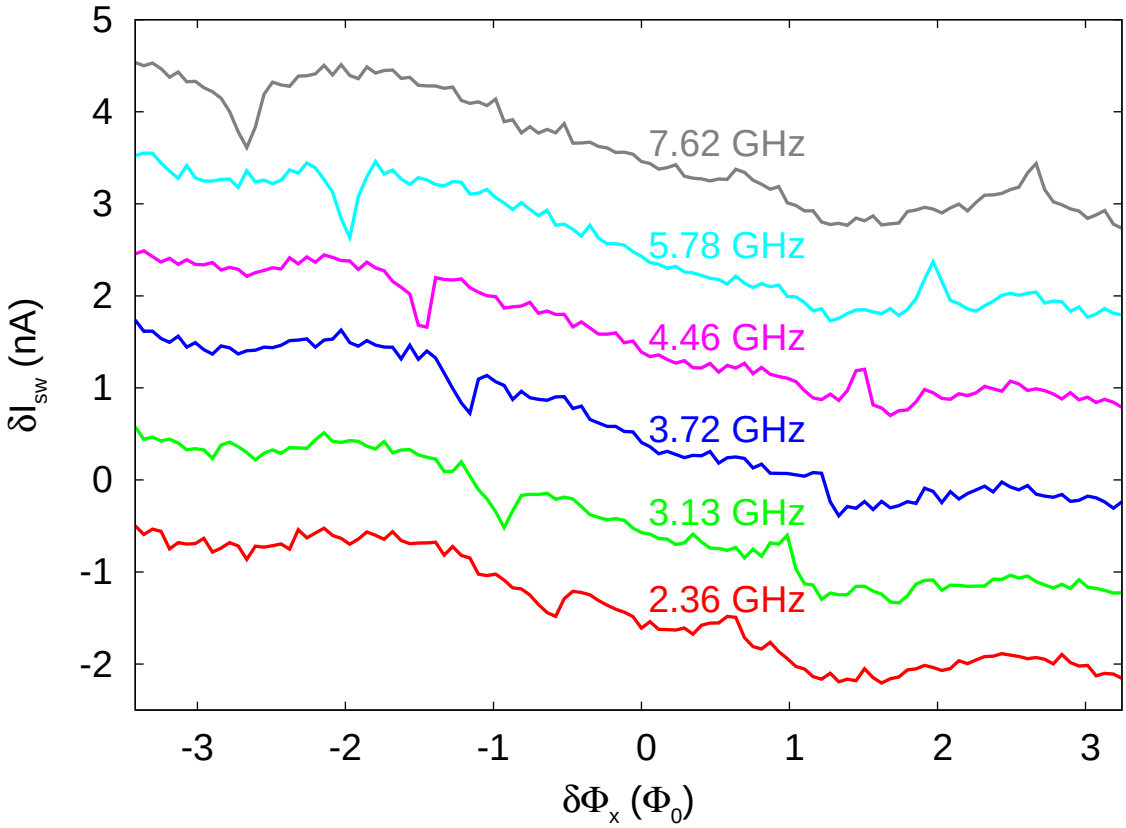

Figure 3.7: Step signature of a flux qubit under continuous microwave irradiation near the qubit step $\Phi_x \simeq 1.5\Phi_0$ recorded with the slow-sweep method. The traces are offset by arbitrary values for clarity and the colored numbers indicate the frequency $\nu = \omega/2\pi$ of the microwave radiation. The frequency-dependent peak-and-dip pairs are clearly visible. The hyperbolic Φ_x-dependence of the peaks/dips is shown in Fig. 3.4. Note that the data shown in Fig. 2.3 and Fig 3.6 is recorded using a different sample.

timal point yields a peak and a dip, whose flux positions vary with E_{ge}. This is shown in Fig. 3.7. The Φ_x-dependence of the peaks/dips, the qubit energy diagram, is plotted in Fig. 3.4. The details of the measurement setup are similar to the one described in appendix B.2. From a numerical fit of the dependence of the peak and dip positions to Eq. (2.18) the qubit gap $\Delta \simeq 2\,\mathrm{GHz}$ and the persistent current $I_p \simeq 450\,\mathrm{nA}$ can be extracted.

3.2.3 Resistive-bias pulsed readout

On the one hand, the low bandwidth of the measurement lines in the slow-sweep readout (cf. Sec. 3.2.1) provides efficient filtering of external noise. On the other hand, it inhibits direct measurements of the qubit dynamics in the time domain, where a resolution of approximately 1 ns is required. Therefore, a pulsed state detection scheme is required to gain more insight into the qubit decoherence properties. This readout protocol is illustrated in Fig. 3.8. A short voltage pulse V_{in} is applied to the DC SQUID bias line and transformed into a bias current pulse I_{bias} via a biasing element, the resistor R_{Rbias}. As shown in Fig. 3.8(b), the pulse is divided into a 60 ns-long switching and an approximately 1 µs-long hold section. The amplitude

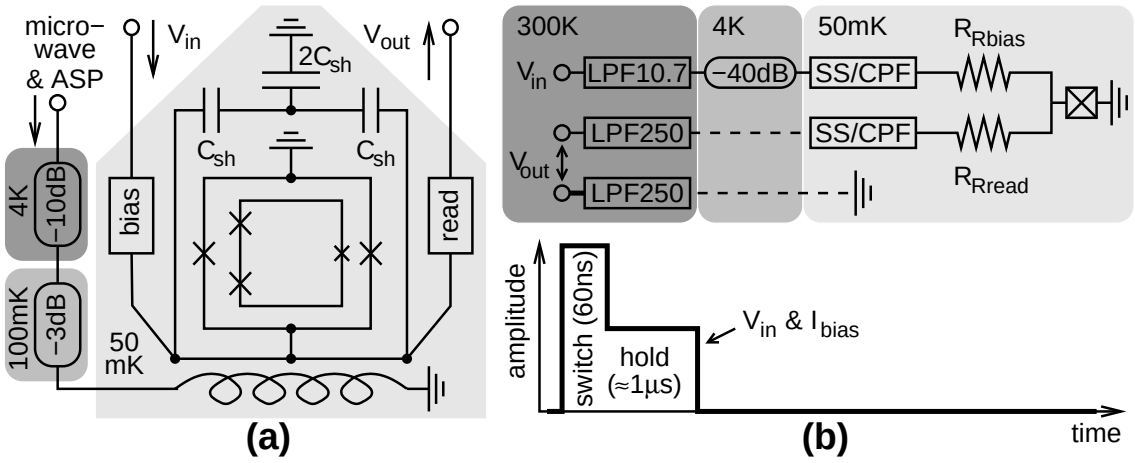

Figure 3.8: **(a)** Sketch of the sample layout. The Josephson junctions are represented by crosses. The effective shunting capacitance of the DC SQUID, C_{sh}, is made of three physical capacitors in a gradiometric design. The boxes titled "bias" and "read" represent the circuit elements used to engineer the electromagnetic environment of the qubit. "microwave & ASP" denotes the microwave control pulse pattern and the adiabatic shift pulse (see Fig. 3.9), which are attenuated (rounded boxes) at low temperature and coupled to the qubit via an on-chip antenna (coiled shape). **(b)** Top: Resistive-bias setup. "LPF10.7(250)" denotes a commercial low-pass filter with $10.7(250)\,\mathrm{MHz}$ cutoff frequency. "SS/CPF" represents the high-frequency filtering, consisting of an ultra-thin stainless-steel coaxial cable in series with a copper powder filter. Qubit, DC SQUID, and effective shunting capacitor are indicated with the symbol ⊠. Solid and broken lines represent high-bandwidth semirigid $\varnothing 1.2\,\mathrm{mm}$ CuNi/Nb and narrower bandwidth stainless-steel braided flexible coaxial cables, respectively. The bias voltage pulse is attenuated by $40\,\mathrm{dB}$ at $4\,\mathrm{K}$. Bottom: Switch&hold readout pulses for the resistive-bias setup. Note that $60\,\mathrm{ns}$ are the width of the portion of switching pulse exceeding the hold level.

of the former is chosen to be half way between the switching currents corresponding to the $|+\rangle$ and $|-\rangle$ states of the qubit. Then, the DC SQUID generates a response voltage V_{out} in the readout line, which is either zero or of the order of $2V_{\mathrm{g}}$, depending on the qubit state. In the latter case, V_{out} is sustained for the duration of the hold pulse, whose level is chosen to be just above the retrapping current in order to minimize quasiparticle generation in the DC SQUID. This provides enough integration time for the detection of V_{out} with a room temperature differential amplifier with an input impedance of $1\,\mathrm{M}\Omega$ against a cold ground taken from the mixing chamber temperature level. Nevertheless, the time interval where a switching event can happen is not larger than the switching pulse length, guaranteeing a good time-resolution.

After performing a single measurement sequence as described above, the response signal of the DC SQUID is binary: either a voltage pulse is recorded or not. By averaging over an ensemble of several thousands of such single-shot measurements we find the switching probability P_{sw}, which is proportional to $\langle\hat{\sigma}_z\rangle$. Under appropriate conditions (cf. Sec. 3.2.4), the qubit state is encoded in the value of P_{sw}. In the best case, the ground state would correspond to $P_{\mathrm{sw}}^{\mathrm{min}} = 0\%$ and the excited state to $P_{\mathrm{sw}}^{\mathrm{max}} = 100\%$, or vice versa. In reality, however, the visibility $P_{\mathrm{sw}}^{\mathrm{max}} - P_{\mathrm{sw}}^{\mathrm{min}}$ is usually significantly smaller than 100% due to noise issues.

Since the pulsed readout scheme requires high-bandwidth (typically $\gtrsim 100\,\mathrm{MHz}$) measurement lines, care has to be taken to design the immediate qubit environment and the filtering in a way that the effects of decoherence are minimized. As shown in the top part of Fig. 3.8(b), the DC SQUID bias and readout lines are heavily filtered against noise in the megahertz and gigahertz range. To this end, room-temperature commercial low-pass filters are used in combination with copper powder filters [133] and stainless steel ultra-thin coaxial cables at the mixing chamber temperature level. The latter have a length of 1 m and an outer diameter of 0.33 mm. The copper powder filters have a wire length of 1 m for the readout line, but only 25 cm for the bias line to avoid pulse distortion. The bias resistance R_{Rbias} is realized partially as a $1\,\mathrm{k}\Omega$ SMD chip resistor on the printed circuit board surrounding the sample chip and partially as an on-chip gold thin film ($250\,\Omega$). Likewise, the resistor R_{Rread} in the readout line consists of an off-chip and an on-chip component of $3\,\mathrm{k}\Omega$ and $2.25\,\mathrm{k}\Omega$, respectively. Furthermore, the DC SQUID is shunted with an $\mathrm{Al/AlO}_x\mathrm{/Al}$ on-chip capacitance $C_{\mathrm{sh}} = 6.3 \pm 0.5\,\mathrm{pF}$ as shown in Fig. 3.8(a). This capacitance, which in combination with R_{Rbias} and R_{Rread} also behaves as a low-pass filter, constitutes the main component of the qubit electromagnetic environment. Previous studies [120, 121] have shown that a purely capacitive shunt results in a much smaller low-frequency noise spectral density compared to an RC-type of shunt. This is crucial since both high- and low-frequency environmental noise have to be reduced as much as possible in order not to deteriorate the qubit coherence times.

The resistive elements in the DC SQUID lines also help to damp resonant modes formed by the shunted DC SQUID and the parasitic inductance/capacitance of its leads. Such modes can be excited by the microwave control signals applied to the qubit via the on-chip antenna, which affect also the readout circuitry. In practice, this has the effect that the readout signal is covered by a wide spectrum of unwanted resonances. In order to avoid these parasitic modes, the bias and readout resistors are placed as close as possible to the shunted DC SQUID. In this way, qubit, DC SQUID, and shunting capacitor are enclosed within a total length scale of about $100\,\mu\mathrm{m}$. Thus, most parasitic resonances in the relevant frequency range of a few gigahertz are strongly damped. The remaining modes involve the shunting capacitor [71], the inductance of the aluminum leads close to the DC SQUID, possible box resonances, microscopic impurities in the substrate or the junctions, and, of course, the qubit.

3.2.4 Adiabatic-shift pulse method

Similarly to the slow-sweep detection scheme described in Sec. 3.2.1, the plain DC SQUID-based pulsed readout fails in close vicinity to the optimal point because the expectation value $I_{\mathrm{p}}\langle\hat{\sigma}_z\rangle$ of the circulating current vanishes there. This phenomenon is best understood by remembering that the flux information is carried by the states $|+\rangle$ and $|-\rangle$. Hence, the flux signal of the energy eigenstates $|\mathrm{g}\rangle$ and $|\mathrm{e}\rangle$ disappears when they become nearly equal superpositions of $|+\rangle$ and $|-\rangle$. Nevertheless, $|\mathrm{g}\rangle$ and $|\mathrm{e}\rangle$ can be detected in this regime by means of the adiabatic-shift pulse method, which is based on the idea of separating the operating point from the readout point. The transition between the two flux points is achieved by applying an adiabatic control pulse to the qubit. In contrast to the quasi-static flux bias setting the readout point, the shift pulse is not generated by the superconducting coil

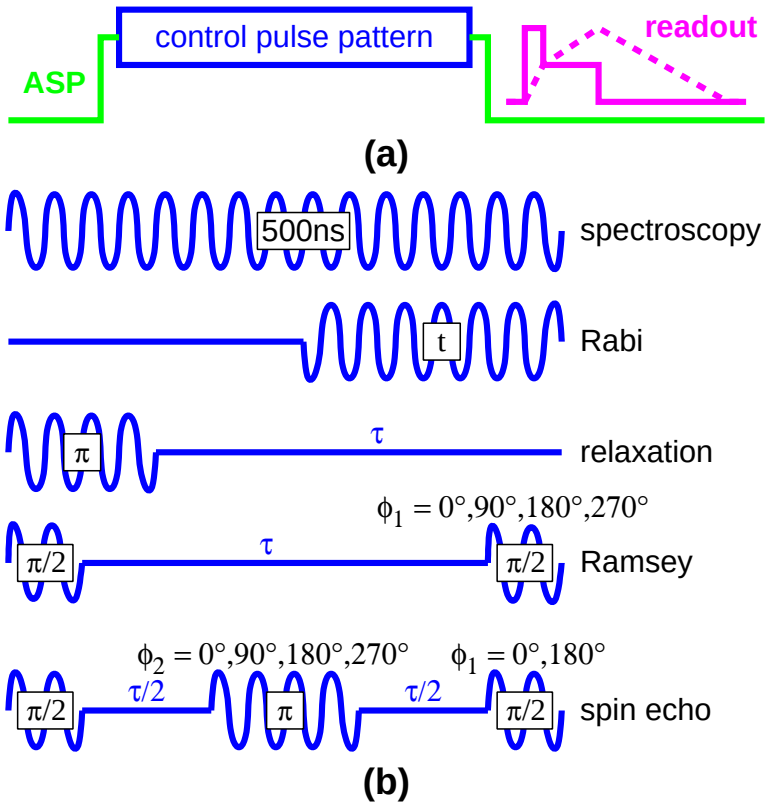

Figure 3.9: Adiabatic shift pulse (ASP) readout. **(a)** General protocol. **(b)** Microwave control pulse patterns for the experiments discussed in this work. The boxed values denote either the pulse duration t or the corresponding rotation angle of the qubit state vector on the Bloch sphere. Free evolution times are denoted by the symbol τ. In the multi-pulse sequences, ϕ_1 and ϕ_2 are the pulse phases relative to the initial pulse necessary for the phase-cycling technique (cf. Sec. 3.4.4).

located in the helium bath of the dilution refrigerator. Instead, it is applied via the on-chip microwave antenna as shown in Fig. 3.8(a). The total control sequence for initialization, manipulation, and readout of the qubit is displayed in Fig. 3.9(a) and can be summarized as follows: First, the qubit is initialized in the ground state $|\mathrm{g}\rangle$ at the readout point far away from the degeneracy point by waiting for approximately 300 µs. Here, the states $|+\rangle$ and $|-\rangle$ practically coincide with $|\mathrm{g}\rangle$ and $|\mathrm{e}\rangle$. Then, a rectangular adiabatic-shift pulse together with the microwave control sequence is applied to the qubit via the on-chip antenna. In this way the qubit is adiabatically shifted to its operation point, where the desired operation is performed by means of a suitably chosen microwave pulse sequence. Finally, immediately after end of the microwave pulse sequence, the qubit is adiabatically shifted back to the readout point, preserving its state. There, the readout is performed applying a pulse to the DC SQUID measurement lines as described in Sec. 3.2.3. Note that, in order to avoid qubit state transitions, the rise and fall times of the shift pulse have to be long with respect to the h/Δ (adiabatic condition), but also short enough to avoid unwanted relaxation processes. In our experiments, the rise-time of the shift pulse is 0.8 ns.

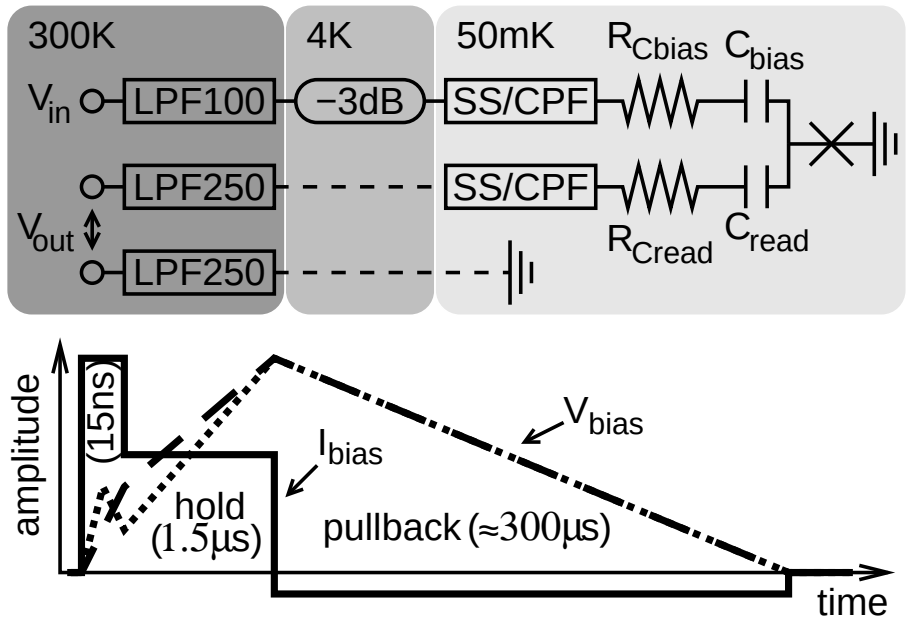

Figure 3.10: Top: Capacitive-bias setup. The acronyms are the same as in Fig. 3.8(b). The DC SQUID biasing circuit forms a band-pass filter. Reduced series resistors still provide sufficient damping of parasitic external modes. Bottom: Switch&hold readout pulses for the integrated-pulse setup: The voltage pulse (dashed line) is the time integral of the desired current pulse (solid line). An approximately $300\,\mu s$ long pullback section is required. In the actual voltage pulses (dotted line) another kink is introduced to avoid discharging effects of the capacitors.

3.3 Capacitive-bias readout of a flux qubit

In this section, we present a novel variant of the DC SQUID-based pulsed qubit state detection. It is based on a capacitive instead of the standard resistive bias for the DC SQUID. We refer to this method as the integrated-pulse readout because the voltage pulse sent to the DC SQUID detector is the time integral of the desired current bias pulse. In this way, low-frequency fluctuations of the DC SQUID bias current, which can reduce the phase coherence of the qubit, are suppressed. In other words, the capacitive-bias method changes from the low-pass filter configuration used in the resistive-bias method to a band-pass filter configuration. Hence, also shorter switching pulses can be achieved, thereby increasing the time-resolution of the detection process and, possibly, the qubit visibility. The properties of a flux qubit measured both with the capacitive- and resistive-bias method is discussed in chapter 4.

In contrast to a bias resistor, the bias capacitor differentiates the incoming voltage pulse when transforming it into a current pulse. This effect has to be taken into account when shaping the readout voltage pulse $V_{\rm in}$. A detailed schematic representation of the capacitive-bias setup and the utilized pulses is displayed in Fig. 3.10. We note that for the integrated pulse setup the different levels of switching and hold part of the current pulse correspond to different slopes of the voltage pulse in these sections. Since the readout protocol is repeated many times in an experiment, the voltage pulse amplitude has to be reduced back to zero after the end of the hold section. This so-called pullback section has to be much longer ($\simeq 300\,\mu s$ in

our experiments) than the hold section in order to avoid spurious switching of the DC SQUID in the negative current direction. Furthermore, the amplitude of the differentiated current pulse falls off the switching to the hold level within a few tens of nanoseconds due to the discharging of the shunting capacitor C_{sh} and can be compensated by introducing a kink in the integrated voltage pulse. In comparison to the resistive-bias setup of Fig. 3.8(b), the cutoff frequency of the room temperature bias line filter is relaxed to 100 MHz. The voltage pulses require a weaker attenuation of 3 dB at 4 K. As biasing elements, the series capacitors $C_{\mathrm{bias}} = 0.5\,\mathrm{pF}$ and $C_{\mathrm{read}} = 470\,\mathrm{pF}$ are inserted into the bias and readout lines. The series resistors are reduced to $R_{\mathrm{Cbias}} = 511\,\Omega$ and $R_{\mathrm{Cread}} = 1.5\,\mathrm{k}\Omega$. For technical reasons, all resistors and capacitors except for C_{sh} are placed off-chip, on the printed circuit board.

We note that a similar readout method, also based on a capacitive bias, has been proposed in an effort to design and implement a switching detector for Cooper-pair transistors and Quantronium circuits [134, 135]. However, there are remarkable differences to the work presented here. First, because of the on-chip shunting capacitor we do not encounter the complication of frequency-dependent damping. Even for low impedances the readout DC SQUID in our experiments remains underdamped (DC SQUID quality factor $Q \simeq 4$ at approximately $50\,\Omega$). Second, and even more importantly, we are able to measure the coherent dynamics of our flux qubit (cf. chapter 4).

In the resistive-bias experiments, the bias lines of the readout DC SQUID are severely low-pass filtered as shown in Fig. 3.8. This is required to reduce the high-frequency noise spectral density $S_\omega(\omega_{\mathrm{ge}} = E_{\mathrm{ge}}/\hbar)$, which is responsible for the energy relaxation [36, 120, 121]. Additionally, filtering is necessary to eliminate part of the low-frequency noise[4] because the phase coherence of the qubit is mainly determined by the low-frequency environmental noise spectral density $S_\omega(\omega \to 0)$. Consequently, the cutoff frequency of the low-pass filter should be chosen as low as possible in order to attenuate low-frequency noise strongly. However, a lower limit is set by the requirement that the readout pulse has to be sufficiently short to avoid any deterioration of visibility. For this reason, the filter cutoff cannot be chosen smaller than approximately 10 MHz in the resistive-bias measurements and any noise below this frequency passes unaffected to the sample.

The integrated-pulse method reduces the effect of low-frequency noise from the DC SQUID measurement lines, especially from the bias current line. For a qubit limited by this type of noise, the use of a capacitive bias should improve the dephasing time as compared to the resistive-bias case. The reason is that a band-pass filter instead of a low-pass filter configuration is obtained by replacing the DC SQUID bias resistor with a 0.5 pF bias capacitor. Consequently, the pass-band is designed to be just broad enough to allow for sufficiently fast readout pulses. Noise at lower and higher frequencies is strongly suppressed. In this way, the rise time of the switching pulses applied to the readout DC SQUID is reduced by a factor of six (R-bias: 60 ns, C-bias: 10 ns)[5]. This is expected to result in a better time resolution and hence in an increased visibility. In Fig. 3.11, we show a comparison of the pulse shapes and filter characteristics of the two different bias schemes. Evidently,

[4] In this manuscript, the term low-frequency noise refers to noise which has a large spectral density at frequencies much smaller than the qubit transition frequency $\Delta/h \simeq 4\,\mathrm{GHz}$.

[5] Throughout this manuscript, resistive and capacitive-bias method are often abbreviated with the terms R-bias and C-bias, respectively.

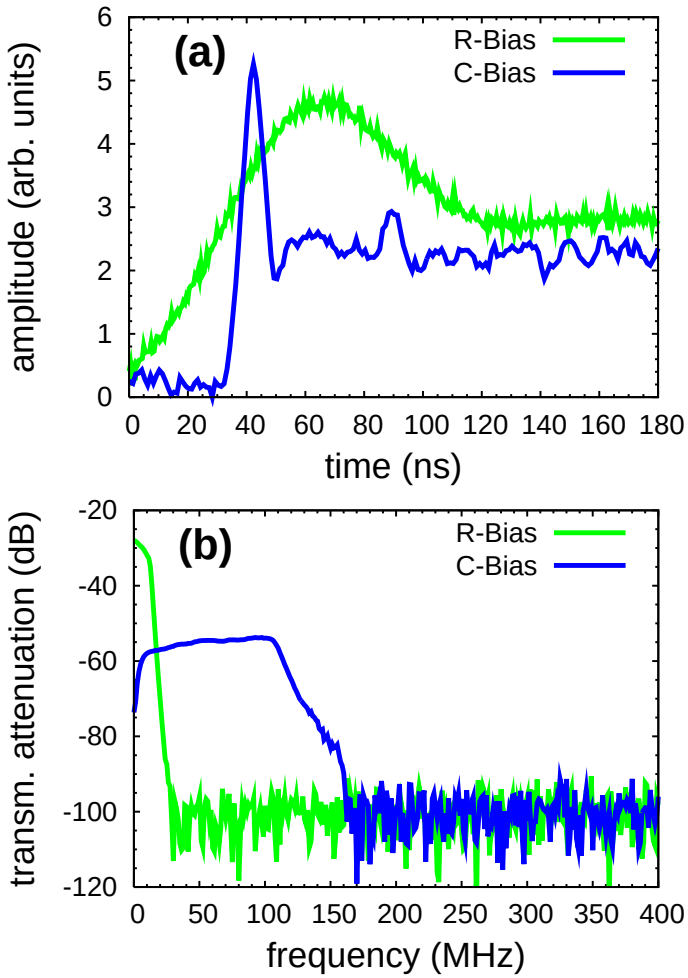

Figure 3.11: Filter characteristics of the DC SQUID bias line. The green and the blue curves are recorded in the resistive and the capacitive bias configuration, respectively. **(a)** Shape of the bias current pulses. The switching pulse width above the hold level in the capacitive-bias setup is approximately 15 ns as compared to approximately 60 ns in the resistive-bias setup. **(b)** Transmission spectra. In both cases, above 170 MHz the transmitted signal is below the noise floor of the network analyzer. In comparison to the resistive-bias setup, stronger attenuation is obtained below 15 MHz for the capacitive-bias setup. However, the attenuation is weaker in the 15-170 MHz frequency window. The width of this window as well as the attenuation factor can be further optimized using a smaller bias capacitor.

the integrated-pulse readout provides a band-pass filtering of the bias line and allows for approximately four times shorter switching pulses than the resistive-bias setup. In part, this is achieved by exchanging the 10.7 MHz commercial low-pass filter from the resistive-bias readout with a 100 MHz filter. The capacitive setup permits us to obtain a narrow-bandwidth band-pass filter of 150 MHz width with a reasonably high center frequency of 90 MHz and minimum attenuation of 55 dB for the DC SQUID bias line. This means that only the frequency band which is absolutely necessary for the readout pulse is opened. In future experiments, the use of smaller on-chip capacitors should allow us to design even narrower band-pass filters with lower minimum attenuation. Since the capacitive filter is not resistive it is especially suitable for mixing-chamber temperature applications.

Parasitic resonances in the bias line are pushed to higher frequencies by the small bias capacitor. In the voltage output line, C_{read} is limited to 470 pF because the outgoing signal must not be attenuated too much. However, the series resistors provide additional damping of external modes. These resistors, which are smaller than in the resistive-bias setup, are placed in a way that their low-frequency Johnson-Nyquist (thermal) noise is filtered out by the capacitors. As explained above, except for C_{sh} the bias and readout resistors and capacitors are located on the printed circuit board surrounding the sample chip. In this case, the on-chip resistors utilized in the resistive-bias measurements are short-circuited with approximately 1.5 mm long gold bonding wires. Nevertheless, the spatial enclosing of the sample to a length scale $\lesssim 3$ mm is still sufficient to avoid parasitic resonances. Finally, we consider the implications of the fact that we are limited to a 0.5 pF surface mount bias capacitor. As a consequence, the bias line filter passband displayed in Fig. 3.11(b) is wider than in the resistive-bias configuration. As we discuss in detail in Sec. 4.3.1, we find that although our qubit is energy relaxation limited at the optimal point, that the relaxation time is not limited by the high-frequency bias current fluctuations.

3.4 Qubit operation

The qubit control is achieved by varying the control parameter $\delta\Phi_{\mathrm{x}}$ (cf. Sec. 3.2.4) and, simultaneously, applying a suitable sequence of microwave pulses.

3.4.1 Qubit rotations on the Bloch sphere

Let us consider a single microwave pulse $A\cos(2\pi\nu t' + \phi)$ of amplitude A, frequency $\nu \approx \nu_{\mathrm{ge}}$, and phase ϕ in the time interval $0 \leq t' \leq t$. In a frame rotating with frequency ν, such a pulse of duration t results in a rotation of the qubit state vector by an angle $\Omega = 2\pi\nu_{\mathrm{R}} t\sqrt{1 + (\delta/\nu_{\mathrm{R}})^2}$ on the Bloch sphere. Here, the Rabi frequency $\nu_{\mathrm{R}} \equiv \nu_{\mathrm{R}}(A)$ is a function of the pulse amplitude A. The relative phase ϕ of the pulse and the detuning $\delta \equiv \nu - \nu_{\mathrm{ge}}$ determine the rotation axis $\mathbf{v} \equiv (v_1, v_2, v_3) = (\nu_{\mathrm{R}}\cos\phi, \nu_{\mathrm{R}}\sin\phi, \delta)/\sqrt{\nu_{\mathrm{R}}^2 + \delta^2}$. Mathematically, we can describe this rotation with the matrix

$$\tilde{R}_{\phi,\delta}(\Omega) = \begin{bmatrix} \mathscr{C} + v_1^2(1-\mathscr{C}) & v_1v_2(1-\mathscr{C}) - v_3\mathscr{S} & v_1v_3(1-\mathscr{C}) + v_2\mathscr{S} \\ v_2v_1(1-\mathscr{C}) + v_3\mathscr{S} & \mathscr{C} + v_2^2(1-\mathscr{C}) & v_2v_3(1-\mathscr{C}) - v_1\mathscr{S} \\ v_3v_1(1-\mathscr{C}) - v_2\mathscr{S} & v_3v_2(1-\mathscr{C}) + v_1\mathscr{S} & \mathscr{C} + v_3^2(1-\mathscr{C}) \end{bmatrix}, \quad (3.2)$$

where $\mathscr{S} \equiv \sin\Omega$ and $\mathscr{C} \equiv \cos\Omega$. For the case $\delta = 0$ and $\phi = 0$, Eq. (3.2) describes a rotation by an angle $2\pi\nu_{\mathrm{R}}t$ about the x-axis. When introducing a finite relative phase ϕ, the orientation of the rotation axis within the x, y-plane changes. Finite detuning results in a change of the rotation angle and a tilt of the rotation axis out of the x, y-plane. In the absence of microwave radiation ($\nu_{\mathrm{R}} = 0$) the qubit evolves freely, i.e., its state vector rotates about the z-axis of the Bloch sphere with a frequency δ. During the free-evolution time τ, this rotation covers the angle $\Omega_{\mathrm{free}} = 2\pi\delta\cdot\tau$. The corresponding rotation matrix, $\tilde{R}_z(\Omega_{\mathrm{free}})$, is obtained from Eq. (3.2) by choosing $\mathbf{v} = \mathbf{v}_z \equiv (0, 0, 1)$.

3.4.2 The microwave antenna

As shown in Fig. 3.8(a), the microwave pulses are applied to the qubit via an on-chip antenna, which is implemented as a coplanar waveguide transmission line short-circuited at one end. The qubit is coupled inductively to this antenna. From a FastHenry[115] simulation the mutual inductance between the antenna and the qubit is determined to be $M_{\mathrm{mw,qb}} \simeq 73\,\mathrm{fH}$. The signal-to-noise ratio of the applied microwave radiation is improved by means of a 10 dB and a 3 dB attenuator, which are thermally anchored at a temperature of 4 K and 100 mK, respectively.

3.4.3 Pulse sequences

The microwave pulse sequences used for the manipulation of the qubit state are shown graphically in Fig. 3.9(b). For the frequency domain measurements (microwave spectroscopy), the qubit is saturated to an equilibrium mixed state by means of a sufficiently long (approximately 100 ns) microwave pulse followed by the readout. Similar to the continuous-wave microwave spectroscopy introduced in Sec. 3.2.2, a peak appears in the switching probability when the driving frequency is close to the qubit eigenfrequency, $\nu \approx \nu_{\mathrm{ge}}$. In the time domain, driven Rabi oscillations are recorded by measuring the qubit state as a function of the duration t of a single microwave pulse of fixed amplitude A. From the measured Rabi frequency ν_{R} of these oscillations, we determine the durations t_π and $t_{\pi/2}$ of the π- and $\pi/2$-pulses, which rotate the qubit state vector by the corresponding angles. In our experiments, we typically choose A such that $t_\pi = 2t_{\pi/2} = 1/2\nu_{\mathrm{R}} \simeq 8\,\mathrm{ns}$. Then, the energy relaxation time is determined by exciting the qubit with a π-pulse and, subsequently, recording the decay of $\langle\hat{\sigma}_z\rangle$ as a function of the waiting time.

The evolution of the in-plane components $\langle\hat{\sigma}_{x,y}\rangle$ of the qubit state vector on the Bloch sphere is probed using the multi-pulse sequences $\pi/2$-pulse–wait–$\pi/2$-pulse–readout (Ramsey experiment) or $\pi/2$-pulse–wait–π-pulse–wait–$\pi/2$-pulse–readout (spin echo experiment). The reason for this is that the switching probability of the readout DC SQUID only reflects the $\hat{\sigma}_z$-component of the Bloch vector and hence $\langle\hat{\sigma}_{x,y}\rangle$ must be mapped onto $\langle\hat{\sigma}_z\rangle$. In contrast to the Ramsey sequence, the spin echo sequence cancels low-frequency phase fluctuations because of the refocusing effect of the intermediate π-pulse.

3.4.4 The Phase-cycling method

In reality, the microwave control pulses are not perfect: The tipping angle can deviate from the desired value and the frequency can be detuned from the qubit resonance frequency. This gives rise to unwanted beatings in the Ramsey and spin echo signals, which can be cured by employing different relative phases between the pulses in the sequence. This so-called phase-cycling method [45] is described in the following. First, we note that the azimuthal angle of the rotational axis in the $\hat{\sigma}_{x,y}$-plane is controlled by the relative phase of the pulses. The detuning δ causes this axis to be rotated out of the $\hat{\sigma}_{x,y}$-plane. Neglecting relaxation and dephasing, the Ramsey signal R_{ϕ_1} and the spin echo signal E_{ϕ_1,ϕ_2} can be described by a series of

rotations on the Bloch sphere,

$$E_{\phi_1,\phi_2} \equiv E_{\phi_1,\phi_2}(\delta) = \left[\tilde{R}_{\phi_1,\delta}(\Omega_{\pi/2})\tilde{R}_z(\pi\delta\tau)\tilde{R}_{\phi_2,\delta}(\Omega_\pi)\tilde{R}_z(\pi\delta\tau)\tilde{R}_{0,\delta}(\Omega_{\pi/2})\,\mathbf{x}_0\right]_z$$
$$\text{and} \tag{3.3}$$
$$R_{\phi_1} \equiv R_{\phi_1}(\delta) = \left[\tilde{R}_{\phi_1,\delta}(\Omega_{\pi/2})\tilde{R}_z(2\pi\delta\tau)\tilde{R}_{0,\delta}(\Omega_{\pi/2})\,\mathbf{x}_0\right]_z .$$

Here, $\mathbf{x}_0 = (0,0,1)$ is the Bloch vector describing the initial state of the qubit. The rotation matrices $\tilde{R}_{\phi,\delta}$ and $\tilde{R}_z$ are those defined in Eq. (3.2). They describe the Rabi dynamics and free evolution of the qubit state vector, respectively. The total free evolution time is τ for both sequences. $\Omega_{\pi/2} \equiv (\pi/2)\sqrt{1+(\delta/\nu_\mathrm{R})^2} + \alpha^\star$ and $\Omega_\pi \equiv \pi\sqrt{1+(\delta/\nu_\mathrm{R})^2} + \beta^\star$ are the angles by which the $\pi/2$- and π-pulses determined at resonance actually rotate the qubit Bloch vector in the presence of a detuning δ and arbitrary pulse length imperfections $\alpha^\star$ and $\beta^\star$. Without loss of generality, the phase of the initial $\pi/2$-pulse is chosen to be 0°, that of the final $\pi/2$-pulse ϕ_1, and that of the intermediate π-pulse ϕ_2. In our experiments, we choose the microwave power such that the corresponding Rabi frequency is $\nu_\mathrm{R} \simeq 65\,\mathrm{MHz}$. This results in a π-pulse length $t_\pi = 2t_{\pi/2} \simeq 8\,\mathrm{ns}$. A more detailed analysis of the measured Rabi oscillations shows that $\alpha^\star, \beta^\star \lesssim 5°$. For perfect pulses ($\alpha^\star = \beta^\star = 0°$) with vanishing detuning ($\delta = 0$) and zero relative pulse phase ($\phi_1 = \phi_2 = 0°$), the measured signals should be $R_0 = -1$ and $E_{0,0} = +1$ independent of τ. This means that in presence of decoherence we should directly observe the decay envelope, from which the decay time can be readily extracted. However, in practice δ, $\alpha^\star$, or $\beta^\star$ are non-zero, giving rise to time-independent (offsets) and time-dependent (oscillations) changes in the signal. In some cases this makes the proper determination of the decay times rather difficult.

By adding or subtracting traces recorded with different relative phases ϕ_1 and ϕ_2 in an appropriate way, the "ideal-pulse" signals can be restored even for imperfect pulses. In the case of the Ramsey traces, which are deliberately measured with detuning $\delta_\mathrm{R} \simeq 50\,\mathrm{MHz}$, we can still cancel offsets by considering $R_0 - R_{180}$ or $R_{90} - R_{270}$. There are two important offsets: a small one ($\lesssim 1\%$) due to pulse imperfections and the calibration offset of the switching probability. The latter is usually chosen to be about 50%. In this way, the switching probability is also close to 50%, when the qubit is in a 50/50-mixture of ground and excited state. In order to improve the signal-to-noise ratio we use all four available Ramsey traces

$$R \equiv R(\delta) \equiv R_0 - R_{180} + R_{90} - R_{270} \tag{3.4}$$

for the data analysis (cf. Fig. 4.6).

In the spin echo measurements there is no deliberate detuning ($\delta \lesssim 20\,\mathrm{MHz}$) and we are able to keep only the non-oscillating spin echo term using the eight phase combinations

$$\begin{aligned} E \equiv E(\delta) \;\equiv\; & E_{0,0} - E_{180,0} - E_{0,90} + E_{180,90} + \\ & E_{0,180} - E_{180,180} - E_{0,270} + E_{180,270}\,, \end{aligned} \tag{3.5}$$

which of course decays with some (usually exponential) envelope in the presence of decoherence. With the aid of numerical simulations we confirmed that, for the usual conditions of our spin echo experiments, these corrections are small. In fact,

they disappear in the noise floor of the switching probability in our measurements. Nevertheless, we apply the phase-cycling method to rule out even small beatings due to imperfect microwave control pulses.

3.5 Pulse generation and detection

In this section, the room-temperature components which are required for the pulsed qubit measurement setup are introduced. They comprise the generation of nanosecond microwave pulses, their combination with an adiabatic shift pulse, the generation of the bias pulse, and the amplification chain for the DC SQUID response signal.

Microwave pulse sequences such as the ones shown in Fig. 3.9, where the individual pulse lengths are of the order of a few nanoseconds, cannot be created out of the box via the pulse mode of our microwave sources. However, the envelope of these pulse sequences can easily be produced by means of a commercially available pulse generator. This envelope signal is fed into the intermediate-frequency (IF) port of a double-balanced mixer, which also has a continuous microwave signal incident at the local-oscillator (LO) port. When the IF signal is in the high-state, the diodes inside the mixer are saturated and the microwave signal at the LO-port is transmitted to the radio-frequency (RF) port. When the IF signal is in the low-state, the LO and RF ports are isolated from each other. Since this isolation is finite, two mixers are used in series to increase the on-off ratio in the produced microwave pulse sequence. The latter is then added to another rectangular pulse (adiabatic-shift pulse) using a high-bandwidth splitter. Additionally, attenuators have to be placed throughout the setup at suitable positions to avoid pulse distortions caused by reflections. The total microwave pulse sequence generating scheme is sketched in Fig. 3.12.

For the experiments discussed in chapter 5, we use an Agilent 83650B microwave source, two Agilent 81110A pulse generators, a Mini-Circuits ZFRSC42 splitter, two M/A-COM MY85C mixers, and an Agilent 11667C broadband splitter. The photographs in the top panel of Fig. 3.13 show this setup variant. For the measurements presented in chapter 4 and in Ref. [45], this simple variant is not suitable because the phase cycling method (cf. Sec. 3.4.4) requires different relative phases of the pulses within a single sequence. Hence, we replace the above microwave source by an Agilent E8267D PSG vector signal generator (VSG) and the Agilent pulse generator for the sequence envelope by a Tektronix DTG 5274 data timing generator (DTG). The VSG has a 2 GHz wideband IQ-modulator port allowing for a phase change of the continuous microwave signal within 0.5 ns. This timescale can be considered as instantaneous in our experiments. The DTG is equipped with two DTGM20 modules, providing enough channels to produce the envelope signal and the IQ-modulator control signal for our pulse sequences.

The readout pulse is generated straightforwardly with an arbitrary waveform generator. Again, suitably placed attenuators suppress pulse distortions caused by reflections. For the resistive-bias measurements (cf. Sec. 3.2.3), we use a Tektronix AWG610 with a sampling rate of 2.6 GS/s and 8 bit vertical resolution. In the capacitive-bias measurements (cf. Sec. 3.3), care has to be taken that the slopes of the integrated voltage pulse are sufficiently smooth to avoid spikes in the bias current pulse. Thus, we use an Tektronix AWG430 with a sampling rate of only 200 MS/s, but 16 bit vertical resolution.

A top view of the fridge is shown in the bottom panel of Fig. 3.13. The

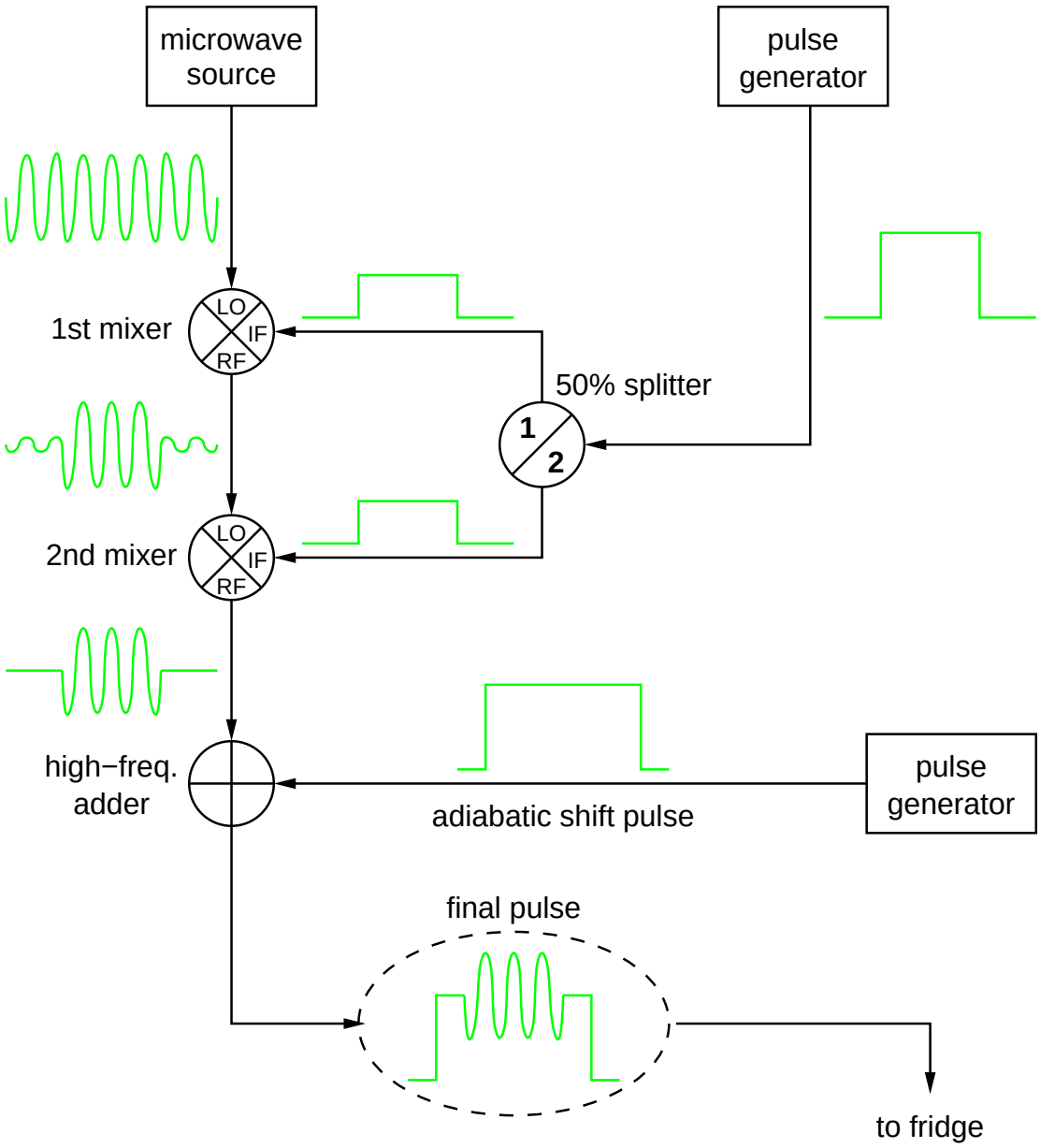

Figure 3.12: Generation scheme for microwave pulse sequences on top of an adiabatic shift pulse. In this example, the sequence consists of a single pulse. The creation of envelopes for more complicated pulse sequences can involve additional splitters, which are used as adders (cf. Fig. 3.13).

DC SQUID response signal is preamplified by means of an NF amplifier (input impedance: 1 MΩ, gain: 46 dB, frequency range: 1 kHz-100 MHz). Then, further amplification is obtained using a Stanford SR560 amplifier (filter settings: 10 kHz high-pass and 100 kHz-1 MHz low-pass, gain: 200-1000, input impedance: 100 MΩ). Finally, the signal is recorded with an AD-converter card in a computer. The effective recording rate is 2000 samples in approximately 1.5 s at a readout pulse rate of $(300\,\mu s)^{-1}$.

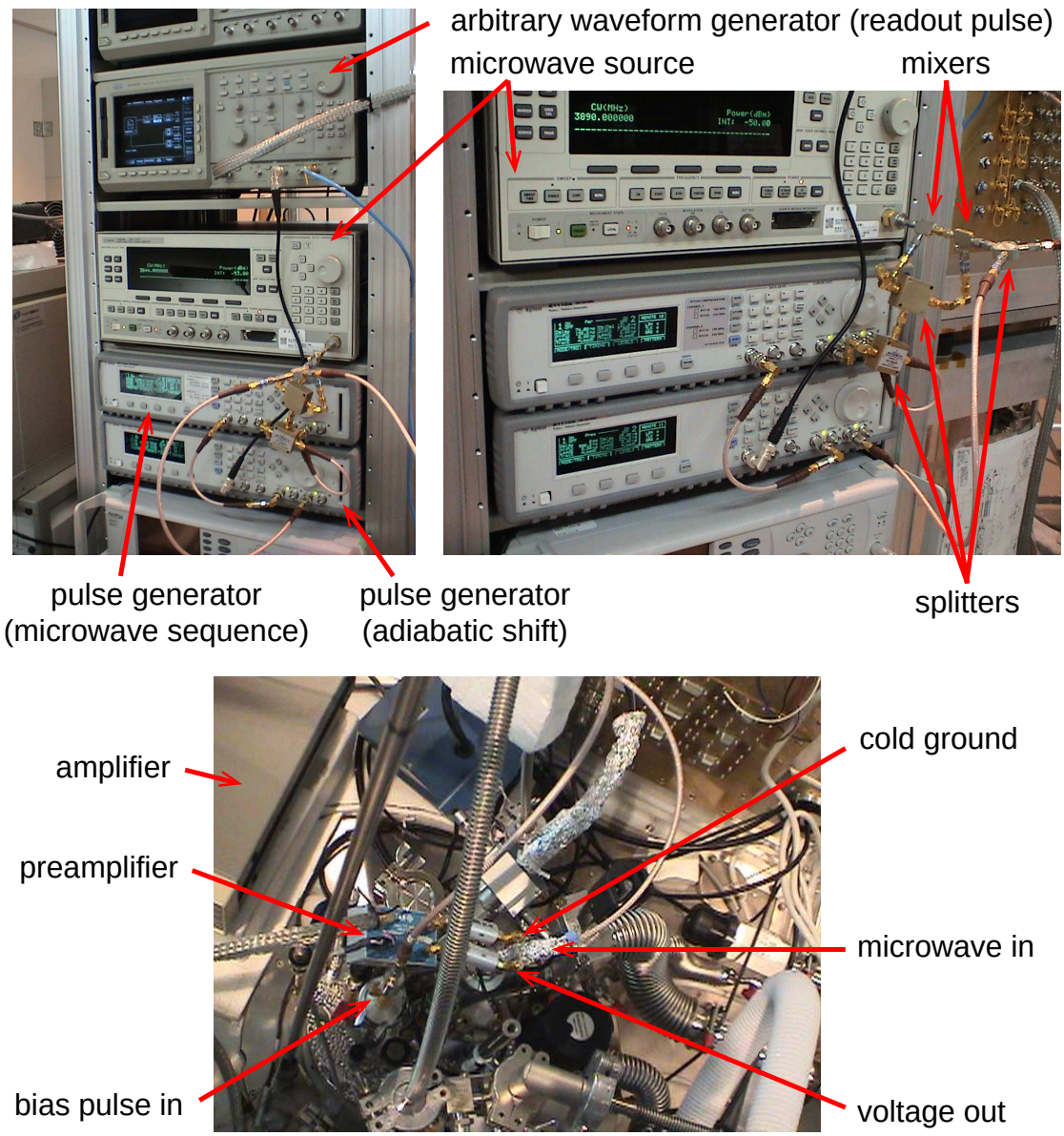

Figure 3.13: Photographs of the room temperature setup for pulse generation and detection. Top panels: Devices needed for the generation of adiabatic shift pulse, microwave pulse sequences and readout pulse. We note that splitters can also be used as adders. Bottom panel: Top of the fridge, showing the ports for the input signals and the amplification chain for the DC SQUID response signal.

Chapter 4

Decoherence of a superconducting flux qubit

The coherence time of a quantum state is one of the key figures of merit both for experiments in fundamental research and for practical quantum information devices. Regarding the latter, it determines the number of qubit operations that can be performed without errors. The presently achieved coherence times in superconducting qubits (ranging from approximately 10 ns to 5 μs) are not sufficient for the realization of more complex quantum circuits. For this reason, decoherence due to the coupling of the qubit to environmental degrees of freedom or due to noise introduced by the control and readout circuitry has been addressed in several recent experimental [23, 32, 36, 39, 44–46, 68, 136, 137] and theoretical studies [16, 22, 36, 138–140]. However, a thorough understanding of the decoherence processes and detailed knowledge of the origin of the noise sources is still missing, making the further clarification of possible sources of decoherence highly desirable. To this end, a promising path to follow is to study the dependence of the characteristic decay times (energy relaxation and dephasing, cf. Sec. 4.1) on suitable external parameters. In the particular case of a superconducting flux qubit, which constitutes the central element of this work, the most obvious choice for this parameter is the external magnetic flux threading the qubit loop [44–46]. Based on these considerations, we present in this chapter a detailed study of both energy relaxation and dephasing rates/times of a superconducting three-Josephson-junction flux qubit close to its optimal point as a function of the applied magnetic flux. In principle, the noise sources limiting the qubit coherence can be of either extrinsic or intrinsic origin. Whereas in the former case, the decoherence is induced by the control and readout circuitry of the qubit [37, 120, 121], it is caused by sources located very close to or within the qubit circuit itself in the latter scenario [39]. In order to find out whether extrinsic or intrinsic sources dominate the decoherence of our flux qubit, we change the readout configuration during our experiments in a controlled way.

For three-Josephson-junction flux qubits, several different readout methods have been proposed and successfully implemented. They range from the simple switching-DC-SQUID method [28, 85, 120, 121] to more sophisticated techniques such as the inductive readout [122–125] or the bifurcation amplifier [127–130]. The two latter have the potential to achieve quantum non-demolition measurements [131] and very large signal visibility, which are very important features for future applications. In this work, however, we have chosen the switching DC SQUID readout. The main

reason is that it is particularly suitable to study the effect of two fundamentally different electromagnetic environments on one and the same flux qubit. In this way, we avoid possible ambiguities arising from a comparison of different samples due to the spread in fabrication and/or the rich variety of different decoherence sources. As described in detail in Sec. 3.2 and Sec. 3.3, the two environments, capacitive and resistive, differ fundamentally with respect to filtering external bias noise. Consequently, they are represented by two different spectral noise densities as we discuss in Sec. 4.3. We furthermore note that the switching-DC-SQUID readout is attractive because of its simple technical implementation: for example, no sophisticated high-frequency components such as amplifiers are needed inside the cryostat.

The chapter is organized as follows. First, we give a short introduction on decoherence of superconducting qubits in Sec. 4.1. In the next sections, we present the results and analysis of the qubit measurements using the novel capacitive-bias readout. We briefly compare these results to those obtained with the traditional resistive-bias method on the same qubit. In Sec. 4.2, we study the basic properties of our superconducting flux qubit spectroscopically. In Sec. 4.3, we investigate the phase-coherent dynamics by means of energy relaxation measurements, Ramsey fringes and spin echo experiments. Comparing to resistive-bias results [45], we reserve special attention to discussing the effect of the different electromagnetic environments on the qubit coherence. From the measured flux dependence of the energy relaxation and dephasing rates, we quantify the contributions of $1/f$- and white noise to the total flux noise spectral density affecting the qubit. Next, in Sec. 4.4, we discuss the origin of non-random beatings in the Ramsey and spin echo decay traces. We show that these beatings are not caused by imperfect control pulses or undesired probe frequency detuning because in our experiments we apply the phase-cycling method described in Sec. 3.4.4. Comparison with numerical simulations strongly suggests that these beatings originate from the interaction of the flux qubit with one (or a few) point-like resonators or fluctuators. Finally, in Sec 4.5, we summarize the noise sources limiting the coherence of our qubit. The results presented in this chapter are published in Ref. [35].

4.1 Quantum coherence and decoherence

As discussed in Sec. 2.3, superconducting quantum circuits have the potential to exhibit quantum mechanically coherent behavior in a macroscopic variable although they are in fact complex solid-state systems consisting of many particles on the microscopic scale [1, 4, 5]. In order to observe and exploit quantum mechanical effects, these systems must remain coherent over the timescale of the application or experiment. In this context, the term "coherent" denotes the fact that during its time evolution the studied system does not develop an unwanted entanglement with environmental degrees of freedom such as, e.g., a thermal bath. Since it is typically impossible to access the latter experimentally, the information about the quantum state of the system will be lost, or, in other words, the system will suffer from "decoherence". As one can see from the above considerations, on the one hand it is desirable to isolate the quantum system as good as possible from its environment. On the other hand, some amount of coupling is necessary to allow for manipulations and readout of the quantum state within a reasonable time frame. It is one of the fundamental challenges in the design of quantum systems to find a good compromise

between these two opposite requirements. As of today, most solid-state quantum circuits lack sufficient coherence times rather than being decoupled too much from their environment. Superconducting systems such as the flux qubit investigated here are decoupled to some extent from the solid-state degrees of freedom due to the superconducting gap [1, 2]. Nevertheless, decoherence still represents a key issue.

Since a quantum state carries phase and amplitude information, in general, both are required to sustain their coherence simultaneously. Hence, in the most simple theoretical description, the Bloch-Redfield theory [141, 142], the decoherence of a quantum two-level system is described in terms of two characteristic rates. The first one is the longitudinal or energy relaxation rate $\Gamma_1 \equiv T_1^{-1}$ describing the transitions $|\mathrm{e}\rangle \rightarrow |\mathrm{g}\rangle$. Because this process involves the emission of a photon of energy E_{ge}, it is induced by high-frequency fluctuations. The second one, the transverse or pure dephasing rate $\Gamma_\varphi \equiv T_\varphi^{-1}$, describes the loss of phase coherence within the same qubit state. Here, the energy eigenstate remains unchanged and, consequently, this process is caused by low-frequency noise. On the Bloch sphere, the energy relaxation corresponds to reduction of the z-component r_z of the qubit state vector. Pure dephasing can be imagined in a way that the qubit state vector spreads out on a circle around the z-axis, resulting in an effective reduction of its r_x- and r_y-components. In both cases, the quantum information is lost due to the degrading of the pure state into a mixed state. It is noteworthy to mention than at low temperatures $T \ll E_{\mathrm{ge}}/k_{\mathrm{B}}$ and in the absence of a high-frequency driving the system finally relaxes to the ground state, which is a pure state again. Nevertheless, the quantum information is obviously destroyed in this case.

While Γ_1 can be measured directly, Γ_φ has to be extracted from the quantity $\Gamma_2 \equiv T_2^{-1}$, which is probed by means of the Ramsey and spin echo experiments (cf. Sec. 3.4.3). Here, T_1, T_φ, and T_2 are the characteristic time scales associated with the rates Γ_1, Γ_φ, and Γ_2, respectively. When the energy relaxation is caused by regular[1] high-frequency noise [36, 143], the total rates of the Ramsey ($\Gamma_{2\mathrm{R}}$) and spin echo ($\Gamma_{2\mathrm{E}}$) decay are given by

$$T_{2\mathrm{R}}^{-1} \equiv \Gamma_{2\mathrm{R}} = \frac{\Gamma_1}{2} + \Gamma_{\varphi\mathrm{R}} \quad \text{and} \quad T_{2\mathrm{E}}^{-1} \equiv \Gamma_{2\mathrm{E}} = \frac{\Gamma_1}{2} + \Gamma_{\varphi\mathrm{E}}\,, \tag{4.1}$$

where $\Gamma_{\varphi\mathrm{R}}$ and $\Gamma_{\varphi\mathrm{E}}$ are the corresponding pure dephasing rates. The factor $1/2$ is due to the fact that Γ_1 is defined from an energy decay, whereas Γ_2 and Γ_φ are defined from an amplitude decay. It is notable that the Bloch-Redfield formalism is suitable for white noise and for high-frequency noise, but not for $1/f$-noise. The latter requires a non-trivial modification of $\Gamma_{\varphi\mathrm{R}}$ and $\Gamma_{\varphi\mathrm{E}}$, which is explained in detail when discussing the time-domain data in Sec. 4.3.

4.2 Spectroscopy results

In this section, we present the experimental results of pulsed qubit microwave spectroscopy recorded with the integrated-pulse method. We first confirm that the considerations made in Sec. 3.3 regarding the feasibility of the capacitive-bias-detection scheme are valid for our three-junction flux qubit. To this end, we verify that the voltage response signals of the DC SQUID, which are due to a switching or a non-switching event, can be clearly distinguished from each other. Inspecting Fig. 4.1,

[1] The term "regular" denotes the fact that the correlation function of the noise is a delta function.

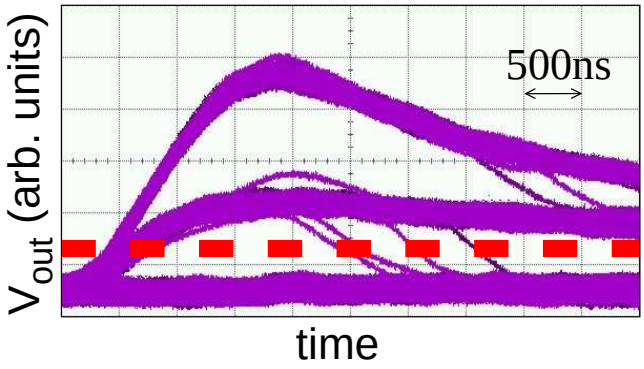

Figure 4.1: Oscilloscope image of the readout DC SQUID signal (solid violet lines) plotted versus time for the integrated-pulse readout. The switching rate is approximately 50%. The broken red line marks the detection threshold used to discriminate between zero-voltage (no switching) and finite-voltage (switching) events. We note that no retrapping (return to the zero-voltage state) occurs before the end of the 1.5 µs hold pulse. The existence of two finite-voltage branches is due to a resonance in the current-voltage characteristic of the DC SQUID. The intermediate branch corresponds to the resonance step and the uppermost branch to the true superconducting gap.

we find that this so-called switching discrimination is unambiguous provided that the length of the hold section of the bias pulse is at least 1.5 µs. Additionally, we find that we do not detect any spurious switching events on the oscilloscope when the readout pulse does not contain the switching segment. This confirms that the detection of the qubit state occurs only during the short switching pulse.

After this initial calibration we perform pulsed qubit microwave spectroscopy. In the inset of Fig. 4.2, two typical spectroscopy traces for $\nu_{\mathrm{ge}} \simeq 17\,\mathrm{GHz}$ measured with the capacitive and resistive-bias method are displayed. When qubit splitting and driving frequency ν are on resonance, a peak appears in the switching probability. For the C-bias readout, the qubit visibility, i.e., two times the height of the spectroscopy peak, is enhanced as compared to the R-bias scheme. We find this increased visibility consistently in all spectroscopy and Rabi oscillation data, which has been recorded over a wide range of frequencies (data not shown). More quantitatively, the qubit visibility is 20-25% for the resistive-bias method and 28-36% for the capacitive-bias scheme. The qubit level splitting E_{ge} as a function of the flux bias is plotted in the main body of Fig. 4.2. Each data point corresponds to the center frequency of the observed resonance peak. In addition to the one-photon resonance, we obtain peaks which correspond to the multi-photon excitations $E_{\mathrm{ge}}/h = n\nu$ for $n = 2, 3, 4$. We measure a tunnel coupling $\Delta/h = 4.22 \pm 0.01\,\mathrm{GHz}$ at the degeneracy point. Utilizing this result, we fit the flux dependence of the resonance signal expected for a two-level system to the data. We include the one-, two-, three-, and four-photon resonance peaks into this fit and find a maximum circulating current $I_{\mathrm{p}} = 360 \pm 1\,\mathrm{nA}$. In order to estimate α, we exploit the fact that the two DC SQUID junctions have the same layout as the two larger qubit junctions. In this way, we can estimate I_{c} from the measured normal resistance $R_{\mathrm{n}} = 258\,\Omega$ and gap voltage $2V_{\mathrm{g}} = 390 \pm 45\,\mu\mathrm{V}$ of the DC SQUID. Using the Ambegaokar-Baratoff relation $2I_{\mathrm{c}}R_{\mathrm{n}} = \pi V_{\mathrm{g}}/2$ of Eq. (2.6), we obtain $2I_{\mathrm{c}} = 1202 \pm 138\,\mathrm{nA}$ and, as a

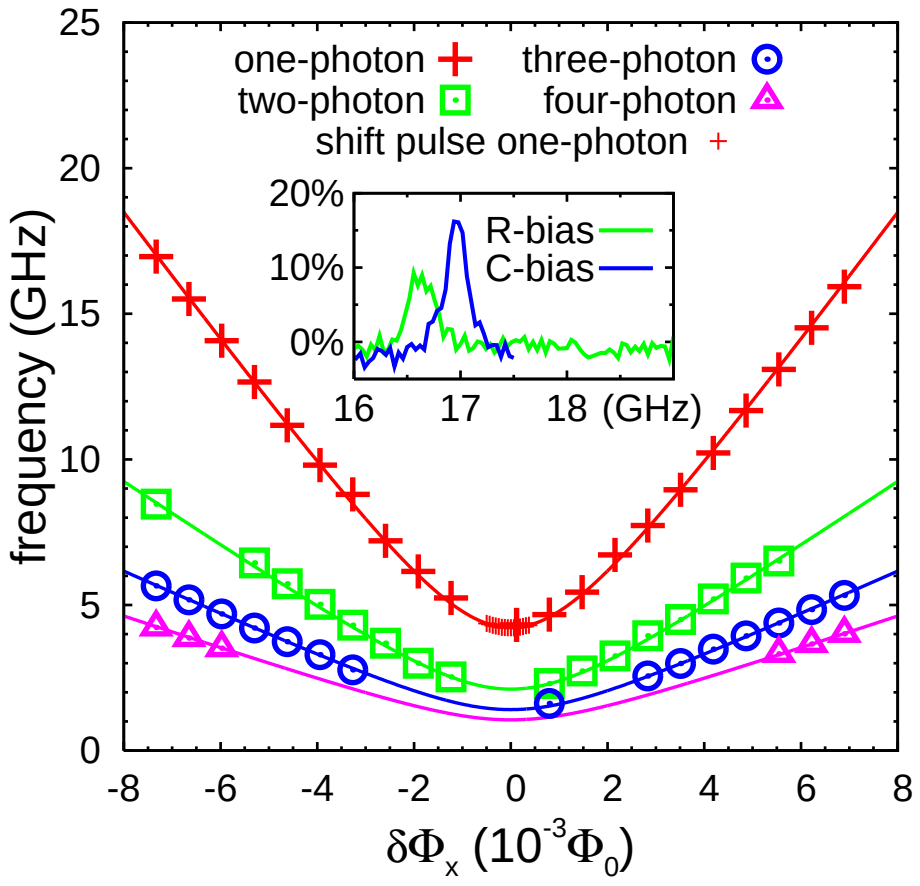

Figure 4.2: Qubit resonance frequency (various symbols) obtained from capacitive-bias spectroscopy at $T \simeq 50\,\mathrm{mK}$ plotted versus the flux bias. Multi-photon resonances are observed up to the four-photon process. The solid lines are two-level system fits to the measured data. In contrast to the large symbols, the small red plus signs denote data recorded with the adiabatic shift-pulse method explained in Sec. 3.2.4. Inset: Spectroscopy traces (switching probability versus excitation frequency ν) for a qubit transition frequency $\nu_{\mathrm{ge}} \simeq 17\,\mathrm{GHz}$. The blue and the green curve are recorded with the capacitive and the resistive-bias readout, respectively.

consequence [27],

$$\alpha = \frac{1}{2\sqrt{1-(I_\mathrm{p}/I_\mathrm{c})^2}} = 0.62 \pm 0.04\,. \tag{4.2}$$

This value is consistent with the result $\alpha_{\mathrm{res}} \simeq 0.63$ obtained with the resistive-bias method and deviates only slightly from the design value $\alpha_{\mathrm{design}} = 0.7$. Knowing α, we can calculate the Josephson coupling energy $E_\mathrm{J}/h = 299 \pm 34\,\mathrm{GHz}$. Here, the error is dominated by the uncertainty of the gap voltage due to significant fluctuations of the quasiparticle branch of the current-voltage characteristic of the DC SQUID detector. From previous measurements of junctions fabricated with the same process [81], the charging energy is estimated to be $E_\mathrm{c}/h \simeq 6.4 \pm 1.6\,\mathrm{GHz}$. Hence, we obtain the ratio $E_\mathrm{J}/E_\mathrm{c} = 47 \pm 13$.

4.3 Coherence properties of the flux qubit

In this section, we present and evaluate the time domain measurement results of our flux qubit using the capacitive-bias method. We conduct energy relaxation, Rabi, Ramsey, and spin echo experiments using the pulse sequences described in Sec. 3.4.3 and Fig. 3.9. We focus on the flux bias region around the optimal point, $\delta\Phi_\mathrm{x} = \pm 6 \times 10^{-4}\Phi_0$, corresponding to $E_\mathrm{ge}/h \simeq 4\,\mathrm{GHz}$, and on the readout point, $\delta\Phi_\mathrm{x} = -6.007 \times 10^{-3}\Phi_0$, corresponding to $E_\mathrm{ge}/h = 14.125\,\mathrm{GHz}$. These experimental decay times are summarized in Fig. 4.3. In the discussion, we first analyze in detail the results obtained with the capacitive-bias readout and then briefly compare them to those achieved with the conventional resistive-bias method on the same qubit.

4.3.1 Energy relaxation

According to Bloch-Redfield theory [141, 142], which is applicable if the noise is short correlated and weak, the energy relaxation rate of a flux qubit is [36]

$$\Gamma_1 \equiv T_1^{-1} = \pi\, S_\omega^{\Gamma_1}(\omega_\mathrm{ge}) = \pi \left(D \frac{\partial \boldsymbol{\omega}}{\partial \Phi_\mathrm{x}} \right)_\perp^2 S_\Phi^{\Gamma_1}(\omega_\mathrm{ge}) = \frac{\pi}{\hbar} \left(\frac{\partial \epsilon(\Phi_\mathrm{x})}{\partial \Phi_\mathrm{x}} \sin\theta \right)^2 S_\Phi^{\Gamma_1}(\omega_\mathrm{ge})\,. \tag{4.3}$$

Here, $S_\omega^{\Gamma_1}(\omega_\mathrm{ge}) = \frac{1}{2}\left[\widetilde{S}_\omega^{\Gamma_1}(-\omega_\mathrm{ge}) + \widetilde{S}_\omega^{\Gamma_1}(\omega_\mathrm{ge})\right]$ is the symmetrized spectral density of the noise at the qubit transition frequency. The appearance of the flux-dependent factor $\sin^2\theta \equiv (\Delta/E_\mathrm{ge})^2 = \Delta^2/\left[\Delta^2 + \epsilon(\Phi_\mathrm{x})^2\right]$ can be understood intuitively because the Bloch-Redfield theory is based on a golden-rule argument: T_1 is related to level transitions of the qubit and $\langle \mathrm{e}|\hat{\sigma}_z|\mathrm{g}\rangle = \langle \mathrm{g}|\hat{\sigma}_z|\mathrm{e}\rangle = \sin\theta$ is the transition matrix element due to the interaction between qubit and noise. Also, the importance of the spectral density at the transition frequency is evident because only at this frequency state transitions can be induced. In order to calculate $S_\omega^{\Gamma_1}(\omega_\mathrm{ge})$ from the flux noise spectral density $S_\Phi^{\Gamma_1}(\omega_\mathrm{ge})$, the latter has to be multiplied by the square of the flux-to-frequency transfer function $C_\perp = \left[D(\partial\boldsymbol{\omega}/\partial\Phi_\mathrm{x})\right]_\perp = \left[\hbar^{-1}\partial\epsilon(\Phi_\mathrm{x})/\partial\Phi_\mathrm{x}\right]\sin\theta = (2I_\mathrm{p}/\hbar)\sin\theta$ because the relaxation rate is determined only by the transverse fluctuations. Close to the degeneracy point, we have $\sin\theta \simeq 1$ and the relaxation rate is expected to show a very weak dependence on $\delta\Phi_\mathrm{x}$. Looking at the experimental data of Fig. 4.3, we note that although there is some structure in the flux dependence of T_1, the relaxation times clearly exhibit a good agreement with the simple Bloch-Redfield model near the degeneracy point. From a numerical fit we derive the flux noise spectral density $S_\Phi^{\Gamma_1}(\omega_\mathrm{ge} \approx \Delta/\hbar) = \left[(1.4 \pm 0.1) \times 10^{-10}\Phi_0\right]^2\ \mathrm{Hz}^{-1}$.

From Eq. (4.3) we can also estimate the relaxation rate, which would be expected if the impedance $Z(\omega)$ of the DC SQUID bias circuitry was the dominating source of energy relaxation. In order to do so, we have to use the voltage noise spectral density $S_V^{\Gamma_1}(\omega_\mathrm{ge})$ associated with the real part of the impedance, $\Re\{Z(\omega_\mathrm{ge})\}$. According to the fluctuation-dissipation theorem, we obtain $S_V^{\Gamma_1}(\omega_\mathrm{ge}) = 2\hbar\omega_\mathrm{ge}\Re\{Z(\omega_\mathrm{ge})\}/2\pi$ for $k_\mathrm{B}T \ll \hbar\omega_\mathrm{ge}$. The latter condition is well satisfied for our experimental situation. Then, the flux noise spectral density in the qubit loop due to $S_V^{\Gamma_1}(\omega_\mathrm{ge})$ is given by $S_\Phi^{\Gamma_1}(\omega_\mathrm{ge}) = M_\mathrm{SQ,q}^2 K^2 S_V^{\Gamma_1}(\omega_\mathrm{ge})$. Here, K^2 is the factor transforming $S_V^{\Gamma_1}(\omega_\mathrm{ge})$ into a current noise spectral density $S_I^{\Gamma_1}(\omega_\mathrm{ge})$ of the current circulating in the readout DC SQUID. The resulting $S_\Phi^{\Gamma_1}(\omega_\mathrm{ge})$ for the qubit is simply obtained by multiplying $S_I^{\Gamma_1}(\omega_\mathrm{ge})$ by the quantity $M_\mathrm{SQ,q}^2$, which is the square of the mutual inductance

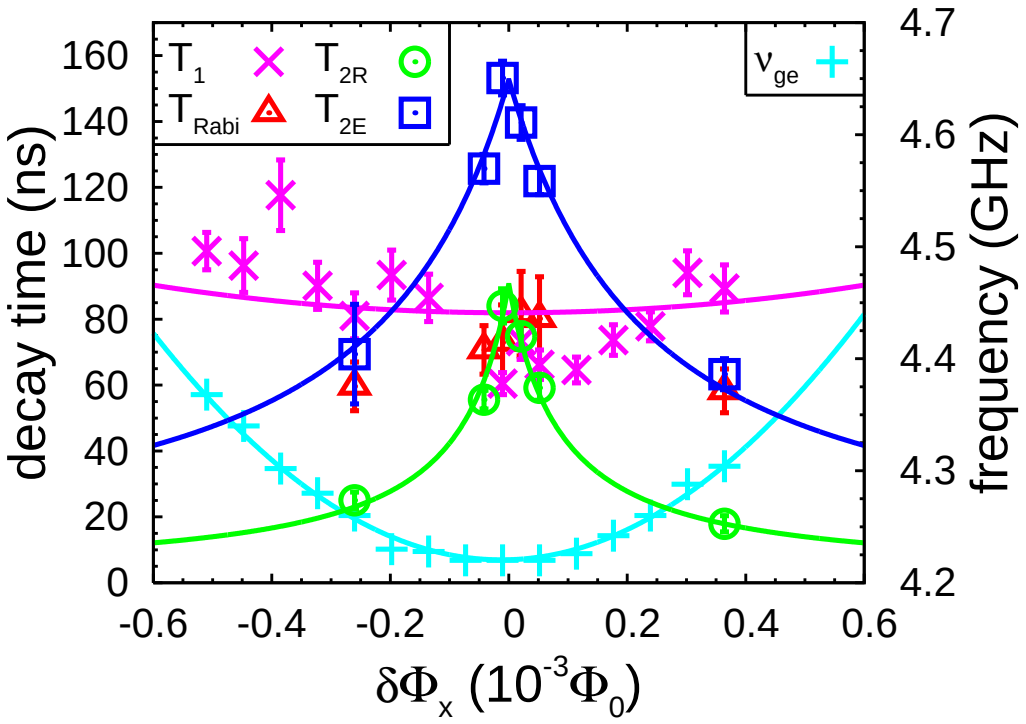

Figure 4.3: Characteristic decay times of the qubit (left scale) plotted versus the flux bias in the vicinity of the qubit degeneracy point. The data is obtained from time domain measurements with the capacitive-bias method. The magenta crosses represent the energy relaxation time T_1, the red open triangles the Rabi decay time T_{Rabi}, the green open circles the Ramsey decay time $T_{2\mathrm{R}}$, and the dark blue open squares the spin echo decay time $T_{2\mathrm{E}}$. Also shown are the results of low-power spectroscopy (right scale): the light blue plus signs represent the positions of the resonance peaks. The solid lines are fits to the data as discussed in the main text. In addition to the data shown in this plot, the results at the qubit readout point ($\delta\Phi_{\mathrm{x}} = 6.007 \times 10^{-3}\Phi_0$, $\nu_{\mathrm{ge}} = E_{\mathrm{ge}}/h = 14.125\,\mathrm{GHz}$) are used for the fits.

between the readout DC SQUID and the qubit. Hence, we obtain

$$\Gamma_{1,Z(\omega_{\mathrm{ge}})} \equiv T^{-1}_{1,Z(\omega_{\mathrm{ge}})} = \frac{\pi}{\hbar}\left[\frac{\partial\epsilon(\Phi_{\mathrm{x}})}{\partial\Phi_{\mathrm{x}}}\sin\theta\right]^2 M^2_{\mathrm{SQ,q}} K^2 \frac{2\hbar\omega_{\mathrm{ge}}\Re\{Z(\omega_{\mathrm{ge}})\}}{2\pi}\,, \tag{4.4}$$

where [120, 121]

$$K^2 = \frac{1}{2}\left[\frac{\pi I_{\mathrm{SQ}}\tan(\pi f_{\mathrm{SQ}})}{\omega_{\mathrm{ge}}\Phi_0}\right]^2 . \tag{4.5}$$

Here, $f_{\mathrm{SQ}} \equiv \Phi_{\mathrm{x}}^{\mathrm{SQ}}/\Phi_0 = 0.97 \times 1.5$ is the magnetic frustration of the DC SQUID due to the flux threading its loop. I_{SQ} is the transport current through the DC SQUID. For the bias circuit configurations displayed in Fig. 4.4, we first calculate the real part of the impedance, $\Re\{Z(\omega)\}$, which is shown in Fig. 4.5. Using Eq. (4.4) and Eq. (4.5), we can then estimate the lower limit for the relaxation time caused by the readout circuit. In this case, we can approximate I_{SQ} with the DC SQUID switching current $I_{\mathrm{sw}} \simeq 120\,\mathrm{nA}$, obtaining $T_{1,Z(\omega_{\mathrm{ge}}=\Delta/\hbar)} \gtrsim 2\,\mu\mathrm{s}$ at the optimal point. This estimate is already much larger than the actually measured decay time $T_1 = 82\,\mathrm{ns}$. Furthermore, since in our T_1 measurement protocol the bias current is non-zero only at the readout time (cf. Fig. 3.9), the readout process itself can only contribute to

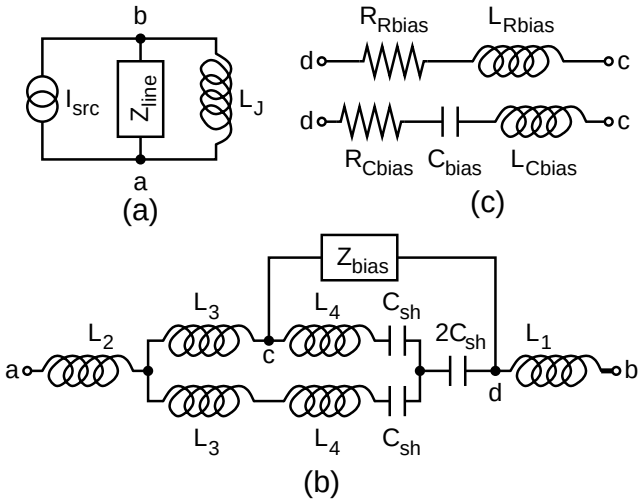

Figure 4.4: Equivalent circuit of the DC SQUID bias line. The cables connecting the bias resistor to the voltage source are not considered here because the corresponding modes are strongly damped. (a) Applying Norton's theorem, the voltage-driven circuits displayed in Fig. 3.8 and Fig. 3.10 are transformed into equivalent current-driven circuits. I_{src} is the effective source current. The DC SQUID is modeled by its Josephson inductance [120, 121] $L_{\mathsf{J}} = 2.6\,\mathrm{nH}$. Z_{line} is calculated using Kirchhoff's laws. (b) Details of the bias line impedance Z_{line}. The inductances $L_1 = 100\,\mathrm{pH}$, $L_2 = 10\,\mathrm{pH}$, $L_3 = 60\,\mathrm{pH}$, and $L_4 = 45\,\mathrm{pH}$ are determined from FastHenry [115] simulations. (c) Details of the bias line impedance Z_{bias} for resistive- (top) and capacitive-bias configuration (bottom). $L_{\mathsf{Rbias}} = 2.7\,\mathrm{nH}$ and $L_{\mathsf{Cbias}} = 1.5\,\mathrm{nH}$ are the self-inductances of the on-chip resistor and of the bonding wire used to short the on-chip resistor, respectively.

the limited qubit visibility. The actual DC SQUID transport current during the T_1 measurement sequence is given by asymmetry currents or other noise currents. This means that our experimental situation is characterized by the condition $I_{\mathrm{SQ}} \ll I_{\mathrm{sw}}$, which implies an even higher expected T_1-time. Thus, we conclude that the noise generated by the bias circuitry is not the dominating high-frequency noise source in our experiments. We find a similar result [45] for the resistive-bias configuration, where the measured relaxation time $T_1 = 140\,\mathrm{ns}$ is also small compared to the calculated lower bound $T_{1,Z(\omega_{\mathrm{ge}}=\Delta/\hbar)} \gtrsim 5\,\mu\mathrm{s}$. The slight differences in the T_1 values measured with the capacitive- and the resistive-bias readout are mainly due to changes in the microwave setup, which occur during the switching between the different experimental configurations. This process involves the warm-up of the cryostat, sample remounting and rebonding, opening and closing of microwave connectors, and a new cool-down of the refrigerator.

In conclusion, we find that the current noise from the bias circuitry is not the dominating relaxation source, neither for the resistive- nor for the capacitive-bias detection scheme. Even changes in the high-frequency setup, which are due to the switching between the two methods, affect the T_1 times by less than a factor of two. However, in the capacitive setup the measured relaxation rates are more than 25 times larger than expected from Eq. (4.4). The actually dominating noise sources for our qubit are discussed in detail in Sec. 4.5. In future works, if these presently dominating noise sources can be reduced to an extent that the bias current noise becomes relevant, the capacitive-bias scheme allows to engineer the circuit impedance and the

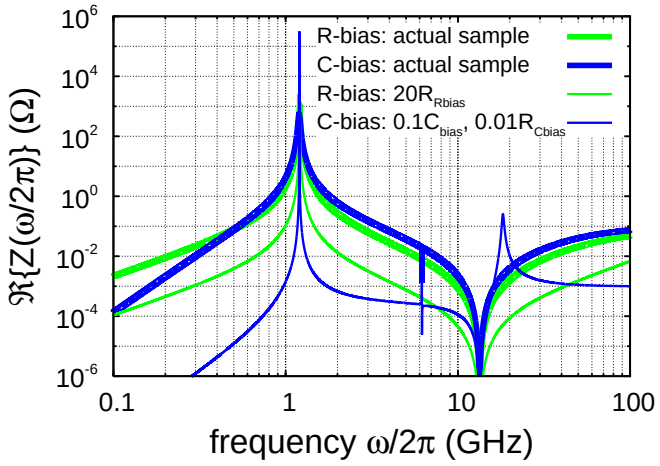

Figure 4.5: Real part of the impedance $\Re\{Z(\omega/2\pi)\}$ of the DC SQUID bias line plotted versus frequency for various configurations. The blue and the green lines show the results for C-bias and R-bias configurations, respectively. The actual configurations used in the experiments ("actual sample", thick lines) are shown in Fig. 4.4. The thin lines show suggestions for improved configurations with a reduced $\Re\{Z(\omega/2\pi)\}$ in the relevant frequency range form 2 GHz to 10 GHz.

resulting spectral noise density in an advantageous way. As shown in Fig. 4.5, in the relevant frequency band from 2 GHz to 10 GHz an impedance, which is almost flat and approximately two to three orders of magnitude smaller than that of the present measurement setup, can be realized by a tenfold reduction of the bias capacitance. In contrast to that, for the resistive-bias readout in the same frequency band such a reduction cannot even be achieved by a twentyfold increase of R_{Rbias}. In other words, the bias line noise can be reduced significantly by applying the bias current via a capacitor instead of a resistor. It is important to note that there are no major technical problems hindering a tenfold reduction of the bias capacitor, whereas a 20-fold increase of R_{Rbias} generates significant problems due to heating effects in the bias circuit.

4.3.2 Dephasing

In order to determine the pure dephasing rate $\Gamma_\varphi(\Phi_\mathrm{x}) \equiv T_\varphi^{-1}$, we study the decay of the $\hat{\sigma}_{x,y}$-evolution of the qubit state vector on the Bloch sphere. To this end, we perform Ramsey and spin echo experiments, which are described in Sec. 3.4.3 and Fig. 3.9). The length of the $\pi/2$- and π-pulses is determined experimentally from driven Rabi oscillations (data not shown). Despite applying the phase-cycling method introduced in Sec. 3.4.4, the corrected Ramsey and spin echo traces very close to the degeneracy point (cf. Fig. 4.6 and Fig. 4.7) still exhibit pronounced beatings. These beatings cannot be caused by pulse imperfections and are discussed in detail in Sec 4.4.

We now turn to the analysis of the Ramsey and spin echo data corrected with the phase-cycling method introduced in Sec. 3.4.4. As described in Sec. 4.1, the traces shown in Fig. 4.6 and Fig. 4.7 contain information on the $\hat{\sigma}_{x,y}$- or transverse dynamics of the qubit and, as a consequence, on the spectral density of the phase noise affecting the qubit. Assuming regular ("white") noise spectral density $S_\omega(\omega)$ at low frequencies $\omega \to 0$, we can apply Bloch-Redfield theory again[141, 142]. In

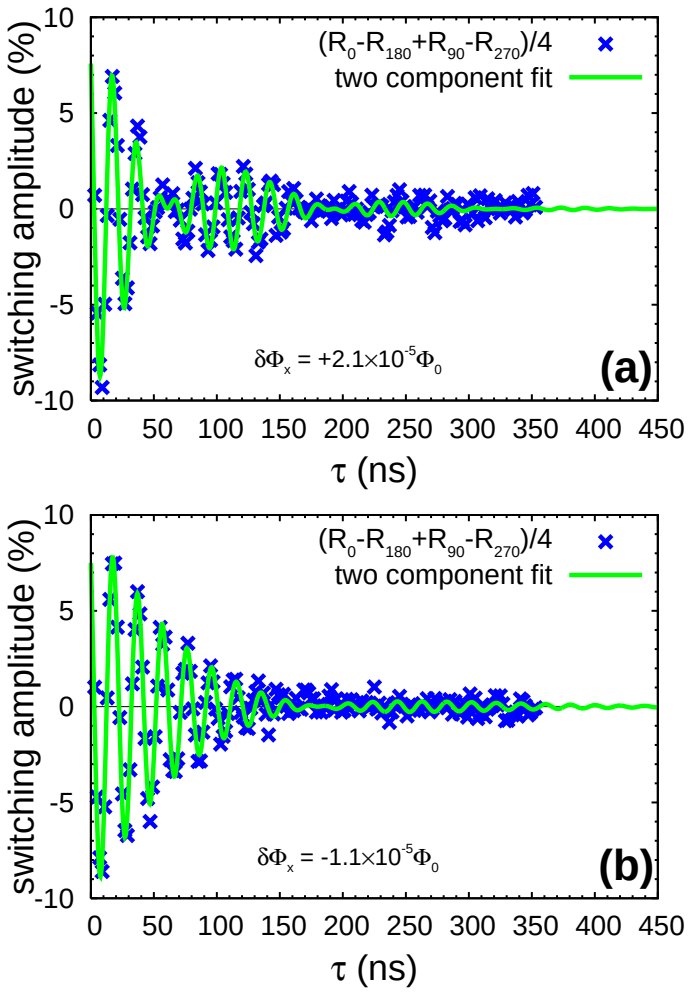

Figure 4.6: Ramsey decay traces measured at two different flux values very close to the degeneracy point using the phase-cycling method. τ is the free evolution time. The labeling of the data (blue crosses) is the same as in Eq. (3.3) and Eq. (3.4). The solid green lines are fits to the data using a split-peak model in combination with an exponentially decaying envelope. **(a)** Decay time $T_{2\mathrm{R}} = 75 \pm 4\,\mathrm{ns}$. **(b)** Decay time $T_{2\mathrm{R}} = 84 \pm 5\,\mathrm{ns}$.

this way, we obtain a simple exponential decay envelope for the pure dephasing and the decay rate is

$$\begin{aligned}\Gamma_{\varphi}^{\mathrm{BR}}(\Phi_{\mathrm{x}}) &= \pi\, S_{\omega}^{\mathrm{BR}}(\omega = 0) = \pi \left(D \frac{\partial \boldsymbol{\omega}}{\partial \Phi_{\mathrm{x}}} \right)_{\parallel}^{2} S_{\Phi}^{\mathrm{BR}}(\omega \to 0) \\ &= \frac{\pi}{\hbar} \left[\frac{\partial \epsilon(\Phi_{\mathrm{x}})}{\partial \Phi_{\mathrm{x}}} \cos\theta \right]^{2} S_{\Phi}^{\mathrm{BR}}(\omega \to 0)\,. \end{aligned} \tag{4.6}$$

Here, in contrast to Eq. (4.3), the flux-to-frequency transfer function $C_{\parallel} = \left[D(\partial \boldsymbol{\omega}/\partial \Phi_{\mathrm{x}}) \right]_{\parallel} = \left[\hbar^{-1} \partial \epsilon(\Phi_{\mathrm{x}})/\partial \Phi_{\mathrm{x}} \right] \cos\theta = (2 I_{\mathrm{p}}/\hbar) \cos\theta$ has to be used because the dephasing rate is determined by the longitudinal fluctuations. The factor $\cos\theta = -\langle \mathrm{g}|\hat{\sigma}_z|\mathrm{g}\rangle = \langle \mathrm{e}|\hat{\sigma}_z|\mathrm{e}\rangle$ can be understood intuitively because low-frequency phase noise does not induce level transitions. Furthermore, we notice that $\Gamma_{\varphi}^{\mathrm{BR}}(\Phi_{\mathrm{x}})$ is dominated by the factor $\cos^2\theta = \epsilon(\Phi_{\mathrm{x}})^2 / \left[\Delta^2 + \epsilon(\Phi_{\mathrm{x}})^2 \right]$, which is proportional to $(\delta \Phi_{\mathrm{x}})^2$ close to the degeneracy point and approaches unity far away from it.

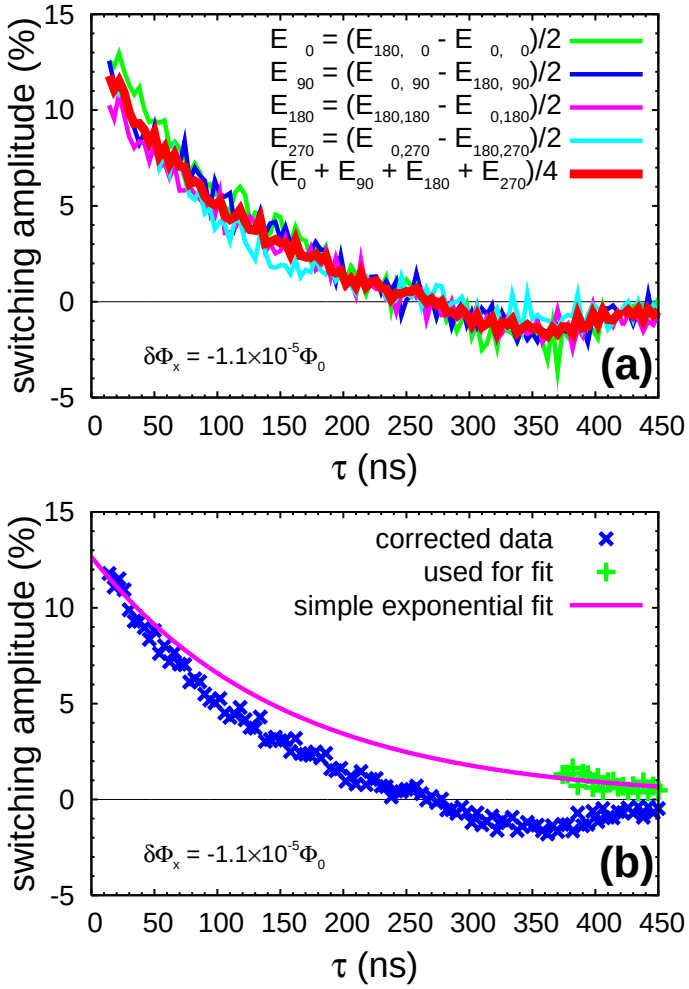

Figure 4.7: Spin echo decay traces measured very close to the degeneracy point using the phase-cycling method. The labeling of the data is the same as in Eq. (3.3) and Eq. (3.5). **(a)** The aperiodic low-frequency beatings ($\lesssim 2\,\mathrm{MHz}$) are independent of the relative phase of the π-pulse and do not cancel in the corrected trace (thick red line). Similar to the Ramsey trace R, the spin echo difference traces $E_{\phi_2} \equiv {}^{+}_{(-)}(E_{180,\phi_2} - E_{0,\phi_2})$ (thin lines) have a built-in offset correction. **(b)** Corrected spin echo decay obtained from (a). The solid magenta line is a numerical fit using a simple exponential envelope function. From all data points (blue crosses), only those with absolute values close to the envelope (green plus signs) are used for the fit. The amplitude is treated as a fixed parameter which is evaluated from the Ramsey amplitude and the Rabi decay time (Rabi data not shown).

We notice that the Bloch-Redfield dephasing rate is determined by $S_\Phi^{\mathrm{BR}}(\omega \to 0)$. Hence, $1/f$-noise is of particular importance for the phase coherence of the qubit. However, $1/f$-noise obviously violates the assumption of regularity and the decay envelopes of the $\langle\hat{\sigma}_{x,y}\rangle$-signal have to be calculated from the total accumulated phase [36]. Depending on the applied control sequence (Ramsey or spin echo), the order of the coupling (linear or quadratic), and the choice of the frequency cutoff (sharp or crossover to $1/f^2$), this envelope can decay with $\exp(-t^\alpha)$, where $\alpha = 2, 3, 4$, or even with an algebraic function of t. Since the limited overall quality of the experimental data shown in Fig. 4.7 (short coherence times, switching probability

fluctuations, and beatings) does not allow a detailed trace-by-trace analysis, we follow a different strategy. We determine the decay rate Γ_2 from a simple exponential fit of the trace envelope. Because of the aperiodic low-frequency beatings we fit the spin echo traces taking the amplitude as a fixed parameter, which is determined from the Ramsey amplitude and the Rabi decay time. Then, we fit the flux dependence of Γ_2 with the expression

$$\Gamma_2(\Phi_\mathrm{x}) = \frac{\Gamma_1(\Phi_\mathrm{x})}{2} + \Gamma_\varphi^\mathrm{BR}(\Phi_\mathrm{x}) + \Gamma_\varphi^{1/f}(\Phi_\mathrm{x}) + \Gamma_\varphi^0 \,. \tag{4.7}$$

Here, the pure dephasing rate has a Bloch-Redfield (white flux noise) contribution $\Gamma_\varphi^\mathrm{BR}$, a Gaussian ($1/f$ flux noise) contribution $\Gamma_\varphi^{1/f}$, and a constant (quadratic coupling, flux-independent sources) contribution Γ_φ^0. For a $1/f$-noise spectral density

$$S_\Phi^{1/f}(\omega) = \mathcal{A}/|\omega| \tag{4.8}$$

one obtains [36]

$$\Gamma_\varphi^{1/f}(\Phi_\mathrm{x}) = \frac{1}{\hbar}\left|\frac{\partial\epsilon(\Phi_\mathrm{x})}{\partial\Phi_\mathrm{x}}\cos\theta\right| \sqrt{\mathcal{A}\ln 2}\,. \tag{4.9}$$

Strictly speaking, Eq. (4.9) is only true for the spin echo decay. However, the correction necessary for the Ramsey decay rate is only of logarithmic order. Its effect is to increase the impact of the noise by a logarithmic factor, which can be regarded as a constant in our considerations. This means that the $T_{2\mathrm{R}}$-fit produces a Ramsey $1/f$-noise magnitude $\mathcal{A}_\mathrm{R}$ (instead of $\mathcal{A}$) which is by itself unphysical. Nevertheless, $\mathcal{A}_\mathrm{R}$ is useful to understand the filtering effects of the spin echo sequence and estimate the infrared cutoff frequency ω_IR of the $1/f$-noise spectrum.

In our experiments, the Ramsey and spin echo data is taken in the vicinity of the degeneracy point ($\delta\Phi_\mathrm{x} = \pm 4\times10^{-4}\Phi_0$, $\nu_\mathrm{ge} = 4.22 - 4.30\,\mathrm{GHz}$) and at the qubit readout point ($\delta\Phi_\mathrm{x} = -6.007\times10^{-3}\Phi_0$, $\nu_\mathrm{ge} = 14.125\,\mathrm{GHz}$). The details of the fitting procedure are different for Ramsey and spin echo data. The Ramsey traces can be fitted properly assuming a simple model in which the main qubit resonance is split into two peaks. Both peaks have equal amplitudes and are detuned by the quantities δ_1 and δ_2 from the main resonance. Using $R(\delta)$ of Eq. (3.4), the total decay function consists of beating oscillations $R_\mathrm{fit} \equiv \big[R(\delta_1) + R(\delta_2)\big]/2$ multiplied by a simple exponential decay envelope. Fitting parameters are the amplitude, the detunings δ_1 and δ_2, and the decay rate $\Gamma_{2\mathrm{E}}$. The observed peak splittings $|\delta_1 - \delta_2|$ vary between 3 and 15 MHz around the degeneracy point. At the readout point no splitting is observed. In contrast to the Ramsey beatings, the spin echo beating cannot be fitted using a phenomenological model. From Fig. 4.7(a) one can see that only the smaller wiggles are canceled by the phase-cycling method. The long-time-scale beatings coincide for all pulse sequences regardless of the relative phase shifts. For this reason these beatings are not considered as an artifact due to imperfect pulses. Consequently, we fit a simple exponential decay to the envelope of the long-time tail of the total spin echo trace as shown in Fig. 4.7(b). Fitting parameter is the decay rate $\Gamma_{2\mathrm{E}}$. A substantial part of the error bars of $T_{2\mathrm{E}}$ in Fig. 4.3 is due to the fact that it is not always easy to define this tail with high accuracy.

The flux dependence of the decay times $T_{2\mathrm{E}} = \Gamma_{2\mathrm{E}}^{-1}$ and $T_{2\mathrm{R}} = \Gamma_{2\mathrm{R}}^{-1}$ are displayed in Fig. 4.3. We first notice that we find $T_{2\mathrm{E}} \simeq 2T_1$ and $T_{\varphi\mathrm{E}}^0 \equiv \left(\Gamma_{\varphi\mathrm{E}}^0\right)^{-1} \simeq 2\,\mu\mathrm{s}$ right at the degeneracy point. In other words, the total qubit coherence is limited by

energy relaxation[2]. Furthermore, the spin echo decay time is considerably longer than the Ramsey decay time. This indicates the presence of low-frequency noise in the system, which is partially canceled by the echo sequence. When fitting the $T_{2\mathrm{E}}$ data with Eq. (4.7), we obtain a $1/f$-flux noise magnitude

$$\mathcal{A} = \left[(4.3 \pm 0.7) \times 10^{-6}\Phi_0\right]^2. \tag{4.10}$$

This value can now be compared to other low-frequency noise measurements on Josephson tunnel junctions. For a wide variety of different fabrication conditions, critical currents I_c, and junction areas A one finds a current noise spectral density $S_I(1\,\mathrm{Hz}) \approx 144\,(I_\mathrm{c}/\mu\mathrm{A})(A/\mu\mathrm{m}^2)\,(\mathrm{pA}^2/\mathrm{Hz})$ for low-frequency critical current fluctuations [144]. Considering that we have three Josephson junctions in series and using the parameters found in Sec. 4.2, the total spectral flux noise density for our qubit is expected to be $S_\Phi(1\,\mathrm{Hz}) = (2+\alpha^2)S_I(1\,\mathrm{Hz})\left[(2+\alpha)L_\mathrm{J}\right]^2 \simeq (1.7 \times 10^{-6}\Phi_0)^2/\mathrm{Hz}$. Here, $L_\mathrm{J} \equiv \Phi_0/(2\pi I_\mathrm{c})$ is the Josephson inductance. Assuming $1/f$-noise, the above estimation yields a noise amplitude $\tilde{\mathcal{A}} \simeq (1.7 \times 10^{-6}\Phi_0)^2$ very similar to the one of Eq. (4.10) extracted from the spin echo data. Finally, the fit to the spin echo data shown in Fig. 4.3 gives a finite Bloch-Redfield contribution

$$S_{\Phi E}^{\mathrm{BR}}(\omega \to 0) = \left[(2.1 \pm 0.1) \times 10^{-10}\Phi_0\right]^2 \mathrm{Hz}^{-1} \tag{4.11}$$

to the spectral flux noise density in addition to the $1/f$-noise contribution. In the case of the Ramsey decay, we also find that the flux dependence of the decay time $T_{2\mathrm{R}}$ is consistent with the existence of $1/f$-noise ($\mathcal{A}_\mathrm{R} = \left[(2.0 \pm 0.2) \times 10^{-5}\Phi_0\right]^2$) and $T_{\varphi\mathrm{R}}^0 \equiv \left(\Gamma_{\varphi\mathrm{R}}^0\right)^{-1} \simeq 200\,\mathrm{ns}$. However, we did not find a significant Bloch-Redfield contribution $S_{\Phi R}^{\mathrm{BR}}(\omega \to 0)$ in the entire flux interval from $\delta\Phi_\mathrm{x} = -6.007 \times 10^{-3}\Phi_0$ to $+4 \times 10^{-4}\Phi_0$. This confirms that in the spin echo experiment a significant part of the low-frequency $1/f$-noise is canceled ($\mathcal{A}_\mathrm{R}/\mathcal{A} \simeq 5$) by the refocusing effect of the intermediate π-pulse.

4.4 Ramsey and spin echo beatings

In this section, we present an explanation for the beatings observed in the Ramsey and spin echo data of Fig. 4.6 and Fig. 4.7. We are able to reproduce these features qualitatively using numerical simulations. It is notable that our discussion is not limited to a specific type of superconducting qubit or readout method.

In the previous sections, we already excluded trivial origins of beatings: First, as pointed out in Sec. 3.4.4, any effect of control pulse imperfections is removed using the phase-cycling method. Second, because of the spatial enclosing of the sample in combination with the filtering conditions of the measurement lines, both explained in Sec. 3.2.3 and Sec. 3.3, parasitic resonances in the readout circuitry present only a remote possibility. Finally, as shown in Fig. 4.5, the electromagnetic environment in the immediate vicinity of the qubit does not exhibit any prominent mode with a

[2]These results coincide with those obtained with the resistive-bias readout method [45], apart from the fact that the maximum $T_{2\mathrm{E}}$ is by a factor of two larger there. This is not surprising, considering the T_1 limitation and the fact that already the T_1-analysis performed in Sec. 4.3.1 suggests an increase of high-frequency noise due to the switching from the resistive- to the capacitive-readout scheme.

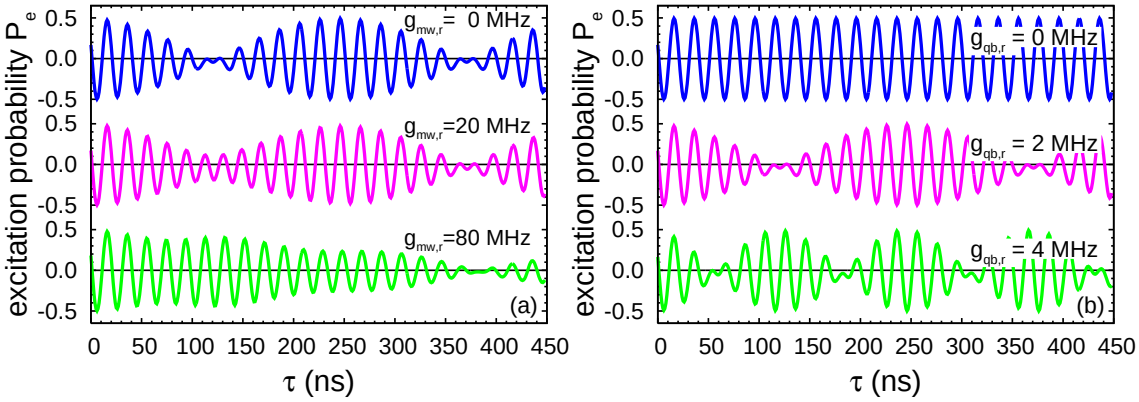

Figure 4.8: Simulated periodic Ramsey beatings due to a qubit-resonator interaction. The resonator (a quantum harmonic oscillator) is truncated to 31 bases. The system parameters are chosen to be similar to those found in the experiment: The qubit persistent current I_p is 370 nA, the qubit gap frequency Δ/h is 4 GHz, and the resonator frequency ν_r is 4 GHz (resonance condition). The maximum free evolution time τ is 450 ns. The microwave excitation frequency is slightly detuned from that of the oscillator ($\nu = \nu_\mathrm{Ramsey} = 4.05\,\mathrm{GHz}$). The coupling constants are chosen in a way that the results resemble our experimental data. **(a)** Variation of the Ramsey signal with increasing $g_\mathrm{mw,r}$. The other parameters are $g_\mathrm{qb,r} = 2\,\mathrm{MHz}$ and $g_\mathrm{mw,qb} = 80\,\mathrm{MHz}$ for the displayed traces. **(b)** Variation of the Ramsey signal with $g_\mathrm{qb,r}$: The beating frequency increases with $g_\mathrm{qb,r}$. Our experimental results indicate $g_\mathrm{qb,r} \simeq$ 2-6 MHz. The other parameters are $g_\mathrm{mw,r} = 0$ and $g_\mathrm{mw,qb} = 80\,\mathrm{MHz}$.

frequency close to the qubit gap frequency Δ/h. Inspired by results from quantum optics showing that the coupling between an atom and the photonic mode of a cavity can give rise to beating signals [145, 146], we suggest a different explanation for the origin of the beatings observed in our experiments. To this end, we exploit the formalism of circuit QED introduced in Sec. 2.8 with the qubit acting as an artificial atom and the cavity being represented by a quantum harmonic oscillator. As we will see below, the latter is located on the sample chip close to the qubit and its nature is microscopic in the sense that its coupling to the microwave driving is much smaller than the qubit-microwave coupling. Still, the coupling strength between qubit and resonator is larger than the characteristic decay rates of each of them. Under these assumptions the system can no longer be described in terms of a spin-boson model. Instead, the qubit and oscillator have to be treated as a single combined quantum system. When the oscillator is not driven and its thermal population negligible, it qualitatively behaves very similarly to a two-level system. Our experimental data does not allow us to distinguish between the two. Although in the literature typically two-level systems are assumed for the fluctuators (cf. Sec. 2.9), we use the formalism for a harmonic oscillator here. However, we reiterate that our conclusions do not depend on this specific choice.

From an experimental point of view, the assumption of a fluctuator interacting with the qubit is motivated by qubit microwave spectroscopy performed with the resistive-bias readout. There, we observe a series of peaks reminiscent of the two-photon blue sideband transition signal of the qubit and a resonator of frequency $\nu_\mathrm{r} \simeq 4\,\mathrm{GHz} \simeq \Delta/h$. As shown in the inset of Fig. 4.9, these peaks have the same flux

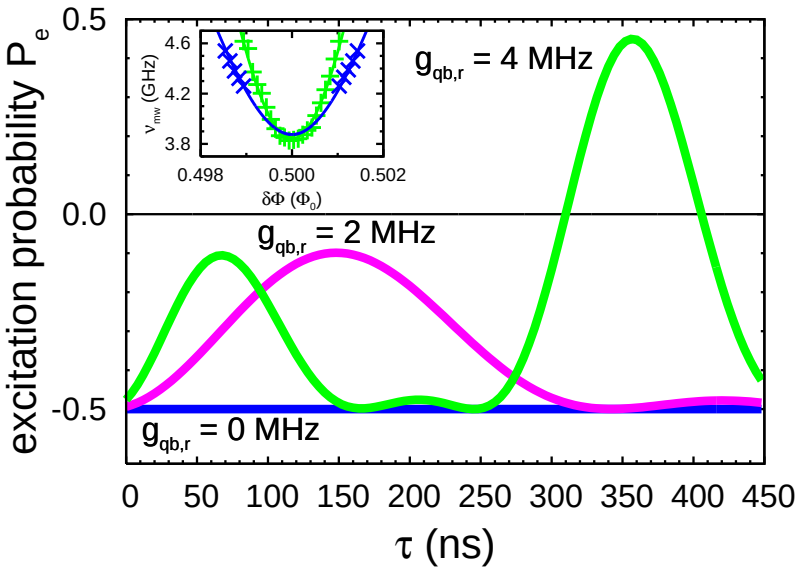

Figure 4.9: Simulated aperiodic spin echo beatings due to the interaction of the qubit with a single harmonic oscillator. The total free evolution time is τ and $g_{\mathrm{mw,r}} = 0$. Unless otherwise stated, the system parameters are the same as in Fig. 4.8. The microwave driving is resonant with the oscillator ($\nu = \nu_{\mathrm{Echo}} = 4\,\mathrm{GHz}$). Depending on $g_{\mathrm{qb,r}}$ the beating spin echo trace crosses the zero axis within the chosen time window or not. If, within the frequency range of interest, the qubit is coupled to several (but not too many) spurious resonators, their influence has a complex dependence on the external flux bias. Hence, the presence or absence of the Ramsey and spin echo beatings does not posses any apparent flux bias dependence. However, for a certain flux bias the same beating pattern occurs reproducibly in agreement with our experimental observations shown in Fig. 4.6 and Fig. 4.7. Inset: Resistive-bias spectroscopy close to the degeneracy point. The green plus symbols correspond to the qubit resonance peaks. The blue crosses are consistent with the two-photon process of the blue sideband transition due to the interaction of the qubit with one specific parasitic resonator.

dependence as the normal two-photon peaks except for a frequency offset. This scenario can be modeled with the following Hamiltonian, which, in the qubit eigenbasis, becomes

$$\frac{\hat{H}_{\mathrm{qb,r}}}{h} = \frac{\nu_{\mathrm{ge}}}{2}\hat{\sigma}_z + \nu_{\mathrm{r}}\left(\hat{a}^\dagger\hat{a} + \frac{1}{2}\right) + ig_{\mathrm{qb,r}}\left(\hat{a}^\dagger - \hat{a}\right)\left(\cos\theta\,\hat{\sigma}_z - \sin\theta\,\hat{\sigma}_x\right) - g_{\mathrm{mw,qb}}\cos\left(2\pi\nu t\right)\left(\cos\theta\,\hat{\sigma}_z - \sin\theta\,\hat{\sigma}_x\right) + ig_{\mathrm{mw,r}}\cos\left(2\pi\nu t\right)\left(\hat{a}^\dagger - \hat{a}\right)\,. \quad (4.12)$$

Here, the first three terms denote an undriven qubit-resonator system, which is similar to the standard Jaynes-Cummings model. The last two terms describe a microwave driving at the frequency ν, which is different for the Ramsey ($\nu = \nu_{\mathrm{Ramsey}}$) and spin echo ($\nu = \nu_{\mathrm{Echo}}$) experiments. These driving terms are only present within the duration of the control pulses, and they are switched off during the free evolution periods. The operators $\hat{a}^\dagger$ and $\hat{a}$ are the usual boson creation and annihilation operators. $g_{\mathrm{qb,r}}$, $g_{\mathrm{mw,qb}}$, and $g_{\mathrm{mw,r}}$ are the coupling constants. The $(\cos\theta\,\hat{\sigma}_z - \sin\theta\,\hat{\sigma}_x)$-terms appear because of the rotation of the interaction Hamiltonian into the qubit eigenbasis. As a matter of fact, the $(\cos\theta\,\hat{\sigma}_z)$-term constitutes the main difference to the Jaynes-Cummings approximation and is accurately accounted for in our simulations. Since we are investigating a flux qubit, all interactions are proportional to

pairwise products of the qubit current operator $\hat{I}_{\mathrm{qb}}$, the oscillator current operator $\hat{I}_{\mathrm{r}}$, and the classical microwave driving current $I_{\mathrm{mw}} \cos(2\pi\nu t)$. Also, we can restrict our discussion to the case of pure linear coupling because the microwave power used in our experiments is relatively small.

Based on Eq. (4.12), we simulate the Ramsey and spin echo traces at the degeneracy point. The time traces are obtained by numerically solving the Schrödinger equation for the desired pulse sequence. The initial state is the energy ground state of the qubit-resonator system in absence of driving. We choose parameters similar to those found in the experiments, but neglect the effects of decoherence for simplicity. The results are shown in Fig. 4.8 and Fig. 4.9. Already at a first glance, it is evident that the simulations can reproduce the two main features of the experimental data. On the one hand, as shown in Fig. 4.8(b), there can be periodic Ramsey beatings. On the other hand, as displayed in Fig 4.9, aperiodic spin echo beatings can appear at the same time. The former are due to an on-resonance qubit-resonator interaction, whereas the latter are caused by the refocusing π-pulse, which generates an unwanted evolution in the resonator part of $\hat{H}_{\mathrm{qb,r}}$. When the resonator driving strength $g_{\mathrm{mw,r}}$ is increased from zero, the Ramsey beatings are washed out as shown in Fig. 4.8(a). This indicates that in our experiments the resonator is not an extended LC-circuit [71], but rather a point-like microscopic entity such as a magnetic impurity or a dangling bond in the dielectric forming the tunnel barrier of the qubit junctions. Here, we use the term "point-like" to denote that the effective area of the resonator interacting with the external microwave must be small compared to the qubit. This implies the condition $g_{\mathrm{mw,r}} \ll g_{\mathrm{mw,qb}}, g_{\mathrm{qb,r}}$ and, consequently, we choose $g_{\mathrm{mw,r}} = 0$ in the subsequent simulations of Fig. 4.8(b) and Fig. 4.9.

Despite its microscopic nature, the spurious resonator is found to be stable enough to survive at least one thermal cycle. In fact, Ramsey beatings can also be observed in the resistive readout measurements (time domain data not shown, for spectroscopy data cf. inset of Fig. 4.9). On closer inspection, we find that the resonance condition is very important for our simulation results. This might seem controversial, given that we observe the beatings over a considerable frequency range around the degeneracy point. However, we have to recall that we neglect decoherence here. As a consequence, in the simulations we have much sharper resonance peaks than in the experiments. Furthermore, we only account for a single oscillator. In reality, there is spectroscopic evidence for several oscillators with slightly different frequencies close to 4 GHz and with different coupling constants (data not shown). It is noteworthy to mention that there is no fundamental restriction for these oscillators to be present only in the frequency range around 4 GHz. However, only there the qubit coherence time is long enough to allow for a clear observation of beatings or splittings. The parasitic resonators are also a possible explanation for the fact that the measured relaxation times are much shorter than the ones calculated in Sec. 4.3.1 from the bias current fluctuations [30].

The fact that the simulations suggest a point-like structure as source of the beatings makes it difficult to decide whether we have to assume a harmonic oscillator or a two-level system. Indeed, as we already pointed out above, an undriven resonator behaves very similar to a two-level system in the simulations. Nevertheless, we continue to use the term "resonator" in order to keep the language simple and easy to understand. We also want to point out that in the experiments performed with the resistive-bias readout we find similar Ramsey splittings, but no clear spin

echo beatings (data not shown). We attribute this to the fact that in the resistive experiments the visibility is worse, while the coherence times are longer. For the rather aperiodic low-frequency spin echo beatings ($\lesssim 2\,\mathrm{MHz}$), this results in the tendency to observe the decay envelope only, whereas for the faster, periodic Ramsey beatings (approximately 10 MHz) the beatings are still visible. Also, the resonance condition discussed above is important for the observability of beatings. The reason is that different oscillators interact with the qubit via different coupling constants. However, beatings cannot be observed unless the resonator frequency falls into the frequency window around the optimal point where the qubit coherence times are longer than $g_{\mathrm{qb,r}}^{-1}$. This window shifts notably when performing thermal cycling. In fact, the qubit gap changes by almost 10% from $\Delta_{\mathrm{Rbias}}/h = 3.9\,\mathrm{GHz}$[45, 59] in the resistive-bias experiments to $\Delta_{\mathrm{Cbias}}/h \equiv \Delta/h = 4.22\,\mathrm{GHz}$ in the capacitive-bias experiments.

4.5 Noise sources

After the quantitative analysis of the influence of the external magnetic flux noise on the qubit decoherence performed in Sec. 4.3 and the discussion of the beatings in Sec. 4.4, we are now ready to put together the results into a general picture in this section. Let us recall that there are three classes of decay rates analyzed in this work. The first one consists of the Bloch-Redfield rates Γ_1 and $\Gamma_\varphi^{\mathrm{BR}}$, which can be derived with a golden-rule type of argument. The second one, $\Gamma_\varphi^{1/f}$, is due to the impact of $1/f$-noise and, finally, there is a flux-independent contribution Γ_φ^0.

In order to understand the interplay of the decoherence mechanisms behind these three classes, we have to consider the derivation of the decay rates in more detail. Focusing on the dephasing first, under the assumption of a Gaussian distribution of the noise amplitudes we obtain the decay envelope [36, 37, 147]

$$f(\tau) = \exp\left[-\frac{\tau^2}{2\hbar}\left[\frac{\partial\epsilon(\Phi_{\mathrm{x}})}{\partial\Phi_{\mathrm{x}}}\cos\theta\right]^2 \int_{-\infty}^{+\infty} S_\Phi(\omega)F(\omega\tau/2)d\omega\right] \tag{4.13}$$

for the $\hat{\sigma}_{x,y}$-component of the qubit state. Here, τ is the free-evolution time visualized in Fig. 3.9(b). The filtering functions $F(\tilde{\omega} \equiv \omega\tau/2) \equiv F_{\mathrm{R,E}}(\tilde{\omega})$ for the Ramsey and spin echo sequences,

$$F_{\mathrm{R}}(\tilde{\omega}) = \frac{\sin^2\tilde{\omega}}{\tilde{\omega}^2} \text{ and} \tag{4.14}$$

$$F_{\mathrm{E}}(\tilde{\omega}) = \frac{\sin^4(\tilde{\omega}/2)}{(\tilde{\omega}/2)^2} \tag{4.15}$$

are plotted in Fig. 4.10. Obviously, the Ramsey sequence is most sensitive to noise close to $\omega = 0$. On the contrary, due to the refocusing effect, the spin echo sequence is completely insensitive to zero-frequency noise. However, the corresponding filtering function exhibits a maximum at the finite frequency $\omega \approx 4/\tau$. Noise at this frequency just cancels the refocusing effect of the intermediate π-pulse. In other words, $1/f$-noise is strongly reduced by the spin echo sequence, while noise which is white in the angular frequency band between zero and $\omega_{\mathrm{c}} \approx 12/\tau$ remains unaffected. For typical time scales of our experiments, $\tau \approx T_1, T_2 \simeq 100\,\mathrm{ns}$ we find that the critical angular

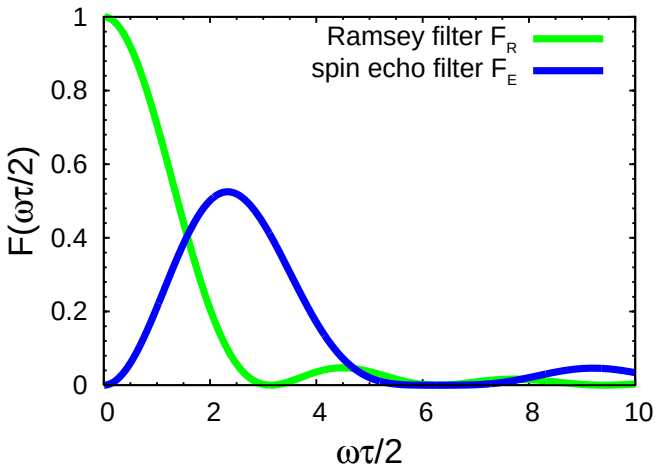

Figure 4.10: Ramsey and spin echo filtering functions.

frequency ω_c is still much smaller than the angular frequency $\Delta/\hbar$ corresponding to the qubit gap Δ.

For $1/f$-noise, both the decay rate of Eq. (4.9) and the Gaussian decay law can be calculated straightforwardly from Eq. (4.8), Eq. (4.13), and Eq. (4.15). However, the Bloch-Redfield dephasing rate of Eq. (4.6) has to be treated carefully: The golden rule argument is only valid for times long compared to ω^{-1}. Since the dephasing is dominated by the low-frequency contribution ($\omega \to 0$) we cannot apply this argument to our time traces (typically $1-450\,\mathrm{ns}$ long). Instead, we notice that Eq. (4.6) and a simple exponential decay law can be derived rigorously from Eq. (4.13) and Eq. (4.15) assuming a frequency-independent spectral density. Thus, a finite $\Gamma_\varphi^{\mathrm{BR}}$ contribution indicates the existence of white noise. If both white and $1/f$-noise are present, near the degeneracy point the peaked shape of $\left(\Gamma_\varphi^{1/f}\right)^{-1} \propto (|\cos\theta|)^{-1}$ dominates over the rounded shape of $\left(\Gamma_\varphi^{\mathrm{BR}}\right)^{-1} \propto (|\cos^2\theta|)^{-1}$. The peaked shape of $T_{2\mathrm{R}}$ and $T_{2\mathrm{E}}$ in Fig. 4.3 thus represents a clear evidence of the influence of $1/f$-noise on our qubit. Near the readout point $\delta\Phi_\mathrm{x} = 6.007\times10^{-3}\Phi_0$, we have $|\cos\theta| \simeq \cos^2\theta$ and the influence of the white noise on $T_{2\mathrm{E}}$ becomes comparable to that of the $1/f$-noise. We find that it is not possible to properly fit the $T_{2\mathrm{E}}$-data (including the readout point), when omitting either the Bloch-Redfield or the $1/f$-term. This means that we find a transition from a $1/f$-noise dominated regime in the direct vicinity of the degeneracy point to another regime near the readout point, where the influence of $1/f$- and white noise is comparable. In the Ramsey data the $1/f$-noise contribution is clearly dominant because of the singularity at $\omega = 0$. For this reason it is difficult to extract the small white noise contribution from the data with a meaningful error bar. The fact that the spin echo sequence strongly reduces $1/f$-noise, but does not affect white noise, allows us to detect the latter.

In order to calculate the true Ramsey decay law due to $1/f$-noise from Eq. (4.13), we need to assume at least an infrared cutoff ω_{IR}. The corresponding decay time is then

$$\Gamma_{\varphi\mathrm{R}}^{1/f}(\Phi_\mathrm{x}) = \frac{1}{\hbar}\left|\frac{\partial\epsilon(\Phi_\mathrm{x})}{\partial\Phi_\mathrm{x}}\cos\theta\right| \sqrt{\mathcal{A}\ln\frac{1}{\omega_{\mathrm{IR}}\tau}}\,. \tag{4.16}$$

Considering a maximal time trace length of about $\tau_0 \simeq 300\,\mathrm{ns}$, we obtain

$$\omega_{\mathrm{IR}}/2\pi = \left[2\pi\tau_0 \exp\left(\frac{\mathcal{A}_{\mathrm{R}} \ln 2}{\mathcal{A}}\right)\right]^{-1} \simeq 0.2\,\mathrm{Hz}\,. \tag{4.17}$$

This result has the same order of magnitude as the inverse time it takes to record a single averaged data point. However, the exponential in Eq. (4.17) makes the result exponentially sensitive to measurement errors. Considering that a better time scale for $(\omega_{\mathrm{IR}}/2\pi)^{-1}$ is the time to record an entire decay trace ($\simeq 1\,\mathrm{h}$), we probably overestimate the infrared cutoff frequency slightly.

Furthermore, we want to point out that the white noise spectral density $S_\Phi^{\mathrm{BR}}(\omega \to 0)$ deduced from the dephasing is of the same order as the Bloch-Redfield spectral density $S_\Phi^{\Gamma_1}(\Delta/\hbar)$ inferred from the energy relaxation rates. The energy relaxation rate of Eq. (4.3) is calculated with the golden rule assuming weak noise characterized by a smooth spectral density at $\omega \approx \Delta/\hbar$. In contrast to the Bloch-Redfield dephasing rate, the long time condition $t \gg (h/\Delta \simeq 250\,\mathrm{ps})$ is fulfilled for our experimental time scales of $1 - 300\,\mathrm{ns}$. The fact that we find $S_\Phi^{\mathrm{BR}}(\omega \to 0) \approx S_\Phi^{\Gamma_1}(\Delta/\hbar) \gg S_\Phi^{1/f}(\Delta/\hbar)$ suggests that the white noise observed in the $T_{2\mathrm{E}}$-analysis is also limiting the energy relaxation times. Considering that the noise created by the bias circuit cannot explain the observed relaxation rates (cf. Sec. 4.3.1) and that T_1 is quite sensitive to changes in the microwave setup, the natural candidate for the dominating white noise source is the high-frequency line. In contrast to that, $1/f$-noise can be modeled with an ensemble of microscopic fluctuators close to or within the qubit junctions [30]. In Sec. 4.4, we show that we can observe the effect of at least one such fluctuator in our time domain traces. Additionally, fluctuators cause dielectric losses in the oxide barrier of the junctions, deteriorating T_1 [30]. In particular, in our three-junction qubit the whole loop acts as a very big fourth junction. Thus, as discussed in more detail in the next paragraph, the controlled introduction of a small fourth junction as well as the use of small loop sizes [44, 46] might be advantageous because the effective amount of dielectric material in the loop is significantly reduced. A summary of the impact of the different noise sources for our flux qubit is shown in Fig. 4.11.

Finally, we compare the performance of our qubit to that of other recently measured flux qubits, which have a galvanic coupling to the readout DC SQUID [44, 46]. To this end, we focus on the results presented in Ref. [44] as a prototypical example. The most striking similarity is the relaxation limitation at the optimal point. Furthermore, the mutual inductance between the qubit and the high-frequency line as well as the bias line filtering are almost the same. However, the T_1-time of our qubit is about one order of magnitude smaller. These observations immediately imply that our qubit is more susceptible to high-frequency noise. We find three main reasons to explain this fact. First, any noise of given amplitude couples more strongly to our qubit because the persistent current is about twice as large as the one in Ref. [44]. Second, the absence of a small fourth junction increases the effective amount of dielectric and hence the number of fluctuators. The effective area A_{diel} of the dielectric material can be estimated from Eq. (2.30) of Sec. 2.9. For our relaxation rate $\Gamma_1 \simeq 10\,\mathrm{MHz}$, we compute $A_{\mathrm{diel}} \simeq 1\,\mu\mathrm{m}^2$. This value is almost an order of magnitude larger that the total area $A_{\mathrm{tot}} \simeq 0.08\,\mu\mathrm{m}^2$ of the three qubit junctions, indicating that part of the loop forms a large fourth junction. Considering that the relaxation time in our experiments is also susceptible to changes in

the high-frequency setup, further experiments are required to clarify whether also the fluctuators can play a significant role. Third, the total coupling between qubit and DC SQUID is much lower in our design due to the absence of kinetic mutual inductance and smaller DC SQUID junctions. For manipulations in the vicinity of the optimal point, we apply an adiabatic shift pulse (cf. Sec 3.2.4) during the qubit operation via the virtually unfiltered high-frequency line. On the contrary, in Ref. [44] the readout pulse was sent through the strongly low-pass filtered bias line and causes a flux shift due to the large coupling. This shift does not take place during the qubit operation. In this respect, the galvanic coupling method turns out to be advantageous. On the other hand, the controlled application of the shift pulse offers a large flexibility in the experiments. In particular, the possibility to operate the superconducting magnet in the persistent mode is attractive. For this reason, we plan to use an additional low-pass filtered control line for the shift pulse in future experiments.

4.6 Conclusions

In summary, we have measured the coherent dynamics of a three-Josephson-junction superconducting flux qubit, which is characterized by a gap frequency $\Delta/h = 4.22\,\mathrm{GHz}$. We used the capacitive-bias detection method, a variant of the switching DC SQUID readout. This method provides a built-in band-pass filtering of the electromagnetic environment of the qubit, thereby allowing for faster readout pulses and a reduction of low-frequency bias current noise. We use the adiabatic shift-pulse method to probe the qubit close to the degeneracy point and the phase-cycling technique to cancel the effects of control pulse imperfections. Right at the degeneracy point, the coherence time of our qubit is limited by energy relaxation and we find $T_1 = 82\,\mathrm{ns}$ and $T_\varphi \simeq 2\,\mu\mathrm{s}$. The flux noise spectral density at the qubit transition frequency is $S_\Phi^{\Gamma_1}(\Delta/\hbar) = \left[(1.4 \pm 0.1) \times 10^{-10}\Phi_0\right]^2 \mathrm{Hz}^{-1}$. In the close vicinity of the degeneracy point, the measured spin echo times exhibit a flux dependence that is expected for the case where flux noise with a $1/f$-frequency spectrum and a magnitude $\mathcal{A} = \left[(4.3 \pm 0.7) \times 10^{-6}\Phi_0\right]^2$ is the dominant source of dephasing. Near the readout point, which in our case means far away from the degeneracy point, we also find a significant white noise contribution $S_\Phi^{\mathrm{BR}}(\omega \to 0) = \left[(2.1 \pm 0.1) \times 10^{-10}\Phi_0\right]^2 \mathrm{Hz}^{-1}$. From the comparison between Ramsey and spin echo decay times we estimate an infrared cutoff $\omega_{\mathrm{IR}}/2\pi \simeq 0.2\,\mathrm{Hz}$ of the $1/f$-noise spectrum.

On one and the same qubit, we compare the results obtained with the capacitive-bias readout to data taken with the conventional resistive-bias method. On the one hand, we find that the capacitive-bias data shows an increased visibility. On the other hand, a slightly reduced (less than a factor of two) T_1-time is observed, suggesting a considerable impact of high-frequency noise from the microwave line. The $1/f$-noise magnitude deduced from the spin echo decay is about $(10^{-6}\Phi_0)^2$ in both setups (cf. Ref. [45] for more details on the resistive-bias results). This value was also found in a study where the flux qubit had a galvanic connection to the readout DC SQUID [44] and in other Josephson-junction-based experiments [144]. Together with the detailed study on the influence of high-frequency environmental bias noise on the energy relaxation time T_1, our work clearly shows that external noise generated by the DC SQUID bias circuitry is not the dominant noise source for

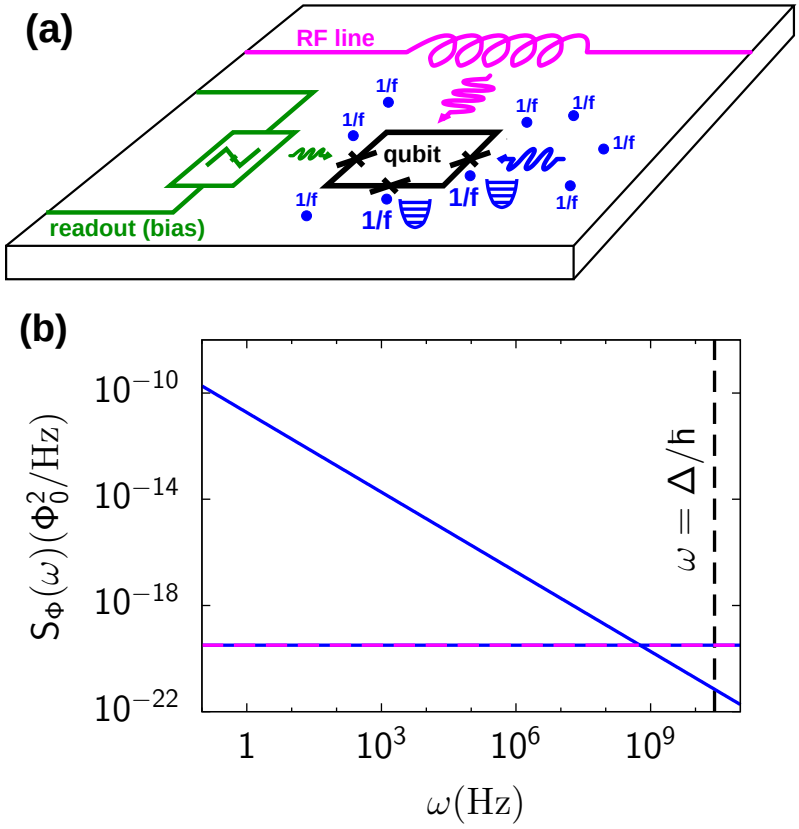

Figure 4.11: Summary of the relevant noise sources affecting the qubit measured in this work. **(a)** We find white noise (arrows), $1/f$-noise (ensemble of blue dots), and a few fluctuators coupled especially strongly to the qubit (blue parabolas). In our experimental scenario, the high-frequency bias noise generated by the DC SQUID lines (green arrow) is much smaller than the noise generated by the high-frequency line (magenta arrow) or by the fluctuators (blue arrow). **(b)** Flux noise spectral densities of $1/f$-noise (solid blue line) and white noise (blue/magenta dashed line). It is interesting to note that the fluctuators can contribute to both relaxation and dephasing.

either T_2- or T_1-time. We attribute the difference in the T_1-times obtained with the capacitive- and resistive-bias measurements to changes in the high-frequency setup, which have occurred during the experiments in the process of switching between the two methods. Finally, we find that in the frequency range of $2 - 10\,\mathrm{GHz}$, which is most important for flux qubit operation, the capacitive-bias scheme allows one to easily engineer an environment with a low and almost flat noise spectral density of the bias current fluctuations. This is not possible for the resistive-bias readout. In other words, if, in the future, the presently dominating noise sources can be reduced to a level that bias circuit noise becomes the limiting factor, the electromagnetic environment of the capacitive-bias method is advantageous. Finally, we compare the white-noise contribution to the dephasing with the noise extracted from the Γ_1-measurements and find $S_\Phi^{\mathrm{BR}}(\omega \to 0) \approx S_\Phi^{\Gamma_1}(\Delta/\hbar) \gg S_\Phi^{1/f}(\Delta/\hbar)$. It is noteworthy to mention that we find $S_\Phi^{\mathrm{BR}}(\omega \to 0) \approx S_\Phi^{\Gamma_1}(\Delta/\hbar)$ from two completely different experiments, suggesting that the white noise contribution is indeed regular for $0 \leq \omega \leq \Delta/\hbar$.

Near the qubit degeneracy point, we find beatings both in the Ramsey and the

spin echo traces. These beatings constitute an experimental evidence of the interaction of the qubit with one (or a few) harmonic oscillators or two-level fluctuators, which are approximately on resonance with the qubit. We support this argument with the aid of numerical simulations, which qualitatively explain our data. In particular, these simulations indicate that the perturbing oscillators are point-like, i.e., their effective area, and thus their coupling strength to the microwave driving, is small compared to the qubit loop area. The observed effect of $1/f$-noise on the qubit dephasing in the close vicinity of the optimal point can be attributed to an ensemble of such microscopic fluctuators or resonators located on the sample chip close to the qubit or in the oxide barrier of its junctions. Additionally, near-resonant fluctuators constitute another possible source of energy relaxation in addition to the microwave line. A summary of the relevant noise sources is shown in Fig. 4.11.

Chapter 5

Controlled symmetry breaking in circuit QED

Superconducting qubits [16, 18], which are introduced in Sec. 2.4, behave as artificial two-level atoms. When they exhibit a sufficient degree of quantum coherence, they can be used to investigate fundamental quantum phenomena. In this context, the study of multi-photon excitations [31, 55–58] occupies a central role. Moreover, coupling superconducting qubits to on-chip microwave resonators has given rise to the field of circuit QED [52, 53, 65, 66, 71, 74, 75, 99]. As outlined in Sec. 2.8, circuit QED is the solid-state analog of quantum-optical cavity QED [60–63] and therefore allows one to probe the fundamental interaction between matter and light. For this purpose, the tunability inherent to solid-state circuits is especially attractive. In this chapter, we report on the observation of key signatures of a two-photon driven Jaynes-Cummings model, which unveils the upconversion dynamics of a superconducting flux qubit [27, 28] (cf. Sec. 2.5 and, regarding quantum coherence, chapter 4) coupled to an on-chip lumped-element microwave resonator (cf. Sec. 2.7). Our experiment and theoretical analysis show clear evidence for the coexistence of one- and two-photon driven level anticrossings of the qubit-resonator system. This results from the controlled symmetry breaking of the system Hamiltonian, causing parity to become a not well-defined property [148]. Our study provides deep insight into the interplay of multiphoton processes and symmetries in a qubit-resonator system.

In cavity QED, a two-level atom interacts with the quantized modes of an optical or microwave cavity. The information on the coupled system is encoded both in the atom and in the cavity states. The latter can be accessed spectroscopically by measuring the transmission properties of the cavity [60], whereas the former can be read out by suitable detectors [62, 63]. In circuit QED, the solid-state counterpart of cavity QED introduced in Sec. 2.8, the first category of experiments was implemented by measuring the microwave radiation emitted by a resonator (acting as a cavity) strongly coupled to a charge qubit [65]. In a dual experiment, the state of a flux qubit was detected with a DC superconducting quantum interference device (SQUID) and vacuum Rabi oscillations were observed [71]. More recently, both approaches have been exploited to extend the toolbox of quantum optics on a chip [52, 53, 64, 74, 75, 99]. Whereas all these experiments employ one-photon driving of the coupled qubit-resonator system, multi-photon studies are available only for sideband transitions [99] or bare qubits [31, 55–58]. The experiments dis-

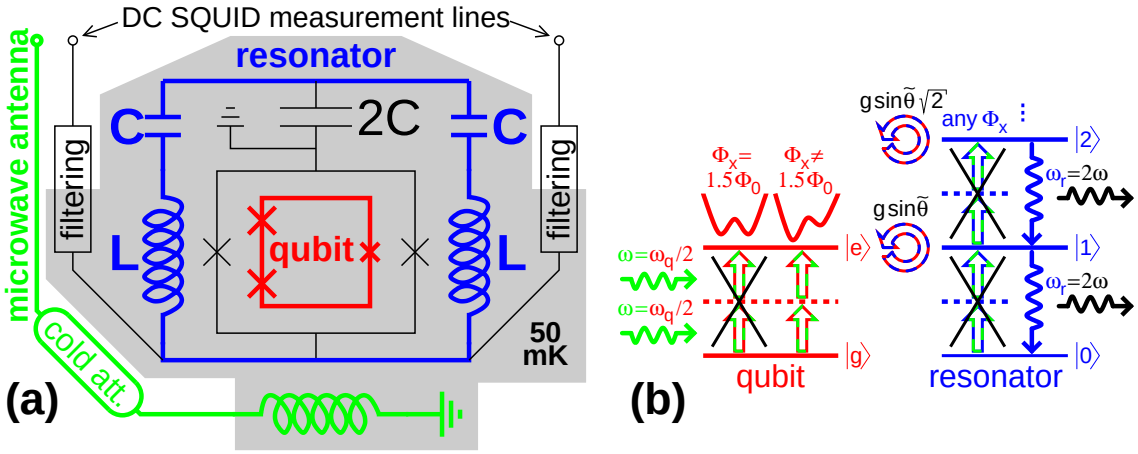

Figure 5.1: Experimental architecture and theoretical model. **(a)** The flux qubit (red, junctions marked by crosses) is inductively coupled to the readout DC SQUID (black rectangle), which is shunted by an LC-circuit acting as a quantized resonator (blue) [71]. All elements within the shaded area are at a temperature $T \simeq 50\,\mathrm{mK}$. Microwave signals and flux-shift pulses are applied via an on-chip antenna (green). The signal-to-noise ratio is improved by cold attenuators. **(b)** Upconversion dynamics describing the physics governing our experiments, cf. Eq. (5.5). The qubit (red) level splitting is $\hbar\omega_{\mathrm{ge}}$ and the resonator (blue) frequency is $\omega_{\mathrm{r}}/2\pi$. In the relevant case of two-photon driving with frequency ω (green), the system predominantly decays via the resonator. The qubit-resonator coupling strength is $g\sin\tilde{\theta} = g\Delta/\omega_{\mathrm{r}} \simeq 0.63g$. For $\Phi_{\mathrm{x}} \neq 1.5\Phi_0$ the mirror symmetry of the qubit potential (red double well; x-axis: phase variable γ_- defined in Sec. 2.5) is broken allowing for two-photon transitions.

cussed in this work explore, to our knowledge for the first time, the physics of the two-photon driven Jaynes-Cummings dynamics in circuit QED. In this context, we show that the dispersive interaction between the qubit and the two-photon driving enables real level transitions. The nature of our experiment can be understood as an upconversion mechanism, which transforms the two-photon coherent driving into single photons of the Jaynes-Cummings dynamics. This process requires energy conservation and a not well-defined parity [148] of the interaction Hamiltonian. In our system, the latter condition is met due to the symmetry breaking of the qubit potential. Our experimental findings reveal that such symmetry breaking can be obtained either in a controlled way by choosing a suitable qubit operation point or by the presence of additional spurious fluctuators [30] such as the ones discussed in Sec. 2.9, Sec. 4.4, and Sec. 4.5. The results presented in this chapter are published in Ref. [59].

5.1 Qubit-resonator system

In this work we used the same flux qubit as for the decoherence measurements presented in chapter 4, however, in the resistive-bias measurement configuration described in Sec. 3.2.3 [35, 45]. For clarity, the main elements of our setup are highlighted in Fig. 5.1(a). They comprise a three-Josephson-junction flux qubit, an LC-resonator, a DC SQUID and a microwave antenna. The qubit is operated near the optimal flux bias $\Phi_{\mathrm{x}} = 1.5\Phi_0$. Following Sec. 2.5, it can be described with

the two-level Hamiltonian of Eq. (2.16), $\hat{H}_\mathrm{q} = (\epsilon\hat{\sigma}_z + \Delta\hat{\sigma}_x)/2$. Here, $\hat{\sigma}_x$ and $\hat{\sigma}_z$ are Pauli operators. From low-level microwave spectroscopy we estimate a qubit gap $\Delta/h = 3.89\,\mathrm{GHz}$. By changing Φ_x, the quantity $\epsilon \equiv 2I_\mathrm{p}(\Phi_\mathrm{x} - 1.5\Phi_0)$ and, in turn, the level splitting $\hbar\omega_\mathrm{ge} \equiv \sqrt{\epsilon^2 + \Delta^2}$ can be controlled. Here, $\pm I_\mathrm{p}$ are the clockwise and counterclockwise circulating persistent currents associated with the eigenstates $|\pm\rangle$ of $\epsilon\hat{\sigma}_z$. Far away from the optimal point, $|\pm\rangle$ correspond to the eigenstates $|\mathrm{g}\rangle$ and $|\mathrm{e}\rangle$ of $\hat{H}_\mathrm{q}$. The qubit is inductively coupled to a lumped-element LC-resonator [71]. As described in Sec. 2.7, the latter behaves as a quantum harmonic oscillator and its Hamiltonian is that of Eq. (2.24), $\hat{H}_\mathrm{r} = \hbar\omega_\mathrm{r}\left(\hat{a}^\dagger\hat{a} + 1/2\right)$. The eigenstates of $\hat{H}_\mathrm{r}$ are the photon number states $|0\rangle$, $|1\rangle$, $|2\rangle, \ldots$ and $\hat{a}^\dagger$ and $\hat{a}$ are the boson creation and annihilation operators, respectively. The resonator is designed such that its fundamental frequency, $\omega_\mathrm{r}/2\pi = 6.16\,\mathrm{GHz}$, is largely detuned from Δ/h. The qubit-resonator interaction Hamiltonian is $\hat{H}_\mathrm{q,r} = \hbar g\hat{\sigma}_z\left(\hat{a}^\dagger + \hat{a}\right)$ (cf. Sec. 2.8), where $g = 2\pi \times 115\,\mathrm{MHz}$ is the coupling strength. As explained in Sec. 3.2.3 and Sec. 4.3.1, the LC-circuit also constitutes a crucial part of the electromagnetic environment of the readout DC SQUID. In this way, the flux signal associated with the qubit states $|\pm\rangle$ can be detected while maintaining reasonable coherence times and measurement fidelity. The antenna consists of an on-chip short-circuited coplanar waveguide structure and allows to apply a microwave driving of angular frequency ω to the sample.

As we show now, our LC-resonator is harmonic and, hence, cannot be populated directly by two-photon driving. Anharmonicities only arise for strong driving, when the maximum induced current density J_max in the LC-resonator approaches the critical current density of the aluminum lines [3], $J_\mathrm{c} \simeq 10^7\,\mathrm{A/cm^2}$. From qubit Rabi oscillation measurements (data not shown), we determine the antenna current $I_\mathrm{a} \lesssim 1\,\mu\mathrm{A}$ resulting in a maximum resonator current $I_\mathrm{max} = M_\mathrm{ar}I_\mathrm{a}/L_\mathrm{r} \simeq 25\,\mathrm{nA}$. Here, $L_\mathrm{r} \simeq 200\,\mathrm{pH}$ is the resonator self-inductance and $M_\mathrm{ar} \simeq 5\,\mathrm{pH}$ the resonator-antenna mutual inductance. Assuming that the supercurrent flows only within the London penetration depth $\lambda_\mathrm{L} = 50\,\mathrm{nm}$, we obtain $J_\mathrm{max} \simeq 2.5 \times 10^2\,\mathrm{A/cm^2}$ for our 100 nm thick film. Since $J_\mathrm{max}/J_\mathrm{c} < 10^{-4}$, anharmonicities can be neglected safely. Indeed, as we will see in Sec. 5.2, we observe a pronounced flux-independent one-photon excitation signal of the resonator in the spectroscopy data of Fig. 5.2(b). On the contrary, two-photon excitation peaks exclusively occur when the qubit is two-photon driven. In other words, the data unambiguously shows that there is no direct two-photon excitation of our resonator.

5.2 Anticrossing under two-photon driving

In order to probe the properties of our system, we perform qubit microwave spectroscopy using the adiabatic-shift pulse technique (cf. Sec. 3.2.4 and Sec. 3.4.3). The main results are shown in Fig. 5.2(a) and Fig. 5.2(b). First, there is a flux-independent feature at approximately 6 GHz due to the resonator. Second, we observe two hyperbolas with minima near $4\,\mathrm{GHz} \simeq \Delta/h$ and $2\,\mathrm{GHz} \simeq \Delta/2h$, one with a broad and the other with a narrow linewidth. They correspond to the one-photon ($\omega = \omega_\mathrm{ge}$) and two-photon ($2\omega = \omega_\mathrm{ge}$) resonance condition between the qubit and the external microwave field. The presence of a large and a small anticrossing in the one- and two-photon branch, respectively, constitutes direct evidence that two-

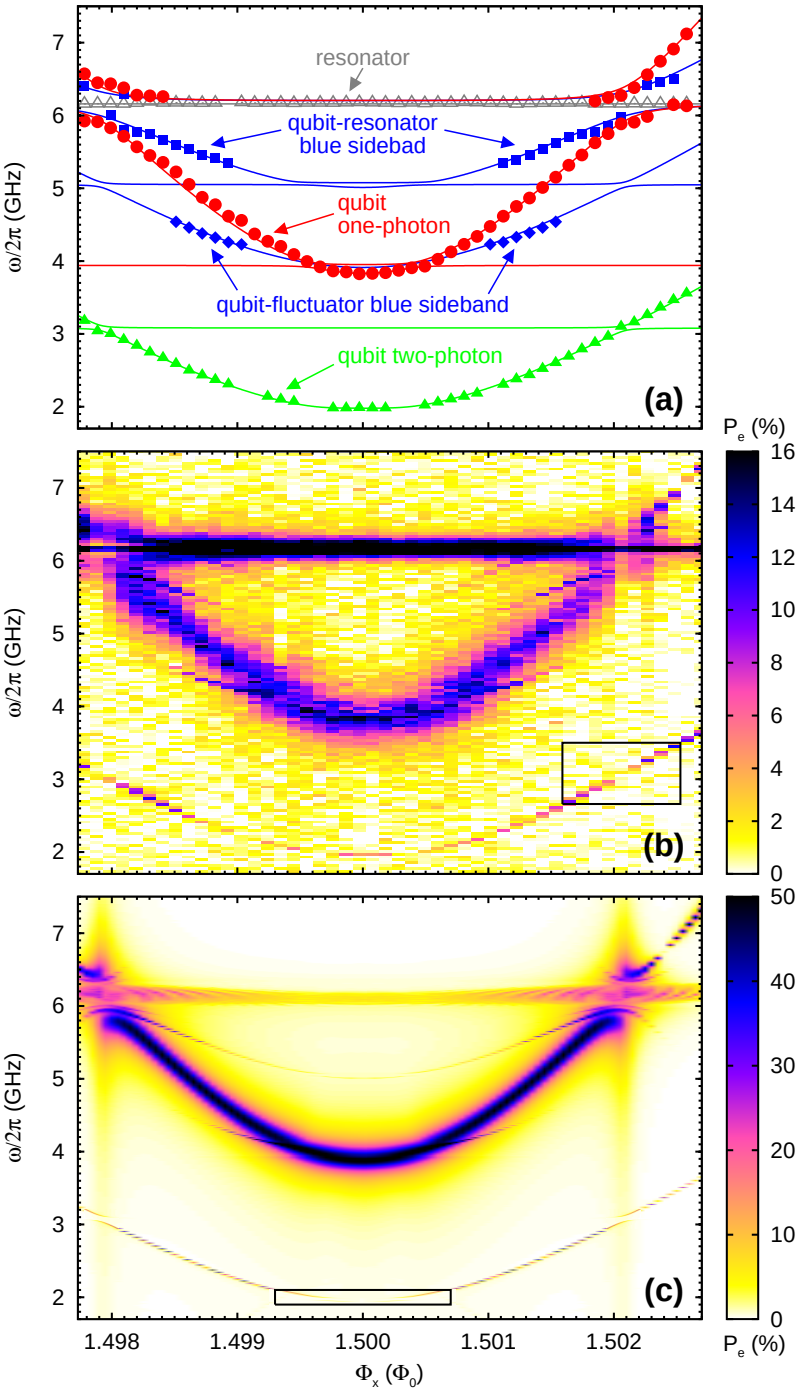

Figure 5.2: Qubit microwave spectroscopy: Data and simulations. **(a)** Center frequencies of the measured absorption peaks (symbols) plotted versus the flux bias. The lines are fits of the energy spectrum of $\hat{H}_{\mathrm{u}}$ of Eq. (5.1) to the data. A large and a small anticrossing is present in the one- ($\omega \approx \omega_{\mathrm{r}}$) and two-photon ($2\omega \approx \omega_{\mathrm{r}}$) branch, respectively. **(b)** Measured probability P_{e} to find the qubit in the excited state plotted versus flux bias and driving frequency. Black box: area shown in Fig. 5.3(a). **(c)** Simulated probability P_{e} obtained with the time-trace-averaging method for $\hat{H}_{\mathrm{d}}$ of Eq. (5.2). The agreement with the experimental data of (b) is excellent. Black box: area shown in Fig. 5.4. Simulation parameters are derived from the fit in (a). The inductance values are based on numerical estimates.

photon spectroscopy selectively drives the qubit, but not the resonator. In other words, the vacuum Rabi coupling g is probed. On the contrary, the one-photon driving populates the cavity resulting in an enhanced coupling $g\langle\hat{N}\rangle^{1/2}$. Additionally, the signatures of two-photon driven blue sideband transitions are partially visible. One can be attributed to the resonator[1], $|g,0\rangle \rightarrow |e,1\rangle$, and the other to a spurious fluctuator[2]. We assume that the latter is represented by the flux-independent Hamil-

[1]In a recent quantum-optical cavity QED experiment it has been shown that the appearance of the two-photon blue sideband peaks proves the quantization of the resonator [149].

[2]In principle, such fluctuators can be either resonators or two-level systems. Since our experimental data does not allow us to distinguish between these two cases, for simplicity, we assume a two-level system in the simulations.

tonian $\hat{H}_\mathrm{f} = \left(\epsilon^\star \hat{\sigma}_z^\star + \Delta^\star \hat{\sigma}_x^\star\right)/2$ and coupled to the qubit via $\hat{H}_\mathrm{q,f} = \hbar g^\star \hat{\sigma}_z \hat{\sigma}_z^\star$, where $\hat{\sigma}_x^\star$ and $\hat{\sigma}_z^\star$ are Pauli operators. Exploiting the different response of the system in the anticrossing region under one- and two-photon driving explained above, the center frequencies of the spectroscopic peaks can be accurately fitted to the Hamiltonian of the undriven system,

$$\hat{H}_\mathrm{u} = \hat{H}_\mathrm{q} + \hat{H}_\mathrm{r} + \hat{H}_\mathrm{f} + \hat{H}_\mathrm{q,r} + \hat{H}_\mathrm{q,f}\,. \tag{5.1}$$

In the numerical fit shown in Fig. 5.2(a), we choose $\epsilon^\star = 0$ due to the limited experimental resolution. Under this condition, we obtain $g/2\pi = 115\,\mathrm{MHz}$, $\langle \hat{N} \rangle \simeq 10$, $I_\mathrm{p} = 367\,\mathrm{nA}$, $\omega_\mathrm{f}/2\pi \equiv \sqrt{\epsilon^{\star 2} + \Delta^{\star 2}}/h = 3.94\,\mathrm{GHz}$ and $g^\star \sin\theta^\star = 37\,\mathrm{MHz}$, where $\sin\theta^\star \equiv \Delta^\star/\hbar\omega_\mathrm{f}$. Obviously, the coupling constant estimated from the fit using $\hat{H}_\mathrm{u}$ is not $g^\star$, but $g^\star \sin\theta^\star$. In this context, it is important to note that, differently from $\sin\theta$ and $\cos\theta$, the fluctuator parameters $\sin\theta^\star$ and $\cos\theta^\star$ are independent of the quasi-static flux bias Φ_x.

Further insight into our experimental results can be gained by numerical spectroscopy simulations based on the Hamiltonian of the driven system,

$$\hat{H}_\mathrm{d} = \hat{H}_\mathrm{u} + \hat{H}_\mathrm{m,q} + \hat{H}_\mathrm{m,r} + \hat{H}_\mathrm{m,f}\,. \tag{5.2}$$

Here, $\hat{H}_\mathrm{m,q} = (\Omega/2)\hat{\sigma}_z \cos\omega t$, $\hat{H}_\mathrm{m,r} = \eta\left(\hat{a}^\dagger + \hat{a}\right)\cos\omega t$ and $\hat{H}_\mathrm{m,f} = (\Omega^\star/2)\hat{\sigma}_z^\star \cos\omega t$ represent the driving of the qubit, resonator and fluctuator respectively. We approximate the steady state with the time average of the probability P_e to find the qubit in $|\mathrm{e}\rangle$. This so-called time-trace-averaging method is explained in detail in appendix D.1. For simplicity, we choose $\sin\theta^\star = 1$, i.e., a pure $\hat{\sigma}_x^\star$-coupling. Inspecting Fig. 5.2(c), we find that for the driving strengths $\Omega/h = 244\,\mathrm{MHz}$, $\eta/h = 655\,\mathrm{MHz}$ and $\Omega^\star = 0$ our simulations match well all the experimental features discussed above. Using η and the relation $\langle \hat{N} \rangle = (\eta/\kappa)^2$ for the steady-state mean number of photons of a driven dissipative cavity [150], we estimate a cavity decay rate $\kappa \simeq 210\,\mathrm{MHz}$. This result is of the same order as $\kappa \simeq 400\,\mathrm{MHz}$ estimated directly from the experimental linewidth of the resonator peak. The large κ is due to the galvanic connection of the resonator to the DC SQUID measurement lines [see Fig. 5.1(a)].

To elucidate the two-photon driving physics of the qubit-resonator system we consider the spectroscopy data near the corresponding anticrossing shown in Fig. 5.3(a). For $2\omega = \omega_\mathrm{ge} = \omega_\mathrm{r}$, the split peaks cannot be observed directly because the spectroscopy signal is decreased below the noise floor $\delta P_\mathrm{e} \simeq 1 - 2\%$. This results from the fact that the resonator cannot absorb a two-photon driving and its excitation energy is rapidly lost to the environment ($\kappa > g/2\pi$). In contrast, for the one-photon case ($\omega = \omega_\mathrm{ge} = \omega_\mathrm{r}$), there is a driving-induced steady-state population of $\langle \hat{N} \rangle \simeq 10$ photons in the cavity. Accordingly, the one-photon peak height shows a reduction by a factor of approximately two, whereas the two-photon peak almost vanishes as shown in Fig. 5.3(b). To support this interpretation, we compare the simulation results from the time-trace-averaging method [Fig. 5.3(c) and Fig. 5.3(d)], which does not directly include dissipation, to those obtained with the standard Lindblad dissipative-bath approach [Fig. 5.3(e) and Fig. 5.3(f)]. In the latter case, the role of qubit decoherence and resonator decay can be studied explicitly solving a master equation (cf. appendix D.2). In the small flux window shown in Fig. 5.3(e) we are allowed to assume the qubit relaxation rate $\gamma_1 = 3.3\,\mathrm{MHz}$ and the qubit dephasing rate $\gamma_\varphi = 67\,\mathrm{MHz}$ to be constant. The resonator quality

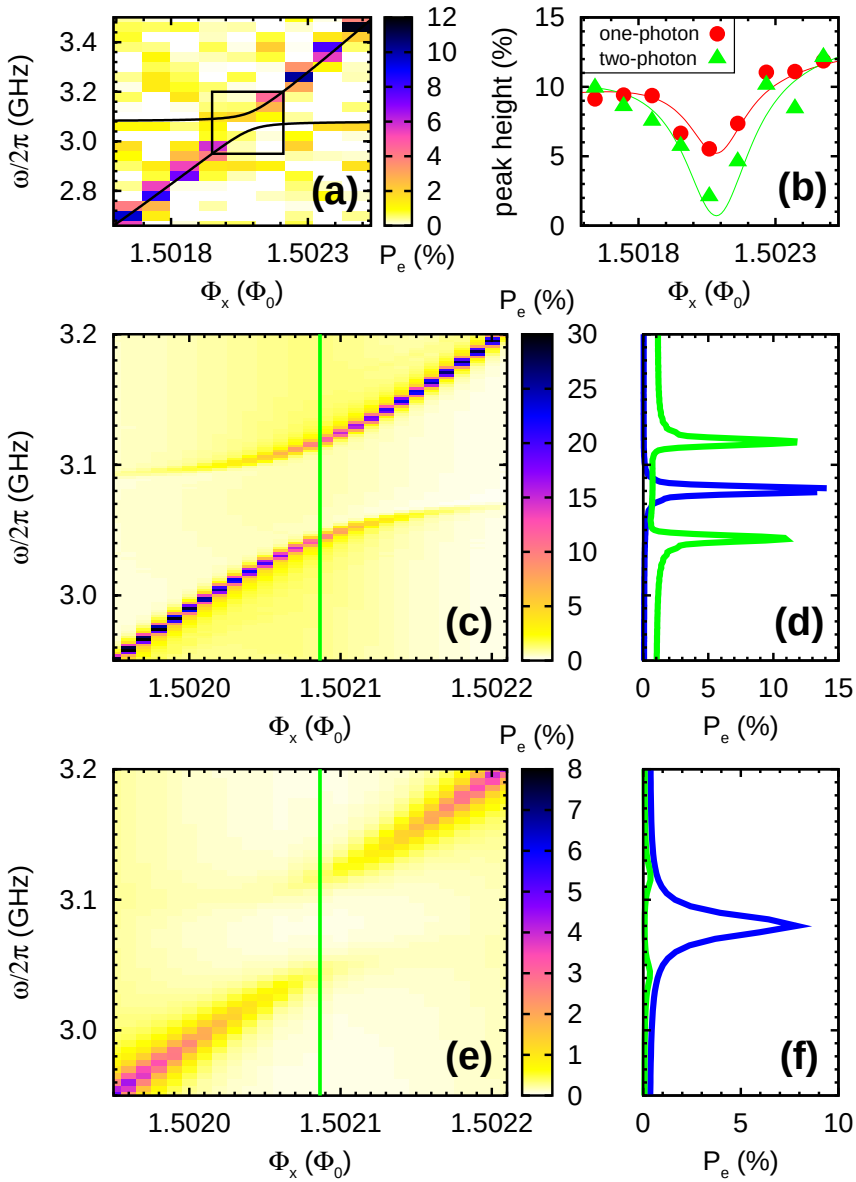

Figure 5.3: Qubit-resonator anticrossing under two-photon driving. **(a)** Measured probability P_e plotted versus flux bias and driving frequency. Black rectangle: area of simulations in (c) and (e). Solid lines: fit to $\hat{H}_\mathrm{u}$ of Eq. (5.1). **(b)**, Maximum height of the spectroscopy peaks under one- and two-photon driving plotted versus the flux bias. Solid lines: guides to the eye. **(c)** Simulated probability P_e revealing an anticrossing signature. Method: time-trace-averaging. Parameters as in Fig. 5.2(c). **(d)** Green curve: split-peak profile of P_e along the vertical line in (c). Blue curve: single-peak result obtained for the same flux bias and $g = 0$. (e) Simulated probability P_e (Lindblad formalism, fluctuator neglected). On qubit-resonator degeneracy, the signal fades away. **(f)** Green curve: split-peak profile of P_e along the vertical line in (e). Blue line: single-peak result obtained for the same flux bias and $g = 0$. The split-peak amplitudes are reduced by a factor of 10 compared to the single peak.

factor is $Q \equiv \omega_\mathrm{r}/\kappa = 2\pi \times 6.16\,\mathrm{GHz}/400\,\mathrm{MHz} \simeq 100$. The simulation results of Fig. 5.3(c) and Fig. 5.3(e) show that the experimentally observed vanishing of the two-photon peak at the anticrossing is indeed caused by decoherence. More specif-

ically, a comparison of Fig. 5.3(d) and Fig. 5.3(f) proves that this effect is due to the rapid resonator decay and not due to qubit decoherence. Altogether, our experimental data and numerical simulations constitute clear evidence for the presence of a qubit-resonator anticrossing under two-photon driving.

5.3 Upconversion dynamics

Using a Dyson-series approach, we now derive the effective second-order Hamiltonian describing the physics relevant for the analysis of the two-photon driven system. We start from the first-order Hamiltonian in the basis $|\pm\rangle$,

$$\hat{H} = \frac{\epsilon}{2}\hat{\sigma}_z + \frac{\Delta}{2}\hat{\sigma}_x + \hbar\omega_\mathrm{r}\left(\hat{a}^\dagger\hat{a} + \frac{1}{2}\right) + \hbar g\,\hat{\sigma}_z\big(\hat{a}^\dagger + \hat{a}\big) + \frac{\Omega}{2}\hat{\sigma}_z\cos\omega t\,. \tag{5.3}$$

Here, in comparison to $\hat{H}_\mathrm{d}$, the terms associated with the fluctuator are not included ($\epsilon^\star = \Delta^\star = \Omega^\star = 0$) because the important features are contained in the driven qubit-resonator system. Additionally, we focus on the two-photon resonance condition $\omega_\mathrm{r} = \omega_\mathrm{ge} = 2\omega$. Thus, the driving angular frequency ω is largely detuned from ω_r and the corresponding term in $\hat{H}_\mathrm{d}$ can be neglected ($\eta = 0$). Next, we transform the qubit into its energy eigenframe and move to the interaction picture with respect to qubit and resonator, $\hat{\sigma}_\pm \to \hat{\sigma}_\pm \mathrm{e}^{\pm i\omega_\mathrm{ge}t}$, $\hat{a} \to \hat{a}\mathrm{e}^{-i\omega_\mathrm{r}t}$ and $\hat{a}^\dagger \to \hat{a}^\dagger\mathrm{e}^{+i\omega_\mathrm{r}t}$. Here, $\hat{\sigma}_+$ and $\hat{\sigma}_-$ are the qubit raising and lowering operators, respectively. After a rotating wave approximation, we identify the expression $\hat{S}^\dagger\mathrm{e}^{+i\omega t} + \hat{S}\mathrm{e}^{-i\omega t}$, where the superoperator $\hat{S} \equiv (\Omega/4)\left(\cos\theta\,\hat{\sigma}_z - \sin\theta\,\hat{\sigma}_-\right)$ and its Hermitian conjugate $\hat{S}^\dagger \equiv (\Omega/4)\left(\cos\theta\,\hat{\sigma}_z - \sin\theta\,\hat{\sigma}_+\right)$. In our experiments the two-photon driving of the qubit is weak, i.e., the large-detuning condition $\omega_\mathrm{ge} - \omega = \omega \gg (\Omega\sin\theta)/2\hbar$ is fulfilled. In such a situation, it can be shown that the Dyson series for the evolution operator associated with the time-dependent Hamiltonian $-\hbar g\sin\theta(\hat{\sigma}_+\hat{a} + \hat{\sigma}_-\hat{a}^\dagger) + (\hat{S}\mathrm{e}^{-i\omega t} + \hat{S}^\dagger\mathrm{e}^{+i\omega t})$ can be rewritten in an exponential form $\hat{U} = \mathrm{e}^{-i\hat{H}_\mathrm{eff}t/\hbar}$, where

$$\begin{aligned}\hat{H}_\mathrm{eff} =& -\hbar g\sin\theta\left(\hat{\sigma}_+\hat{a}\mathrm{e}^{+i\delta t} + \hat{\sigma}_-\hat{a}^\dagger\mathrm{e}^{-i\delta t}\right) + \frac{\left[\hat{S}^\dagger,\hat{S}\right]}{\hbar\omega} \\ =& -\hbar g\sin\theta\left(\hat{\sigma}_+\hat{a}\mathrm{e}^{+i\delta t} + \hat{\sigma}_-\hat{a}^\dagger\mathrm{e}^{-i\delta t}\right) + \frac{\Omega^2}{4\Delta}\left(\sin^2\theta\cos\theta\,\hat{\sigma}_x + \frac{1}{2}\sin^3\theta\,\hat{\sigma}_z\right).\end{aligned} \tag{5.4}$$

The details of this calculation can be found in appendix C.1. In the above equation, $\delta \equiv \omega_\mathrm{ge} - \omega_\mathrm{r}$ denotes the qubit-resonator detuning. The dispersive shift $(\Omega^2/8\Delta)\sin^3\theta\,\hat{\sigma}_z$ is a reminiscence of the full second-order $\hat{\sigma}_z$-component of the interaction Hamiltonian[3], $(\Omega^2/8\Delta)\sin^3\theta\,\hat{\sigma}_z\,(\mathrm{e}^{+i2\omega t} + \mathrm{e}^{-i2\omega t} + 1)$. The terms proportional to $\hat{\sigma}_z\exp^{\pm i2\omega t}$ are neglected implicitly by a rotating wave approximation when deriving the effective Hamiltonian $\hat{H}_\mathrm{eff}$ of Eq. (5.4). In this equation, the $\hat{\sigma}_z$-term renormalizes the qubit transition frequency, and, in the vicinity of the anticrossing ($|\delta| \lesssim g\sin\tilde{\theta}$, $\sin\tilde{\theta} = \Delta/\omega_\mathrm{r} \simeq 0.63$), the Hamiltonian $\hat{H}_\mathrm{eff}$ can be considered

[3]We note that the expression $(\Omega^2\sin^3\theta/16\Delta)(\mathrm{e}^{+i\omega t} + \mathrm{e}^{-i\omega t})^2$ given in Ref. [59] is marginally different from the correct expression $(\Omega^2\sin^3\theta/8\Delta)(\mathrm{e}^{+i2\omega t} + \mathrm{e}^{-i2\omega t} + 1)$ derived in appendix C.2. The difference only affects terms which are neglected by a rotating-wave approximation anyways. Hence, all relevant conclusions remain the same as in Ref. [59].

equivalent to

$$\hat{H}^{(2)} = \frac{\hbar\omega_{\mathrm{ge}}}{2}\hat{\sigma}_z + \frac{\Omega^2}{4\Delta}\sin^2\theta\cos\theta\left(\hat{\sigma}_+ \mathrm{e}^{-i2\omega t} + \hat{\sigma}_- \mathrm{e}^{+i2\omega t}\right) - \hbar g \sin\theta\left(\hat{\sigma}_+\hat{a} + \hat{\sigma}_-\hat{a}^\dagger\right) + \hbar\omega_{\mathrm{r}}\left(\hat{a}^\dagger\hat{a} + \frac{1}{2}\right) . \tag{5.5}$$

Here, $\sin\theta \equiv \Delta/\hbar\omega_{\mathrm{ge}}$ and $\cos\theta \equiv \epsilon/\hbar\omega_{\mathrm{ge}}$. The upconversion dynamics sketched in Fig. 5.1(d) is clearly described by Eq. (5.5). The first two terms represent the qubit and its coherent two-photon driving with angular frequency ω. The last two terms show the population transfer via the Jaynes-Cummings interaction to the resonator. We find it noteworthy to mention that it is only the Jaynes-Cummings term in Eq. (5.5), whose validity is restricted to the anticrossing region. Finally, as discussed in detail in Sec. 5.2, the resonator will decay emitting radiation of angular frequency 2ω.

5.4 Selection rules and symmetry breaking

The model outlined in Sec. 5.3 allows us to unveil the symmetry properties of our system. Even though the two-photon coherent driving fulfills the large-detuning condition, $\omega_{\mathrm{ge}} - \omega = \omega \gg (\Omega\sin\theta)/2\hbar$, a not well-defined symmetry of the qubit potential permits level transitions away from the optimal point. Because of energy conservation, i.e., frequency matching, these transitions are real and can be used to probe the qubit-resonator anticrossing. The effective two-photon qubit driving strength, $\left(\Omega^2\sin^2\theta/4\Delta\right)\cos\theta$, has the typical structure of a second-order dispersive interaction with the extra factor $\cos\theta$. The latter causes this coupling to disappear at the optimal point. There, the qubit potential is symmetric and the parity of the interaction operator is well defined. Consequently, selection rules similar to those governing electric dipole transitions hold [148]. This is easiest understood in our analytical two-level model, where the first-order Hamiltonian for the driven diagonalized qubit becomes

$$\hat{H}^{(1)}_{\mathrm{OP}} = \frac{\Delta}{2}\hat{\sigma}_z + \frac{\Omega}{4}\hat{\sigma}_x\left(\mathrm{e}^{+i\omega t} + \mathrm{e}^{-i\omega t}\right) \tag{5.6}$$

at the optimal point. In this case, one-photon transitions are allowed because the driving couples to the qubit via the odd-parity operator $\hat{\sigma}_x$. On the contrary, the two-photon driving effectively couples via the second-order Hamiltonian

$$\hat{H}^{(2)}_{\mathrm{OP}} = \frac{\Delta}{2}\hat{\sigma}_z + \frac{\Omega^2}{8\Delta}\hat{\sigma}_z\left(\mathrm{e}^{+i2\omega t} + \mathrm{e}^{-i2\omega t} + 1\right) . \tag{5.7}$$

Since $\hat{\sigma}_z$ is an even-parity operator, real level transitions are forbidden. We note that the second $\hat{\sigma}_z$-term of $\hat{H}^{(2)}_{\mathrm{OP}}$ renormalizes the qubit transition frequency slightly and can be neglected in Eq. (5.5), which describes the real level transitions corresponding to our spectroscopy peaks.

Deeper inside into the selection rules and the symmetry breaking mechanism of our system is gained by means of the following considerations. The potential of the three-Josephson-junction flux qubit can be reduced to a one-dimensional double

well with respect to γ_-, the phase variable[4]. At the optimal point ($\Phi_\mathrm{x} = 1.5\Phi_0$), this potential is a symmetric function of γ_-. For our experimental parameters, the shape of the qubit potential is such that we can assume an effective two-level system. Then, the two lowest energy eigenstates $|\mathrm{g}\rangle$ and $|\mathrm{e}\rangle$ are, respectively, symmetric and antisymmetric superpositions[5] of $|+\rangle$ and $|-\rangle$. Thus, $|\mathrm{g}\rangle$ has even parity and $|\mathrm{e}\rangle$ is odd. In this situation, the parity operator $\hat{\Pi}$ can be defined via the relations

$$\begin{array}{l} \hat{\Pi}\,|\mathrm{g}\rangle = +\,|\mathrm{g}\rangle \\ \hat{\Pi}\,|\mathrm{e}\rangle = -\,|\mathrm{e}\rangle \end{array}. \tag{5.8}$$

The Hamiltonian of the classically driven qubit at the optimal point is $(\Delta/2)\hat{\sigma}_z - (\Omega/2)\cos\omega t\,\hat{\sigma}_x$. For a one-photon driving, $\omega = \Delta/\hbar$ (energy conservation), the Hamiltonian in the interaction picture is $-(\Omega/4)\hat{\sigma}_x$, where $\hat{\sigma}_x \equiv |\mathrm{g}\rangle\langle\mathrm{e}| + |\mathrm{e}\rangle\langle\mathrm{g}|$. This is an odd-parity operator because the anticommutator $\{\hat{\Pi}, \hat{\sigma}_x\} = 0$. Consequently, one-photon transitions are allowed. Under two-photon driving, $\omega = \Delta/2\hbar$ (energy conservation), the effective interaction Hamiltonian becomes $(\Omega^2/8\Delta)\hat{\sigma}_z$, where $\hat{\sigma}_z \equiv |\mathrm{e}\rangle\langle\mathrm{e}| - |\mathrm{g}\rangle\langle\mathrm{g}|$. Since the commutator $[\hat{\Pi}, \hat{\sigma}_z] = 0$, this is an even-parity operator and two-photon transitions are forbidden [6]. These selection rules are analogous to those governing electric dipole transitions in quantum optics. There, the interaction between natural atoms and photons is mediated by the dipole operator, which is an odd-parity operator. For a natural two-level atom, the first- and second order dipole interaction are of $\hat{\sigma}_x$- and $\hat{\sigma}_z$-type, respectively [151]. In circuit QED, however, the qubit can be biased away from its optimal point. In this case, the symmetry is broken in a controlled way and the discussed selection rules do not hold. Instead, we find the finite transition matrix elements $(\Omega/4)\sin\theta$ and $(\Omega^2/4\Delta)\sin^2\theta\cos\theta$ for the one- and two-photon process, respectively. Beyond the two-level approximation, the selection rules for a flux qubit at the optimal point are best understood by the observation that the double-well potential is symmetric there as shown in Fig. 2.5(b), Fig. 2.6, and Fig. 5.1(d). Hence, the interaction operator of the one-photon driving is odd with respect to the phase variable γ_- of the qubit potential [27, 148], whereas the one of the two-photon driving is even. Away from the optimal point ($\Phi_\mathrm{x} \neq 1.5\Phi_0$), the qubit potential has no well-defined symmetry and no selection rules apply.

The intimate nature of the symmetry breaking resides in the coexistence of $\hat{\sigma}_x$- and $\hat{\sigma}_z$-operators in the first-order Hamiltonian $\hat{H}_\mathrm{d}$ of Eq. (5.2), which produces a nonvanishing $\hat{\sigma}_x$-term in the second-order Hamiltonian $\hat{H}^{(2)}$ of Eq. (5.5). As illustrated by the simulation results shown in Fig. 5.4, this scenario can also be realized at the qubit optimal point when considering the $\hat{\sigma}_x^\star$- and $\hat{\sigma}_z^\star$-terms of the fluctuator. Their presence breaks the symmetry of the total system at the optimal point and, again, parity becomes not well defined. Consequently, the discussed strict selection rules no longer apply and the spectroscopy signal is partially revived. Accordingly, we observe only a reduction instead of a complete suppression of the two-photon peaks near the qubit optimal point in the experimental data of Fig. 5.2(b). In reality, an ensemble of fluctuators with some distribution of frequencies and coupling

[4]The corresponding operator is called $\hat{\varphi}_\mathrm{m}$ in Ref. [27] and Ref. [148].

[5]Strictly speaking, from the definition of our qubit Hamiltonian in Eq. (2.16) one finds $|\mathrm{g}\rangle$ to be antisymmetric and $|\mathrm{e}\rangle$ to be symmetric [6]. However, the conclusions drawn in this chapter and in Ref. [59] only require $|\mathrm{g}\rangle$ and $|\mathrm{e}\rangle$ to have opposite parity and, hence, remain completely valid. The more physical situation of a symmetric $|\mathrm{g}\rangle$ and an antisymmetric $|\mathrm{e}\rangle$ can be obtained by changing Δ to $-\Delta$ in Eq. (2.16). We note that this change would not alter the simulation results presented in chapter 4 and in this chapter.

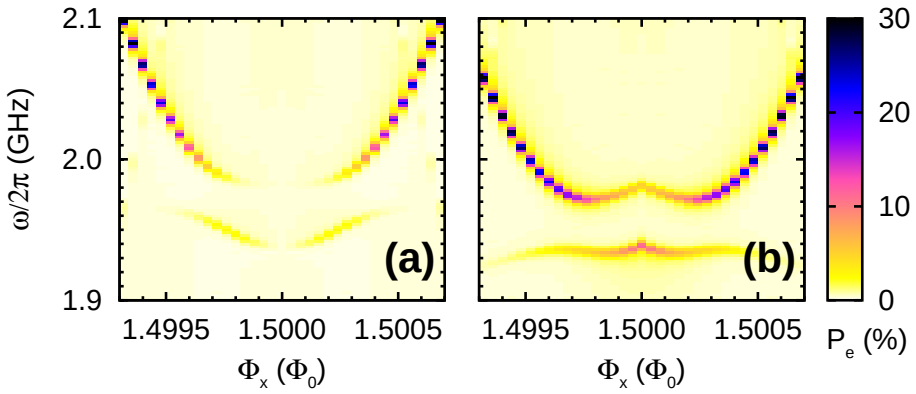

Figure 5.4: Two-photon spectroscopy simulations close to the optimal point using the time-trace-averaging method. **(a)** Probability P_e to find the qubit in $|\mathrm{e}\rangle$ plotted versus driving frequency and flux bias (parameters as in Fig. 5.2(c); in particular, the fluctuator parameters are $\epsilon^\star = 0 \leftrightarrow \sin\theta^\star = 1$ and $\Omega^\star = 0$). The spectroscopy signal vanishes completely at the optimal point, $\Phi_\mathrm{x} = 1.5\Phi_0$, because of the specific selection rules associated with the symmetry properties of the Hamiltonian [148]. **(b)** Same as in (a), however, for $\sin\theta^\star = 0.3$ and $\Omega^\star = 280\,\mathrm{MHz}$. Here, the coexistence of the flux-independent first-order $\hat{\sigma}_x^\star$- and $\hat{\sigma}_z^\star$-terms of the fluctuator gives rise to a nonvanishing second-order $\hat{\sigma}_x^\star$-term even at the qubit optimal point. The presence of the fluctuator breaks the symmetry of the total system at the optimal point and the spectroscopy signal is partially revived. When the experimental resolution is limited, as it is the case in our measurements, a single peak will be detected instead of the splitting structure.

strengths rather than a single fluctuator is expected to contribute to the symmetry breaking.

5.5 Conclusions

In conclusion, we use two-photon qubit spectroscopy to study the interaction of a superconducting flux qubit with an LC-resonator. We show experimental evidence for the presence of an anticrossing under two-photon driving, permitting us to estimate the vacuum Rabi coupling. Our experiments and theoretical analysis shed new light on the fundamental symmetry properties of quantum circuits and the nonlinear dynamics inherent to circuit QED. In particular, we show that the symmetries of the system can be broken in a controlled way by varying the external flux bias. This can be exploited in a wide range of applications such as parametric up-conversion, generation of microwave single photons on demand [74, 100, 103] or squeezing [101].

Chapter 6

Summary

In this thesis, we design and build a three-Josephson-junction flux qubit, which is carefully characterized in terms of its quantum coherence and then used in circuit QED experiments demonstrating controlled symmetry breaking. The scientific results can be summarized in three major points.

In a first step, we determine one important property of the nanoscale $\mathrm{Al/AlO}_x\mathrm{/Al}$ Josephson junctions used in our flux qubits, the junction capacitance. Employing a DC measurement method based on voltage steps in the current-voltage characteristics of DC SQUIDs, we find a capacitance per unit area $C_\mathrm{s} = 100 \pm 25\,\mathrm{fF}/\mu\mathrm{m}^2$.

Second, we use this result to design a three-Josephson-junction flux qubit and verify its quantum coherence properties. In these experiments, the qubit state is measured with the capacitive-bias readout, which is a novel variant of the switching-DC-SQUID detection scheme. We compare the capacitive-bias results to those obtained with a conventional resistive bias and, hence, experimentally test the impact of two different electromagnetic environments on the qubit coherence. We show that our qubit is relaxation-limited at the optimal point with a relaxation time of approximately 100 ns and a pure dephasing time of approximately 2 µs. We calculate the noise spectral density due to fluctuations of the bias current of the readout DC SQUID. As it turns out, its value is much smaller than $S_\Phi^{\Gamma_1}(\Delta/\hbar) = \left[(1.4 \pm 0.1) \times 10^{-10}\Phi_0\right]^2\,\mathrm{Hz}^{-1}$ of the dominating source of high-frequency noise responsible for the qubit energy relaxation. Instead, there are indications that noise input via the microwave antenna plays an important role. Also, a possible influence of fluctuators in the tunnel barrier could not be excluded. The low-frequency noise is also not dominated by DC SQUID bias current fluctuations. However, beatings in the Ramsey and spin echo traces suggest the presence of spurious fluctuators in or close to the tunnel barriers, which can produce $1/f$-noise. Indeed, we find evidence for $1/f$-noise. Its magnitude $\mathcal{A} = \left[(4.3 \pm 0.7) \times 10^{-6}\Phi_0\right]^2$ is very similar to that found in many other Josephson-junction-based experiments. Interestingly, we still recover a white noise contribution $S_\Phi^\mathrm{BR}(\omega \to 0) \approx S_\Phi^{\Gamma_1}(\Delta/\hbar)$ independently from, but in agreement with our high-frequency result.

Finally, we notice that the observed coherence times of our qubit are sufficient to investigate its interplay with other quantum circuits, following the lines of circuit QED. We spectroscopically probe the interaction of our qubit with an inductively coupled quantized LC-resonator. Under two-photon driving, the resonator is not significantly populated and we observe an anticrossing, which reflects the vacuum Rabi coupling. Additionally, at the qubit optimal point, the qubit potential is sym-

metric and parity is a well-defined property. Consequently, selection rules analogous to those for electric dipole transitions in natural atoms hold. In this situation, analytical calculations and numerical simulation confirm that the qubit cannot be excited with a two-photon driving. However, away from the optimal point, the symmetries are broken and the qubit-resonator system can be probed spectroscopically with two-photon driving, stimulating an upconversion dynamics with real level transitions. We further find that the spurious fluctuators mentioned above can, under opportune circumstances, cause symmetry breaking even at the qubit optimal point.

Chapter 7

Outlook: Two-resonator circuit QED

To this day, the central elements in most experiments with superconducting solid-state quantum circuits are devices containing one or several Josephson junctions of the superconductor-insulator-superconductor type[1]. The latter constitutes a nonlinearity on the quantum level. In this way, as detailed for the example of the three-Josephson-junction flux qubit in Sec. 2.5, one can design quantum circuits where the lowest energy levels (operational levels) are well separated from the higher ones (spurious levels). Restricting the number of operational levels to two, Josephson qubits acting as artificial two-level atoms can be built. However, due to the influence of the solid-state environment (qubit control and readout circuitry, fluctuators in the insulator etc.; cf. chapter 4 for details), the typical coherence times of these qubits currently range between 100 ns and a few microseconds [23, 44, 46].

In contrast to their nonlinear counterparts, circuits forming linear LC-resonators (harmonic oscillators) have so far been considered mostly as auxiliary elements extending standard Josephson qubit setups. In chapter 5 we give an example how the coupling of an LC-resonator to a superconducting flux qubit allows one to probe fundamental symmetry properties of the joint system [59]. Furthermore, the application of a resonator as a qubit readout device [65], a quantum bus between two transmon or phase qubits [52, 53], and a quantum memory [53] has recently been accomplished. The particular attractiveness of resonator circuits resides mainly in the fact that they can easily be designed to exhibit coherence times which are significantly longer than those presently achieved for Josephson qubits [153]. Hence, we propose to exchange the roles of Josephson qubits and resonators, making the former the auxiliary and the latter the central elements. We explore this new field of two-resonator circuit QED, where one qubit mediates a controllable interaction between two resonators, in detail in Ref. [102]. Apart from the obviously exciting physics of coupling two microwave photons, possibly strongly, in a controlled way, one can also think of creating entanglement between a macroscopic and a microscopic degree of freedom (Schrödinger cat states) in such a setup [102]. Furthermore, applications in quantum information processing can be imagined. In particular, despite being of a bosonic nature, a photon inside a resonator can form a so-called flying qubit [154]. Essentially, the two states are encoded in the information "photon present" or "pho-

[1] A notable exception are the so-called phase-slip qubits [152], which contain nanowires instead of superconductor-insulator-superconductor Josephson junctions.

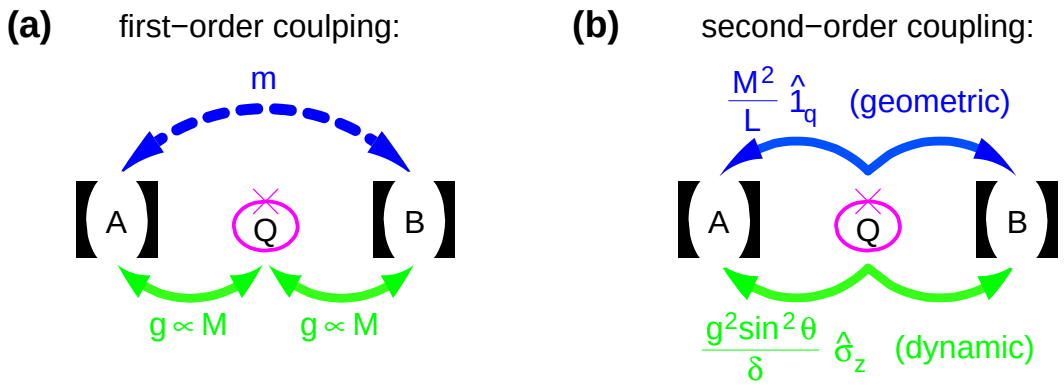

Figure 7.1: Two-resonator circuit QED: symbolic sketch of the quantum switch setup. The resonators A and B are symbolized by the black mirror pairs, the qubit Q by the magenta ellipse. Blue and green arrows denote geometric and dynamic coupling channels, respectively. **(a)** First-order coupling channels. The geometric first-order coupling coefficient $g_{\mathrm{AB}}^{(1)}$ between the resonators is proportional to their first-order mutual inductance m. The first-order dynamic coupling strength between qubit and resonators is characterized by the vacuum-Rabi coupling coefficient g, which is proportional to the corresponding mutual inductance M. **(b)** Second-order coupling channels. L is the qubit self-inductance and $\hat{1}_{\mathrm{q}}$ the unity operator in the qubit subspace. The geometric second-order coupling coefficient is $g_{\mathrm{AB}}^{(2)} \propto M^2/L$. The total geometric coupling coefficient $g_{\mathrm{AB}} \equiv g_{\mathrm{AB}}^{(1)} + g_{\mathrm{AB}}^{(2)}$ has a first- and a second-order contribution. In contrast, the dynamic coupling is always of second order in the dispersive regime.

ton absent" in the resonator [155]. Consequently, two-resonator circuit QED allows for the generation of tripartite entangled states of the Greenberger-Horne-Zeilinger class [156].

As a particular example, we briefly outline the concept of a superconducting flux qubit functioning as a quantum switch between two distributed-element on-chip resonators (more details can be found in Ref. [102]). For simplicity, the resonators are assumed to have the same frequencies $\omega_{\mathrm{r}}/2\pi$ and the same first-order coupling coefficients g to the qubit. The qubit is positioned at a current antinode of both resonators. Furthermore, the inductive qubit-resonator coupling is assumed to be strong (cf. Sec. 2.8) and the qubit is operated in the dispersive regime, $|g| \ll |\delta|$, where $\delta \equiv \omega_{\mathrm{ge}} - \omega_{\mathrm{r}}$ is the qubit-resonator detuning and $\hbar\omega_{\mathrm{ge}}$ the (controllable) qubit level splitting. In the following discussion, we focus on the two main coupling channels between the two resonators. The first one is the *geometric coupling*, which reflects the simple fact that the resonator and qubit circuits are pieces of metal interacting by way of a mutual inductance. We choose the term "geometric" because this coupling channel will still persist when the qubit is replaced by a simple metal loop without any Josephson junctions. Although the first-order geometric coupling between the resonators can, in principle, be engineered to be small, the second-order geometric coupling via the qubit loop cannot be reduced arbitrarily because we require a strong qubit-resonator coupling. The second channel is the *dynamic coupling*, which makes use of the fact that the resonator-resonator interaction is mediated not by a plain loop, but by the nonlinear qubit circuit. Hence, this coupling is necessarily of second order. Similar to the ac Stark/Zeeman shift of Eq. (2.28), this coupling is qubit state-dependent in the dispersive regime. All relevant first-

and second order coupling channels are summarized in Fig. 7.1(a) and Fig. 7.1(b), respectively.

The effective dynamics of the coupled two-resonator-qubit system in the dispersive regime is described by the interaction Hamiltonian [102]

$$\hat{H}_{\text{eff}} = \hbar \left(\frac{g^2 \sin^2 \theta}{\delta} \hat{\sigma}_z + g_{\text{AB}} \right) \left(\hat{a}^\dagger \hat{b} + \hat{a} \hat{b}^\dagger \right) . \tag{7.1}$$

Here, $\hat{\sigma}_z$ is a Pauli operator and $\hat{a}^\dagger$, $\hat{a}$, $\hat{b}^\dagger$, and $\hat{b}$ are the creation and annihilation operators of resonators A and B, respectively. θ is the Bloch angle defined in Sec. 2.6, and g_{AB} is the sum of geometric first- and second-order coupling between the resonators. Inspecting Eq. (7.1), we note that the operator $\left(\hat{a}^\dagger \hat{b} + \hat{a} \hat{b}^\dagger \right)$ describes the exchange of a real photon between the resonators. The prefactor constitutes an effective coupling coefficient, which can be controlled in two ways. The magnitude and sign of the term $(g^2 \sin^2 \theta / \delta) \hat{\sigma}_z$ depend on the external flux bias and on the qubit state, respectively. As a consequence, when the switch setting condition

$$|g_{\text{AB}}| = \frac{g^2 \sin^2 \theta}{|\delta|} \tag{7.2}$$

is fulfilled and the qubit is in an appropriate state ($|\text{g}\rangle$ or $|\text{e}\rangle$, depending on the sign of δ), the geometric and dynamic couplings are *balanced* and the interaction between the resonators is switched off. It can be switched on by changing either the qubit state or the flux bias. In the latter case, the sensitivity of the switch to relaxation and dephasing is strongly reduced when δ is chosen such that the qubit satisfies Eq. (7.2) in the ground state.

The most obvious application of the quantum switch is a controllable coupling between the two resonators. When the geometric first-order coupling coefficient is small, the second-order coupling can be studied. As explained above, tripartite entanglement and Schrödinger cat states can be generated. For some of these experiments, few additional elements like local flux control lines or ancilla qubits are needed. Finally, we want to point out that for the typical coherence times of today's flux qubits already many of the above exciting experiments can be realized. More details about the results presented in this chapter are published in Ref. [102].

Appendix A

Sample fabrication

In this chapter, we give brief description of the fabrication process of the samples used in this work. All samples are made on a SiO_2-passivated Si substrate. All samples were fabricated at the NTT Basic Research Laboratories[1].

A.1 Josephson junctions

The Josephson junctions are fabricated using electron-beam lithography (EBL) and a two-angle shadow evaporation technique [157]. The details of this process are comprised of the following steps:

1. The sample chip is spin coated with 3200 Å of Polymethylglutarimide (PMGI) and baked for 3 min at 180 °C.
2. On top of the PMGI, 870 Å of Zeon's Electron beam Positive resist (ZEP), dissolved in ortho-dichlorobenzene (o-DCB), is spun (ZEP : o-DCB = 1 : 1), followed by another baking step (again for 3 min at 180 °C)
3. Next, a bridge structure is patterned with EBL.
4. The ZEP layer is developed in butyl acetate for 90 s at 20 °C and in isopropanol for 30 s.
5. The PMGI layer is developed in a SAL101/ethanol (10:1) mixture for 90 s and in deionized water for 60 s.
6. Evaporation of 400 Å of aluminum under an angle of +17 ° at a rate of 10 Å/s.
7. Oxidation with 10 mTorr of oxygen/argon mixture (1 % of oxygen) for 20 min. The gas flow is 5.3 standard cubic centimeters per minute (sccm).
8. Evaporation of 500 Å of aluminum under an angle of −17 ° at a rate of 10 Å/s.
9. Finally, the lift-off is performed using PMGI remover at 60 °C for 90 min.

After this process, an $Al/AlO_x/Al$ Josephson junction with the lateral dimensions of the bridge and a oxide layer of a few angstroms thickness has formed. The numerical values of the junction fabrication parameters are those which have been

[1]NTT Basic Research Laboratories, NTT Corp., Kanagawa, 243-0198, Japan

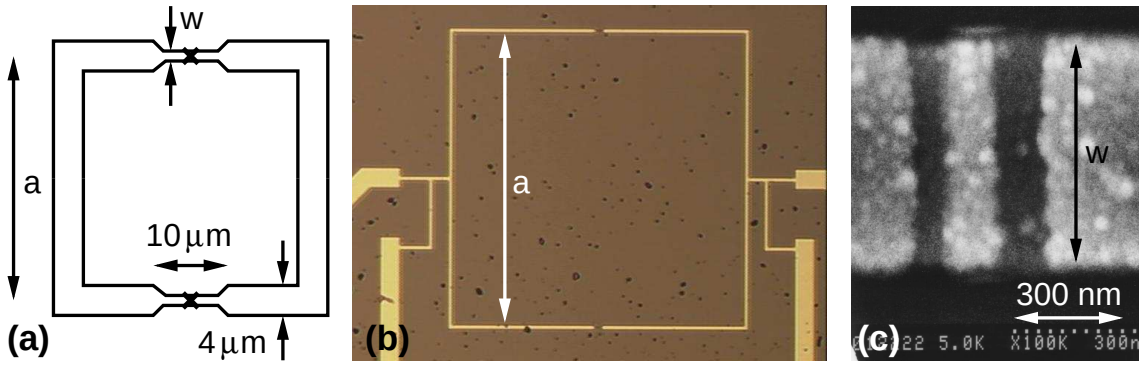

Figure A.1: DC SQUIDs used for the junction capacitance measurements. **(a)** Schematic layout. **(b)** Optical micrograph of the DC SQUID loop. The two Josephson junctions are located in the gaps in the middle of the horizontal loop sides. **(c)** SEM micrograph of a typical Josephson junction fabricated with the shadow evaporation technique described in Sec. A.1. The bright island in the center of the image is interpreted as the junction area.

used to fabricate the sample discussed in chapter 4 and chapter 5. The junctions used for the measurements presented in Sec. 3.1 have been fabricated using similar parameters.

A.2 DC SQUIDs

The layout of the DC SQUIDs used for the capacitance measurements in Sec. 3.1 is shown in Fig. A.1. The DC SQUIDs are square loops containing two nanoscale Josephson junctions. Three different loop sizes, $a = 80, 160, 300\,\mu\text{m}$, and three different junction sizes, $w = 0.3, 0.5, 1.0\,\mu\text{m}$ yield nine different geometries. The geometric inductance is mainly determined by the parameter a. The filtering of the measurement lines is described in appendix B.2. In contrast to the flux qubit designs described in appendix A.3, no specific effort is made to control the electromagnetic environment of the qubit on or near the sample chip.

A.3 Flux qubits

In this section, we describe the fabrication process of the sample used for the measurements presented in chapter 4 and chapter 5. The sample layout and some SEM micrographs are shown in Fig. A.2. The qubit consists of an aluminum loop interrupted by three nanoscale Josephson junctions and fabricated approximately in the center of a $3.5 \times 3.5\,\text{mm}^2$ substrate. It has lateral dimensions of approximately $5\,\mu\text{m}$ and is tightly surrounded by a DC SQUID loop. Additionally, there is a microwave antenna and the elements controlling the electromagnetic environment of the qubit. The latter is explained in detail in Sec. 3.2.3 and Sec. 3.3.

The sample is fabricated using a three-layer process. First, the oxidized aluminum capacitor ground plane is evaporated onto the substrate. The second layer is made of gold and contains the resistors, ground connections and the body of the microwave antenna. Finally, the top aluminum layer comprises qubit, DC SQUID, capacitor top plates, and the superconducting part of microwave antenna and ground

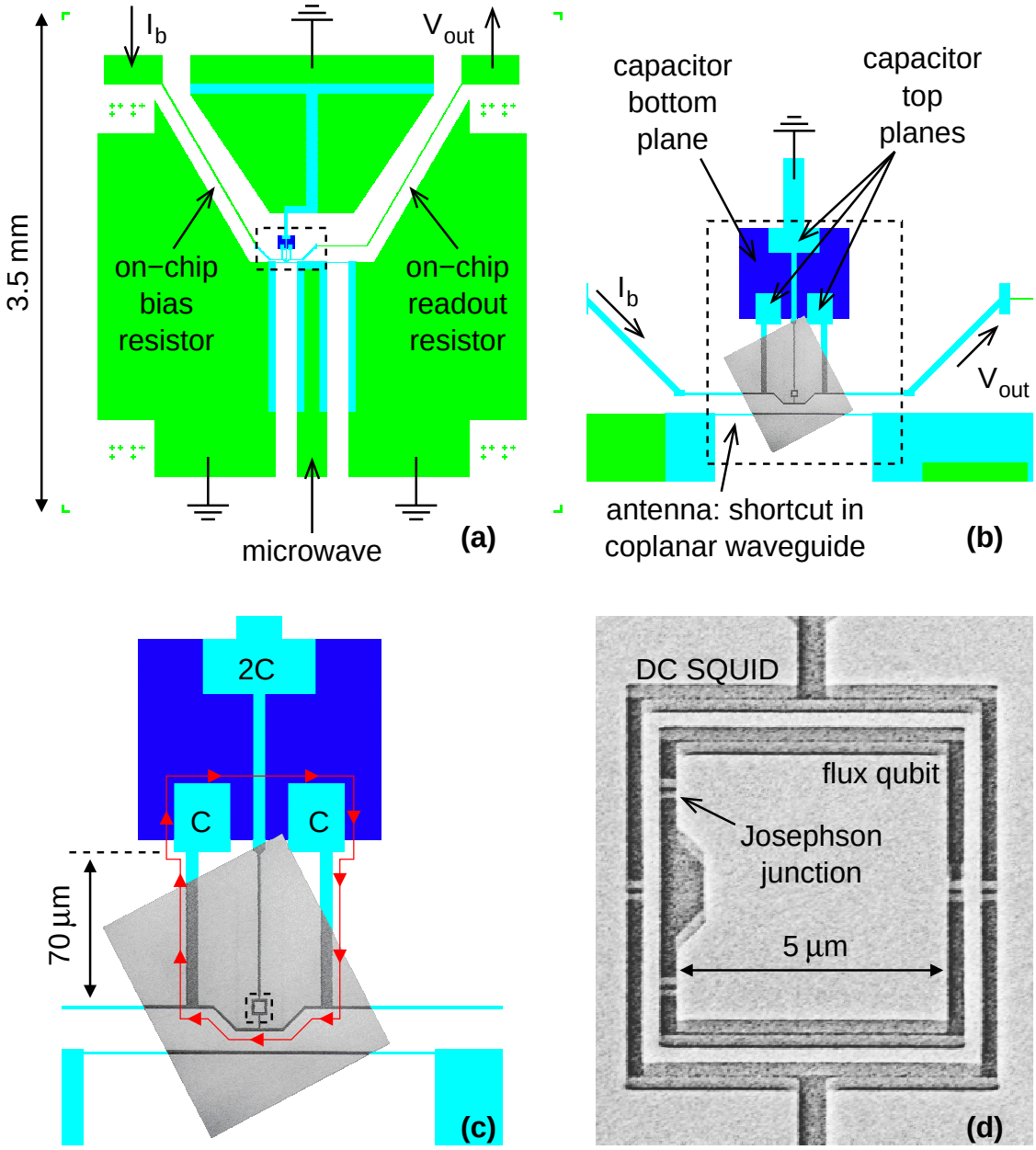

Figure A.2: The sample used for the measurements of chapter 4 and chapter 5. The colors encode the different metal layers: light blue – aluminum top layer, dark blue – aluminum bottom layer, green – gold layer. The grayscale images are SEM micrographs. **(a)** The design of the sample chip. The black dashed box marks the area shown in (b). I_b and V_out denote the DC SQUID bias current and response voltage, respectively. **(b)** Closeup of the region containing DC SQUID, qubit, the microwave antenna, and the shunting capacitors. The black dashed box marks the region shown in (c). **(c)** The areas of the top plates determine the capacitance values C and $2C$ of the shunting capacitors. The effective shunting capacitance is C. The red loop marks the superconducting LC-resonator discussed in chapter 5. The dashed box marks the area shown in (d). **(d)** Inner loop: the flux qubit. Outer loop: the DC SQUID

connections.
The capacitor ground plane is fabricated as follows:

1. The substrate is spin-coated with a double resist layer, 3270 Å of PMGI and 870 Å of ZEP/o-DCB (1:1). Each layer is baked for 3 min at 180 °C.
2. Next, the structure is patterned with EBL.
3. The ZEP layer is developed in butyl acetate at 20 °C for 90 s and in isopropanol for 30 s.
4. The PMGI layer is developed in a SAL101/ethanol (10:1) mixture for 90 s and in deionized water for 60 s.
5. After argon-sputter cleaning, 300 Å aluminum are evaporated at a rate of 1 Å/min. During the evaporation, the substrate has been turned from $-10\,^\circ$ to $+10\,^\circ$ at a rate of approximately $5\,^\circ/60$ Å.
6. Lift-off is performed in PMGI remover at 60 °C for 90 min.
7. Finally, the aluminum is oxidized by means of plasma oxidation in the loadlock of the evaporator in pure oxygen at a pressure of 150 mTorr.

In the next step, the gold layer is fabricated with the following recipe:

1. First, the substrate containing the oxidized aluminum ground plane of the capacitor is cleaned in an ultrasonic bath with acetone and isopropanol for 5 min each. After flushing with isopropanol it is dried by blowing nitrogen gas onto it.
2. The substrate is spin-coated with a double resist layer, 3270 Å of PMGI and 870 Å of ZEP/o-DCB (1:1). Each layer is baked for 3 min at 180 °C.
3. Next, the structure is patterned with EBL.
4. The ZEP layer is developed in butyl acetate at 20 °C for 90 s and in isopropanol for 30 s.
5. The PMGI layer is developed in a SAL101/ethanol (10:1) mixture for 90 s and in deionized water for 60 s.
6. Then, 100 nm of titanium and 300 nm of gold are evaporated onto the substrate at the rates of 3 Å/s and 3.5 Å/s, respectively.
7. Lift-off is performed with PMGI remover at 60 °C for 90 min.

The fabrication conditions of the aluminum top-layer are exactly those described for the Josephson junctions in appendix A.1. This layer has to be fabricated last in order not to destroy the sensitive Josephson junctions. Also, due to the natural oxidation of the aluminum in ambient atmosphere, high-quality gold-aluminum contacts can only be obtained for aluminum on top of gold, not vice versa. Finally, care has to be taken when leads of an upper layer cross structures of a lower one. In this case, the upper layer should be thicker than the lower one. Otherwise, the leads tend to tear, giving rise to open circuits. All the conditions discussed above are fulfilled in our sample design.

Appendix B

Cryogenic setup

In this appendix, we briefly describe the cryogenic equipment used for our measurements. First, we introduce the dilution fridge used for the experiments. Then, we present the details of the cryogenic setup for the slow-sweep measurements of Sec. 3.1 and for the pulsed qubit measurements of chapter 4 and chapter 5. Except for the bare dilution refrigerator, most of the experimental systems used for the measurements presented in this work has been set up and tested within this thesis. In particular, this includes the design and machining of many parts, the wiring of the cryostat, and the development of measurement software.

B.1 The dilution refrigerator

All experiments discussed in this thesis are performed in a ^{3}He/^{4}He dilution refrigerator at a base temperature of 20-50 mK near the sample holder. The fridge is a "Kelvinox 100" system from Oxford Instruments and has approximately 100 μW cooling power at a temperature of 100 mK inside the mixing chamber. The left panel of Fig. B.1 shows the dilution unit, which is precooled by a bath of liquid ^{4}He. Also located in this bath is a superconducting magnet, which can reach a maximum magnetic flux density of 12 T at the center of its 2-inch bore. The sample holder is located at the center of the magnet and thermally anchored at the mixing chamber plate via a 30 cm long annealed copper rod with a cross-sectional area of 1 cm × 1 cm (see right panel of Fig. B.1). Four permalloy shields protect the sample from external magnetic noise: three at room temperature around the He^4-dewar and one in the helium bath around the coil.

B.2 Slow-sweep qubit spectroscopy

In the slow-sweep setup, the DC SQUID measurement lines are not required to have a large bandwidth. Thus, we use twisted-pair constantan wires from room temperature to the mixing chamber plate. Thermal anchoring is achieved by winding the wires many times around copper cylinders, which are connected to several critical temperature stages of the fridge (see left panel of Fig. B.1). In combination with a 10 nF pass-through capacitance at the fridge top and an additional 200 Ω resistor at the sample holder (see Fig. B.2), the wire resistance of approximately 150 Ω forms a low-pass filter.

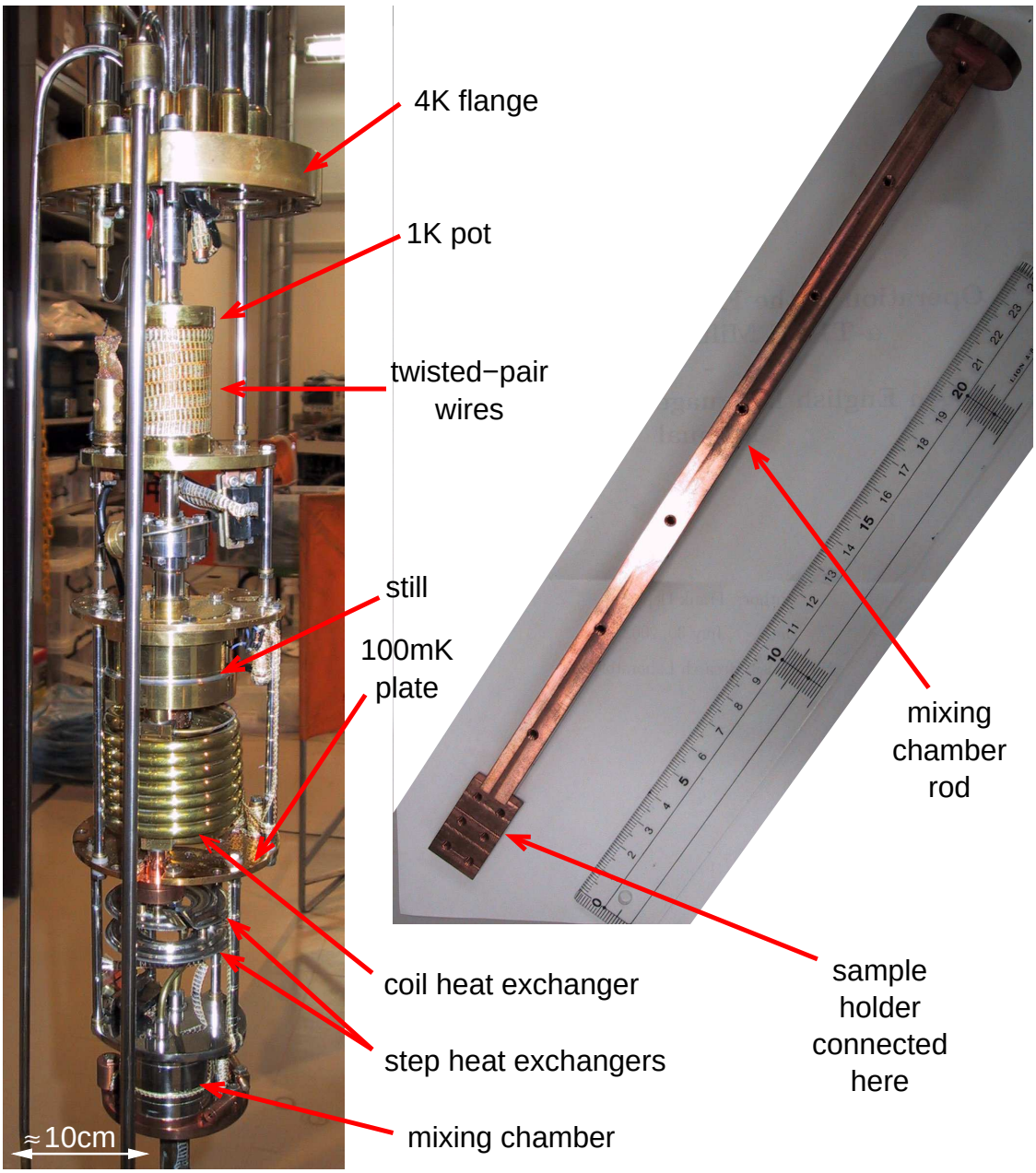

Figure B.1: Photographs of the dilution refrigerator without mounted experiments. Left panel: Dilution unit. Right panel: Mixing chamber rod.

Fig. B.2 shows the sample holder. Its copper lid is permanently connected to the mixing chamber rod. A copper adapter is used to fix a socket to the lid. This socket can accept a 16-pin ceramics chip carrier. The adapter allows for a direct heat contact between the sample holder and the chip carrier, which is further enhanced by a thin layer of vacuum grease to increase the effective contact area. The sample chip is glued with GE varnish onto a standard 16-pin chip carrier. The connections between chip and carrier are made by means of bonding with a gold wire of 25 µm diameter. Then, with the twisted pair wires short-circuited on the fridge top, the chip carrier is pushed carefully into the socket. Due to the vulnerability of the Josephson junctions to static charges, it is important to avoid touching the pins of the chip carrier during the mounting process. Finally, the box is connected to the

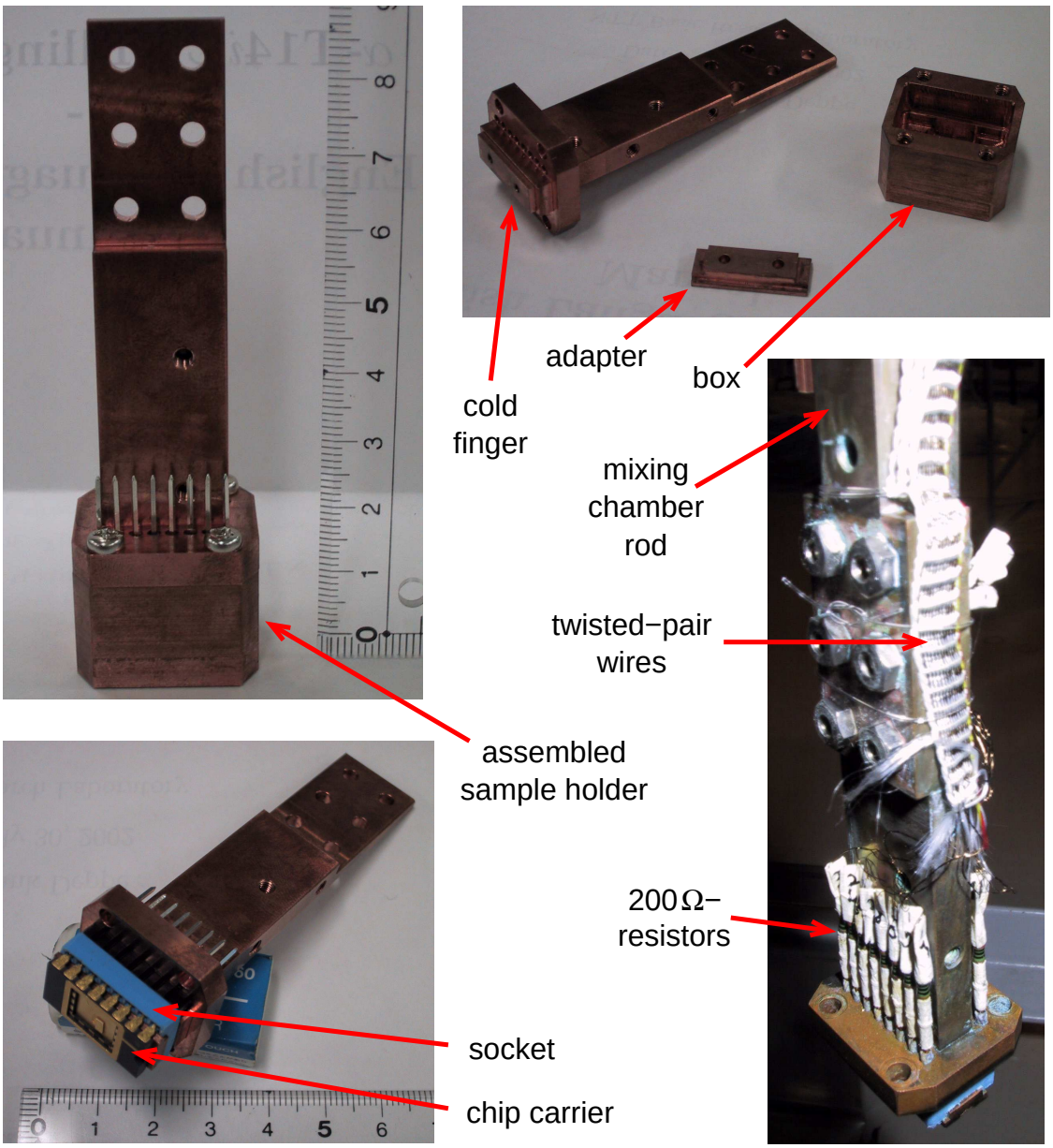

Figure B.2: Photographs of the sample holder used for slow-sweep experiments. For microwave spectroscopy, a coaxial cable is fed from the side into the sample holder box and wound to a loop antenna 1-2 mm above the sample chip (not shown).

lid to provide shielding against high-frequency radiation. The whole arrangement is placed such that the sample chip is located at the center of the superconducting magnet.

For slow-sweep microwave spectroscopy, a microwave antenna has to be installed. This antenna consists of a simple CuNi/Nb coaxial cable of 1.2 mm diameter. Cold attenuators at 4 K and mixing chamber temperature clean the signal from thermal noise. The cable is fed into the sample box from the side and the inner conductor is connected in a small loop to the outer conductor at the end. This loop antenna is placed 1-2 mm above the sample chip.

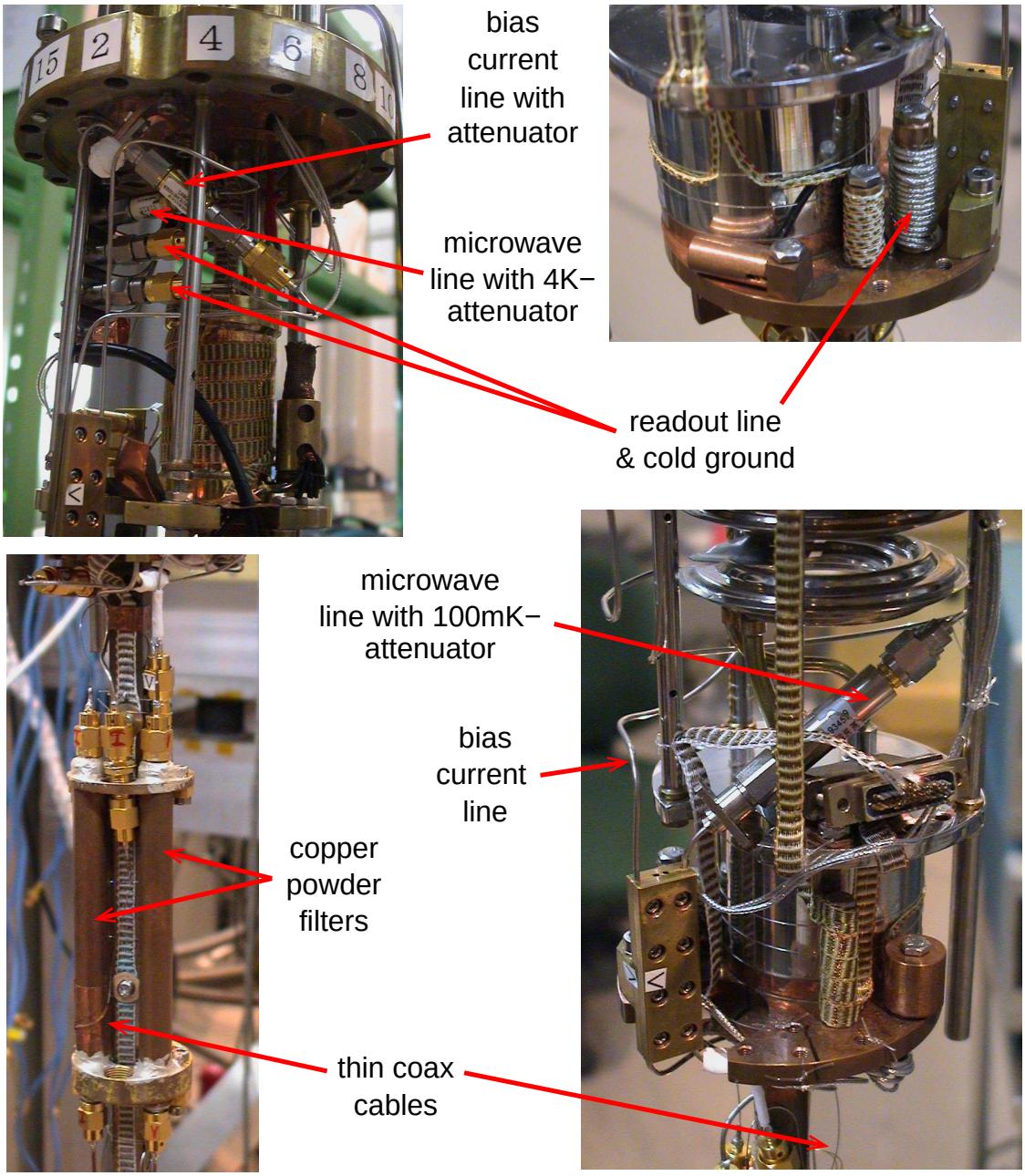

Figure B.3: Cabling inside the dilution unit for the pulsed qubit measurements.

B.3 Pulsed qubit measurements

In this section, we describe the cryogenic setup for the pulsed qubit readout introduced in Sec. 3.2 and Sec. 3.3. In this case, the twisted pair wires cannot be used for the DC SQUID because of their low bandwidth. Hence, it is necessary to switch to high-bandwidth coaxial cables. This, in turn, requires a modification of the fridge setup (see Fig. B.3) and a different sample holder. The latter also has to accommodate for the fact that the microwave loop antenna is replaced by a short-circuited on-chip coplanar wave guide.

Figure B.4 shows the sample holder, which is made of oxygen-free copper and plated with gold to avoid surface oxidation. Inside the sample holder, there is a

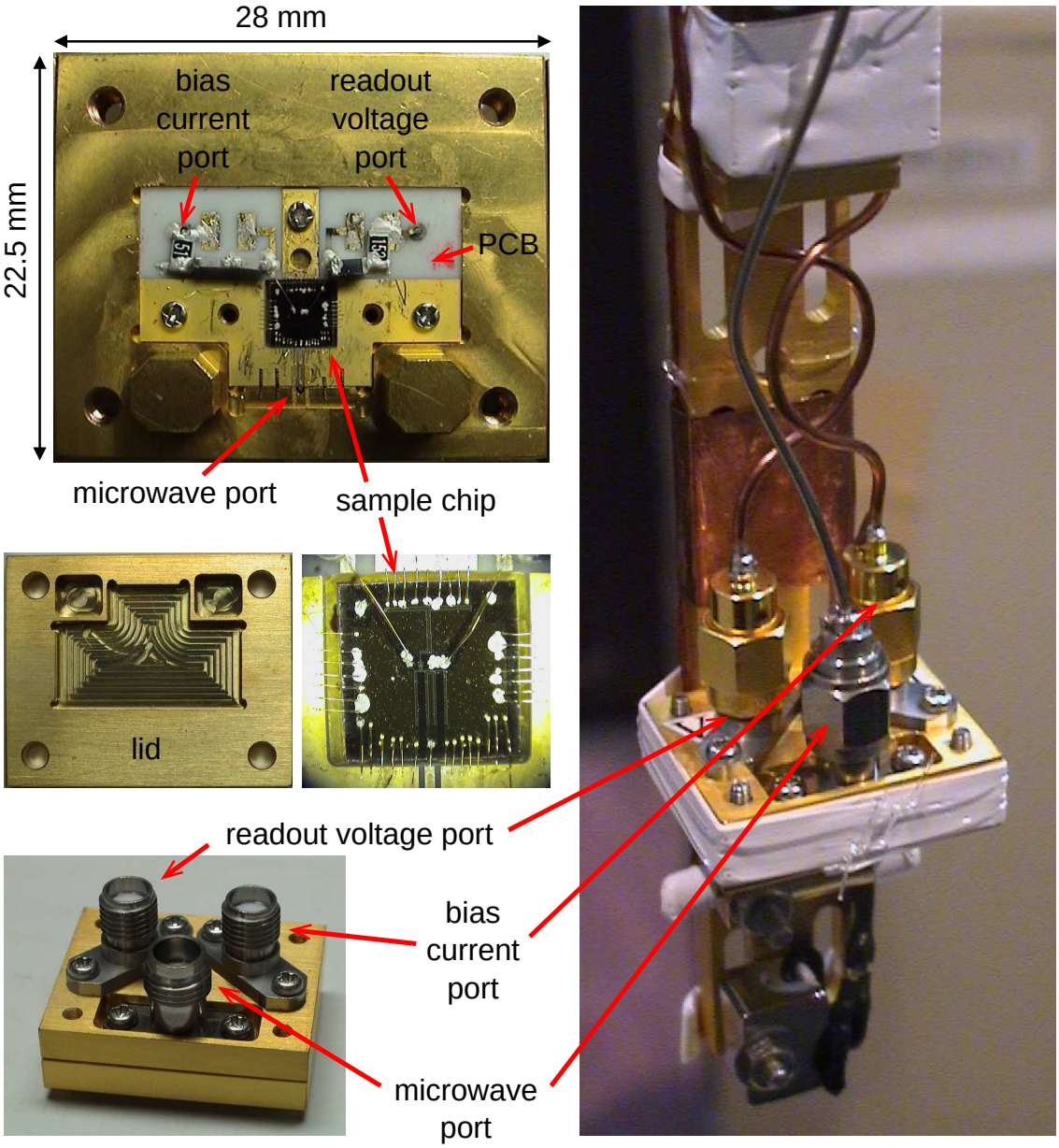

Figure B.4: Sample holder used for the pulsed qubit measurements.

T-shaped alumina printed circuit board (PCB), where the off-chip capacitors and resistors for the DC SQUID line are mounted. Two SMA-connectors serve as input and output port for bias current and response voltage of the DC SQUID, respectively. The microwave cable is connected via a V-band spring connector. The center conductors of these connectors are connected to the PCB inside the sample holder. To this end, simple soldering is sufficient for the DC SQUID lines because the relevant frequency range of the pulses is below 100 MHz. In contrast, the microwave line connection must be designed carefully to avoid excessive signal loss due to reflections. Into the spring of the V-connector we insert a tiny copper pin, which has a gold ribbon soldered to it at the other end. This gold ribbon is bonded to the center conductor of a coplanar waveguide on the PCB. Pin diameter, ribbon width and coplanar waveguide are designed such that 50 Ω-matching is guaranteed. The sample chip is glued with GE varnish to the metal surface of the sample holder inside

a 4 mm × 4 mm opening in the PCB. All connections from the PCB to the sample chip are made by bonding with gold wire of 25 µm diameter. For the capacitive-bias experiments, the on-chip resistors are short-circuited via long bonds.

Appendix C

Multiphoton excitations of a qubit-resonator system

In appendix C.1, we first present the details of the derivation of the second-order Hamiltonian of Sec. 5.3 with a Dyson-series approach. In addition, this second-order Hamiltonian of Eq. (5.5) can be derived in alternative ways. As shown in Sec. C.2, using the Schrieffer-Wolff transformation certainly involves more cumbersome calculations, but it has the advantage that no implicit rotating-wave approximations are performed. In this way, insight into the underlying physics is gained more easily. The Bessel-expansion approach of Sec. C.3 allows us to extend the treatment of multiphoton excitations beyond the two-photon process, but gives different shifts.

C.1 Dyson-series approach

C.1.1 The commutator theorem

We assume a Hamiltonian, which in an interaction picture has the time-dependent form

$$\hat{H}(t) = \hbar \sum_j g_j \left(\hat{S}_j^\dagger \mathrm{e}^{+i\delta_j t} + \hat{S}_j \mathrm{e}^{-i\delta_j t} \right) , \tag{C.1}$$

where g_j is a complex number, $\hat{S}_j$ a time-independent operator and $\hat{S}_j^\dagger$ its Hermitian conjugate. The operators $\hat{S}_j$ and $\hat{S}_j^\dagger$ have to be suitably normalized. Furthermore, the conditions

$$|\delta_j| \gg g_j \quad \forall j \tag{C.2}$$

$$|\delta_j \pm \delta_k| \gg g_k \quad \forall \{j \neq k\} \tag{C.3}$$

are required. Then it can be shown [158] that the Dyson series for the time evolution operator $\hat{U}$ associated with $\hat{H}$ can be rewritten in the exponential form $\hat{U} = \mathrm{e}^{-i\hat{H}_{\mathrm{eff}}t/\hbar}$, where

$$\hat{H}_{\mathrm{eff}} = \hbar \sum_j \frac{g_j^2}{\delta_j} \left[\hat{S}_j^\dagger, \hat{S}_j \right] . \tag{C.4}$$

The commutator theorem is quite powerful for generating second-order Hamiltonians with minimal mathematical effort. This becomes evident when comparing the simple calculations in appendix C.1.2 with those done in appendix C.2.

C.1.2 Two-photon driving via commutator theorem

We analyze the classically driven qubit-resonator system described by the Hamiltonian of Eq. (5.3),

$$\hat{H} = \frac{\epsilon}{2}\hat{\sigma}_z + \frac{\Delta}{2}\hat{\sigma}_x + \hbar\omega_\mathrm{r}\left(\hat{a}^\dagger\hat{a} + \frac{1}{2}\right) + \hbar g\,\hat{\sigma}_z\big(\hat{a}^\dagger + \hat{a}\big) + \frac{\Omega}{2}\hat{\sigma}_z\cos\omega t\,. \tag{C.5}$$

Here, the direct cavity driving is already neglected because the cavity is largely detuned from the driving frequency near the two-photon anticrossing. A transformation into the energy eigenbasis yields

$$\begin{aligned}\hat{H} = \frac{\hbar\omega_\mathrm{ge}}{2}\hat{\sigma}_z + \hbar\omega_\mathrm{r}\hat{a}^\dagger\hat{a} + \hbar g\big(\hat{a}^\dagger + \hat{a}\big)\left(\cos\theta\,\hat{\sigma}_z - \sin\theta\,\hat{\sigma}_x\right)\\ + \frac{\Omega}{2}\left(\cos\theta\,\hat{\sigma}_z - \sin\theta\,\hat{\sigma}_x\right)\cos\omega t\,.\end{aligned} \tag{C.6}$$

In the interaction picture with respect to qubit and resonator ($\hat{\sigma}_\pm \to \hat{\sigma}_\pm \mathrm{e}^{\pm i\omega_\mathrm{ge}t}$, $\hat{a} \to \hat{a}\mathrm{e}^{-i\omega_\mathrm{r}t}$, $\hat{a}^\dagger \to \hat{a}^\dagger\mathrm{e}^{+i\omega_\mathrm{r}t}$) and under two-photon driving ($\omega_\mathrm{ge} = 2\omega$), we can write

$$\begin{aligned}\hat{H} &= \hbar g\cos\theta\left(\hat{a}\mathrm{e}^{-i\omega_\mathrm{r}t} + \hat{a}^\dagger\mathrm{e}^{+i\omega_\mathrm{r}t}\right)\hat{\sigma}_z\\ &\quad - \hbar g\sin\theta\left(\hat{a}\mathrm{e}^{-i\omega_\mathrm{r}t} + \hat{a}^\dagger\mathrm{e}^{+i\omega_\mathrm{r}t}\right)\left(\hat{\sigma}_+\mathrm{e}^{+i2\omega t} + \hat{\sigma}_-\mathrm{e}^{-i2\omega t}\right)\\ &\quad + \frac{\Omega}{4}\cos\theta\left(\mathrm{e}^{+i\omega t} + \mathrm{e}^{-i\omega t}\right)\hat{\sigma}_z - \frac{\Omega}{4}\sin\theta\left(\mathrm{e}^{+i\omega t} + \mathrm{e}^{-i\omega t}\right)\left(\hat{\sigma}_-\mathrm{e}^{-i2\omega t} + \hat{\sigma}_+\mathrm{e}^{+i2\omega t}\right)\\ &= \hbar g\cos\theta\left(\hat{a}\mathrm{e}^{-i\omega_\mathrm{r}t} + \hat{a}^\dagger\mathrm{e}^{+i\omega_\mathrm{r}t}\right)\hat{\sigma}_z\\ &\quad - \hbar g\sin\theta\left(\hat{a}\hat{\sigma}_+\mathrm{e}^{+i\delta t} + \hat{a}\hat{\sigma}_-\mathrm{e}^{-i(2\omega+\omega_\mathrm{r})t} + \hat{a}\hat{\sigma}_+\mathrm{e}^{+i(2\omega+\omega_\mathrm{r})t} + \hat{a}^\dagger\hat{\sigma}_-\mathrm{e}^{-i\delta t}\right)\\ &\quad + \frac{\Omega}{4}\cos\theta\left(\mathrm{e}^{+i\omega t} + \mathrm{e}^{-i\omega t}\right)\hat{\sigma}_z\\ &\quad - \frac{\Omega}{4}\sin\theta\left[\left(\mathrm{e}^{-i\omega t} + \mathrm{e}^{-i3\omega t}\right)\hat{\sigma}_- + \left(\mathrm{e}^{+i3\omega t} + \mathrm{e}^{+i\omega t}\right)\hat{\sigma}_+\right]\,,\end{aligned} \tag{C.7}$$

where $\delta \equiv \omega_\mathrm{r} - \omega_\mathrm{ge}$ is the qubit-resonator detuning. Next we perform a rotating-wave approximation. The terms containing $\pm\omega_\mathrm{r}$ and $\pm(2\omega + \omega_\mathrm{r})$ in the exponential can be neglected because typically $|g| \ll |\omega_\mathrm{r}|$ in the experiments. The terms containing $\pm 3\omega$ can be neglected for the relevant case of weak driving, $\Omega/4\hbar \ll \omega$. Hence we find

$$\begin{aligned}\hat{H} = &-\hbar g\sin\theta\left(\hat{a}\hat{\sigma}_+\mathrm{e}^{+i\delta t} + \hat{a}^\dagger\hat{\sigma}_-\mathrm{e}^{-i\delta t}\right)\\ &+ \frac{\Omega}{4}\left[\left(\cos\theta\,\hat{\sigma}_z - \sin\theta\,\hat{\sigma}_+\right)\mathrm{e}^{+i\omega t} + \left(\cos\theta\,\hat{\sigma}_z - \sin\theta\,\hat{\sigma}_-\right)\mathrm{e}^{-i\omega t}\right]\,.\end{aligned} \tag{C.8}$$

In the above equation, we immediately identify the superoperators

$$\hat{S}^\dagger \equiv \frac{\Omega}{4}\left(\cos\theta\,\hat{\sigma}_z - \sin\theta\,\hat{\sigma}_+\right) \quad \text{and} \quad \hat{S} \equiv \frac{\Omega}{4}\left(\cos\theta\,\hat{\sigma}_z - \sin\theta\,\hat{\sigma}_-\right)\,. \tag{C.9}$$

Because of the weak driving $\Omega/4\hbar \ll \omega$, the commutator theorem of Eq. (C.4) can be used to derive the second-order Hamiltonian

$$\hat{H}_\mathrm{eff} = -\hbar g\sin\theta\left(\hat{a}\hat{\sigma}_+\mathrm{e}^{+i\delta t} + \hat{a}^\dagger\hat{\sigma}_-\mathrm{e}^{-i\delta t}\right) + \frac{\left[\hat{S}^\dagger, \hat{S}\right]}{\hbar\omega}\,. \tag{C.10}$$

Using the relations $\hat{\sigma}_z\hat{\sigma}_+ - \hat{\sigma}_+\hat{\sigma}_z = 2\hat{\sigma}_+$, $\hat{\sigma}_-\hat{\sigma}_z - \hat{\sigma}_z\hat{\sigma}_- = 2\hat{\sigma}_-$, and $\hat{\sigma}_+\hat{\sigma}_- - \hat{\sigma}_-\hat{\sigma}_+ = \hat{\sigma}_z$, we calculate the commutator

$$\begin{aligned}
\left[\hat{S}^\dagger, \hat{S}\right] &= \hat{S}^\dagger\hat{S} - \hat{S}\hat{S}^\dagger \\
&= \frac{\Omega^2}{16}\left[\left(\cos\theta\,\hat{\sigma}_z - \sin\theta\,\hat{\sigma}_+\right)\left(\cos\theta\,\hat{\sigma}_z - \sin\theta\,\hat{\sigma}_-\right)\right. \\
&\qquad \left. - \left(\cos\theta\,\hat{\sigma}_z - \sin\theta\,\hat{\sigma}_-\right)\left(\cos\theta\,\hat{\sigma}_z - \sin\theta\,\hat{\sigma}_+\right)\right] \\
&= \frac{\Omega^2}{16}\left[\cos^2\theta\,\hat{\sigma}_z^2 - \sin\theta\cos\theta\,\hat{\sigma}_z\hat{\sigma}_- - \sin\theta\cos\theta\,\hat{\sigma}_+\hat{\sigma}_z + \sin^2\theta\,\hat{\sigma}_+\hat{\sigma}_-\right. \\
&\qquad \left. - \cos^2\theta\,\hat{\sigma}_z^2 + \sin\theta\cos\theta\,\hat{\sigma}_z\hat{\sigma}_+ + \sin\theta\cos\theta\,\hat{\sigma}_-\hat{\sigma}_z - \sin^2\theta\,\hat{\sigma}_-\hat{\sigma}_+\right] \\
&= \frac{\Omega^2}{8}\sin\theta\cos\theta\,\hat{\sigma}_x + \frac{\Omega^2}{16}\sin^2\theta\,\hat{\sigma}_z\,. \qquad \text{(C.11)}
\end{aligned}$$

Then, the final effective Hamiltonian of the system under two-photon driving reads

$$\begin{aligned}
\hat{H}_{\text{eff}} = &-\hbar g\sin\theta\left(\hat{a}\hat{\sigma}_+ e^{+i\delta t} + \hat{a}^\dagger\hat{\sigma}_- e^{-i\delta t}\right) \\
&+ \frac{\Omega^2}{4\Delta}\sin^2\theta\cos\theta\,\hat{\sigma}_x + \frac{\Omega^2}{8\Delta}\sin^3\theta\,\hat{\sigma}_z\,. \qquad \text{(C.12)}
\end{aligned}$$

which is the result stated in Eq. (5.4) of chapter 5. We note that the first term of $\hat{H}_{\text{eff}}$ describing the qubit-resonator interaction is valid only near the anticrossing, where $|\delta| \lesssim |g|$.

C.2 Schrieffer-Wolff transformation

We consider the case of a qubit-resonator system under two-photon driving. In the calculations, the driving is quantized and treated as a strongly detuned resonator. We note that constant energy offsets in the Hamiltonians, e.g., the resonator vacuum, are always neglected without explicit notice in this section. As in chapter 5, the resonator is described by means of the annihilation operator $\hat{a}$ and the creation operator $\hat{a}^\dagger$. Likewise, the quantized driving is denoted with $\hat{b}$ and $\hat{b}^\dagger$. The indices a or b denote that the indexed quantity relates to the resonator or the driving, respectively. Then, the Hamiltonian in the diabatic basis is

$$\begin{aligned}
\hat{H}' = &\frac{\epsilon}{2}\hat{\sigma}_z + \frac{\Delta}{2}\hat{\sigma}_x + \hbar\omega_{\text{a}}\hat{a}^\dagger\hat{a} + \hbar\omega_{\text{b}}\hat{b}^\dagger\hat{b} \\
&+ \hbar g_{\text{a}}\left(\hat{a}^\dagger + \hat{a}\right)\hat{\sigma}_z + \hbar g_{\text{b}}\left(\hat{b} + \hat{b}^\dagger\right)\hat{\sigma}_z + \hbar F\left(\hat{a}^\dagger + \hat{a}\right)\left(\hat{b} + \hat{b}^\dagger\right)\,. \qquad \text{(C.13)}
\end{aligned}$$

Here, the first two terms represent the qubit, followed by the resonator, the quantized driving, the qubit-resonator interaction, the qubit-driving interaction, and the resonator-driving interaction. As in appendix C.1.2, we immediately neglect the direct two-photon driving of the resonator by setting $F = 0$ and define the coupling coefficients $K_{\text{a}} \equiv g_{\text{a}}\cos\theta$, $K_{\text{b}} \equiv g_{\text{b}}\cos\theta$, $G_{\text{a}} \equiv -g_{\text{a}}\sin\theta$ and $G_{\text{b}} \equiv -g_{\text{b}}\sin\theta$. Then, a rotation into the qubit energy eigenbasis yields

$$\begin{aligned}
\frac{\hat{H}}{\hbar} = &\frac{\omega_{\text{ge}}}{2}\hat{\sigma}_z + \omega_{\text{a}}\hat{a}^\dagger\hat{a} + \omega_{\text{b}}\hat{b}^\dagger\hat{b} + g_{\text{a}}\cos\theta\left(\hat{a}^\dagger + \hat{a}\right)\hat{\sigma}_z - g_{\text{a}}\sin\theta\left(\hat{a}^\dagger + \hat{a}\right)\hat{\sigma}_x \\
&+ g_{\text{b}}\cos\theta\left(\hat{b} + \hat{b}^\dagger\right)\hat{\sigma}_z - g_{\text{b}}\sin\theta\left(\hat{b} + \hat{b}^\dagger\right)\hat{\sigma}_x
\end{aligned}$$

$$
\begin{aligned}
&= \frac{\omega_{\mathrm{ge}}}{2}\hat{\sigma}_z + \omega_{\mathrm{a}}\hat{a}^\dagger\hat{a} + \omega_{\mathrm{b}}\hat{b}^\dagger\hat{b} + K_{\mathrm{a}}\big(\hat{a}^\dagger + \hat{a}\big)\hat{\sigma}_z + K_{\mathrm{b}}\big(\hat{b} + \hat{b}^\dagger\big)\hat{\sigma}_z \\
&\quad + G_{\mathrm{a}}\big(\hat{a}^\dagger + \hat{a}\big)\hat{\sigma}_x + G_{\mathrm{b}}\big(\hat{b} + \hat{b}^\dagger\big)\hat{\sigma}_x \\
&= \frac{\omega_{\mathrm{ge}}}{2}\hat{\sigma}_z + \omega_{\mathrm{a}}\hat{a}^\dagger\hat{a} + \omega_{\mathrm{b}}\hat{b}^\dagger\hat{b} + K_{\mathrm{a}}\hat{a}\hat{\sigma}_z + K_{\mathrm{a}}\hat{a}^\dagger\hat{\sigma}_z + K_{\mathrm{b}}\hat{b}\hat{\sigma}_z + K_{\mathrm{b}}\hat{b}^\dagger\hat{\sigma}_z \\
&\quad + G_{\mathrm{a}}\hat{a}\hat{\sigma}_x + G_{\mathrm{a}}\hat{a}^\dagger\hat{\sigma}_x + G_{\mathrm{b}}\hat{b}\hat{\sigma}_x + G_{\mathrm{b}}\hat{b}^\dagger\hat{\sigma}_x\,. \qquad \text{(C.14)}
\end{aligned}
$$

When qubit and driving are strongly detuned, $G_{\mathrm{b}} \ll \delta_{\mathrm{b}} \equiv \omega_{\mathrm{ge}} - \omega_{\mathrm{b}}$, we can derive the effective Hamiltonian by means of the Schrieffer-Wolff transformation $\hat{H}_{\mathrm{eff}} = \hat{U}\hat{H}\hat{U}^\dagger$, where

$$
\hat{U} = \mathrm{e}^{\left(G_{\mathrm{b}}/\delta_{\mathrm{b}}\right)\left(\hat{b}\hat{\sigma}_+ - \hat{b}^\dagger\hat{\sigma}_-\right)} \quad \text{and} \quad \hat{U}^\dagger = \mathrm{e}^{\left(G_{\mathrm{b}}/\delta_{\mathrm{b}}\right)\left(-\hat{b}\hat{\sigma}_+ + \hat{b}^\dagger\hat{\sigma}_-\right)}\,. \qquad \text{(C.15)}
$$

With the definition

$$
\hat{H}_{nm} \equiv \frac{1}{n!m!}\left(\frac{G_{\mathrm{b}}}{\delta_{\mathrm{b}}}\right)^{n+m}\left(\hat{b}\hat{\sigma}_+ - \hat{b}^\dagger\hat{\sigma}_-\right)^n \hat{H}\left(-\hat{b}\hat{\sigma}_+ + \hat{b}^\dagger\hat{\sigma}_-\right)^m, \qquad \text{(C.16)}
$$

the effective Hamiltonian $\hat{H}_{\mathrm{eff}}$ is approximated to second order by expanding the exponentials and discarding terms of the order $(G_{\mathrm{b}}/\delta_{\mathrm{b}})^2$ or higher:

$$
\hat{H}_{\mathrm{eff}} \approx \hat{H}_{00} + \hat{H}_{10} + \hat{H}_{01} + \hat{H}_{11} + \hat{H}_{20} + \hat{H}_{02}\,. \qquad \text{(C.17)}
$$

In the calculations, we often use the relations

$$
\begin{array}{llll}
\hat{\sigma}_+\hat{\sigma}_z = -\hat{\sigma}_+ & & \hat{\sigma}_z = \hat{\sigma}_+\hat{\sigma}_- - \hat{\sigma}_-\hat{\sigma}_+ \\
\hat{\sigma}_z\hat{\sigma}_+ = +\hat{\sigma}_+ & \text{and} & \hat{1}_{\mathrm{q}} = \hat{\sigma}_+\hat{\sigma}_- + \hat{\sigma}_-\hat{\sigma}_+ \\
\hat{\sigma}_-\hat{\sigma}_z = +\hat{\sigma}_- & & \hat{1}_{\mathrm{r}} = \hat{a}\hat{a}^\dagger - \hat{a}^\dagger\hat{a} \\
\hat{\sigma}_z\hat{\sigma}_- = -\hat{\sigma}_- & & \hat{1}_{\mathrm{r}} = \hat{b}\hat{b}^\dagger - \hat{b}^\dagger\hat{b}
\end{array}\,. \qquad \text{(C.18)}
$$

Furthermore, the commutators $[\hat{a},\hat{b}]$,$[\hat{a},\hat{b}^\dagger]$, $[\hat{a}^\dagger,\hat{b}]$, and $[\hat{a}^\dagger,\hat{b}^\dagger]$ vanish because resonator and driving occupy different Hilbert spaces.

The first step is to calculate the sum $\hat{H}_1 \equiv \hat{H}_{10} + \hat{H}_{01}$,

$$
\begin{aligned}
\frac{\delta_{\mathrm{b}}}{G_{\mathrm{b}}}\frac{\hat{H}_1}{\hbar} &= \left(\hat{b}\hat{\sigma}_+ - \hat{b}^\dagger\hat{\sigma}_-\right)\Big(\frac{\omega_{\mathrm{ge}}}{2}\hat{\sigma}_z + \omega_{\mathrm{a}}\hat{a}^\dagger\hat{a} + \omega_{\mathrm{b}}\hat{b}^\dagger\hat{b} + K_{\mathrm{a}}\hat{a}\hat{\sigma}_z + K_{\mathrm{a}}\hat{a}^\dagger\hat{\sigma}_z \\
&\qquad + K_{\mathrm{b}}\hat{b}\hat{\sigma}_z + K_{\mathrm{b}}\hat{b}^\dagger\hat{\sigma}_z + G_{\mathrm{a}}\hat{a}\hat{\sigma}_x + G_{\mathrm{a}}\hat{a}^\dagger\hat{\sigma}_x + G_{\mathrm{b}}\hat{b}\hat{\sigma}_x + G_{\mathrm{b}}\hat{b}^\dagger\hat{\sigma}_x\Big) \\
&\quad + \Big(\frac{\omega_{\mathrm{ge}}}{2}\hat{\sigma}_z + \omega_{\mathrm{a}}\hat{a}^\dagger\hat{a} + \omega_{\mathrm{b}}\hat{b}^\dagger\hat{b} + K_{\mathrm{a}}\hat{a}\hat{\sigma}_z + K_{\mathrm{a}}\hat{a}^\dagger\hat{\sigma}_z + K_{\mathrm{b}}\hat{b}\hat{\sigma}_z + K_{\mathrm{b}}\hat{b}^\dagger\hat{\sigma}_z \\
&\qquad + G_{\mathrm{a}}\hat{a}\hat{\sigma}_x + G_{\mathrm{a}}\hat{a}^\dagger\hat{\sigma}_x + G_{\mathrm{b}}\hat{b}\hat{\sigma}_x + G_{\mathrm{b}}\hat{b}^\dagger\hat{\sigma}_x\Big)\left(-\hat{b}\hat{\sigma}_+ + \hat{b}^\dagger\hat{\sigma}_-\right) \\
&= -\frac{\omega_{\mathrm{ge}}}{2}\left(\hat{b}\hat{\sigma}_+ + \hat{b}^\dagger\hat{\sigma}_- + \hat{b}\hat{\sigma}_+ + \hat{b}^\dagger\hat{\sigma}_-\right) \\
&\quad + \omega_{\mathrm{a}}\left(\hat{b}\hat{a}^\dagger\hat{a}\hat{\sigma}_+ - \hat{b}^\dagger\hat{a}^\dagger\hat{a}\hat{\sigma}_- - \hat{a}^\dagger\hat{a}\hat{b}\hat{\sigma}_+ + \hat{a}^\dagger\hat{a}\hat{b}^\dagger\hat{\sigma}_-\right) \\
&\quad + \omega_{\mathrm{b}}\left(\hat{b}\hat{b}^\dagger\hat{b}\hat{\sigma}_+ - \hat{b}^{\dagger 2}\hat{b}\hat{\sigma}_- - \hat{b}^\dagger\hat{b}^2\hat{\sigma}_+ + \hat{b}^\dagger\hat{b}\hat{b}^\dagger\hat{\sigma}_-\right) \\
&\quad - K_{\mathrm{a}}\left(\hat{b}\hat{a}\hat{\sigma}_+ + \hat{b}^\dagger\hat{a}\hat{\sigma}_- + \hat{a}\hat{b}\hat{\sigma}_+ + \hat{a}\hat{b}^\dagger\hat{\sigma}_- + \hat{b}\hat{a}^\dagger\hat{\sigma}_+ + \hat{b}^\dagger\hat{a}^\dagger\hat{\sigma}_- + \hat{a}^\dagger\hat{b}\hat{\sigma}_+ + \hat{a}^\dagger\hat{b}^\dagger\hat{\sigma}_-\right) \\
&\quad - K_{\mathrm{b}}\left(\hat{b}^2\hat{\sigma}_+ + \hat{b}^\dagger\hat{b}\hat{\sigma}_- + \hat{b}^2\hat{\sigma}_+ + \hat{b}\hat{b}^\dagger\hat{\sigma}_- + \hat{b}\hat{b}^\dagger\hat{\sigma}_+ + \hat{b}^{\dagger 2}\hat{\sigma}_- + \hat{b}^\dagger\hat{b}\hat{\sigma}_+ + \hat{b}^{\dagger 2}\hat{\sigma}_-\right)
\end{aligned}
$$

$$
\begin{aligned}
&+ G_{\mathrm{a}}\left(\hat{b}\hat{a}\hat{\sigma}_{+}\hat{\sigma}_{-} - \hat{b}^{\dagger}\hat{a}\hat{\sigma}_{-}\hat{\sigma}_{+} - \hat{a}\hat{b}\hat{\sigma}_{-}\hat{\sigma}_{+} + \hat{a}\hat{b}^{\dagger}\hat{\sigma}_{+}\hat{\sigma}_{-}\right)\\
&+ G_{\mathrm{a}}\left(\hat{b}\hat{a}^{\dagger}\hat{\sigma}_{+}\hat{\sigma}_{-} - \hat{b}^{\dagger}\hat{a}^{\dagger}\hat{\sigma}_{-}\hat{\sigma}_{+} - \hat{a}^{\dagger}\hat{b}\hat{\sigma}_{-}\hat{\sigma}_{+} + \hat{a}^{\dagger}\hat{b}^{\dagger}\hat{\sigma}_{+}\hat{\sigma}_{-}\right)\\
&+ G_{\mathrm{b}}\left(\hat{b}^{2}\hat{\sigma}_{+}\hat{\sigma}_{-} - \hat{b}^{\dagger}\hat{b}\hat{\sigma}_{-}\hat{\sigma}_{+} - \hat{b}^{2}\hat{\sigma}_{-}\hat{\sigma}_{+} + \hat{b}\hat{b}^{\dagger}\hat{\sigma}_{+}\hat{\sigma}_{-}\right)\\
&+ G_{\mathrm{b}}\left(\hat{b}\hat{b}^{\dagger}\hat{\sigma}_{+}\hat{\sigma}_{-} - \hat{b}^{\dagger 2}\hat{\sigma}_{-}\hat{\sigma}_{+} - \hat{b}^{\dagger}\hat{b}\hat{\sigma}_{-}\hat{\sigma}_{+} + \hat{b}^{\dagger 2}\hat{\sigma}_{+}\hat{\sigma}_{-}\right). \qquad \text{(C.19)}
\end{aligned}
$$

From this, we immediately find

$$
\begin{aligned}
\frac{\hat{H}_1}{\hbar} = &-G_{\mathrm{b}}\left(\hat{b}\hat{\sigma}_{+} + \hat{b}^{\dagger}\hat{\sigma}_{-}\right) - 2\frac{K_{\mathrm{a}}G_{\mathrm{b}}}{\delta_{\mathrm{b}}}\left(\hat{a}\hat{b}\hat{\sigma}_{+} + \hat{a}\hat{b}^{\dagger}\hat{\sigma}_{-} + \hat{a}^{\dagger}\hat{b}\hat{\sigma}_{+} + \hat{a}^{\dagger}\hat{b}^{\dagger}\hat{\sigma}_{-}\right)\\
&- 2\frac{K_{\mathrm{b}}G_{\mathrm{b}}}{\delta_{\mathrm{b}}}\left(\hat{b}^{2}\hat{\sigma}_{+} + \hat{b}^{\dagger 2}\hat{\sigma}_{-} + \hat{b}^{\dagger}\hat{b}\hat{\sigma}_{x}\right) - \frac{K_{\mathrm{b}}G_{\mathrm{b}}}{\delta_{\mathrm{b}}}\hat{\sigma}_{x}\\
&+ \frac{G_{\mathrm{a}}G_{\mathrm{b}}}{\delta_{\mathrm{b}}}\left(\hat{a}\hat{b} + \hat{a}\hat{b}^{\dagger} + \hat{a}^{\dagger}\hat{b} + \hat{a}^{\dagger}\hat{b}^{\dagger}\right)\hat{\sigma}_{z}\\
&+ \frac{G_{\mathrm{b}}^{2}}{\delta_{\mathrm{b}}}\left(\hat{b}^{2} + \hat{b}^{\dagger 2} + 2\hat{b}^{\dagger}\hat{b}\right)\hat{\sigma}_{z} + 2\frac{G_{\mathrm{b}}^{2}}{\delta_{\mathrm{b}}}\hat{\sigma}_{+}\hat{\sigma}_{-}. \qquad \text{(C.20)}
\end{aligned}
$$

In a second step, we calculate $\hat{H}_2 \equiv \hat{H}_{11} + \hat{H}_{20} + \hat{H}_{02}$. Using $(\hat{b}\hat{\sigma}_{+} - \hat{b}^{\dagger}\hat{\sigma}_{-})^2 = -(\hat{b}^{\dagger}\hat{b} + \hat{\sigma}_{+}\hat{\sigma}_{-})$, we find

$$
\begin{aligned}
\left(\frac{\delta_{\mathrm{b}}}{G_{\mathrm{b}}}\right)^{2}\frac{\hat{H}_2}{\hbar} = &\left(\hat{b}\hat{\sigma}_{+} - \hat{b}^{\dagger}\hat{\sigma}_{-}\right)\left(\frac{\omega_{\mathrm{ge}}}{2}\hat{\sigma}_{z} + \omega_{\mathrm{a}}\hat{a}^{\dagger}\hat{a} + \omega_{\mathrm{b}}\hat{b}^{\dagger}\hat{b}\right)\left(-\hat{b}\hat{\sigma}_{+} + \hat{b}^{\dagger}\hat{\sigma}_{-}\right)\\
&- \frac{1}{2}\left(\hat{b}^{\dagger}\hat{b} + \hat{\sigma}_{+}\hat{\sigma}_{-}\right)\left(\frac{\omega_{\mathrm{ge}}}{2}\hat{\sigma}_{z} + \omega_{\mathrm{a}}\hat{a}^{\dagger}\hat{a} + \omega_{\mathrm{b}}\hat{b}^{\dagger}\hat{b}\right)\\
&- \frac{1}{2}\left(\frac{\omega_{\mathrm{ge}}}{2}\hat{\sigma}_{z} + \omega_{\mathrm{a}}\hat{a}^{\dagger}\hat{a} + \omega_{\mathrm{b}}\hat{b}^{\dagger}\hat{b}\right)\left(\hat{b}^{\dagger}\hat{b} + \hat{\sigma}_{+}\hat{\sigma}_{-}\right)\\
= &-\frac{\omega_{\mathrm{ge}}}{2}\left(\hat{b}\hat{b}^{\dagger}\hat{\sigma}_{+}\hat{\sigma}_{-} - \hat{b}^{\dagger}\hat{b}\hat{\sigma}_{-}\hat{\sigma}_{+} + \hat{b}^{\dagger}\hat{b}\hat{\sigma}_{z} + \hat{\sigma}_{+}\hat{\sigma}_{-}\right)\\
&+ \omega_{\mathrm{a}}\left(\hat{b}\hat{b}^{\dagger}\hat{a}^{\dagger}\hat{a}\hat{\sigma}_{+}\hat{\sigma}_{-} + \hat{b}^{\dagger}\hat{b}\hat{a}^{\dagger}\hat{a}\hat{\sigma}_{-}\hat{\sigma}_{+} - \hat{a}^{\dagger}\hat{a}\hat{b}^{\dagger}\hat{b} - \hat{a}^{\dagger}\hat{a}\hat{\sigma}_{+}\hat{\sigma}_{-}\right)\\
&+ \omega_{\mathrm{b}}\left[\left(\hat{b}\hat{b}^{\dagger}\right)^{2}\hat{\sigma}_{+}\hat{\sigma}_{-} + \hat{b}^{\dagger 2}\hat{b}^{2}\hat{\sigma}_{-}\hat{\sigma}_{+} - \left(\hat{b}^{\dagger}\hat{b}\right)^{2} - \hat{b}^{\dagger}\hat{b}\hat{\sigma}_{+}\hat{\sigma}_{-}\right]\\
= &-\omega_{\mathrm{ge}}\left(\hat{b}^{\dagger}\hat{b}\hat{\sigma}_{z} + \hat{\sigma}_{+}\hat{\sigma}_{-}\right) + \omega_{\mathrm{b}}\left(\hat{b}^{\dagger}\hat{b}\hat{\sigma}_{z} + \hat{\sigma}_{+}\hat{\sigma}_{-}\right) \qquad \text{(C.21)}
\end{aligned}
$$

and, consequently,

$$
\frac{\hat{H}_2}{\hbar} = -\frac{G_{\mathrm{b}}^{2}}{\delta_{\mathrm{b}}}\left(\hat{b}^{\dagger}\hat{b}\hat{\sigma}_{z} + \hat{\sigma}_{+}\hat{\sigma}_{-}\right). \qquad \text{(C.22)}
$$

The effective second-order Hamiltonian can now be written as

$$
\begin{aligned}
\frac{\hat{H}_{\mathrm{eff}}}{\hbar} = &\frac{\omega_{\mathrm{ge}}}{2}\hat{\sigma}_{z} + \omega_{\mathrm{a}}\hat{a}^{\dagger}\hat{a} + \omega_{\mathrm{b}}\hat{b}^{\dagger}\hat{b} + K_{\mathrm{a}}\big(\hat{a}^{\dagger} + \hat{a}\big)\hat{\sigma}_{z} + K_{\mathrm{b}}\big(\hat{b} + \hat{b}^{\dagger}\big)\hat{\sigma}_{z} + G_{\mathrm{a}}\big(\hat{a}^{\dagger} + \hat{a}\big)\hat{\sigma}_{x}\\
&+ G_{\mathrm{b}}\left(\hat{b}\hat{\sigma}_{-} + \hat{b}^{\dagger}\hat{\sigma}_{+}\right) - 2\frac{K_{\mathrm{a}}G_{\mathrm{b}}}{\delta_{\mathrm{b}}}\left(\hat{a}\hat{b}\hat{\sigma}_{+} + \hat{a}\hat{b}^{\dagger}\hat{\sigma}_{-} + \hat{a}^{\dagger}\hat{b}\hat{\sigma}_{+} + \hat{a}^{\dagger}\hat{b}^{\dagger}\hat{\sigma}_{-}\right)\\
&- 2\frac{K_{\mathrm{b}}G_{\mathrm{b}}}{\delta_{\mathrm{b}}}\left(\hat{b}^{2}\hat{\sigma}_{+} + \hat{b}^{\dagger 2}\hat{\sigma}_{-} + \hat{b}^{\dagger}\hat{b}\hat{\sigma}_{x}\right) - \frac{K_{\mathrm{b}}G_{\mathrm{b}}}{\delta_{\mathrm{b}}}\hat{\sigma}_{x}\\
&+ \frac{G_{\mathrm{a}}G_{\mathrm{b}}}{\delta_{\mathrm{b}}}\left(\hat{a}\hat{b} + \hat{a}\hat{b}^{\dagger} + \hat{a}^{\dagger}\hat{b} + \hat{a}^{\dagger}\hat{b}^{\dagger}\right)\hat{\sigma}_{z}\\
&+ \frac{G_{\mathrm{b}}^{2}}{\delta_{\mathrm{b}}}\left(\hat{b}^{2} + \hat{b}^{\dagger 2} + \hat{b}^{\dagger}\hat{b}\right)\hat{\sigma}_{z} + \frac{G_{\mathrm{b}}^{2}}{\delta_{\mathrm{b}}}\hat{\sigma}_{+}\hat{\sigma}_{-}. \qquad \text{(C.23)}
\end{aligned}
$$

More insight into the physics described by the above equation is gained by a transformation of $\hat{H}_{\rm eff}$ into the interaction picture with respect to qubit, resonator, and driving, $\hat{\sigma}_\pm \to \hat{\sigma}_\pm \mathrm{e}^{\pm i\omega_{\rm ge}t}$, $\hat{a} \to \hat{a}\mathrm{e}^{-i\omega_{\rm a}t}$, $\hat{a}^\dagger \to \hat{a}^\dagger \mathrm{e}^{+i\omega_{\rm a}t}$, $\hat{b} \to \hat{b}\mathrm{e}^{-i\omega_{\rm b}t}$, and $\hat{b}^\dagger \to \hat{b}^\dagger \mathrm{e}^{+i\omega_{\rm b}t}$. We further assume that the influence of possible shifts of the qubit or resonator frequencies on the resonance conditions are negligible. Then, under two-photon driving ($\omega_{\rm b} = \omega = \omega_{\rm ge}/2$ and $\delta_{\rm b} = \omega$) and near the qubit-resonator degeneracy ($\delta \equiv \omega_{\rm ge} - \omega_{\rm a}$, $|\delta| \lesssim |G_{\rm a}|$), we find

$$\begin{aligned}
\frac{\hat{H}^{\rm I}_{\rm eff}}{\hbar} = {} & K_{\rm a}\left(\hat{a}\mathrm{e}^{-i(2\omega-\delta)t} + \hat{a}^\dagger \mathrm{e}^{+i(2\omega-\delta)t}\right)\hat{\sigma}_z + K_{\rm b}\left(\hat{b}\mathrm{e}^{-i\omega t} + \hat{b}^\dagger \mathrm{e}^{+i\omega t}\right)\hat{\sigma}_z \\
& + G_{\rm a}\left(\hat{a}\hat{\sigma}_+ \mathrm{e}^{+i\delta t} + \hat{a}\hat{\sigma}_- \mathrm{e}^{-i(4\omega-\delta)t} + \hat{a}^\dagger\hat{\sigma}_+\mathrm{e}^{+i(4\omega-\delta)t} + \hat{a}^\dagger\hat{\sigma}_-\mathrm{e}^{-i\delta t}\right) \\
& + G_{\rm b}\left(\hat{b}\hat{\sigma}_-\mathrm{e}^{-i3\omega t} + \hat{b}^\dagger\hat{\sigma}_+\mathrm{e}^{+i3\omega t}\right) \\
& - 2\frac{K_{\rm a}G_{\rm b}}{\omega}\Big(\hat{a}\hat{b}\hat{\sigma}_+\mathrm{e}^{-i(\omega-\delta)t} + \hat{a}\hat{b}^\dagger\hat{\sigma}_-\mathrm{e}^{-i(3\omega-\delta)t} \\
& \qquad + \hat{a}^\dagger\hat{b}\hat{\sigma}_+\mathrm{e}^{+i(3\omega-\delta)t} + \hat{a}^\dagger\hat{b}^\dagger\hat{\sigma}_-\mathrm{e}^{+i(\omega-\delta)t}\Big) \\
& - 2\frac{K_{\rm b}G_{\rm b}}{\omega}\left(\hat{b}^2\hat{\sigma}_+ + \hat{b}^{\dagger 2}\hat{\sigma}_- + \hat{b}^\dagger\hat{b}\hat{\sigma}_+\mathrm{e}^{+i2\omega t} + \hat{b}^\dagger\hat{b}\hat{\sigma}_-\mathrm{e}^{-i2\omega t}\right) \\
& - \frac{K_{\rm b}G_{\rm b}}{\omega}\left(\hat{\sigma}_+\mathrm{e}^{+i2\omega t} + \hat{\sigma}_-\mathrm{e}^{-i2\omega t}\right) \\
& + \frac{G_{\rm a}G_{\rm b}}{\omega}\left(\hat{a}\hat{b}\mathrm{e}^{-i(3\omega-\delta)t} + \hat{a}\hat{b}^\dagger\mathrm{e}^{-i(\omega-\delta)t} + \hat{a}^\dagger\hat{b}\mathrm{e}^{+i(\omega-\delta)t} + \hat{a}^\dagger\hat{b}^\dagger\mathrm{e}^{+i(3\omega-\delta)t}\right) \\
& + \frac{G_{\rm b}^2}{\omega}\left(\hat{b}^2\mathrm{e}^{-i2\omega t} + \hat{b}^{\dagger 2}\mathrm{e}^{+i2\omega t}\right)\hat{\sigma}_z + \frac{G_{\rm b}^2}{\omega}\left(\hat{b}^\dagger\hat{b}\hat{\sigma}_z + \hat{\sigma}_+\hat{\sigma}_-\right). \qquad \text{(C.24)}
\end{aligned}$$

When $|\delta| \ll \omega$ and $\max\{|K_{\rm a}|, |K_{\rm b}|, |G_{\rm a}|, |G_{\rm b}|\} \ll \omega$ we can perform a rotating-wave approximation and write

$$\begin{aligned}
\frac{\hat{H}^{\rm I}_{\rm eff}}{\hbar} = {} & G_{\rm a}\left(\hat{a}\hat{\sigma}_+\mathrm{e}^{+i\delta t} + \hat{a}^\dagger\hat{\sigma}_-\mathrm{e}^{-i\delta t}\right) \\
& - 2\frac{K_{\rm a}G_{\rm b}}{\omega}\left(\hat{b}^2\hat{\sigma}_+ + \hat{b}^{\dagger 2}\hat{\sigma}_-\right) + \frac{G_{\rm b}^2}{\omega}\left(\hat{b}^\dagger\hat{b} + \frac{1}{2}\right)\hat{\sigma}_z \\
= {} & -g\sin\theta\left(\hat{a}\hat{\sigma}_+\mathrm{e}^{+i\delta t} + \hat{a}^\dagger\hat{\sigma}_-\mathrm{e}^{-i\delta t}\right) \\
& + 4\frac{g_{\rm b}^2}{\Delta/\hbar}\sin^2\theta\cos\theta\left(\hat{b}^2\hat{\sigma}_+ + \hat{b}^{\dagger 2}\hat{\sigma}_-\right) + 2\frac{g_{\rm b}^2}{\Delta/\hbar}\sin^3\theta\left(\hat{b}^\dagger\hat{b} + \frac{1}{2}\right)\hat{\sigma}_z \qquad \text{(C.25)}
\end{aligned}$$

Here, we use $g \equiv g_{\rm a}$ and $\sin\theta = \Delta/2\hbar\omega$. We immediately identify the first term in the above equation to be the near-resonant Jaynes-Cummings interaction between the qubit and the resonator. The two-photon driving of the qubit, $(\hat{b}^2\hat{\sigma}_+ + \hat{b}^{\dagger 2}\hat{\sigma}_-)$, has a second-order coupling coefficient. This coefficient contains the factor $\cos\theta$ and, thus, the two-photon driving is forbidden at the qubit optimal point. There, only the $\hat{\sigma}_z$-terms, i.e., the AC-Stark and Lamb shifts, survive. Hence, also this formalism recovers the features of electric-dipole-type selection rules and controlled symmetry breaking discussed in chapter 5.

Finally, we recover the classical driving by replacing the quantized driving with a coherent state $|\beta\rangle$. We use the relations $\hat{b}\,|\beta\rangle = \beta\,|\beta\rangle$ and $\langle\beta|\,\hat{b}^\dagger = \beta^\star\,\langle\beta|$ and choose $\beta = \beta^\star$ to be real because the global phase of the driving is unimportant for our considerations. In this situation, the interaction Hamiltonian for the classical

driving becomes

$$\begin{aligned}\frac{\hat{H}_{\rm eff}^{\rm I,cl}}{\hbar} = & -g\sin\theta\left(\hat{a}\hat{\sigma}_{+}\mathrm{e}^{+i\delta t}+\hat{a}^{\dagger}\hat{\sigma}_{-}\mathrm{e}^{-i\delta t}\right)\\ & +4\frac{g_{\rm b}^2\beta^2}{\Delta/\hbar}\sin^2\theta\cos\theta\left(\hat{b}^2\hat{\sigma}_{+}+\hat{b}^{\dagger 2}\hat{\sigma}_{-}\right)+2\frac{g_{\rm b}^2}{\Delta/\hbar}\sin^3\theta\left(\beta^2+\frac{1}{2}\right)\hat{\sigma}_z\end{aligned} \tag{C.26}$$

The coherent state β can be considered equivalent to a classical field only for large photon numbers, i.e., for $\beta^2 \gg 1$. Then, our definition of the driving amplitude $\Omega/4 \equiv \hbar g_{\rm b}\beta$ yields

$$\begin{aligned}\hat{H}_{\rm eff}^{\rm I,cl} = & -\hbar g\sin\theta\left(\hat{a}\hat{\sigma}_{+}\mathrm{e}^{+i\delta t}+\hat{a}^{\dagger}\hat{\sigma}_{-}\mathrm{e}^{-i\delta t}\right)\\ & +\frac{\Omega^2}{4\Delta}\sin^2\theta\cos\theta\,\hat{\sigma}_x+\frac{\Omega^2}{8\Delta}\sin^3\theta\,\hat{\sigma}_z\,.\end{aligned} \tag{C.27}$$

This is exactly the same result as the one of Eq. (5.4) found with the commutator theorem in chapter 5 and appendix C.1.2.

C.3 Bessel expansion in a nonuniformly rotating frame

In this section, we shed some light on the appearance of higher multiphoton excitations of a driven qubit-resonator system. Our derivations are inspired by the work presented in Ref. [55] on Landau-Zener interferometry on a flux qubit. We note that our discussion takes us beyond this result in two major aspects. First of all, we investigate a driven qubit-resonator system instead of a mere driven qubit[1]. Second, and more importantly, our flux qubit does not satisfy the condition $\Delta \ll \epsilon$ near the qubit-resonator anticrossing. The latter is particularly important for the interpretation of the results, as we will see below.

C.3.1 Weak-driving regime

As in the Dyson-series approach of appendix C.1.2, we begin our analysis with the first-order Hamiltonian in the diabatic basis,

$$\hat{H} = \frac{\epsilon}{2}\hat{\sigma}_z+\frac{\Delta}{2}\hat{\sigma}_x+\hbar\omega_{\rm r}\left(\hat{a}^{\dagger}\hat{a}+\frac{1}{2}\right)+\hbar g\left(\hat{a}^{\dagger}+\hat{a}\right)\hat{\sigma}_z+\frac{\Omega}{2}\hat{\sigma}_z\cos\omega t\,, \tag{C.28}$$

where the direct cavity driving is already neglected. Higher-order Hamiltonians can now be derived by means of a time-dependent unitary transformation into a nonuniformly rotating frame [55, 159],

$$\begin{gathered}\hat{H}_{\rm eff} = \hat{U}^{\dagger}\hat{H}\hat{U}-i\hbar\hat{U}\dot{\hat{U}}^{\dagger}\,,\\ \hat{U}\equiv\mathrm{e}^{+i(\lambda/2)\sin\omega t\,\hat{\sigma}_z}\,,\quad \hat{U}^{\dagger}\equiv\mathrm{e}^{-i(\lambda/2)\sin\omega t\,\hat{\sigma}_z}\,,\quad \lambda\equiv\Omega/\hbar\omega\geq 0\,.\end{gathered} \tag{C.29}$$

[1] In this context, we acknowledge that the appearance of selection rules for a driven qubit coupled to a dissipative bath was studied theoretically in the framework of Floquet theory [159]. The results can be mapped to a driven qubit-resonator system [160]. However, the important concept of *controlled symmetry breaking* is not discussed in these works.

This transformation yields the Hamiltonian

$$\hat{H}' = \frac{\epsilon}{2}\hat{\sigma}_z + \frac{\Delta}{2}\Big(\hat{\sigma}_- \mathrm{e}^{-i\lambda\sin\omega t} + \hat{\sigma}_+ \mathrm{e}^{+i\lambda\sin\omega t}\Big) + \hbar g\left(\hat{a}^\dagger + \hat{a}\right)\hat{\sigma}_z\,. \tag{C.30}$$

The exponential sine functions can be expanded into Bessel series,

$$\begin{aligned}
&\Big(\hat{\sigma}_- \mathrm{e}^{-i\lambda\sin\omega t} + \hat{\sigma}_+ \mathrm{e}^{+i\lambda\sin\omega t}\Big) \\
&= \quad \hat{\sigma}_-\left[J_0(\lambda) + 2\sum_{n=1}^{\infty} J_{2n}(\lambda)\cos 2n\omega t - 2i\sum_{n=1}^{\infty} J_{2n-1}(\lambda)\sin(2n-1)\omega t\right] \\
&\quad + \hat{\sigma}_+\left[J_0(\lambda) + 2\sum_{n=1}^{\infty} J_{2n}(\lambda)\cos 2n\omega t + 2i\sum_{n=1}^{\infty} J_{2n-1}(\lambda)\sin(2n-1)\omega t\right] \\
&= J_0(\lambda)\,\hat{\sigma}_x + 2\sum_{n=1}^{\infty} J_{2n}(\lambda)\cos 2n\omega t\,\hat{\sigma}_x - 2\sum_{n=1}^{\infty} J_{2n-1}(\lambda)\sin(2n-1)\omega t\,\hat{\sigma}_y\,.
\end{aligned} \tag{C.31}$$

With $\omega_\epsilon \equiv \epsilon/\hbar$ and $\omega_\Delta \equiv \Delta/\hbar$, the Hamiltonian of Eq. (C.30) can now be rewritten as

$$\begin{aligned}
\frac{\hat{H}'}{\hbar} = \frac{\omega_\epsilon}{2}\hat{\sigma}_z + \frac{\omega'_\Delta}{2}\hat{\sigma}_x + \omega_\mathrm{r}\hat{a}^\dagger\hat{a} + g\left(\hat{a}^\dagger + \hat{a}\right)\hat{\sigma}_z \\
+ \omega_\Delta\sum_{n=1}^{\infty} J_{2n}(\lambda)\cos 2n\omega t\,\hat{\sigma}_x - \omega_\Delta\sum_{n=1}^{\infty} J_{2n-1}(\lambda)\sin(2n-1)\omega t\,\hat{\sigma}_y\,.
\end{aligned} \tag{C.32}$$

We note that the above Hamiltonian is still in the diabatic basis $|\pm\rangle$. The expression $\omega'_\Delta \equiv J_0(\lambda)\,\omega_\Delta = \mathrm{J}_0(\Omega/\omega)\omega_\Delta$ is discussed in appendix C.3.2. Here, we focus on the weak-driving regime $\lambda \ll 1$, where $\omega'_\Delta \approx \omega_\Delta$. A rotation into the qubit eigenbasis yields

$$\begin{aligned}
\frac{\hat{H}'}{\hbar} = \frac{\omega_\mathrm{ge}}{2}\hat{\sigma}_z + \omega_\mathrm{r}\hat{a}^\dagger\hat{a} + g\left(\cos\theta\,\hat{\sigma}_z - \sin\theta\,\hat{\sigma}_x\right)\left(\hat{a}^\dagger + \hat{a}\right) \\
+ \omega_\Delta\sum_{n=1}^{\infty} J_{2n}(\lambda)\cos 2n\omega t\left(\sin\theta\,\hat{\sigma}_z + \cos\theta\,\hat{\sigma}_x\right) \\
- \omega_\Delta\sum_{n=1}^{\infty} J_{2n-1}(\lambda)\sin(2n-1)\omega t\,\hat{\sigma}_y\,.
\end{aligned} \tag{C.33}$$

The above Hamiltonian already exhibits the main features of the multiphoton driving: In contrast to the odd transition terms ($\hat{\sigma}_y$), the even ones ($\hat{\sigma}_x$) contain the factor $\cos\theta$ and, hence, vanish at the qubit optimal point.

Near the m-photon resonance, we can assume $\omega_\mathrm{ge} = m\omega$. Then, a transformation into the interaction picture with respect to the qubit and resonator, $\hat{\sigma}_\pm \to \hat{\sigma}_\pm \mathrm{e}^{\pm i\omega_\mathrm{ge}t}$, $\hat{a} \to \hat{a}\mathrm{e}^{-i\omega_\mathrm{r}t}$, and $\hat{a}^\dagger \to \hat{a}^\dagger\mathrm{e}^{+i\omega_\mathrm{r}t}$, yields the effective m-th order Hamiltonian

$$\begin{aligned}
\frac{\hat{H}^{(m)}_\mathrm{eff}}{\hbar} = \; & g\cos\theta\left(\hat{a}\mathrm{e}^{-i\omega_\mathrm{r}t} + \hat{a}^\dagger\mathrm{e}^{+i\omega_\mathrm{r}t}\right)\hat{\sigma}_z \\
& - g\sin\theta\left(\hat{a}\mathrm{e}^{-i\omega_\mathrm{r}t} + \hat{a}^\dagger\mathrm{e}^{+i\omega_\mathrm{r}t}\right)\left(\hat{\sigma}_+\mathrm{e}^{+im\omega t} + \hat{\sigma}_-\mathrm{e}^{-im\omega t}\right) \\
& + \frac{\omega_\Delta}{2}\sum_{n=1}^{\infty} J_{2n-1}(\lambda)\left(\mathrm{e}^{+i(2n-1)\omega t} - \mathrm{e}^{-i(2n-1)\omega t}\right)\left(\hat{\sigma}_+\mathrm{e}^{+im\omega t} - \hat{\sigma}_-\mathrm{e}^{-im\omega t}\right) \\
& + \frac{\omega_\Delta}{2}\cos\theta\sum_{n=1}^{\infty} J_{2n}(\lambda)\left(\mathrm{e}^{+i2n\omega t} + \mathrm{e}^{-i2n\omega t}\right)\left(\hat{\sigma}_+\mathrm{e}^{+im\omega t} + \hat{\sigma}_-\mathrm{e}^{-im\omega t}\right)\,.
\end{aligned} \tag{C.34}$$

Under the conditions $|g\sin\theta| \ll (m\omega + \omega_{\rm r})$ and $|g\cos\theta| \ll \omega_{\rm r}$, we can perform a rotating-wave approximation. Then the effective m-photon Hamiltonian can be written as the sum of a qubit-resonator contribution $\hat{\tilde{H}}_{\rm r,eff}$ and a qubit-driving contribution $\hat{H}^{(m)}_{\rm q,eff}$, i.e.,

$$\hat{H}^{(m)}_{\rm eff} = \hat{\tilde{H}}_{\rm r,eff} + \hat{H}^{(m)}_{\rm q,eff}\,. \tag{C.35}$$

The qubit-resonator contribution

$$\hat{\tilde{H}}_{\rm r,eff} = -\hbar g\sin\theta^{\star}\left(\hat{a}\hat{\sigma}_{+}\mathrm{e}^{+i\delta t} + \hat{a}^{\dagger}\hat{\sigma}_{-}\mathrm{e}^{-i\delta t}\right) \tag{C.36}$$

is exactly equivalent to the one found in chapter 5, appendix C.1, and appendix C.2. The qubit contribution is directly affected by the driving. Introducing the indices $n_{\rm e}$ for the even photon processes and $n_{\rm o}$ for the odd ones, the qubit-driving contribution reads

$$\begin{aligned}\hat{H}_{\rm q,eff} = &+\hbar\frac{\omega_\Delta}{2}\cos\theta\sum_{n_{\rm e}=1}^{\infty}J_{2n}(\lambda)\Big[\;\hat{\sigma}_{+}\left(\mathrm{e}^{+i(m-2n)\omega t}+\mathrm{e}^{+i(m+2n)\omega t}\right)\\ &\qquad+\hat{\sigma}_{-}\left(\mathrm{e}^{-i(m-2n)\omega t}+\mathrm{e}^{-i(m+2n)\omega t}\right)\Big]\\ &-\hbar\frac{\omega_\Delta}{2}\sum_{n_{\rm o}=1}^{\infty}J_{2n-1}(\lambda)\Big[\;\hat{\sigma}_{+}\left(\mathrm{e}^{+i(m-2n+1)\omega t}-\mathrm{e}^{+i(m+2n-1)\omega t}\right)\\ &\qquad+\hat{\sigma}_{-}\left(\mathrm{e}^{-i(m-2n+1)\omega t}-\mathrm{e}^{-i(m+2n-1)\omega t}\right)\Big]\,.\end{aligned} \tag{C.37}$$

We analyze the above equation for one-photon ($m=1$), two-photon ($m=2$), and three-photon ($m=3$) driving. Time-independent terms are obtained only when $m = 2n_{\rm e}$ or $m = 2n_{\rm o} - 1$. For $m = 1, 2, 3$ this corresponds to $n_{\rm o} = 1$, $n_{\rm e} = 1$, and $n_{\rm o} = 2$, respectively. In the limit of weak driving, the remaining rotating terms can only produce shifts. The exact evaluation of these shifts is complicated by the fact that we are working in the nonuniformly rotating frame. For the purpose of this work, we focus on the time-independent transition terms. Expanding the Bessel functions in power series and keeping only the lowest order yields

$$\begin{aligned}
&\text{one-photon} && \frac{\hat{H}^{(1)}_{\rm q,eff}}{\hbar} = -\frac{\omega_\Delta}{2}\frac{\Omega}{2\hbar\omega}\hat{\sigma}_x = -\frac{\Omega}{4}\Big[\quad\sin\theta\quad\Big]\hat{\sigma}_x\\
&\text{two-photon} && \frac{\hat{H}^{(2)}_{\rm q,eff}}{\hbar} = \frac{\omega_\Delta}{2}\cos\theta\frac{\Omega^2}{8\hbar^2\omega^2}\hat{\sigma}_x = +\frac{\Omega}{4}\left[\left(\frac{\Omega}{\Delta}\right)\sin^2\theta\cos\theta\right]\hat{\sigma}_x\\
&\text{three-photon} && \frac{\hat{H}^{(3)}_{\rm q,eff}}{\hbar} = -\frac{\omega_\Delta}{2}\frac{\Omega^3}{48\hbar^3\omega^3}\hat{\sigma}_x = -\frac{\Omega}{4}\left[\;\frac{9}{8}\left(\frac{\Omega}{\Delta}\right)^2\sin^3\theta\;\right]\hat{\sigma}_x
\end{aligned} \tag{C.38}$$

For one- and two-photon process, the above results coincide with those found in chapter 5, appendix C.1, and appendix C.2. As expected, the three-photon process is allowed at the qubit optimal point.

C.3.2 Beyond the weak-driving regime

In this section we investigate the shifts of the multi-photon resonance peaks beyond the weak driving regime, i.e., for $\Omega \lesssim 3\Delta$. To this end, we compare analytical

results from this work and from the literature to spectroscopy simulations with the time-averaging method (cf. appendix D.1) and with the Lindblad formalism (cf. appendix D.2). Since in our analytical results the qubit-resonator and qubit-driving contributions constitute separate terms in the final effective Hamiltonians, we study a driven two-level system without resonator in this section. The corresponding first-order Hamiltonian is

$$\hat{H}_{\mathrm{q}} = \frac{\epsilon}{2}\hat{\sigma}_z + \frac{\Delta}{2}\hat{\sigma}_x + \frac{\Omega}{2}\cos\omega t\,\hat{\sigma}_z\,. \tag{C.39}$$

We first analyze the effective first-order Hamiltonian. To this end, we rotate $\hat{H}_{\mathrm{q}}$ into the energy eigenbasis and perform a transformation into the interaction picture with respect to the qubit, $\hat{\sigma}_\pm \to \hat{\sigma}_\pm \mathrm{e}^{\pm i\omega_{\mathrm{ge}}t}$. Under resonant conditions, $\omega_{\mathrm{ge}} = \omega$, and by applying the commutator theorem of Eq. (C.4) to the rotating terms we obtain the effective first-order Hamiltonian

$$\hat{H}^{(1)}_{\mathrm{q,eff}} = -\frac{\Omega}{4}\sin\theta\,\hat{\sigma}_x + \frac{\Omega^2}{32\Delta}\sin^3\theta\,\hat{\sigma}_z\,. \tag{C.40}$$

The transition term ($\hat{\sigma}_x$-term) is consistent with the result found in chapter 5 and appendix C.3.1 and is valid for $(\Omega/4)\sin\theta \ll 2\hbar\omega_{\mathrm{ge}}$. At the qubit optimal point, the $\hat{\sigma}_z$-term of Eq. (C.40) describes the well-known Bloch-Siegert shift [159, 161], i.e., the center frequency of the resonance peak is

$$\widetilde{\omega} = \omega_{\mathrm{ge}} + \Omega^2/16\hbar\Delta\,. \tag{C.41}$$

In a second step, we transform the Hamiltonian of Eq. (C.39) to the nonuniformly rotating frame in order to gain insight into the multiphoton driving. Following the procedure shown in appendix C.3.1, we obtain

$$\begin{aligned}\frac{\hat{H}'}{\hbar} = {}& \frac{\omega'_{\mathrm{ge}}}{2}\hat{\sigma}_z + \omega'_\Delta \sum_{n=1}^{\infty} J_{2n}(\lambda)\cos 2n\omega t\left(\sin\theta'\,\hat{\sigma}_z + \cos\theta'\,\hat{\sigma}_x\right)\\ & - \omega'_\Delta \sum_{n=1}^{\infty} J_{2n-1}(\lambda)\sin(2n-1)\omega t\,\hat{\sigma}_y\,.\end{aligned} \tag{C.42}$$

Here, $\lambda = \Omega/\hbar\omega$, $\omega'_\Delta \equiv J_0(\lambda)\,\omega_\Delta$, $\omega'_{\mathrm{ge}} \equiv \sqrt{\omega_\epsilon^2 + \omega_\Delta'^2}$, $\sin\theta' \equiv \omega'_\Delta/\omega'_{\mathrm{ge}}$, and $\cos\theta' \equiv \omega_\epsilon/\omega'_{\mathrm{ge}}$. The expression ω'_Δ represents an effective tunneling matrix element and is known in the literature in the context of "coherent destruction of tunneling" [159, 162–168]. This means that under high-frequency driving ($\omega \gg \omega_\Delta$) of suitable amplitude[2], $J_0(\lambda)$ vanishes. In this situation, for the initial state $|-\rangle$ (eigenstate in the diabatic basis $\{|-\rangle, |+\rangle\}$) the probability $P_{|-\rangle}$ to find the qubit in $|-\rangle$ is unity for all times [159, 169]. The high-frequency limit can be realized by either strongly off-resonant driving or, alternatively, $\epsilon \gg \Delta$ and resonant driving [31, 55–58].

In this work, however, we focus on qubit spectroscopy, where the initial state of the qubit is the ground state $|\mathrm{g}\rangle$, which is an eigenstate of the energy eigenbasis (or adiabatic basis) $\{|\mathrm{g}\rangle, |\mathrm{e}\rangle\}$. Also, the quantity of interest is the equilibrium value of the probability P_{e} to find the qubit in the excited state $|\mathrm{e}\rangle$. Furthermore, we are not interested in the high-frequency driving regime. Instead, we are concerned with two

[2]The first root of the $J_0(\lambda)$ occurs for $\lambda = \Omega/\hbar\omega \simeq 2.4$.

quite different regimes. The first one describes resonant one-photon driving for $\epsilon \lesssim \Delta$. For the particular case of $\epsilon = 0$, this implies $\omega \approx \omega_\Delta$. In absence of dissipation, the effective Rabi-frequency is not expected to be significantly different from the one obtained from the first-order Hamiltonian of Eq. (C.39) under the rotating-wave approximation [168]. As a consequence, even when the weak-driving condition is not satisfied, no Bloch-Siegert shift is expected in the time-trace-averaging simulation results for this scenario. The second regime of interest is the adiabatic regime, $\omega \ll \omega_\Delta$, which can be used to describe multi-photon spectroscopy. Following [164], for $\epsilon = 0$ the center frequencies of the m-photon spectroscopy peaks can be written as

$$\widetilde{\omega}^{(m)} = \frac{2\omega_\Delta}{n\pi}\sqrt{1+q^2}\,E\left(\frac{q}{\sqrt{1+q^2}}\right), \tag{C.43}$$

where $q = q(\Omega) \equiv \Omega/(\hbar\omega_\Delta)$, $E(k)$ is the complete elliptic integral of the second kind, and $n = 3, 5, 7, \ldots$ is the order of the uneven photon excitations. Eq. (C.43) reduces to the linear relation $\widetilde{\omega}^{(m)} = 2\Omega/(n\pi\hbar)$ for strong driving, $\Omega \gg \hbar\omega_\Delta$. For the two-photon driving peaks, which appear in the case of $\epsilon = \Delta \neq 0$, the weak-driving treatments presented in appendix C.1 and appendix C.2 predict a shifted resonance with the center frequency

$$\widetilde{\omega}^{(2)} = \frac{\omega_{\mathrm{ge}}}{2} + \frac{\Omega^2}{8\hbar\Delta}\sin^3\theta\,. \tag{C.44}$$

Next, we compare the theoretical considerations presented above with results obtained from numerical simulations. In Fig. C.1 we show the result of qubit spectroscopy simulations. The equilibrium probability P_{e} is plotted against the amplitude and the frequency of the driving signal. Two paradigmatic flux bias points are chosen, $\epsilon = 0$ and $\epsilon = \Delta$. In both cases, $\omega_{\mathrm{ge}} = 3.91\,\mathrm{GHz}$ in order to preserve the scale. The driving amplitude is varied between approximately 500 MHz and 12 GHz. Additionally, we compare the time-trace-averaging results (cf. appendix D.1) to those obtained using the Lindblad formalism (cf. appendix D.2). We note that in comparison to the description of appendix D we omit the resonator and choose slightly different parameters. For the time-trace-averaging results, P_{e} is computed from the average of a 500 ns long time trace consisting of 10^5 time points. In the Lindblad simulations we choose a relaxation time $T_1 = 140\,\mathrm{ns}$ and a dephasing time $T_\varphi = 2.4\,\mu\mathrm{s}$ for the qubit. P_{e} is taken to be the average over the last 5 ns of a 1 µs long time trace.

The spectroscopy simulation results for the qubit at the optimal point ($\epsilon = 0$) using the time-trace-averaging method are displayed in Fig. C.1(a). As expected, only the odd photon processes are present for symmetry reasons. Furthermore, no Bloch-Siegert shift can be observed for the one-photon resonance. Instead, the center frequency of the corresponding peak remains almost constant up to approximately 6 GHz driving amplitude[3]. An analytical motivation for this surprising result can be found in Ref. [168]. The center frequency of the odd multiphoton peaks is qualitatively described by Eq. (C.43). The quantitative agreement improves with increasing order m because the adiabatic condition $\omega \ll \omega_\Delta$ is fulfilled increasingly well. The impact of Lindblad-type dissipation on the spectroscopy simulations is

[3] Above this value, no clear maximum can be detected due to the overlap with the three-photon peak. Precise numerical fitting is not possible because the shape of the peaks is strongly irregular

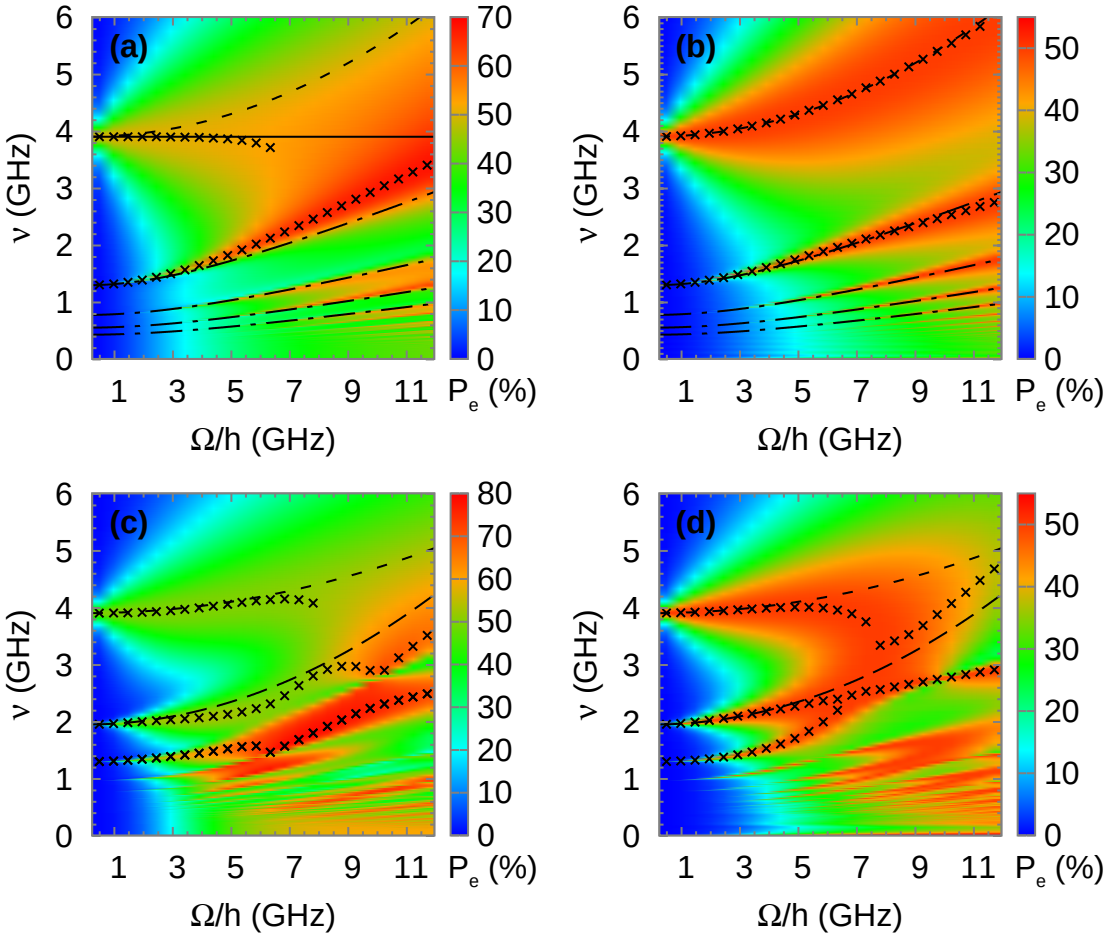

Figure C.1: Simulated probability P_e to find a driven qubit in $|\mathrm{e}\rangle$ plotted as a function of the driving frequency $\nu = \omega/2\pi$ and the driving amplitude Ω. The black crosses denote the center frequencies of the highest maxima. The short-dashed black lines represent the Bloch-Siegert-type shifts of Eq. (C.41) **(a)** The symmetric case $\epsilon = 0$, simulated using the time-trace-averaging method. The solid black line denotes the one-photon resonance condition $\omega = \omega_\Delta$, the dash-dotted black line the shift predicted by Eq (C.43) for $\omega \ll \omega_\Delta$. **(b)** As in (a), but simulated using the Lindblad approach. **(c)** The asymmetric case $\epsilon = \Delta$, simulated using the time-trace-averaging method. The long-dashed black line is the two-photon shift of Eq. (C.44). **(d)** As in (c), but simulated using the Lindblad approach.

shown in Fig. C.1(b). Notably, the Ω-dependence of the center frequency of the one-photon peak is excellently described by the second-order Bloch-Siegert shift of Eq. (C.41) throughout the whole range of the plot. Similarly, the center frequencies of multiphoton peaks agree almost perfectly with Eq. (C.43). This is remarkable because the derivation does not involve the effects of dissipation.

For $\epsilon = \Delta$, spectroscopy simulation results are presented in Fig. C.1(c) and Fig. C.1(d). Partially owing to the appearance of even-photon resonances, the overall structure is much more complicated compared to the symmetric case $\epsilon = 0$. In particular, it is not possible to clearly identify the order m of a resonance peak for driving amplitudes $\Omega/h \gtrsim 7\,\mathrm{GHz}$. In Fig. C.1(c), one can see that the time-averaging-method reproduces the Bloch-Siegert-type shift of Eq. (C.41) up to

$\Omega/h \simeq 6.5\,\mathrm{GHz}$ for the asymmetric qubit. The two-photon shift of Eq. (C.44) is only reproduced for driving amplitudes $\Omega/h \lesssim 2\,\mathrm{GHz}$. Analytical theory matches better with the center frequencies of the simulated two-photon peaks when switching to the Lindblad dissipative-bath approach. Inspecting Fig. C.1(d) yields an agreement up to $\Omega/h \simeq 4\,\mathrm{GHz}$ for both Bloch-Siegert and two-photon shift. For higher driving amplitude, the shift of the second maximum is less pronounced than the analytically predicted two-photon shift.

In conclusion, the simulation results presented in this section indicate that the effective second-order Hamiltonian for the two-photon driving presented in this work is valid for the driving strength found in chapter 5. Furthermore, we find that the dependence of the resonance spectrum on the driving amplitude becomes more complicated for an asymmetric than for a symmetric qubit. In general, the agreement between analytical theory and numerical simulations is better when using the Lindblad approach instead of the time-trace averaging method. Nevertheless, for parameters similar to those of chapter 5 the time-trace averaging method is still adequate. In specific situations, when the properties of the time-evolution of the Hamiltonian without explicit treatment of dissipations are studied, the time-trace-averaging simulations can be even superior to the Lindblad approach.

Appendix D

Spectroscopy simulations

The analytical solution of a problem in physics enables one to interpret measurement results in terms of the underlying mechanism. However, the corresponding calculations typically require severe simplifications of the actual experimental scenario, i.e., they shine a spot light onto a specific regime or feature rather than revealing the overall picture. Especially in a situation where it is not clear which simplifications are allowed, important insight can be gained by supplementing the analytics with computer-based numerical simulations. Although these give only a limited insight into the physical mechanisms, they help to understand to what degree the chosen model describes the experimental findings. In this way, numerical simulations act as a link between the measured data and analytical theory.

Based on this motivation, we perform numerical simulations of the qubit microwave spectroscopy experiments presented in chapter 5. In general, spectroscopy reveals information on the steady state of a driven system. Analytically, this is typically realized by considering the state of the system at the time $t \to \infty$. In an experiment or a simulation, the system must be driven for a time much longer than the shortest coherence time of the studied system before recording its state. In our specific case of microwave spectroscopy of a flux qubit coupled to an LC-resonator, we measure the probability to find the qubit in the excited state $|\mathrm{e}\rangle$ as a function of the driving frequency and the flux bias after a long microwave pulse. In this chapter, we discuss two different implementations of a qubit microwave spectroscopy simulator. First, in appendix D.1, we introduce a simple variant, which does not require the explicit treatment of dissipation on the level of the Hamiltonian. This is possible despite the fact that, at a first glance, there seems to be a conflict with the above definition of a spectroscopy experiment or simulation. Then, in appendix D.2, we discuss a more advanced version of qubit microwave spectroscopy based on the Lindblad formalism.

D.1 Time-trace-averaging method

In this section, we describe a simple but powerful method to simulate a qubit spectroscopy experiment without the explicit treatment of dissipation on the level of the Hamiltonian. First, we motivate the basic idea behind this method. The amplitude of driven qubit Rabi-oscillations is maximum when the driving and the qubit transition frequency are on resonance [6]. With increasing detuning from this resonance, the amplitude decreases with a Lorentz function behavior. In this situation,

the probability P_e^∞ to find the qubit in the excited state $|\mathrm{e}\rangle$ after an infinitely long time[1] is well approximated by the time average of $P_\mathrm{e}(t)$. Hence, we choose the name time-trace-averaging method. We compute $P_\mathrm{e}(t)$ numerically by solving the Schrödinger equation for the driven Hamiltonian $\hat{H}_\mathrm{d}$ of Eq. (5.2). The initial state is taken to be the ground state of the undriven Hamiltonian $\hat{H}_\mathrm{u}$ of Eq. (5.1). Finally, we compute the time average over a 100 ns time trace consisting of 10000 points. The number of basis states used for the discretization of the harmonic oscillator is 21. Care has to be taken when choosing length and resolution of the simulated time trace $P_\mathrm{e}(t)$. Short traces with low resolution shorten the execution time of the code and reduce the computer memory consumption. However, the simulation time has to be long enough to average out possible low-frequency beatings. Also, the resolution has to be high enough to capture high-frequency components of the traces properly. Since no terms describing dissipation are included in the Schrödinger equation, the linewidth of the simulated spectroscopy peaks is determined by the driving power.

One of the big advantages of the time-trace-averaging method is the fact that it works in the wave function formalism and does not require density matrices. In this way, the numerical effort is considerably reduced. Nevertheless, despite its intriguing simplicity, the time-trace-averaging method reproduces all main features of the experimental data as discussed in chapter 5. In particular, the energy level structure of the system is predicted properly and the order of the mutual inductances found from FastHenry [115] simulations is confirmed. Additionally, even the decay rate of the resonator is estimated reasonably well.

When using the time-trace-averaging method to perform spectroscopy simulations, it is important to be aware of its limitations. One of these resides in the fact that the method cannot be applied directly to systems with an infinite-dimensional Hilbert space, e.g., a driven harmonic oscillator. The latter is continuously excited to higher levels due to the absence of explicit decay mechanisms. Since in reality the number of basis states is limited to a finite number, artificial population oscillations occur. Such a result is completely different from the actual balancing mechanism based on resonator excitation and decay. Nevertheless, when the infinite-dimensional Hilbert space is coupled to a finite-dimensional one, such issues are partially resolved by probing only the latter. This is exactly the reason why the qubit microwave spectroscopy simulations of the qubit-resonator-fluctuator system presented in chapter 5 succeed to reproduce the experimental data so well. Another limitation of the time-trace-averaging method is that it is bound to fail when probing phenomena related to a particular dissipation mechanism. Then, the mechanism has to be included directly into the simulations. One common way to do that is the Lindblad formalism introduced in appendix D.2.

D.2 Lindblad approach

A system coupled to a dissipative bath can be described in terms of a Lindblad master equation in absence of memory effects in the bath. This situation is also called Markovian approximation. For a qubit-resonator system, which is subject to

[1] We use the symbol P_e instead of P_e^∞ in chapter 5 to make the notation less cumbersome. Thus, in order to avoid confusion, we explicitly write $P_\mathrm{e}(t)$ when referring to the time traces in this appendix.

qubit relaxation and dephasing as well as to resonator decay, this master equation can be written as [126, 170]

$$\frac{\partial \rho}{\partial t} = \frac{1}{i\hbar}\left(\hat{H}'_{\mathrm{d}}\rho - \rho\hat{H}'_{\mathrm{d}}\right) + \sum_{k=1}^{3}\gamma_k\left[\hat{L}_k\rho\hat{L}_k^{\dagger} - \frac{1}{2}\left(\hat{L}_k^{\dagger}\hat{L}_k\rho + \rho\hat{L}_k^{\dagger}\hat{L}_k\right)\right]. \tag{D.1}$$

Here, ρ is the density matrix of the system, which is defined as $\rho \equiv |\psi\rangle\langle\psi|$ for a pure state $|\psi\rangle$. The Hamiltonian $\hat{H}'_{\mathrm{d}}$ is found from $\hat{H}_{\mathrm{d}}$ of Eq. (5.2) by neglecting all terms related to the spurious fluctuator, $\hat{H}'_{\mathrm{d}} = \hat{H}_{\mathrm{d}} - \hat{H}_{\mathrm{f}} - \hat{H}_{\mathrm{q,f}} - \hat{H}_{\mathrm{m,q}}$. Since we are interested in characterizing the qubit-resonator anticrossing region, where the fluctuator is strongly off-resonant, the fluctuator can be safely neglected. We note that $(\partial\rho/\partial t) = (1/i\hbar)(\hat{H}'_{\mathrm{d}}\rho - \rho\hat{H}'_{\mathrm{d}})$ is the standard von-Neumann equation for the unitary time-evolution of ρ. The other terms of Eq. (D.1), the so-called Lindblad terms, describe the dissipation. For the qubit relaxation, one needs to substitute $\hat{L}_1 = \hat{\sigma}_-$ and $\hat{L}_1^{\dagger} = \hat{\sigma}_+$. The rate $\gamma_1 = \gamma_{\mathrm{r}} = T_1^{-1}$ is the qubit relaxation rate. For the qubit dephasing, one needs to substitute $\hat{L}_2 = \hat{L}_2^{\dagger} = \hat{\sigma}_z$ and $\gamma_2 = \gamma_\varphi/2$, where γ_φ is the pure dephasing rate. For the resonator decay one needs to substitute $\hat{L}_3 = \hat{a}$ and $\hat{L}_3^{\dagger} = \hat{a}^{\dagger}$. The resonator decay rate $\gamma_3 = \kappa = \omega_{\mathrm{r}}/Q$ can be expressed in terms of the quality factor Q. Within the simulated region shown in Fig. 5.3(e) and Fig. 5.3(f), the rates γ_φ and γ_{r} can be considered to be constants. P_{e}^{∞} is obtained by averaging over the last 5 ns of the time trace $P_{\mathrm{e}}(t)$. In order to maintain acceptable execution times of the code, the resonator discretization is restricted to 11 basis states. Although this number appears low, it is well sufficient for two reasons. First, in the two-photon anticrossing region the average resonator population $\langle\hat{N}(t)\rangle$ is always smaller than one due to the absence of direct resonator excitation. Second, a reasonable bosonic behavior of the resonator is guaranteed. As a cross-check, we verified that the code gives the expected results for the simulation of qubit relaxation and Ramsey experiments (without resonator) and for the resonator decay (without qubit).

Bibliography

[1] T. P. Orlando & K. A. Delin. *Foundations of Applied Superconductivity* (Addison-Wesley Publishing Company, New York, 1991).

[2] M. Tinkham. *Introduction to Superconductivity* (McGraw-Hill, New York, 1996).

[3] W. Buckel & R. Kleiner. *Superconductivity* (Wiley-VCH, Berlin, 2004).

[4] A. J. Leggett. Macroscopic Quantum Systems and the Quantum Theory of Measurement. *J. Prog. Theor. Phys.* **69**, 80–100 (1980).

[5] A. J. Leggett. In *Chance and Matter* (eds. J. Souletie, J. Vannimenus & R. Stora) 395 (Elsevier, Amsterdam, 1987).

[6] C. Cohen-Tannoudji, B. Diu & F. Laloë. *Quantum Mechanics* (Wiley-Interscience, New York, 1977).

[7] M. A. Nielsen & I. L. Chuang. *Quantum Computation and Quantum Information* (Cambridge University Press, Cambridge, 2000).

[8] D. Deutsch. Quantum Theory, the Church-Turing principle and the universal quantum computer. *Proc. R. Soc. London, Ser. A* **400**, 97–117 (1985).

[9] D. Deutsch & R. Jozsa. Rapid Solution of Problems by Quantum Computation. *Proc. R. Soc. London, Ser. A* **439**, 553–558 (1992).

[10] P. W. Shor. Algorithms for quantum computation, discrete log and factoring. In *Proceedings of the 35th Annual Symposium on the Foundations of Computer Science* (ed. S. Goldwasser) 124–134 (IEEE Computer Society, Los Alamitos, 1994).

[11] L. K. Grover. A fast quantum mechanical algorithm for database search. In *Proceedings of the Twenty-Eighth Annual Symposium on Theory of Computing* 212–219 (ACM, New York, 1996).

[12] D. R. Simon. On the power of quantum computation. *SIAM J. Comput.* **26**, 1474–1483 (1997).

[13] P. W. Shor. Polynomial-time algorithms for prime factorization and discrete logarithms on a quantum computer. *SIAM J. Comput.* **26**, 1484–1509 (1997).

[14] R. P. Feynman. Simulating Physics with Computers. *Int. J. Theo. Phys.* **81**, 467–488 (1982).

[15] K. K. Likharev. *Dynamics of Josephson Junctions and Circuits* (Taylor & Francis Ltd., Gordon and Breah Publishers, 1986).

[16] Yu. Makhlin, G. Schön & A. Shnirman. Quantum-state engineering with Josephson-junction devices. *Rev. Mod. Phys.* **73**, 357–400 (2001).

[17] M. H. Devoret, A. Wallraff & J. M. Martinis. Superconducting qubits: A short review. `arXiv:cond-mat/0411174v1` (2004).

[18] G. Wendin & V. S. Shumeiko. In *Handbook of Theoretical and Computational Nanotechnology* Vol. 3 (eds. M. Rieth & W. Schommers) 223–309 (American Scientific Publishers, Los Angeles, 2006).

[19] J. Clarke & F. K. Wilhelm. Superconducting quantum bits. *Nature* **453**, 1031–1042 (2008).

[20] Y. Nakamura, Yu. A. Pashkin & J. S. Tsai. Coherent control of macroscopic quantum states in a single-Cooper-pair box. *Nature (London)* **398**, 786–788 (1999).

[21] D. Vion, A. Aassime, A. Cottet, P. Joyez, H. Pothier, C. Urbina, D. Esteve & M. H. Devoret. Manipulating the Quantum State of an Electrical Circuit. *Science* **296**, 886–889 (2002).

[22] J. Koch, T. M. Yu, J. Gambetta, A. A. Houck, D. I. Schuster, J. Majer, A. Blais, M. H. Devoret, S. M. Girvin & R. J. Schoelkopf. Charge-insensitive qubit design derived from the Cooper pair box. *Phys. Rev. A* **76**, 042319 (2007).

[23] J. A. Schreier, A. A. Houck, J. Koch, D. I. Schuster, B. R. Johnson, J. M. Chow, J. M. Gambetta, J. Majer, L. Frunzio, M. H. Devoret, S. M. Girvin & R. J. Schoelkopf. Suppressing charge noise decoherence in superconducting charge qubits. *Phys. Rev. B* **77**, 180502(R) (2008).

[24] A. A. Houck, J. A. Schreier, B. R. Johnson, J. M. Chow, J. Koch, J. M. Gambetta, D. I. Schuster, L. Frunzio, M. H. Devoret, S. M. Girvin & R. J. Schoelkopf. Controlling the Spontaneous Emission of a Superconducting Transmon Qubit. *Phys. Rev. Lett.* **101**, 080502 (2008).

[25] J. R. Friedman, V. Patel, W. Chen, S. K. Tolpygo & J. E. Lukens. Quantum superposition of distinct macroscopic states. *Nature (London)* **406**, 43–46 (2000).

[26] Z. Zhou, S.-I Chu & S. Han. Quantum computing with superconducting devices: A three-level SQUID qubit. *Phys. Rev. B* **66**, 054527 (2002).

[27] T. P. Orlando, J. E. Mooij, L. Tian, C. H. van der Wal, L. S. Levitov, S. Lloyd & J. J. Mazo. Superconducting persistent-current qubit. *Phys. Rev. B* **60**, 15398–15413 (1999).

[28] J. E. Mooij, T. P. Orlando, L. Levitov, L. Tian, C. H. van der Wal & S. Lloyd. Josephson Persistent-Current Qubit. *Science* **285**, 1036–1039 (1999).

[29] J. M. Martinis, S. Nam, J. Aumentado & C. Urbina. Rabi Oscillations in a Large Josephson-Junction Qubit. *Phys. Rev. Lett.* **89**, 117901 (2002).

[30] R. W. Simmonds, K. M. Lang, D. A. Hite, S. Nam, D. P. Pappas & J. M. Martinis. Decoherence in Josephson Phase Qubits from Junction Resonators. *Phys. Rev. Lett.* **93**, 077003 (2004).

[31] Y. Nakamura, Yu. A. Pashkin & J. S. Tsai. Rabi Oscillations in a Josephson-Junction Charge Two-Level System. *Phys. Rev. Lett.* **87**, 246601 (2001).

[32] Y. Nakamura, Yu. A. Pashkin, T. Yamamoto & J. S. Tsai. Charge Echo in a Cooper-Pair Box. *Phys. Rev. Lett.* **88**, 047901 (2002).

[33] Y. Yu, S. Han, X. Chu, S.-I. Chu & Z. Wang. Coherent Temporal Oscillations of Macroscopic Quantum States in a Josephson Junction. *Science* **296**, 889–892 (2002).

[34] I. Chiorescu, Y. Nakamura, C. J. P. M. Harmans & J. E. Mooij. Coherent Quantum Dynamics of a Superconducting Flux Qubit. *Science* **299**, 1869–1871 (2003).

[35] F. Deppe, M. Mariantoni, E. P. Menzel, S. Saito, K. Kakuyanagi, H. Tanaka, T. Meno, K. Semba, H. Takayanagi & R. Gross. Phase coherent dynamics of a superconducting flux qubit with capacitive bias readout. *Phys. Rev. B* **76**, 214503 (2007).

[36] G. Ithier, E. Collin, P. Joyez, P. J. Meeson, D. Vion, D. Esteve, F. Chiarello, A. Shnirman, Yu. Makhlin, J. Schriefl & G. Schön. Decoherence in a superconducting quantum bit circuit. *Phys. Rev. B* **72**, 134519 (2005).

[37] J. M. Martinis, S. Nam, J. Aumentado, K. M. Lang & C. Urbina. Decoherence of a superconducting qubit due to bias noise. *Phys. Rev. B* **67**, 094510 (2003).

[38] E. Paladino, L. Faoro, G. Falci & R. Fazio. Decoherence and $1/f$ Noise in Josephson Qubits. *Phys. Rev. Lett.* **88**, 228304 (2002).

[39] J. M. Martinis, K. B. Cooper, R. MCDermott, M. Steffen, M. Ansmann, K. D. Osborn, K. Cicak, S. Oh, D. P. Pappas, R. W. Simmonds & C. C. Yu. Decoherence in Josephson Qubits from Dielectric Loss. *Phys. Rev. Lett.* **95**, 210503 (2005).

[40] M. Constantin & C. C. Yu. Microscopic Model of Critical Current Noise in Josephson Junctions. *Phys. Rev. Lett.* **88**, 228304 (2002).

[41] R. H. Koch, D. P. DiVincenzo & J. Clarke. Model for $1/f$ Flux Noise in SQUIDs and Qubits. *Phys. Rev. Lett.* **98**, 267003 (2007).

[42] G. Heinrich & F. K. Wilhelm. Current Fluctuations in Rough Superconducting Tunnel Junctions. `arXiv:0808.3705v1` (2008).

[43] A. Lupaşcu, P. Bertet, E. F. C. Driessen, C. J. P. M. Harmans & J. E. Mooij. One- and two-photon spectroscopy of a flux qubit coupled to a microscopic defect. `arXiv:0810.0590v1` (2008).

[44] F. Yoshihara, K. Harrabi, A. O. Niskanen, Y. Nakamura & J. S. Tsai. Decoherence of Flux Qubits due to $1/f$ Flux Noise. *Phys. Rev. Lett.* **97**, 167001 (2006).

[45] K. Kakuyanagi, T. Meno, S. Saito, H. Nakano, K. Semba, H. Takayanagi, F. Deppe & A. Shnirman. Dephasing of a Superconducting Flux Qubit. *Phys. Rev. Lett.* **98**, 047004 (2007).

[46] P. Bertet, I. Chiorescu, G. Burkard, K. Semba, C. J. P. M. Harmans, D. P. DiVincenzo & J. E. Mooij. Dephasing of a Superconducting Qubit Induced by Photon Noise. *Phys. Rev. Lett.* **95**, 257002 (2005).

[47] T. Yamamoto, Yu. A. Pashkin, O. Astafiev, Y. Nakamura & J. S. Tsai. Demonstration of conditional gate operation using superconducting charge qubits. *Nature (London)* **425**, 941–944 (2003).

[48] R. McDermott, R. W. Simmonds, M. Steffen, K. B. Cooper, K. Cicak, K. D. Osborn, S. Oh, D. P. Pappas & J. M. Martinis. Simultaneous State Measurement of Coupled Josephson Phase Qubits. *Science* **307**, 1299–1302 (2005).

[49] M. Steffen, M. Ansmann, R. C. Bialczak, N. Katz, E. Lucero, R. McDermott, M. Neeley, E. M. Weig, A. N. Cleland & J. M. Martinis. Measurement of the Entanglement of Two Superconducting Qubits via State Tomography. *Science* **313**, 1423–1425 (2006).

[50] J. H. Plantenberg, P. C. de Groot, C. J. P. M. Harmans & J. E. Mooij. Demonstration of controlled-NOT quantum gates on a pair of superconducting quantum bits. *Nature* **447**, 836–839 (2007).

[51] T. Hime, P. A. Reichardt, B. L. T. Plourde, T. L. Robertson, C.-E. Wu, A. V. Ustinov & J. Clarke. Solid-State Qubits with Current-Controlled Coupling. *Science* **314**, 1427–1429 (2006).

[52] J. Majer, J. M. Chow, J. M. Gambetta, J. Koch, B. R. Johnson, J. A. Schreier, L. Frunzio, D. I. Schuster, A. A. Houck, A. Wallraff, A. Blais, M. H. Devoret, S. M. Girvin & R. J. Schoelkopf. Coupling superconducting qubits via a cavity bus. *Nature* **449**, 443–447 (2007).

[53] M. A. Sillanpää, J. I. Park & R. W. Simmonds. Coherent quantum state storage and transfer between two phase qubits via a resonant cavity. *Nature* **449**, 438–442 (2007).

[54] A. Fay, E. Hoskinson, F. Lecocq, L. P. Lévy, F. W. J. Hekking, W. Guichard & O. Buisson. Strong Tunable Coupling between a Superconducting Charge and Phase Qubit. *Phys. Rev. Lett.* **100**, 187003 (2008).

[55] W. D. Oliver, Y. Yu, J. C. Lee, K. K. Berggren, L. S. Levitov & T. P. Orlando. Mach-Zehnder Interferometry in a Strongly Driven Superconducting Qubit. *Science* **310**, 1653–1657 (2005).

[56] S. Saito, T. Meno, M. Ueda, H. Tanaka, K. Semba & H. Takayanagi. Parametric Control of a Superconducting Flux Qubit. *Phys. Rev. Lett.* **96**, 107001 (2006).

[57] M. Sillanpää, T. Lehtinen, A. Paila, Y. Makhlin & P. Hakonen. Continuous-Time Monitoring of Landau-Zener Interference in a Cooper-Pair Box. *Phys. Rev. Lett.* **96**, 187002 (2006).

[58] C. M. Wilson, T. Duty, F. Persson, M. Sandberg, G. Johansson & P. Delsing. Coherence Times of Dressed States of a Superconducting Qubit under Extreme Driving. *Phys. Rev. Lett.* **98**, 257003 (2007).

[59] F. Deppe, M. Mariantoni, E. P. Menzel, A. Marx, S. Saito, K. Kakuyanagi, T. Meno, K. Semba, H. Takayanagi, E. Solano & R. Gross. Two-photon probe of the Jaynes-Cummings model and controlled symmetry breaking in circuit QED. *Nature Physics* **4**, 686–691 (2008).

[60] R. J. Thompson, G. Rempe & H. J. Kimble. Observation of normal-mode splitting for an atom in an optical cavity. *Phys. Rev. Lett.* **68**, 1132–1135 (1992).

[61] H. Mabuchi & A. C. Doherty. Cavity Quantum Electrodynamics: Coherence in Context. *Science* **298**, 1372–1377 (2002).

[62] S. Haroche & J.-M. Raimond. *Exploring the Quantum* (Oxford University Press Inc., New York, 2006).

[63] H. Walther, B. T. H. Varcoe, B.-G. Englert & T. Becker. Cavity Quantum Electrodynamics. *Rep. Prog. Phys.* **69**, 1325–1382 (2006).

[64] A. Blais, R.-S. Huang, A. Wallraff, S. M. Girvin & R. J. Schoelkopf. Cavity quantum electrodynamics for superconducting electrical circuits: An architecture for quantum computation. *Phys. Rev. A* **69**, 062320 (2004).

[65] A. Wallraff, D. I. Schuster, A. Blais, L. Frunzio, R.-S. Huang, J. Majer, S. Kumar, S. M. Girvin & R. J. Schoelkopf. Strong coupling of a single photon to a superconducting qubit using circuit quantum electrodynamics. *Nature* **431**, 162–167 (2004).

[66] I. Chiorescu, P. Bertet, K. Semba, Y. Nakamura, C. J. P. M. Harmans & J. E. Mooij. Coherent dynamics of a flux qubit coupled to a harmonic oscillator. *Nature* **431**, 159–162 (2004).

[67] M. Sandberg, C. M. Wilson, F. Persson, T. Bauch, G. Johansson, V. Shumeiko, T. Duty & P. Delsing. Tuning the field in a microwave resonator faster than the photon lifetime. *Appl. Phys. Lett.* **92**, 203501 (2008).

[68] D. I. Schuster, A. Wallraff, A. Blais, L. Frunzio, R.-S. Huang, J. Majer, S. M. Girvin & R. J. Schoelkopf. ac Stark Shift and Dephasing of a Superconducting Qubit Strongly Coupled to a Cavity Field. *Phys. Rev. Lett.* **94**, 123602 (2005).

[69] D. I. Schuster, A. A. Houck, J. A. Schreier, A. Wallraff, J. M. Gambetta, A. Blais, L. Frunzio, J. Majer, B. Johnson, M. H. Devoret, S. M. Girvin & R. J. Schoelkopf. Resolving photon number states in a superconducting circuit. *Nature* **445**, 515–518 (2007).

[70] R. J. Schoelkopf & S. M. Girvin. Wiring up quantum systems. *Nature* **451**, 664–669 (2008).

[71] J. Johansson, S. Saito, T. Meno, H. Nakano, M. Ueda, K. Semba & H. Takayanagi. Vacuum Rabi Oscillations in a Macroscopic Superconducting Qubit *LC* Oscillator System. *Phys. Rev. Lett.* **96**, 127006 (2006).

[72] J. M. Fink, M. Göppl, M. Baur, R. Bianchetti, P. J. Leek, A. Blais & A. Wallraff. Climbing the Jaynes-Cummings ladder and observing its $\sqrt{n}$ nonlinearity in a cavity QED system. *Nature* **454**, 315–318 (2008).

[73] L. S. Bishop, J. M. Chow, J. Koch, A. A. Houck, M. H. Devoret, E. Thuneberg, S. M. Girvin & R. J. Schoelkopf. Nonlinear response of the vacuum Rabi resonance. *Nature Physics* (advanced online publication) (2008).

[74] A. A. Houck, D. I. Schuster, J. M. Gambetta, J. A. Schreier, B. R. Johnson, J. M. Chow, L. Frunzio, J. Majer, M. H. Devoret, S. M. Girvin & R. J. Schoelkopf. Generating single microwave photons in a circuit. *Nature* **449**, 328–331 (2007).

[75] O. Astafiev, K. Inomata, A. O. Niskanen, T. Yamamoto, Yu. A. Pashkin, Y. Nakamura & J. S. Tsai. Single artificial-atom lasing. *Nature* **449**, 588–590 (2007).

[76] S. O. Valenzuela, W. D. Oliver, D. M. Berns, K. K. Berggren, L. S. Levitov & T. P. Orlando. Microwave-Induced Cooling of a Superconducting Qubit. *Science* **314**, 1589–1592 (2006).

[77] M. Grajcar, S. H. W. van der Ploeg, A. Izmalkov, E. Il'ichev, H.-G. Meyer, A. Fedorov, A. Shnirman & G. Schön. Sisyphus cooling and amplification by a superconducting qubit. *Nature Physics* **4**, 612–616 (2008).

[78] P. J. Leek, S. Filipp, P. Maurer, M. Baur, R. Bianchetti, J. M. Fink, M. Göppl, L. Steffen & A. Wallraff. Using Sideband Transitions for Two-Qubit Operations in Superconducting Circuits. `arXiv:0812.2678v1` (2008).

[79] S. Filipp, P. Maurer, P. J. Leek, M. Baur, R. Bianchetti, J. M. Fink, M. Göppl, L. Steffen, J. M. Gambetta, A. Blais & A. Wallraff. Two-Qubit State Tomography using a Joint Dispersive Read-Out. `arXiv:0812.2485v1` (2008).

[80] J. M. Fink, R. Bianchetti, M. Baur, M. Göppl, L. Steffen, S. Filipp, P. J. Leek, A. Blais & A. Wallraff. Collective Qubit States and the Tavis-Cummings Model in Circuit QED. `arXiv:0812.2651v1` (2008).

[81] F. Deppe, S. Saito, H. Tanaka & H. Takayanagi. Determination of the capacitance of nm scale Josephson junctions. *J. Appl. Phys.* **95**, 2607–2613 (2004).

[82] Y. Chen. Macroscopic Quantum Tunneling in a dc SQUID. *J. Low Temp. Phys.* **65**, 133–147 (1986).

[83] V. Ambegaokar & A. Baratoff. Tunneling Between Superconductors. *Phys. Rev. Lett.* **10**, 486–489 (1963).

[84] D. B. Tuckerman & J. H. Magerlein. Resonances in symmetric Josephson interferometers. *Appl. Phys. Lett.* **37**, 241–243 (1980).

[85] C. H. van der Wal, A. C. J. ter Haar, F. K. Wilhelm, R. N. Schouten, C. J. P. M. Harmans, T. P. Orlando, S. Lloyd & J. E. Mooij. Quantum Superposition of Macroscopic Persistent-Current States. *Science* **290**, 773–777 (2000).

[86] G. Schön & A. D. Zaikin. Distinguishing Phases in Josephson Junctions and the Choice of States. *Physica B* **152**, 203–206 (1988).

[87] T. P. Spiller, T. D. Clark, R. J. Prance & A. Widom. Quantum phenomena in circuits at low temperature. In *Progress in Low Temperature Physics* Vol. XIII (ed. D. F. Brewer) chap. 4, 219–265 (Elsevier, New York, 1992).

[88] D. P. DiVincenzo. The Physical Implementation of Quantum Computation. *Fortschr. Phys.* **48**, 771–783 (2000).

[89] L. M. K. Vandersypen, M. Steffen, G. Breyta, C. S. Yannoni, M. H. Sherwood & I. L. Chuang. Experimental realization of Shor's quantum factoring algorithm using nuclear magnetic resonance. *Nature (London)* **414**, 883–887 (2001).

[90] J. I. Cirac & P. Zoller. Quantum computation with cold trapped ions. *Phys. Rev. Lett.* **74**, 4091–4094 (1995).

[91] D. Leibfried, R. Blatt, C. Monroe & D. Wineland. Quantum dynamics of single trapped ions. *Rev. Mod. Phys* **75**, 281–324 (2003).

[92] J. Raimond, M. Brune & S. Haroche. Manipulating quantum entanglement with atoms and photons in a cavity. *Rev. Mod. Phys.* **73**, 565–582 (2001).

[93] C. Monroe. Quantum Information Processing with Atoms and Photons. *Nature (London)* **416**, 238–246 (2002).

[94] J. I. Cirac & P. Zoller. New Frontiers in Quantum Information with Atoms and Ions. *Phys. Today* **57**, 38–44 (March 2004).

[95] J. Clarke, A. N. Cleland, M. H. Devoret, D. Esteve & J. M. Martinis. Quantum Mechanics of a Macroscopic Variable: The Phase Difference of a Josephson Junction. *Science* **239**, 992–997 (1988).

[96] F. Schwabl. *Quantenmechanik* (Springer Verlag, Berlin, 2002).

[97] A. Blais, J. Gambetta, A. Wallraff, D. I. Schuster, S. M. Girvin, M. H. Devoret & R. J. Schoelkopf. Quantum-information processing with circuit quantum electrodynamics. *Phys. Rev. A* **75**, 032329 (2007).

[98] A. Wallraff, D. I. Schuster, A. Blais, L. Frunzio, J. Majer, M. H. Devoret, S. M. Girvin & R. J. Schoelkopf. Approaching Unit Visibility for Control of a Superconducting Qubit with Dispersive Readout. *Phys. Rev. Lett.* **95**, 060501 (2005).

[99] A. Wallraff, D. I. Schuster, A. Blais, J. M. Gambetta, J. Schreier, L. Frunzio, M. H. Devoret, S. M. Girvin & R. J. Schoelkopf. Sideband Transitions and Two-Tone Spectroscopy of a Superconducting Qubit Strongly Coupled to an On-Chip Cavity. *Phys. Rev. Lett.* **99**, 050501 (2007).

[100] M. Mariantoni, M. J. Storcz, F. K. Wilhelm, W. D. Oliver, A. Emmert, A. Marx, R. Gross, H. Christ & E. Solano. On-Chip Microwave Fock States and Quantum Homodyne Measurements. `arXiv:cond-mat/0509737v2` (2005).

[101] K. Moon & S. M. Girvin. Theory of Microwave Parametric Down-Conversion and Squeezing Using Circuit QED. *Phys. Rev. Lett.* **95**, 140504 (2005).

[102] M. Mariantoni, F. Deppe, A. Marx, R. Gross, F. K. Wilhelm & E. Solano. Two-resonator circuit quantum electrodynamics: A superconducting quantum switch. *Phys. Rev. B* **78**, 104508 (2008).

[103] Yu-xi. Liu, L. F. Wei & F. Nori. Generation of non-classical photon states using a superconducting qubit in a microcavity. *Europhys. Lett.* **67**, 941–947 (2004).

[104] E. T. Jaynes & F. W. Cummings. Comparison of quantum and semiclassical radiation theories with application to the beam maser. *Proc. IEEE* **51**, 89–109 (1963).

[105] I. Martin, L. Bulaevskii & A. Shnirman. Tunneling Spectroscopy of Two-Level Systems Inside a Josephson Junction. *Phys. Rev. Lett.* **95**, 127002 (2005).

[106] P. Dutta & P. M. Horn. Low-frequency fluctuations in solids: $1/f$ noise. *Rev. Mod. Phys.* **53**, 497–516 (1981).

[107] F. C. Wellstood, C. Urbina & J. Clarke. Low-frequency noise in dc superconducting quantum interference devices below 1K. *Appl. Phys. Lett.* **50**, 772–774 (1987).

[108] M. B. Weissman. $1/f$ noise and other slow, nonexponential kinetics in condensed matter. *Rev. Mod. Phys.* **60**, 537–571 (1988).

[109] P. Wahlgren, P. Delsing & D. B. Haviland. Crossover from global to local rule for the Coulomb blockade in small tunnel junctions. *Phys. Rev. B* **52**, R2293–R2296 (1995).

[110] A. Barone & G. Paternò. *Physics and Applications of the Josephson Effect* (Wiley-Interscience, New York, 1982).

[111] J. H. Magerlein. SPECIFIC CAPACITANCE OF JOSEPHSON TUNNEL JUNCTIONS. *IEEE Trans. Mag.* **MAG-17**, 286–289 (1981).

[112] K. Nabors & J. K. White. Fastcap: A multipole accelerated 3-D capacitance extraction program. *IEEE Trans. Computer-Aided Design* **10**, 1447–1459 (1991).

[113] FastCap capacitance analysis program. RLE Computational Prototyping Group, Boston.

[114] K. Kamon, M. J. Tsuk & J. K. White. Fasthenry: A Multipole Accelerated 3-D Inductance Extraction Program. *IEEE Trans. Microwave Theory Tech.* **42**, 1750–1758 (1994).

[115] FastHenry inductance analysis program. RLE Computational Prototyping Group, Boston.

[116] R. Meservey & P. M. Tedrow. Measurements of the Kinetic Inductance of Superconducting Linear Structures. *J. Appl. Phys.* **40**, 2028–2034 (1969).

[117] J. Schuler. *Ferromagnetische Einzelladungstransistoren*. Ph.D. thesis, TU München (2005).

[118] V. B. Braginsky & F. Ya. Khalili. *Quantum Measurement* (Cambridge Univ. Press, Cambridge, 1992).

[119] V. B. Braginsky & F. Ya. Khalili. Quantum nondemolition measurements: the route from toys to tools. *Rev. Mod. Phys.* **68**, 111 (1996).

[120] C. H. van der Wal. *Quantum Superpositions of Persistent Josephson Currents*. Ph.D. thesis, TU Delft (2001).

[121] C. van der Wal, F. Wilhelm, C. Harmans & J. Mooij. Engineering decoherence in Josephson persistent-current qubits. *Eur. Phys. J. B* **31**, 111–124 (2003).

[122] A. B. Zorin. Cooper-pair qubit and Cooper-pair electrometer in one device. *Physica C* **368**, 284–288 (2002).

[123] Ya.. S. Greenberg, A. Izmalkov, M. Grajcar, E. Il'ichev, W. Krech, H.-G. Meyer, M. H. S. Amin & A. Maassen van den Brink. Low-frequency characterization of quantum tunneling in flux qubits. *Phys. Rev. B* **66**, 214525 (2002).

[124] A. Lupaşcu, C. J. M. Verwijs, R. N. Schouten, C. J. P. M. Harmans & J. E. Mooij. Nondestructive Readout for a Superconducting Flux Qubit. *Phys. Rev. Lett.* **93**, 177006 (2004).

[125] A. Lupaşcu, C. J. P. M. Harmans & J. E. Mooij. Quantum state detection of a superconducting flux qubit using a dc-SQUID in the inductive mode. *Phys. Rev. B* **71**, 184506 (2005).

[126] T. Lindström, C. H. Webster, A. Ya. Tzalenchuk, J. E. Healey, M. S. Colclough & C. M. Muirhead. Circuit QED with a Flux Qubit Strongly Coupled to a Coplanar Transmission Line Resonator. *Supercond. Sci. Technol.* **20**, 814–821 (2007).

[127] I. Siddiqi, R. Vijay, F. Pierre, C. M. Wilson, M. Metcalfe, C. Rigetti, L. Frunzio & M. H. Devoret. RF-Driven Josephson Bifurcation Amplifier for Quantum Measurement. *Phys. Rev. Lett.* **93**, 207002 (2004).

[128] I. Siddiqi, R. Vijay, F. Pierre, C. M. Wilson, L. Frunzio, M. Metcalfe, C. Rigetti, R. J. Schoelkopf, M. H. Devoret, D. Vion & D. Esteve. Direct Observation of Dynamical Bifurcation between Two Driven Oscillation States of a Josephson Junction. *Phys. Rev. Lett.* **94**, 027005 (2005).

[129] I. Siddiqi, R. Vijay, M. Metcalfe, E. Boaknin, L. Frunzio, R. J. Schoelkopf & M. H. Devoret. Dispersive measurements of superconducting qubit coherence with a fast latching readout. *Phys. Rev. B* **73**, 054510 (2006).

[130] A. Lupaşcu, E. F. C. Driessen, L. Roschier, C. J. P. M. Harmans & J. E. Mooij. High-Contrast Dispersive Readout of a Superconducting Flux Qubit Using a Nonlinear Resonator. *Phys. Rev. Lett.* **96**, 127003 (2006).

[131] A. Lupaşcu, S. Saito, T. Picot, P. C. de Groot, C. J. P. M. Harmans & J. E. Mooij. Quantum non-demolition measurement of a superconducting two-level system. *Nature Physics* **3**, 119–125 (2007).

[132] H. Tanaka, Y. Sekine, S. Saito & H. Takayanagi. Single-Shot Readout of Macroscopic Quantum Superposition State in a Superconducting Flux Qubit. `arXiv:cond-mat/0407299v1` (2004).

[133] K. Bladh, D. Gunnarsson, E. Hürfeld, S. Devi, C. Kristoffersson, B. Smålander, S. Pehrson, T. Claeson, P. Delsing & M. Taslakov. Comparison of cryogenic filters for use in single electronics experiments. *Rev. Sci. Instrum.* **74**, 1323–1327 (2003).

[134] J. Walter, S. Corlevi & D. B. Haviland. Fast switching current detection at low critical currents. `arXiv:cond-mat/0403467v2` (2004).

[135] J. Walter, E. Tholén, J. Sjostrand & D. B. Haviland. Pulse and hold strategy for switching current measurements. *Phys. Rev. B* **75**, 094515 (2007).

[136] O. Astafiev, Yu. A. Pashkin, Y. Nakamura, T. Yamamoto & J. S. Tsai. Quantum Noise in the Josephson Charge Qubit. *Phys. Rev. Lett.* **93**, 267007 (2004).

[137] O. Astafiev, Yu. A. Pashkin, Y. Nakamura, T. Yamamoto & J. S. Tsai. Temperature Square Dependence of the Low Frequency $1/f$ Charge Noise in the Josephson Junction Qubits. *Phys. Rev. Lett.* **96**, 137001 (2006).

[138] A. Shnirman, Yu. Makhlin & G. Schön. Noise and Decoherence in Quantum Two-Level Systems. *Phys. Scr.* **T 102**, 147–154 (2002).

[139] Yu. Makhlin & A. Shnirman. Dephasing of Solid-State Qubits at Optimal Points. *Phys. Rev. Lett.* **92**, 178301 (2004).

[140] A. Shnirman, G. Schön, I. Martin & Yu. Makhlin. Low- and High-Frequency Noise from Coherent Two-Level Systems. *Phys. Rev. Lett.* **94**, 127002 (2005).

[141] R. K. Wangsness & F. Bloch. The Dynamical Theory of Nuclear Induction. *Phys. Rev.* **89**, 728–739 (1953).

[142] A. G. Redfield. On the Theory of Relaxation Processes. *IBM J. Res. Dev.* **1**, 19–31 (1957).

[143] Yu. Makhlin & A. Shnirman. Dephasing of qubits by transverse low-frequency noise. *JETP Lett.* **78**, 497–501 (2003).

[144] D. J. V. Harlingen, T. L. Robertson, B. L. T. Plourde, P. A. Reichardt, T. A. Crane & J. Clarke. Decoherence in Josephson-junction qubits due to critical-current fluctuations. *Phys. Rev. B* **70**, 064517 (2004).

[145] T. Meunier, S. Gleyzes, P. Maioli, A. Auffeves, G. Nogues, M. Brune, J. M. Raimond & S. Haroche. Rabi Oscillations Revival Induced by Time Reversal: A Test of Mesoscopic Quantum Coherence. *Phys. Rev. Lett.* **94**, 010401 (2005).

[146] G. Morigi, E. Solano, B.-G. Englert & H. Walther. Measuring irreversible dynamics of a quantum harmonic oscillator. *Phys. Rev. A* **65**, 040102(R) (2002).

[147] R. de Sousa. Electron spin as a spectrometer of nuclear spin noise and other fluctuations (Springer, 2008).

[148] Yu-xi. Liu, J. Q. You, L. F. Wei, C. P. Sun & F. Nori. Optical Selection Rules and Phase-Dependent Adiabatic State Control in a Superconducting Quantum Circuit. *Phys. Rev. Lett.* **95**, 087001 (2005).

[149] I. Schuster, A. Kubanek, A. Fuhrmanek, T. Puppe, P. W. H. Pinske, K. Murr & G. Rempe. Nonlinear spectroscopy of photons bound to one atom. *Nature Physics* **4**, 382–385 (2008).

[150] P. Lougovski, F. Casagrande, A. Lulli & E. Solano. Strongly driven one-atom laser and decoherence monitoring. *Phys. Rev. A* **76**, 033802 (2007).

[151] M. O. Scully & M. S. Zubairy. *Quantum optics* (Cambridge University Press, Cambridge, 1997).

[152] J. E. Mooij & C. Harmans. Phase-slip flux qubits. *New J. of Phys.* **7**, 219 (2005).

[153] M. Göppl, A. Fragner, M. Baur, R. Bianchetti, S. Filipp, J. M. Fink, P. J. Leek, G. Puebla, L. Steffen & A. Wallraff. Coplanar waveguide resonators for circuit quantum electrodynamics. *J. Appl. Phys.* **104**, 113904 (2008).

[154] Y. L. Lim, S. D. Barrett, A. Beige, P. Kok & L. C. Kwek. Repeat-until-success quantum computing using stationary and flying qubits. *Phys. Rev. A* **73**, 012304 (2006).

[155] S. J. van Enk, J. I. Cirac & P. Zoller. Photonic Channels for Quantum Communication. *Science* **279**, 205–208 (1998).

[156] D. M. Greenberger, M. A. Horne & A. Zeilinger. Going Beyond Bell's Theorem. In *Bell's Theorem, Quantum Theory, and Conceptions of the Universe* (ed. M. Kafatos) 69–72 (Kluwer, Dordrecht, 1989).

[157] G. J. Dolan. Offset masks for lift-off photoprocessing. *Appl. Phys. Lett.* **31**, 337–339 (1977).

[158] E. Solano. Private communication.

[159] M. Grifoni & P. Hänggi. Driven Quantum Tunneling. *Phys. Rep.* **304**, 229–354 (1998).

[160] M. C. Goorden, M. Thorwart & M. Grifoni. Spectroscopy of a driven solid-state qubit coupled to a structured environment. *Eur. Phys. B* **45**, 405–417 (2005).

[161] F. Bloch & A. Siegert. Magnetic Resonance for Nonrotating Fields. *Phys. Rev.* **57**, 522–527 (1940).

[162] F. Grossmann, T. Dittrich, P. Jung & P. Hänggi. Coherent destruction of tunneling. *Phys. Rev. Lett.* **67**, 516–519 (1991).

[163] F. Grossmann & P. Hänggi. Localization in a Driven Two-Level Dynamics. *Europhys. Lett.* **18**, 571–576 (1992).

[164] J. M. Gomez-Llorente & J. Plata. Tunneling control in a two-level system. *Phys. Rev. A* **45**, R6958–R6961 (1992).

[165] L. Wang & J. Shao. Localization of two-level systems. *Phys. Rev. A* **49**, R637–R640 (1994).

[166] H. Cheng, M.-L. Ge & J. Shao. Localization conditions for two-level systems. *Phys. Lett. A* **191**, 1–6 (1994).

[167] X.-G. Zhao. A formal solution of the evolution operator and its application in two-level systems. *Phys. Lett. A* **193**, 5–10 (1994).

[168] J. C. A. Barata & W. F. Wreszinski. Strong-Coupling Theory of Two-Level Atoms in Periodic Fields. *Phys. Rev. Lett.* **84**, 2112–2115 (2000).

[169] Y. Dakhnovskii & R. Bavli. Selective manipulation of the emission spectrum of an electron in a biased double-well heterostructure driven by a free-electron laser. *Phys. Rev. B* **48**, 11010–11013 (1993).

[170] H.-P. Breuer & F. Petruccione. *The theory of open quantum systems* (Oxford University Press, Oxford, 2004).

List of Publications

F. Deppe, S. Saito, H. Tanaka & H. Takayanagi. Determination of the capacitance of nm scale Josephson junctions. *J. Appl. Phys.* **95**, 2607–2613 (2004).

K. Kakuyanagi, T. Meno, S. Saito, H. Nakano, K. Semba, H. Takayanagi, F. Deppe & A. Shnirman. Dephasing of a Superconducting Flux Qubit. *Phys. Rev. Lett.* **98**, 047004 (2007).

F. Deppe, M. Mariantoni, E. P. Menzel, S. Saito, K. Kakuyanagi, H. Tanaka, T. Meno, K. Semba, H. Takayanagi & R. Gross. Phase coherent dynamics of a superconducting flux qubit with capacitive bias readout. *Phys. Rev. B* **76**, 214503 (2007).

F. Deppe, M. Mariantoni, E. P. Menzel, A. Marx, S. Saito, K. Kakuyanagi, T. Meno, K. Semba, H. Takayanagi, E. Solano & R. Gross. Two-photon probe of the Jaynes-Cummings model and controlled symmetry breaking in circuit QED. *Nature Physics* **4**, 686–691 (2008).

M. Mariantoni, F. Deppe, A. Marx, R. Gross, F. K. Wilhelm & E. Solano. Two-resonator circuit quantum electrodynamics: A superconducting quantum switch. *Phys. Rev. B* **78**, 104508 (2008).

Acknowledgments

In the very first place, I would like to express gratitude to my family, in particular to my wife, parents, and parents-in-law, for their support. And to my beautiful children, who help me every day to see the world from a very different angle.

I am particularly grateful to my advisor here at the Walther-Meißner-Institut, Rudolf Gross. Inn addition to the scientific discussions, he provided invaluable help "from home" for me during the time I spent in Japan.

Next, I want to thank Hideaki Takayanagi and Kouichi Semba for the opportunity to work in the Superconducting Quantum Physics Research Group at the NTT Basic Research Laboratories in Atsugi/Japan. All the experimental results shown in this thesis were obtained there. During my stay, in particular S. Saito, H. Tanaka, K. Kakuyanagi, T. Meno, H. Nakano, J. Johansson, A. Richter, A. Kasper, and T. Eichler greatly supported me in many theoretical, experimental, and organizational tasks. I will always remember the time in Japan as a unique experience.

Furthermore, I acknowledge many fruitful discussions with Matteo Mariantoni, Edwin P. Menzel, A. Marx, E. Hoffmann, G. Wild, T. Niemczyk, M. A. Araque Caballero, S. Dandl, and T. Weißl. All of them are current or former colleagues of the Qubit Group at the Walther-Meißner-Institut. Particularly the discussions with Matteo often were the key to a deeper understanding of experimental findings.

Finally, I would like to thank E. Solano, F. K. Wilhelm, and H. Christ for the valuable discussion about theoretical aspects of this work.